The impacts of land use-induced land cover change on climate extremes

Francia Bismonte Avila

Climate Change Research Centre and the

ARC Centre of Excellence for Climate System Science

Faculty of Science

The University of New South Wales, Sydney, Australia

A thesis submitted in fulfilment of the requirement for the degree of

Doctor of Philosophy

October 2012

COPYRIGHT STATEMENT

'I hereby grant the University of New South Wales or its agents the right to archive and to make available my thesis or dissertation in whole or part in the University libraries in all forms of media, now or here after known, subject to the provisions of the Copyright Act 1968. I retain all proprietary rights, such as patent rights. I also retain the right to use in future works (such as articles or books) all or part of this thesis or dissertation.

I also authorise University Microfilms to use the 350 word abstract of my thesis in Dissertation Abstract International (this is applicable to doctoral theses only). I have either used no substantial portions of copyright material in my thesis or I have obtained permission to use copyright material; where permission has not been granted I have applied/will apply for a partial restriction of the digital copy of my thesis or dissertation.'

FBAvila

Francia Bismonte Avila

15 Nov 2012

AUTHENTICITY STATEMENT

'I certify that the Library deposit digital copy is a direct equivalent of the final officially approved version of my thesis. No emendation of content has occurred and if there are any minor variations in formatting, they are the result of the conversion to digital format.'

FBAvila

Francia Bismonte Avila

15 Nov 2012

Originality Statement

'I hereby declare that this submission is my own work and to the best of my knowledge it contains no materials previously published or written by another person, or substantial proportions of material which have been accepted for the award of any other degree or diploma at UNSW or any other educational institution, except where due acknowledgement is made in the thesis. Any contribution made to the research by others, with whom I have worked at UNSW or elsewhere, is explicitly acknowledged in the thesis. I also declare that the intellectual content of this thesis is the product of my own work, except to the extent that assistance from others in the project's design and conception or in style, presentation and linguistic expression is acknowledged.'

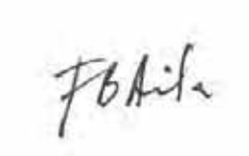

Francia Bismonte Avila
15 Nov 2012

Abstract

Simulations from the CSIRO Mk3L climate model, coupled to the CABLE land surface model, indicate that climate extremes indices are significantly affected by land use-induced land cover change (LULCC). The changes in the extremes are correlated to regions of intense LULCC and vary seasonally. The changes in temperature extremes are more spatially coherent than the change in precipitation extremes. Compared to the impact of doubling atmospheric carbon dioxide (CO_2), some indices are systematically affected by LULCC in the same direction as increasing CO_2 while for other indices LULCC opposes the impact of increasing CO_2. In some regions, the scale of the LULCC impact is of a magnitude similar to the impact of CO_2 alone. This suggests that increases in greenhouse gases alone cannot account for anthropogenically-induced changes in climate extremes as LULCC may regionally mask or amplify the impact of increasing CO_2 on climate extremes. The analysis performed on the Mk3L-CABLE model was applied to the simulations from independent models participating in the "Land-Use and Climate, IDentification of robust impacts" (LUCID) project. Results show that the changes in the temperature extremes are robust although not all the models agree on the degree and sign of the change. These differences between the models are explained by the differences in how the models imposed LULCC and how they calculated the changes in albedo and surface fluxes. The changes in the precipitation extremes were not as spatially coherent as those of the temperature extremes but these may be explained by the limited capacity of the models to simulate precipitation which may be related to model resolution or its sensitivity to LULCC processes that affect precipitation and associated processes.

Acknowledgements

This thesis is one of the fruits of the generosity and kindness of all those who accompanied me through my Ph.D. journey.

I would like to thank my supervisor, Prof. Andy Pitman, whose constant guidance and abundant patience got me through all the twists and turns, ups and downs of this incredible ride.

Thanks to my co-supervisor, Dr. Gab Abramowitz, and my other mentors at the CCRC: Dr. Lisa Alexander, Dr. Markus Donat, Dr. Steven Phipps, Dr. Steve Sherwood, Dr. Joe Kidston and Dr. Katrin Meissner, for inspiring, challenging and cheering me on.

Thanks to the LUCID group, especially Dr. Nathalie de Noblet-Ducoudré, Dr. Juan-Pablo Boisier Dr. Victor Brovkin, Dr. Veronika Gayler, Dr. Bart van den Hurk and Dr. Aurore Voldoire, for sharing their data and insights.

Thanks to Dr. Debbie Verzosa, Dr. Faye Cruz and Dr. Enzo dela Fuente for the friendship and laughter; and for the technical and moral support during my thesis writing.

Thanks to the many CCRC post-docs (especially Sarah Perkins, Andrea Taschetto, Laura Ciasto, Caro Ummenhofer and Agus Santoso) and students (Kat Borman, Ian McAdam, Karin Kvale, Penny Maher and Qian Zhang, to name a few) for sharing data, code and laughter. Special thanks to the Precipitation and Land Surface discussion groups for sharing their thoughts and time.

Thanks to the administrative staff at CCRC (Sophie, Stephen, Simone, Sarah, Vilia, Bronwen and Alvin); the IT staff at the NCI (Dr. Margaret Kahn), APAC data center and UNSW IT services (especially Chris Cannon); and the staff at the UNSW Library, Graduate Research School, Student Development International and Careers and Counselling for providing much needed support.

Thanks to the many families who welcomed me into their homes: the Holdsworths (John, Clovia, James and Mark), Frazers (Ross, Chrysnan, Thomas and Andrew), Castillos (Ella and Trey), Aldanas (Agnes and Linaia), Diazes (Manny, Girlie and Marielle), Singsons (Saidee, Sari and family), Remorozas (Alvin, Che and Atom) and Krazovitsky-Wainers (Irene and Simona).

Thanks to my friends for keeping me company: in Sydney (Faye, Debbie, Joyce, Reydick, Sunsan, Edwin, Joyeth, Delfin, Cel, Saidee, Nic, Ken and Kelvin) and online (especially Kath, Kai, Tatit, Tetet, Chi and Chie).

Thanks to my friends in MO and Ateneo: Faye, Liz, Carina, Niño, Genie, Randell, Melle, Grace, Soli, Toad, Sandee, K. Andy, John Ong, James Simpas, Nofel Lagrosas, Gemma Narisma, Marina Mallare and Karen Cardenas for showing me how to be a person for others.

Thanks to my mentors and spiritual fathers in Ateneo (Fr. Dan McNamara, Fr. Jett Villarin, Fr. Sergio Su, Fr. Vic Badillo, Dr. Emman Anglo and Dr. Mar Estoque) for keeping the light shining bright, constant and true.

Thanks to my family for giving me the freedom, the inspiration and the confidence to pursue my passion. Thank you, Pong; Jun, Julie and Jan-jan; Bing and Jasmin. *Nanay*, this is for you. *Tatay*, thanks for dreaming with me.

Thank you, Lord, for being with me: rain or shine, and through the dark and cold nights.

Ad majorem Dei gloriam.

Table of Contents

List of Figures

List of Tables

List of Acronyms

AR4	IPCC Fourth Assessment Report
ASCII	American Standard Code for Information and Interchange
BuFEx	Bunny Fence Experiment
CABLE	Community Atmosphere Biosphere Land Exchange
CAPE	Convective Available Potential Energy
CCAM	Conformal-Cubic Atmosphere Model
CCl	WMO Commission for Climatology
CLIVAR	WCRP project for climate variability and predictability
CMAP	CPC Merged Analysis of Precipitation
CMIP	Coupled Model Intercomparison Project
C20C	Climate of the 20th Century
CO_2	Carbon dioxide
CORDEX	COordinated Regional Downscaling EXperiment
CPC	Climate Prediction Center
CSIRO	Commonwealth Scientific and Industrial Research Organization
DJF	December-January-February
ETCCDI	Joint CCl/CLIVAR/JCOMM Expert Team on Climate Change Detection and Indices
IGBP	International Geosphere-Biosphere Program
IOC	Intergovernmental Oceanographic Commission
IPCC	Intergovernmental Panel on Climate Change
ISCCP-FD	International Satellite Cloud Climatology Project radiative flux profile dataset
ISLSCP II	International Satellite Land Surface Climatology Project, Initiative II
JCOMM	Joint WMO-IOC Technical Commission for Oceanography and Marine Meteorology
JJA	June-July-August
LAI	Leaf are index
LHF	Latent heat flux
LSM	Land Surface Model
LUCID	Land-Use and Climate, IDentification of robust impacts project
LULCC	Land-use induced land cover change
MAM	March-April-May
MODIS	Moderate Resolution Imaging Spectroradiometer project
NOAA	National Oceanic & Atmospheric Administration
O_3	Ozone
OI	Optimum Interpolation (e.g. NOAA OI SST V2 dataset)
SAR	IPCC Second Assessment Report
SON	September-October-November
SPM	Summary for Policy Makers
SRES	Special Report on Emissions Scenarios
SREX	Special Report on Managing the Risks of Extreme Events and Disasters to Advance Climate Change Adaptation
SST	Sea Surface Temperature
TAR	IPCC Third Assessment Report
UNESCO	United Nations Educational, Scientific and Cultural Organization
WCRP	World Climate Research Programme
WMO	World Meteorological Organization

Chapter 1
Introduction

Far from being just a topic for idle conversation, the surprises brought about by the daily weather as well as changes in the global climate have now taken centre stage in the public's consciousness. Major technological advances are now geared towards satisfying the public's demand for weather and climate information, from weather phone applications to the various earth observing satellites and petascale computers providing weather forecasts and climate predictions. From a personal decision whether or not to bring an umbrella, to a government's decision on the budget for farm subsidies and health services, to the global community's decisions on CO_2 emissions and associated developmental goals, there is no doubt that weather and climate matters.

The Intergovernmental Panel on Climate Change 4th assessment report [AR4, *IPCC*, 2007] has established that the global climate is changing and these changes are due to a combination of natural variability and anthropogenic forcing. Thus far, despite the acknowledgement that other anthropogenic forcings influence the Earth's climate, most studies within the climate science community have focused on the radiative forcing due to the increased atmospheric concentrations of greenhouse gases (GHG) and aerosols. The IPCC does note the relevance of land use-induced land cover change (LULCC), but mainly in the context of a globally integrated radiative forcing [*Forster et al.*, 2007] such that the role of the land surface expressed through LULCC has been under-represented [*Pielke*, 2005; *Pielke et al.*, 2011]. Further, while the effect of changes in GHGs on extremes has been examined more considerably in the last few years, the vast majority of global and regional climate change studies have thus far have focussed mainly on examining the mean climate response.

While the changes in the global climate, and the mean climate, do matter, it is the changes at regional scales, and more importantly the changes in the extremes, that immediately affect society. It is the extremes, the rare cases which communities are not accustomed to, that expose their vulnerabilities. It is therefore important to investigate these regional changes and, in particular, changes in extreme events associated with weather and climate.

There has been an increased attention focussed on the impact of increased GHGs on extremes in recent years and several recent studies using models associated with AR4 have investigated changes in temperature extremes at global or regional scales [e.g. *Kharin and Zwiers*, 2000; *Kharin et al.*, 2007; *Fischer and Schar*, 2010]. Hegerl et al. [2004], for example, showed that changes in temperature extremes were significantly different from changes in seasonal means. Tebaldi et al. [2006] demonstrated that the twentieth century trend in temperature extremes would likely be amplified under higher GHGs. Finally, Kharin et al. [2007] showed that globally averaged cold extremes warmed faster than warm extremes under all available emission scenarios. However, these studies all focused on GHGs and did not incorporate regional-forcing changes such as LULCC.

Regional climate is influenced by the global climate but it is also substantially defined by the region's surface characteristics (e.g. geographical location, topography, land cover, etc.) and changes in land surface characteristics have the potential to cause significant change in the surface climate [*Pielke et al.*, 2011]. Almost all studies on land cover change have focused on the changes in the regional and local climate and have provided important insights on how specific land cover types at specific locations affect the local climate [see *Pielke et al.*, 2011]. However, where links between LULCC and extremes have been studied, a clear global picture has been slow to emerge. Because different regions have different climate types (e.g. tropical Asia versus arid Australia), different research groups focus on different extremes (e.g. floods and cyclones versus droughts and bush fires), and different approaches to the analyses associated with different definitions of "extreme" have been used, it has been hard to create a general sense of any association between land cover change and changes in extremes at global scales. There is a need therefore for a global assessment of how changes in the characteristics of the land surface, relative to changes due to CO_2, affects climate extremes.

To address this gap, this thesis focuses on the following questions:

Does LULCC significantly affect simulated climate extremes?

How does the impact of LULCC compare relative to the impact of elevated CO_2?

To help answer these questions, a computationally efficient global model coupled to a sophisticated land surface model and a set of extremes indices, defined by an international group of experts, are used. To test the robustness of the results, simulations from four other models, provided by independent modelling groups will also be analysed.

The aims of this thesis, designed to answer the these questions, are therefore to:

1. configure a computationally efficient global climate model which is coupled to a sophisticated land surface model to simulate changes in the land surface and atmospheric CO_2 concentrations;
2. develop the input datasets required for the LULCC simulations;
3. evaluate whether this coupled model is suitable for the analysis of changes due to LULCC by analysing changes in the mean climate;
4. investigate changes in the extremes due to LULCC relative to changes due to increases in the CO_2 concentrations using a specific set of extremes indices; and
5. verify whether these changes in the extremes are robust using results from the independent model simulations.

This thesis is structured as follows. Chapter 2 provides a background on how the changes in the land surface affects the climate and how changes in the climate extremes have been detected. Chapter 3 provides details on how the model used in this thesis was configured and analysed. Chapter 4 presents the results from the simulations, focusing on the changes in the mean climate. The changes in the climate extremes as simulated by one model is presented in Chapter 5 while estimates from the four independent models are presented in Chapter 6. Key results are discussed in Chapter 7 and Chapter 8 presents the conclusions from this work and recommendations for further work.

Chapter 2
Review of related literature

2.1 Defining LULCC

Humans modify the climate in many ways: via the release of greenhouse gases [*Forster et al.*, 2007], via emissions of aerosols [*Forster et al.*, 2007] and via direct energy release associated with urban areas [*McCarthy et al.*, 2010]. One of the earliest forms of human activity, with the potential to affect climate, is land use and land cover change. Indeed, Williams [2002] suggests that large-scale landscape modification is intimately connected to human development, with a long history stretching from the moment fire was used to clear forests for food, then timber and agriculture, up to the present day urban sprawl.

Large-scale landscape modification may be achieved directly (e.g. clearing the forest by burning or cutting the trees), or indirectly (e.g. via the CO_2 fertilization effect [*Collatz et al.*, 1991; *Field et al.*, 1995; *Sellers et al.*, 1996], via competition of species types [*Didham et al.*, 2007; *Fischer and Lindenmayer*, 2007] and via the evolution of the nature of the vegetation itself [*Foley et al.*, 1996]. This thesis focuses on the direct modification of the landscape by humans.

Land-use-induced land cover change (LULCC) or anthropogenic land cover change, come in various forms including deforestation, afforestation, urbanization, irrigation and modification of bodies of water (e.g. building of reservoirs, draining of wetlands). Among these, deforestation stands out because of its large spatial scale and extensive history [*Williams*, 2002]. Estimates indicate that approximately 36% of the total global land area is now used as croplands and pasture [*Goldewijk et al.*, 2010] and that, in most regions in the globe, the growth of the human population is related to the increase in areas converted to cropland and pasture (Figure 2-1) [*Pielke et al.*, 2011].

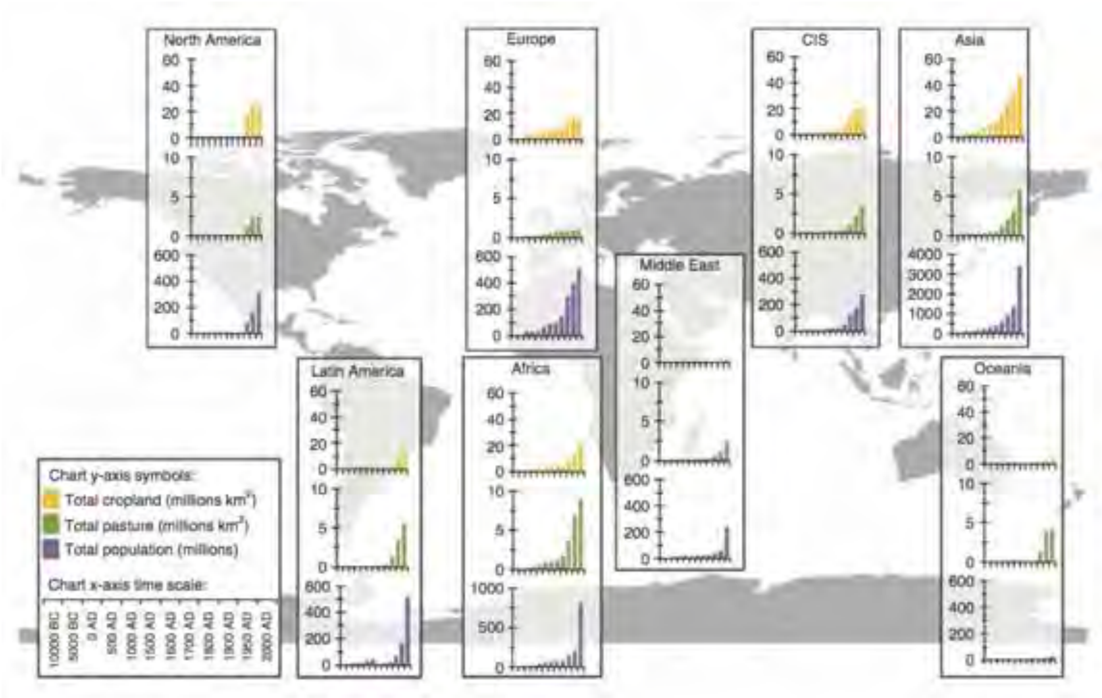

Figure 2-1: Long-term historical global estimates for population, cropland and pasture (figure 1 of Pielke et al., 2011).

Recent studies highlight that urbanized areas are rapidly increasing [e.g. *Fragkais and Seto*, 2012; *UN*, 2012] and significant impacts on climate are expected to accompany this rapid expansion [e.g. *Aoyagi et al.*, 2012; *Georgescu* *et al.*, 2012]. There is also increasing evidence [e.g. *DeAngelis et al.*, 2010; *Puma and Cook*, 2010] that the rapid increase in use of irrigation during the 20th century is likewise impacting climate.

Agricultural expansion and intensification are considered to be the major drivers of global LULCC [*Pielke et al.*, 2011] and this study focuses on deforestation, specifically the conversion of natural forests to cropland. In this thesis, crops and pasture are combined into one vegetation type called cropland because the land surface model used here does not distinguish between these two vegetation types.

Figure 2-2 shows the estimated LULCC calculated from both crops and pasture fractions, from various time periods based on the Land Use Harmonisation dataset [LUH, *Hurtt et al.*, 2006]. By 1500, large areas of Western Europe had been partially cleared for agriculture and timber harvesting (Figure 2-2a). From then, through 1800s, LULCC intensified (Figure 2-2b to 2-2d), particularly in Western Europe, and significant LULCC also occurred over much of Asia including India and China [*Pielke et al.*, 2011]. More intense and widespread LULCC has occurred since the 1900s (Figure 2-2e) such that at the end of the millennium (Figure 2-2f) few significant land areas had not been affected by human activity. Of course, these LULCC estimates are also still undergoing refinements. For example, over Australia some areas currently assigned as pasture are more likely ungrazed semiarid and arid areas [*Pielke et al.*, 2011]. However, overall, Figure 2-2 provides a robust picture of the scale of LULCC at large spatial scales.

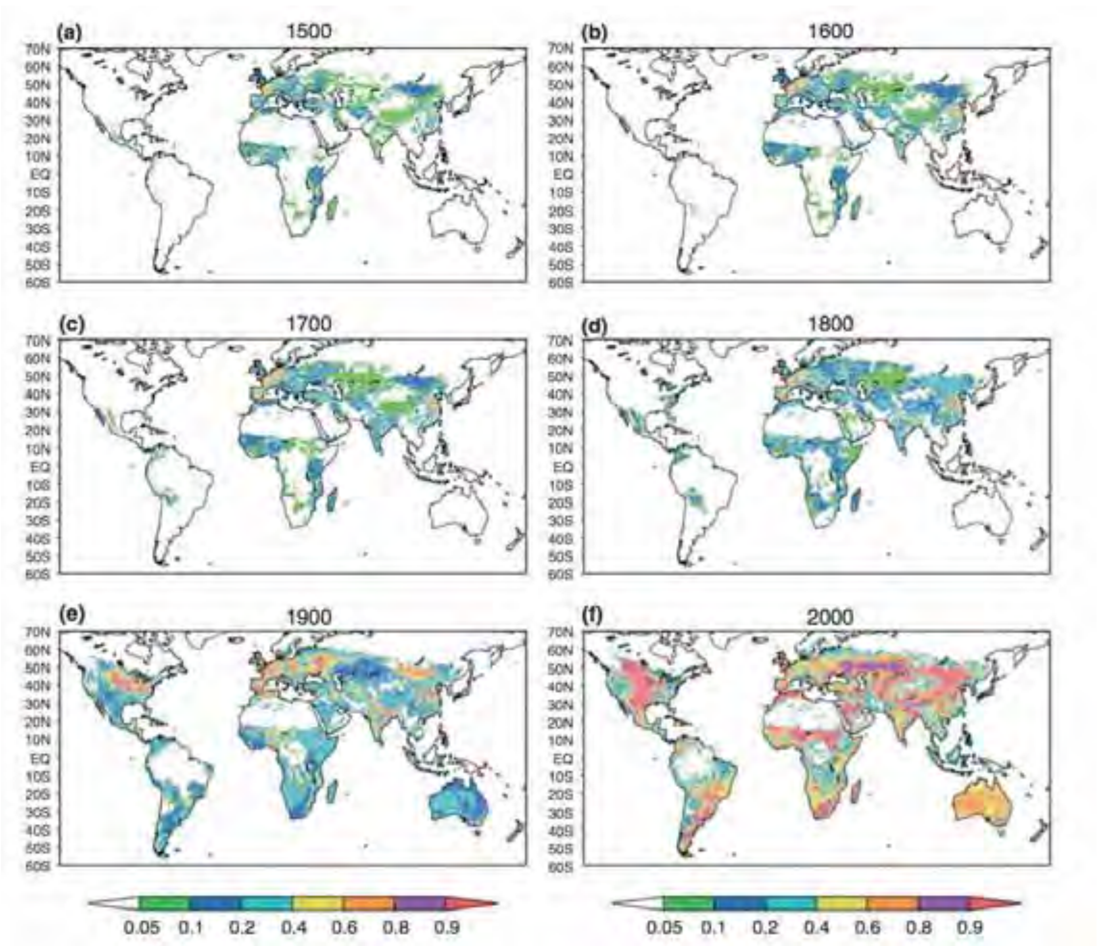

Figure 2-2: Reconstructed and projected LULCC for various time periods. The scale is the relative fraction of any grid box containing pasture or crops. These data were obtained from the LULCC dataset downloaded from the Land Use Harmonization web site (http://luh.unh.edu). Note: The analysis of the type of landscape continues to undergo refinement (e.g. over Australia where ungrazed semiarid and arid areas are shown as pasture) (figure 2 of Pielke et al., 2011).

2.2 How does LULCC affect climate?

LULCC affects the climate in two ways: (1) biogeochemically, via the capture and storage of CO_2, the release of other greenhouse gases and the cycling of mineral and organic compounds; and (2) biogeophysically, via changes in surface characteristics such as albedo and roughness length and changes in processes such as transpiration [*Levis*, 2010]. This study focuses on the biophysical impacts of LULCC, which are illustrated in Figure 2-3.

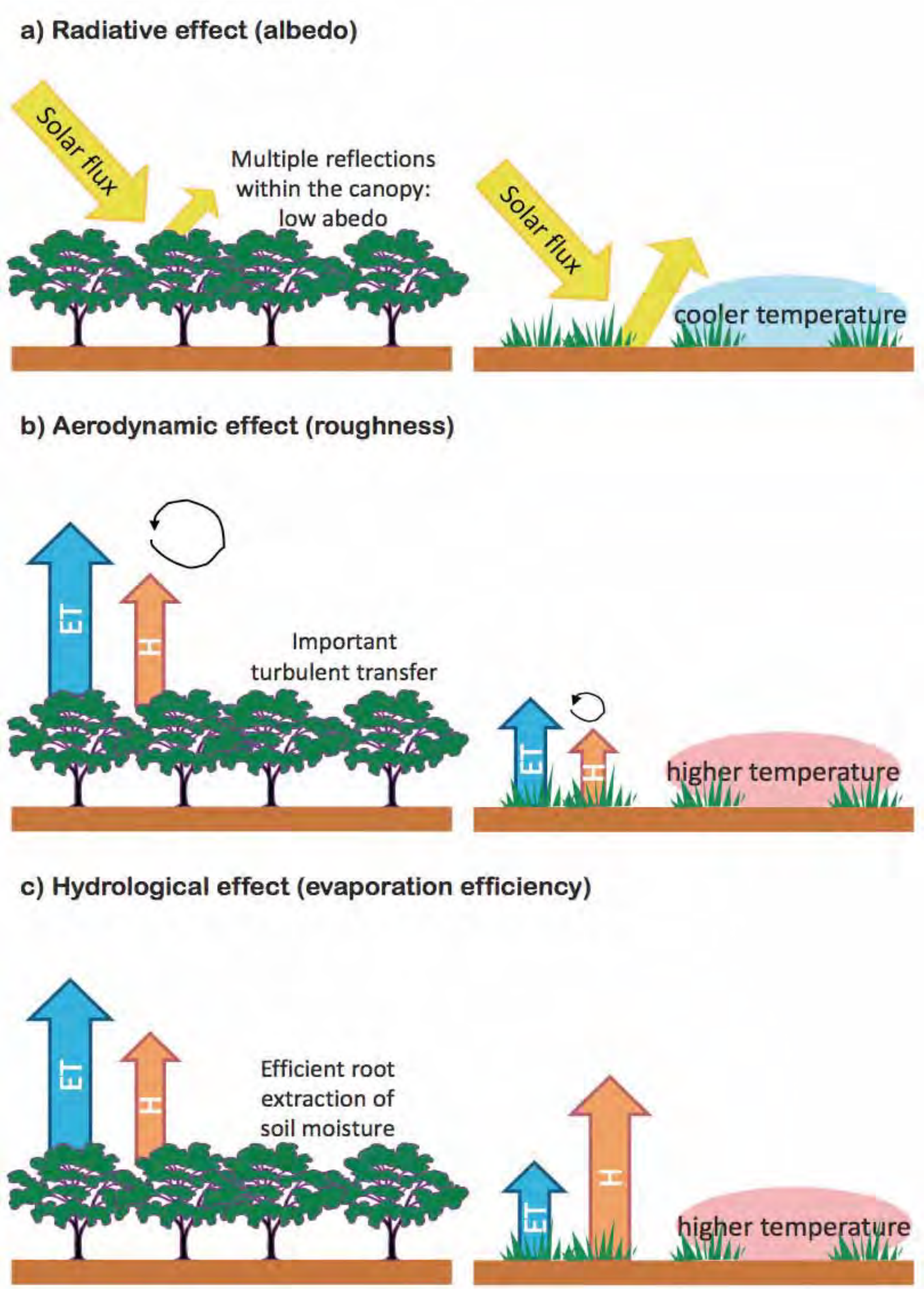

Figure 2-3: Schematic overview of the processes contributing to the biophysical effect of deforestation (figure 2 of Davin and de Noblet-Ducoudré, 2010). The left column shows the processes over forests while the right column shows the same processes over crops and grasslands.

Since crops generally have higher albedo than forests, the increase in the reflected solar radiation results in a cooler surface temperature (Figure 2-3a). In the presence of snow (for example in the mid- and high-latitudes during winter), this effect is particularly pronounced as snow can entirely cover the short cropland and significantly increase the surface albedo. Crops also commonly have lower surface roughness compared to forests. LULCC therefore tends to reduce turbulent heat fluxes resulting in surface warming (Figure 2-3b). Further, because crops have generally shallower root systems, they have a lower capacity to extract soil water resulting in lower evapotranspiration and an increased sensible heat flux, which tends to further warm the surface (Figure 2-3c). The effect of LULCC on albedo (Figure 2-3a) is more dominant over the temperate regions while the effects on the turbulent fluxes (Figures 2-3b and 2-3c) are more dominant over the tropics [*Davin and de Noblet-Ducoudré*, 2010]. Overall, LULCC tends to cool mid-latitudes because the albedo effect dominates, while warming the tropics because the effects linked to turbulence and roots dominate [*Lawrence and Chase*, 2010]. While these effects may seem straightforward, quantification of these impacts is complicated by feedback mechanisms and by impacts due to other climate forcings [*Davin and de Noblet-Ducoudré*, 2010; *de Noblet-Ducoudré et al.*, 2012].

The next section describes the fundamental equations that represent the key role played by the land surface in climate in terms of the surface energy balance and the surface water balance.

2.2.1 Surface energy balance

The surface energy balance is given by:

$$R_{net} = S(1-\alpha) + L_{in} - L_{out} \qquad \text{Eq. 2-1}$$

$$R_{net} = H + \lambda E + G \qquad \text{Eq. 2-2}$$

where R_{net} is the net radiation (W m^{-2}), S is the incoming shortwave radiation (W m^{-2}), α is the surface albedo and L_{in} and L_{out} are the incoming and outgoing longwave radiation (both in W m^{-2}). H is the sensible heat flux (W m^{-2}), λ is the latent heat of vaporization (J kg^{-1}), E is evaporation (kg m^{-2} s^{-1}) and the quantity λE is the latent heat flux (W m^{-2}). G is the soil heat flux (W m^{-2}). Equation 2-1 describes how the incoming solar radiation gets reflected back into space or absorbed and re-emitted in the form of longwave radiation. In terms of energy flux, net radiation (R_{net}) is balanced by the sensible (H) and latent (λE) heat fluxes, which described the exchange of energy between the land surface and the atmosphere, as well as the storage of energy within the soil.

H may be defined as:

$$H = \frac{T_s - T_r}{r_a} \rho c_p \qquad \text{Eq. 2-3}$$

where T_s is the surface temperature (K), T_r is a reference temperature (K) above the surface, ρ is the density of the air (kg m^{-3}) and c_p is the specific heat of air (J kg^{-1} K^{-1}). The aerodynamic resistance (s m^{-1}), represented by r_a, is related to the surface roughness length and thus, vegetation height.

λE is more complex to estimate than H because it also involves biological processes associated with stomates. It is commonly represented using the aerodynamic approach [*Sellers*, 1992]:

$$\lambda E = \left(\frac{e^*(T_s) - e_r}{r_s + r_a} \right) \frac{\rho c_p}{\gamma} \qquad \text{Eq. 2-4}$$

where $e^*(T_s)$ is the saturated vapour pressure (Pa) at T_s, e_r is the vapour pressure at reference height (Pa) and γ is the psychometric constant (Pa K^{-1}). The remaining term, r_s, is the surface resistance (s m^{-1}), which describes how easily water can evaporate from the soil. Plants differ on the physiology of the stomata, evolving to manage the conflicting goals of permitting CO_2 uptake during photosynthesis and restricting water loss during transpiration. The inclusion of the stomates in r_s tightly couples λE to biological activity via photosynthetic activity, and thus carbon uptake by plants.

The soil heat flux is a diffusion-conduction process, which can be generalized by:

$$G = -K \frac{dT_s}{dz} \qquad \text{Eq. 2-5}$$

Where z (m) is the soil depth and K (W m^{-1} K^{-1}) is the thermal conductivity, which determines the heat flow rate by conduction within the soil. Equation 2-5 simplifies the complexity of soil heat conduction which is usually treated with care in climate models following, for example, Hillel [1982]. In the model used in this thesis, this is not dependent on vegetation type (i.e. it does not change when forests are converted to cropland) and thus will not be discussed further.

2.2.1.1 Albedo

The radiative effect of albedo as shown in Figure 2-3a is expanded in Figure 2-4, which shows the feedback mechanisms involved as surface albedo is changed when forests are replaced with crops and grass.

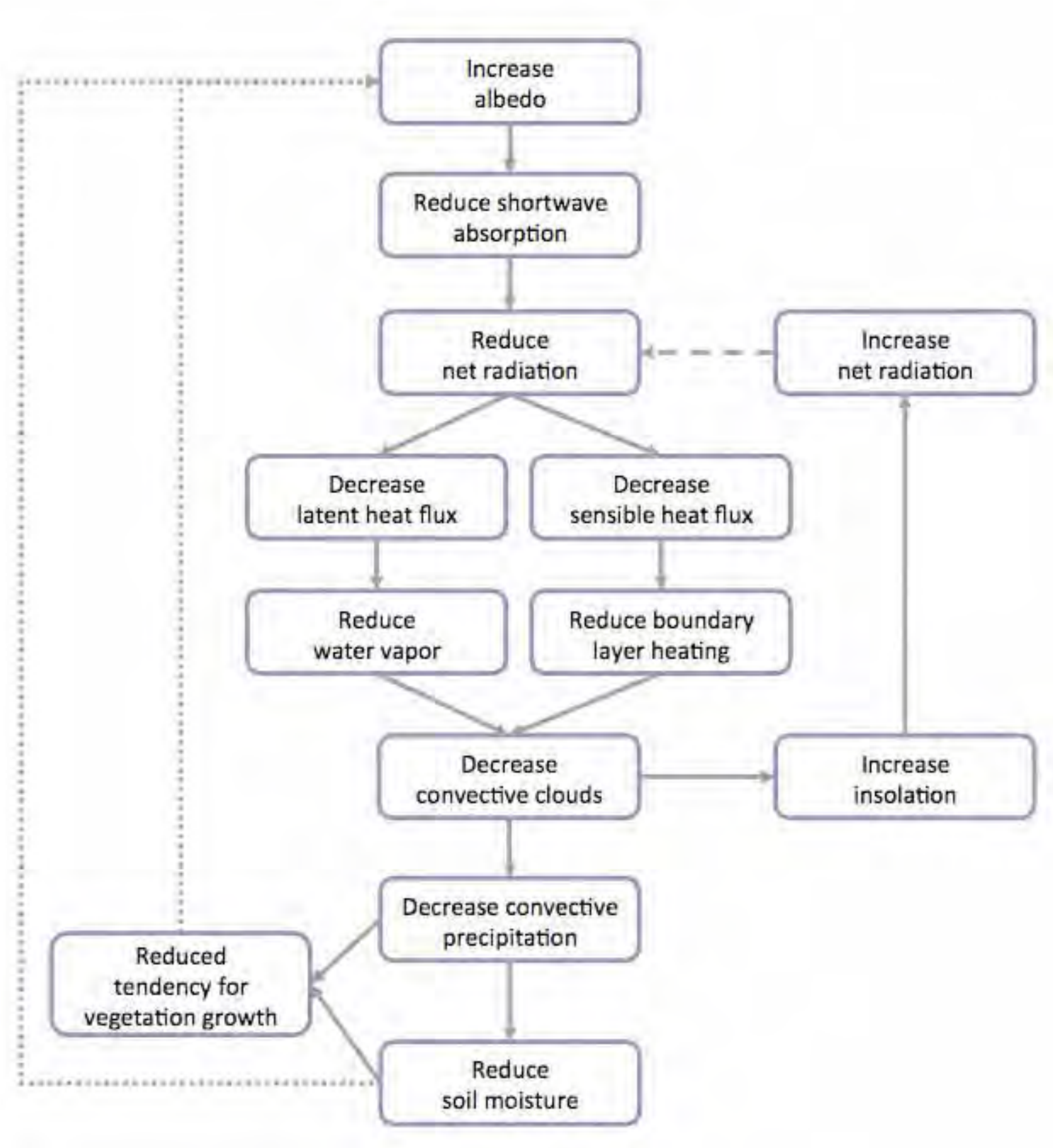

Figure 2-4: Conceptual diagram of the impact of an increase in albedo on the land surface and some elements of the boundary layer climate. The dotted line represents a positive feedback while the dashed line represents a negative feedback (adapted from figure 2 of Pitman, 2003).

Instead of simply cooling the surface by reducing the absorbed solar radiation, the increased albedo reduces the net radiation at the surface, which affects the surface fluxes and the forcing to the boundary layer. This potentially affects the amount of convective clouds, which in turn affects the solar energy reaching the surface. Any increase in solar energy reaching the ground would tend to warm the surface. A reduction in convective cloud cover would result in reduced convective precipitation and soil moisture that could, in time, hinder plant growth and result in a surface with a higher albedo via a positive feedback. These feedback mechanisms make it difficult to quantify the net effect of LULCC because we do not know which mechanisms will dominate, how these relationships change in the presence of other forcings, and how these mechanisms change spatially or on different time scales.

LULCC can modify the surface in contact with the atmosphere and therefore the balance between fluxes from the soil and vegetation. These changes are important because a decrease in λE means a decrease in water vapour supplied to the atmosphere and therefore, at least potentially, a decrease in cloudiness and precipitation. A decrease in the H means a cooler planetary boundary layer and potentially less convection, and thus less clouds and precipitation. Changes in the cloud and precipitation feedback may also affect the initial albedo perturbation. Given the key role of the H and λE in the climate system, it is important to properly simulate the diurnal, seasonal and longer-term variations of these fluxes [*Pitman*, 2003].

Different surfaces have different optical properties. Different soil types have different albedo but generally barren soil has higher albedo than vegetated areas. Different plant functional types have different characteristics (e.g. leaf size and shape, photosynthetic capacity, leaf nitrogen, etc.), which allow them to interact differently with the environment. In particular, the leaf area index (LAI, the surface area of leaf per surface area of ground), leaf orientation and other optical properties affect how the incoming solar radiation is absorbed or reflected within the canopy, and therefore the surface albedo. The following tables illustrate show how the forest vegetation types can be very different from croplands (Table 2-1) and how different surfaces can have very different albedo (Table 2-2).

Table 2-1: Leaf orientation, reflection (R), transmission (T), and absorption (A) of solar radiation by a leaf for visible and near-infrared wavebands (from table 18.1 of Bonan, 2008).

Vegetation type	**Leaf orientation**	**Visible**			**Near-infrared**		
		R	**T**	**A**	**R**	**T**	**A**
Needleleaf tree	Random	0.07	0.05	0.88	0.35	0.10	0.55
Broadleaf tree	Semi-horizontal	0.10	0.05	0.85	0.45	0.25	0.30
Grass, crop	Semi-vertical	0.11	0.07	0.82	0.58	0.25	0.17

Table 2-2: Broadband albedo of various surfaces (from table 13.1 of Bonan, 2008)

Surface	**Albedo**
Fresh snow	0.80-0.95
Old snow	0.45-0.70
Desert	0.20-0.45
Glacier	0.20-0.40
Soil	0.05-0.40
Cropland	0.18-0.25
Grassland	0.16-0.26
Deciduous forest	0.15-0.20
Coniferous forest	0.05-0.15
Water	0.03-0.10

2.2.1.2 Leaf area index

The amount of foliage in the canopy is measured by the leaf area index (LAI), which is the projected area of leaves per unit of ground area. Figure 2-5 shows how LAI typically varies across vegetation types. Tall evergreen forests with thick canopies and understories commonly have high LAI while short grass and shrubs commonly have small LAI.

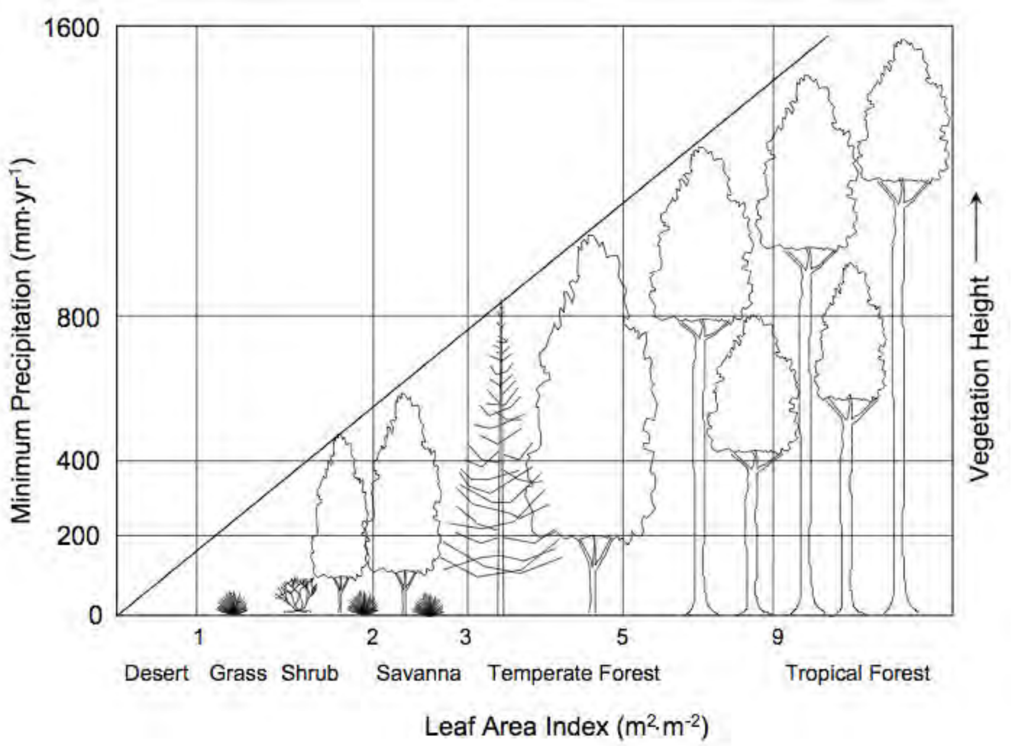

Figure 2-5: Vegetation height and leaf area index in relation to the minimum annual precipitation needed to sustain the vegetation (figure 24.7 of Bonan, 2008).

Figure 2-6 illustrates how changes in the LAI can influence the exchange of H and λE. Converting forests with thick canopies to croplands decreases the LAI and likely results in increased net radiation at the soil surface. Decreased LAI could also result in a reduction in the ability of the surface to transpire, reducing water uptake through the roots. Finally, lower LAI means less precipitation can be intercepted which reduces the quick evaporation from the plant surfaces; but it also means that more precipitation would reach the ground via throughfall, resulting in increased soil moisture. The availability of moisture in the soil, combined with the increase in net radiation, could result in increased soil-based water exchange with the atmosphere.

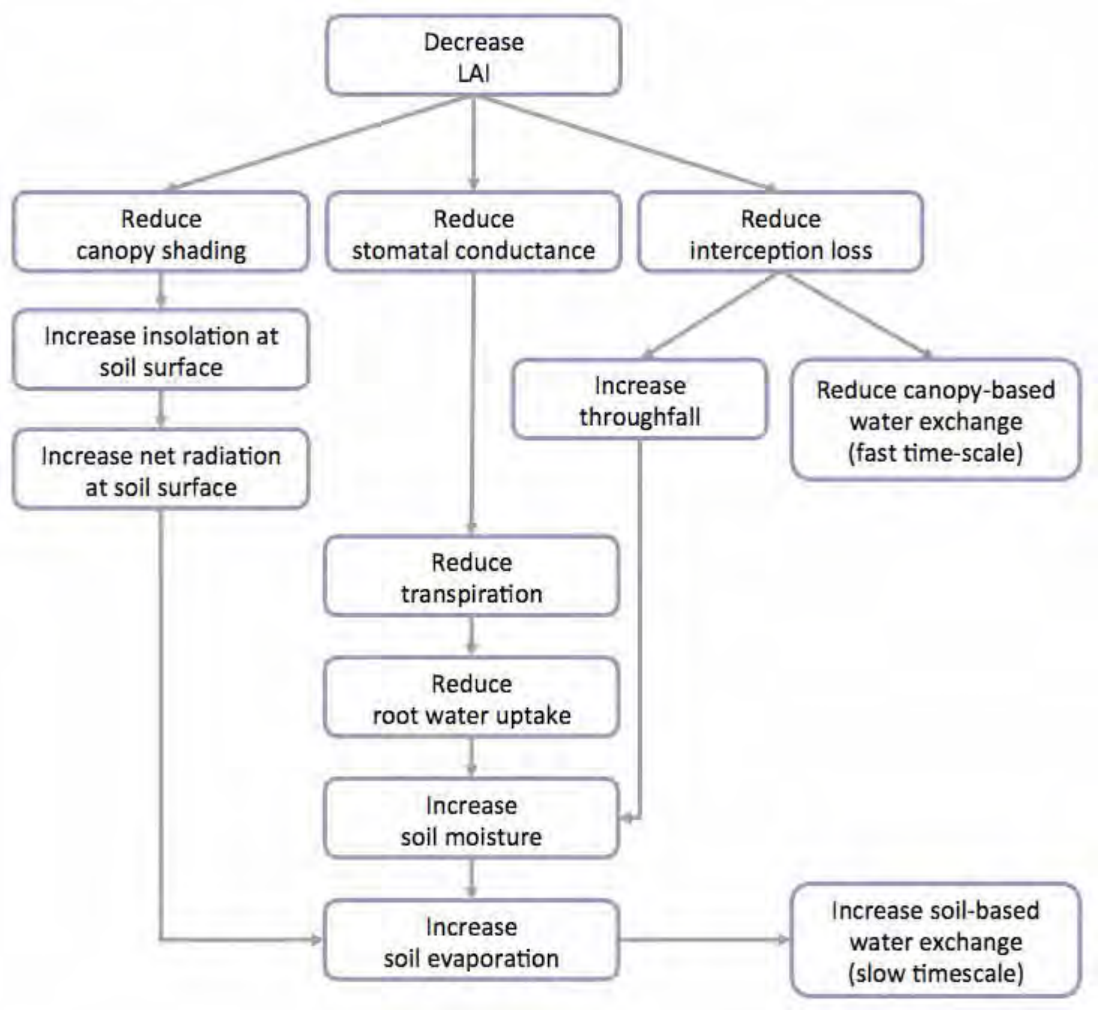

Figure 2-6: As Figure 2-4 but for decrease in LAI (adapted from figure 3 of Pitman, 2003).

2.2.1.3 Root distribution

The depth to which the roots of different vegetation types penetrate in soil affects the overall supply of water for transpiration as deeper roots can access a greater volume of soil from which water can be extracted. Root distribution is typically represented in models following, for example, Gale and Grigal [1987]. Figure 2-7 shows how the cumulative root fraction as a function of soil depth may be defined for different vegetation types [*Jackson et al.*, 1996].

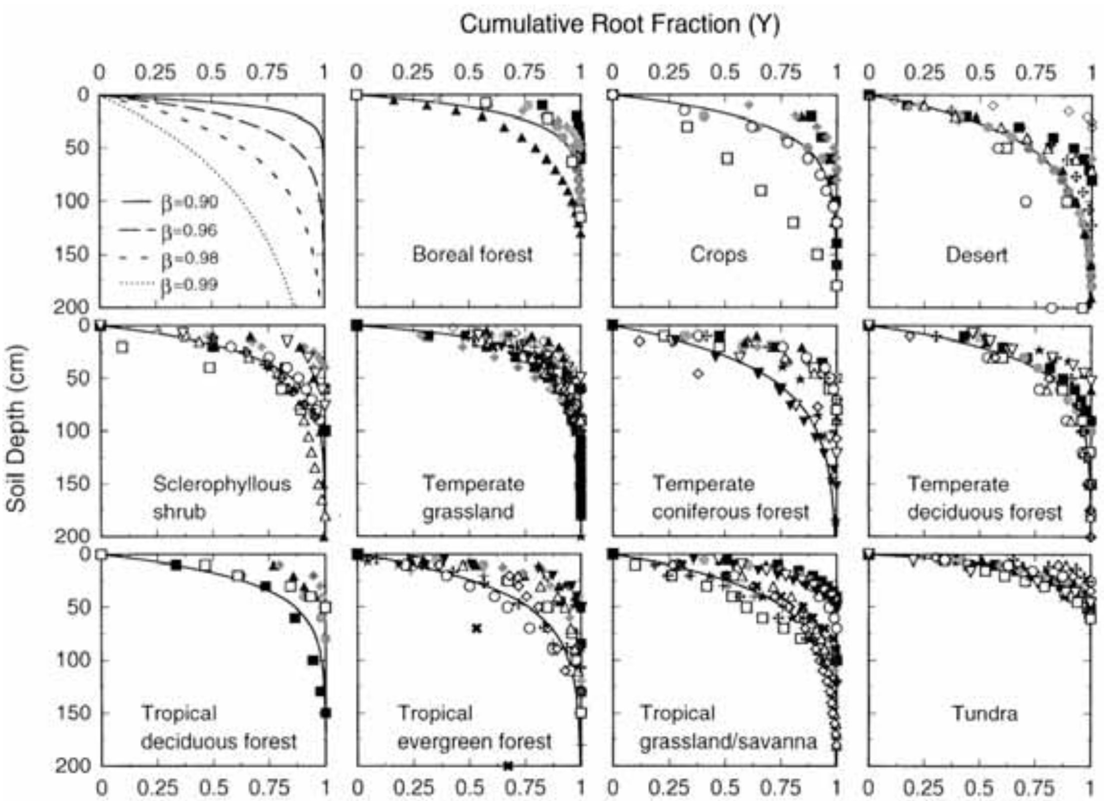

Figure 2-7: Cumulative root distribution as a function of soil depth for eleven terrestrial biomes and for the theoretical model of Gale and Grigal (1987). The curve in each biome panel is the least squares fit of β for all studies with data to at least 1 m depth in the soil. Gale and Grigal's equation is of the form $Y=1-\beta^d$, where Y is the cumulative root fraction, d is soil depth (in cm), and β is the fitted parameter. Larger values of β imply deeper rooting profiles. Symbols represent values from various studies (figure 1 of Jackson et al., 1996).

Changes in the distribution of roots (Figure 2-8) can change the amount of soil moisture available for transpiration and a positive feedback between reduced water uptake, rainfall, and further reductions in root depth may exist.

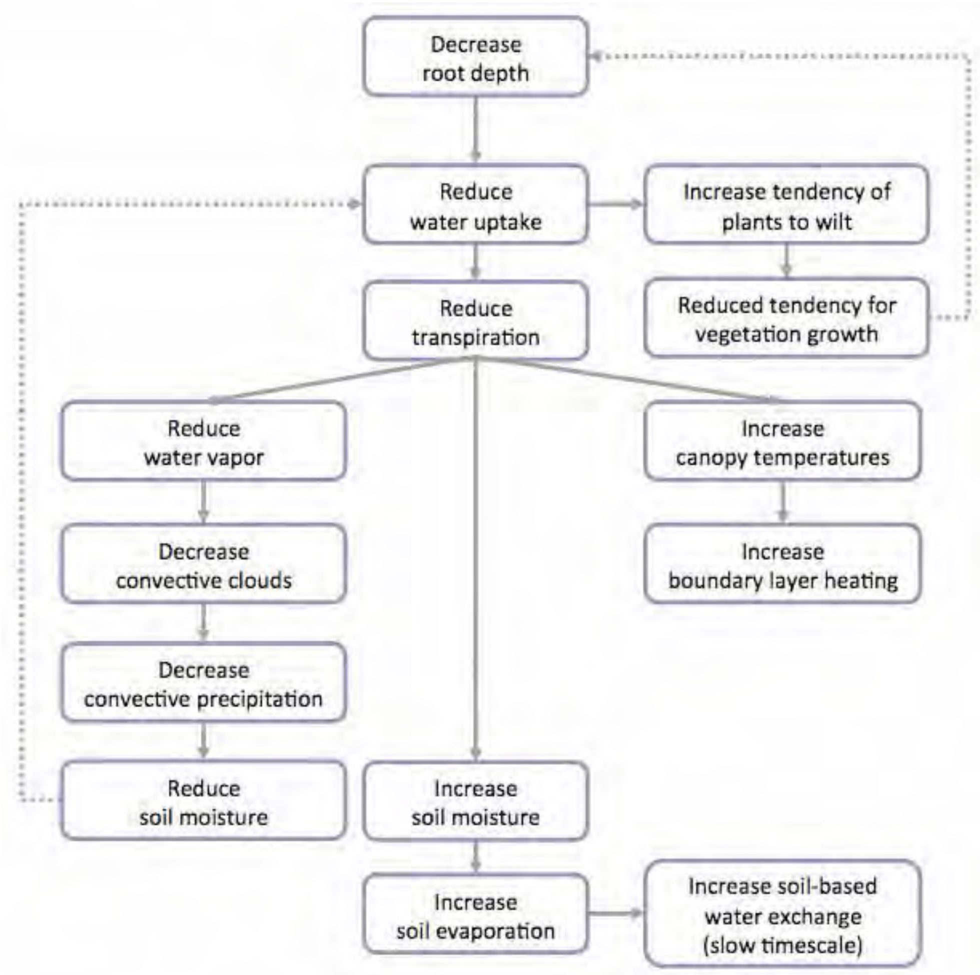

Figure 2-8: As Figure 2-4 but for decrease in root depth (adapted from figure 4 of Pitman, 2003).

The conversion of deep-rooted forests to shallow-rooted crops could induce less transpiration and a reduction in the atmospheric water vapour necessary for cloud formation and precipitation, resulting in decreased soil moisture. The reduction in transpiration could also allow more of the available water in the soil to evaporate directly and increase the soil-based water exchange; or increase the boundary layer heating by increasing the canopy temperature. Finally, in moisture-limited conditions, shallow roots increase the tendency of plants to wilt, which may eventually reduce the plant growth. Deforestation can thus lead to drier conditions and further decreases in vegetation cover.

2.2.1.4 Roughness length

The aerodynamic resistance (r_a) links the surface characteristics to the turbulence that drives the exchange of H and λE. With all other factors being equal, rough surfaces generate more turbulence and have higher H and λE than smoother surfaces. However, surface roughness length, which is a function of the drag properties of the land surface, varies greatly with vegetation cover (Figure 2-5 and Table 2-3). Roughness length for vegetation is commonly assumed to be one-tenth of canopy height and displacement height is seven-tenths canopy height, such that aerodynamic resistance decreases with increasing vegetation height [*Bonan*, 2008a]. More precisely, aerodynamic resistance is inversely related to the wind speed and the logarithm of the surface roughness.

Table 2-3: Roughness length of various surfaces (from table 14.1 of Bonan, 2008)

Surface	**Roughness length (m)**
Soil	0.001-0.01
Grass	
Short	0.003-0.01
Tall	0.04-0.10
Crop	0.04-0.20
Forest	1.0-6.0

The impact of the decreased roughness length through conversion of forest to cropland is shown schematically in Figure 2-9. Conversion of forests to cropland reduces the surface roughness length and reduces turbulence. Less turbulence means less heat and moisture gets transferred from the surface to the atmosphere resulting in increased surface temperature. The reduction in H and λE could result in decreased atmospheric water vapour and heating within the boundary layer, potentially resulting in less clouds, precipitation and thus reduced soil moisture which could, in turn, lead to reduction in vegetation cover which would further reduce the surface roughness length.

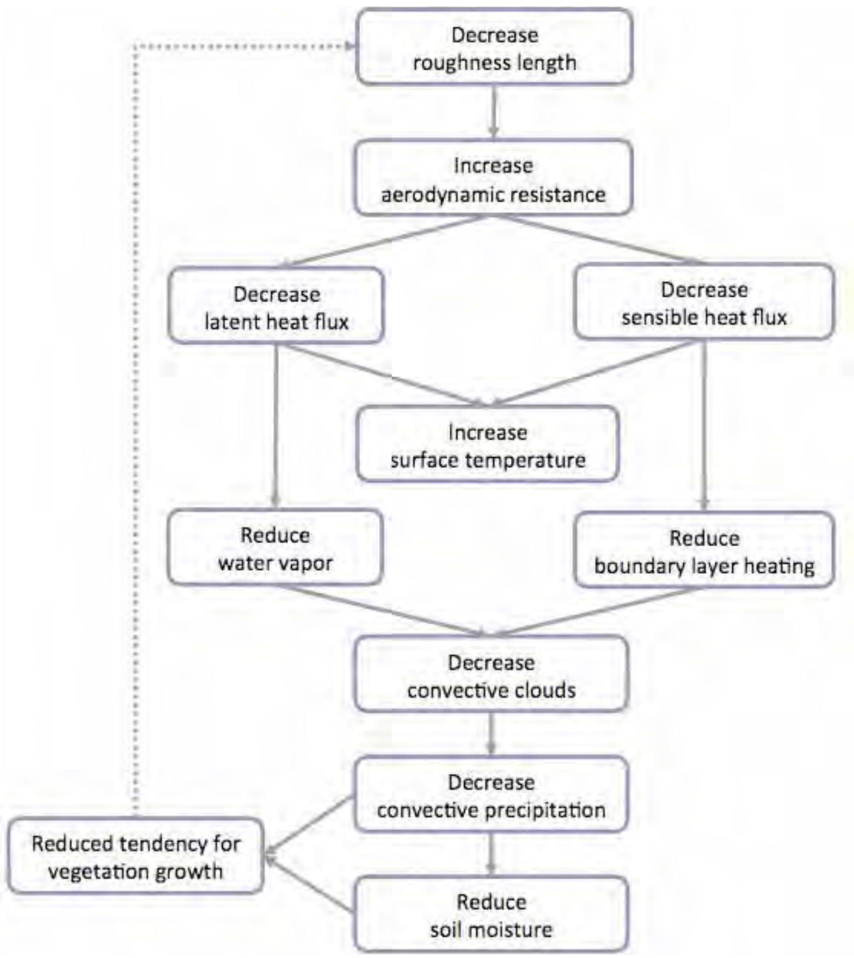

Figure 2-9: As Figure 2-4 but for decrease in roughness length (adapted from figure 5 of Pitman, 2003).

2.2.2 Surface water balance

The surface water balance (Equation 2-6) describes how available precipitation (P) is partitioned to evaporation (E), runoff (R_{surf} and R_{drain}) and change in soil moisture storage (ΔS), all in kg m^{-2} s^{-1}. The surface water balance equation is related to the energy balance equation via the evaporation term. Runoff is split into the fast (R_{surf}) and slow (R_{drain}) components, which are influenced by the characteristics and wetness of the soil.

$$P = E - R_{drain} - R_{surf} - \Delta S \qquad \text{Eq. 2-6}$$

LULCC affects the surface water balance by changing the way vegetation affects interception and transpiration. Changes in the vegetation distribution affect the balance between fluxes originating from the soil and those derived from canopy processes (see Section 2.2.1.2). Changes in E (via evapotranspiration, soil evaporation, re-evaporation from of intercepted water) affect runoff (R) and soil moisture change (ΔS). These then affect a variety of other processes through the link with the surface energy balance as shown in Figure 2-10.

Thus, the key characteristics of the land surface that influence climate are albedo, roughness length and the characteristics of plants that influence their surface area or their ability to take water from soil and transpire it. A major impact of changes in the nature of the land surface is the effect on the time scale of surface–atmospheric exchanges [*Betts*, 2009]. Extremes, especially temperature, are affected by the nature of the surface and whether moisture can be supplied for evaporation. Thus, modifications in the nature of the land surface could affect not only mean surface–atmospheric exchanges, but also the extremes and the time scale of the response of the land surface to various external perturbations.

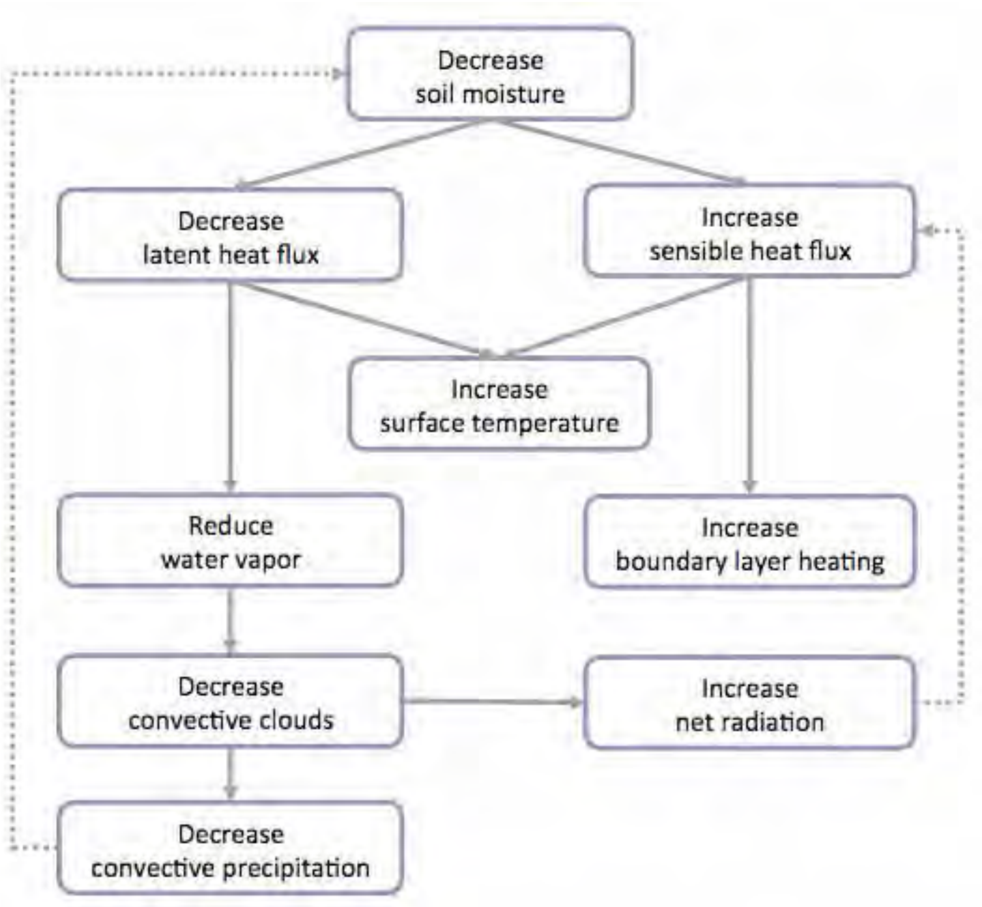

Figure 2-10: As Figure 2-4 but for decrease in soil moisture (adapted from figure 6 of Pitman, 2003).

2.3 Evidence from observational and modelling studies

Figure 2-11 illustrates how the differences in the characteristics of the forest and agricultural land cover can affect the local and regional climate. The impacts of the two different surfaces generally oppose each other but other factors (e.g., irrigation) and the feedback from the atmosphere makes the system highly nonlinear and complex. Moreover, the influence of LULCC has been shown to influence climate over a range of spatial and temporal scales [Pielke et al., 2007].

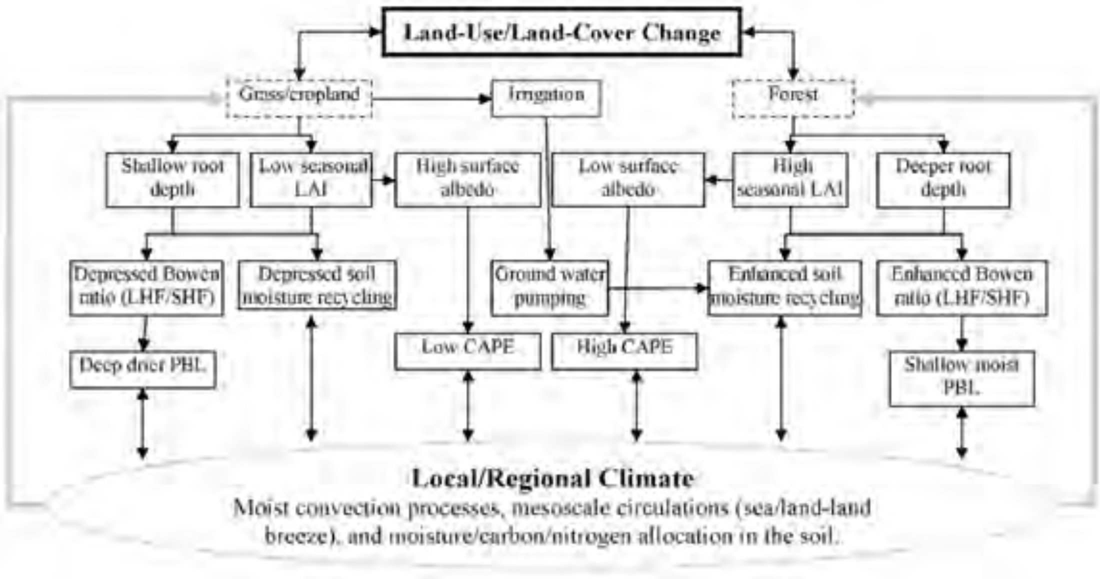

Figure 2-11: A conceptual diagram of the influence of LULCC on local/regional climate (figure 4 of Pielke et al., 2007).

Observational and modelling studies provide ample evidence that LULCC has a significant effect on local and regional climate [*Pielke et al.*, 2011]. Regional surface temperatures are clearly affected by landscape type [*Bonan*, 1997; *Gallo et al.*, 1999; *Lim et al.*, 2005; *Roy et al.*, 2007; *Wichansky et al.*, 2008; *Fall et al.*, 2010b; *Mahmood et al.*, 2010]. However, compared to the effects of greenhouse gases (warming) and sulphate aerosols (cooling), the temperature response to LULCC is multidirectional, depends on the type of change [*Pielke et al.*, 2011] and may be subject to interaction with soil conditions [*Seneviratne et al.*, 2006b].

2.3.1 Changes in local climate

Changes in the surface and near surface variables such as the latent heat flux, sensible heat flux and planetary boundary layer can change the local climate as shown by observational studies and confirmed by modelling studies. Local studies have shown that deforestation can alter cloud climatology over South

America [*Wang et al.*, 2009], local circulation [*Souza et al.*, 2000] and the onset of the rainy season [*Butt et al.*, 2011] over the Amazon as well as affect local weather phenomena such as thunderstorms over areas as diverse as the Canadian Prairies [*Raddatz*, 1998] and the Sahel [*Taylor et al.*, 2011a]. Replacing native vegetation with pastures and crops have also increased temperatures over the Brazilian Cerrado [*Loarie et al.*, 2011], USA and Canada [*Sun et al.*, 2003; *McPherson et al.*, 2004; *Strack et al.*, 2008].

Studies over South America [*Silva Dias et al.*, 2002; *Wang et al.*, 2009], Australia [*Lyons et al.*, 1993; *Ray et al.*, 2003; *Lyons et al.*, 2008; *Nair et al.*, 2011] and Oklahoma [*Sun et al.*, 2003] indicate that changes in the sensible heat flux can change planetary boundary layer development. For example, during the Bunny Fence Experiment [BuFEx, *Lyons et al.*, 1993] in Australia, the latent heat flux over the agricultural region varied between 40 to 80 W m^{-2} during winter and without exceeding 30 W $^{m-2}$ during summer, while the latent heat flux over the native vegetation remained relatively low throughout the year, rarely exceeding 40 W m^{-2} [*Nair et al.*, 2011]. The sensible heat flux over the native vegetation was also consistently higher resulting in vigorous boundary layer development and increased planetary boundary layer height. This is illustrated in Figure 2-12a which shows boundary cloud formation over the native vegetation area but none over the agricultural areas of southwest Australia. Figure 2-12b shows the land use map over the region with crop and pastures west of the rabbit proof fence and native vegetation east of the fence. Cloud-free satellite images of the region (Figure 2-12c) show marked differences between the agricultural region, native vegetation and forest areas.

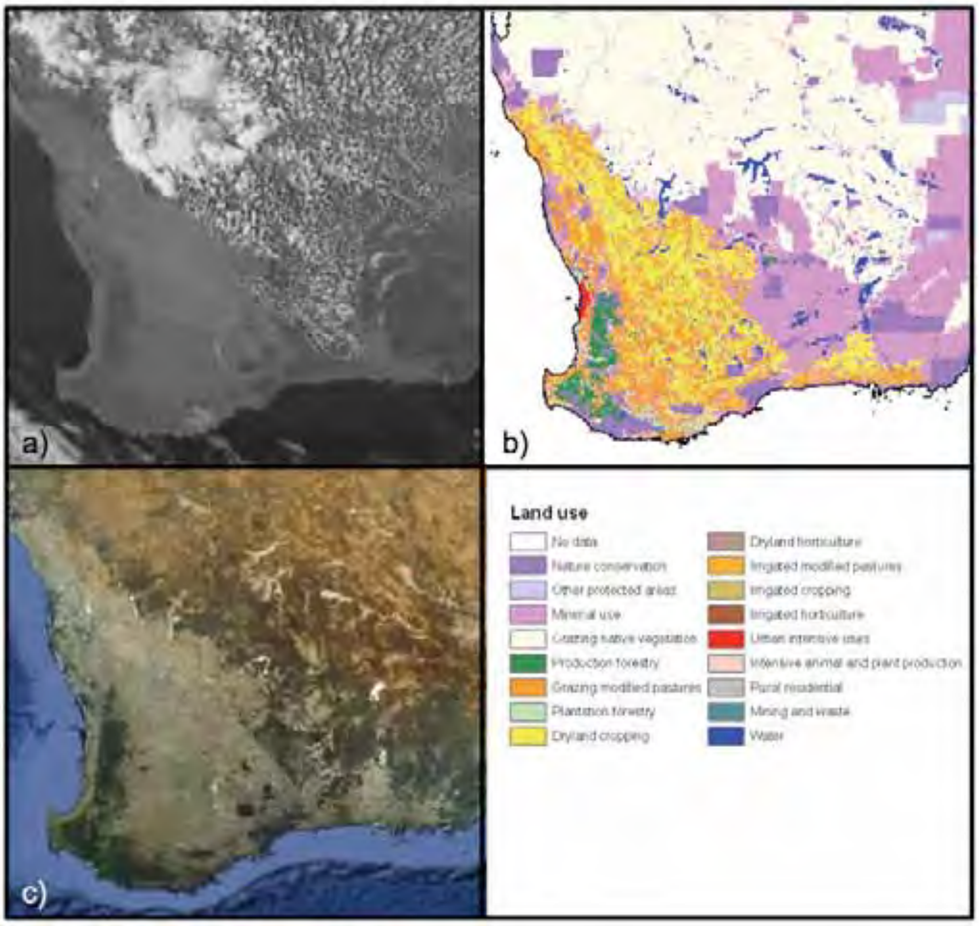

Figure 2-12: (a) Geostationary Meteorological Satellite (GMS) visible imagery for January 3, 1999, 1500 LST over southwest Australia. The agricultural areas are clear, while boundary cloud formation occur over native vegetation areas. Note that the western extent of the cloud fields coincide approximately with the rabbit proof fence that demarcates the cleared areas from the regions of remnant native vegetation (figure 4 of Pielke et al., 2011); (b) land use map of southwest Australia with the native vegetation areas shown in shades of purple, pink and off white, agricultural regions shown in shades of yellow and orange, forestry areas shown in shades of green and urban areas shown in red (from http://www.abares.gov.au/landuse); (c) composite image of the region (image courtesy of Google Earth).

2.3.2 Changes in the regional and global climate

While the impact of LULCC on local climate is clear, there seems to be spatial thresholds that determine how LULCC can affect change in the mesoscale and regional-scale. Small-scale landscape changes (in the range of 2-5 km) may be sufficient to trigger boundary layer dynamics but spatial heterogeneity of approximately 10-20 km is required for creating mesoscale circulations [*Pielke and Uliasz*, 1993; *Baidya Roy et al.*, 2003; *Baldi et al.*, 2005]. To affect the synoptic convergence patterns, the required landscape change may be in the order of 50-100 km. This is because, below a certain threshold, the convective boundary layer or regional flow could homogenize any heterogeneity before they reach very high into the atmosphere [*Avissar and Pielke*, 1989], essentially losing any LULCC signal.

Other regional-scale studies suggest that LULCC may alter the intensity of monsoons [*Takata et al.*, 2009; *Kishtawal et al.*, 2010], the post-landfall rainfall of tropical systems [*Chang et al.*, 2009; *Kishtawal et al.*, 2010] and the rainfall and temperature over some regions of Australia [*Narisma and Pitman*, 2003; *Pitman et al.*, 2004; *McAlpine et al.*, 2007].

Global LULCC studies [e.g., *Findell et al.*, 2009; *Pitman et al.*, 2009; *Davin and de Noblet-Ducoudré*, 2010; *Lawrence and Chase*, 2010; *de Noblet-Ducoudré et al.*, 2012] have shown that on a global scale, the physical impacts of LULCC on temperature and rainfall are less important than large-scale sea surface temperature (SST) anomalies such as ENSO [*Findell et al.*, 2009]. However, in regions of LULCC, the impact can be equally or more important than the SST forcing patterns in determining the seasonal cycle of the surface water and energy balance [*Findell et al.*, 2009]. LULCC generally causes year round warming in tropical and subtropical regions and winter cooling and summer warming in the higher northern latitudes [*Lawrence and Chase*, 2010]. The cooling over the temperate and boreal zones is due to the stronger albedo effect over that region; while the warming over the tropics is due to the dominance of evapotranspiration efficiency, surface roughness over the region [*Davin and de Noblet-Ducoudré*, 2010]. Multi-model simulations such as those from the "Land-Use and Climate, IDentification of robust impacts" (LUCID) project show that, despite imposing a common land cover change map, it is still not possible to show one common impact of LULCC because of model differences [*Pitman et al.*, 2009; *de Noblet-Ducoudré et al.*, 2012]. To complicate the situation further, the impact of LULCC on climate depends on the background climate [*Pitman et al.*, 2011].

LULCC can clearly alter regional climate and global studies indicate the differences in the impact of LULCC on different regions. However, these studies focus mainly on changes in the mean climate and not on the extremes.

2.4 Focus on the extremes

While changes in the mean climate are important, it is the extremes that have immediate yet profound impact on society. Communities eventually adapt to changes in the norm but because the rarity of extremes makes them difficult to get used to, they tend to expose vulnerabilities which could, in unfortunate circumstances, lead to disaster. For society to come up with strategies to withstand the severe impact of these unexpected events, it is imperative to identify these extremes and how they are changing. This thesis uses a set of indices, identified by a group of international experts as the key indicators of changes in the extremes, to determine whether LULCC can significantly change their intensity, duration and frequency. But what exactly are climate extremes?

There is no consistent definition of what constitutes an extreme in the context of climate research [*Stephenson*, 2008]. An extreme climatic event may be defined as one that is rare at a particular place and time of year [*IPCC*, 2007] or one that causes extraordinary economic and social damage and disruption [*Easterling et al.*, 2000b]. Mathematically, an extreme might be categorized as the infrequent events at the high and low end of the distribution of a particular variable. The function describing the probability of occurrence of particular values of a variable is known as a probability distribution or density function. For many variables this distribution follows a 'normal' or 'Gaussian' distribution (i.e., the familiar 'bell' curve) shown in Figure 2-13a for daily temperature. Other variables, such as daily precipitation, tend to have different probability distributions as shown in Figure 2-13b.

Changes in the extremes may occur because of a shift of the entire distribution (Figure 2-14a). In this case, the shift of the distribution results in more hot extremes and less cold extremes. A change in variability without a change in the mean (Figure 2-14b) may result on changes in both extremes. In this case, there is an increased probability of both hot and cold extremes. A change in shape of the distribution (Figure 2-14c) could result in almost no change in one extreme but a change in the other extreme, implying that changes in the extremes can be much greater than the relative changes in the mean and standard deviation.

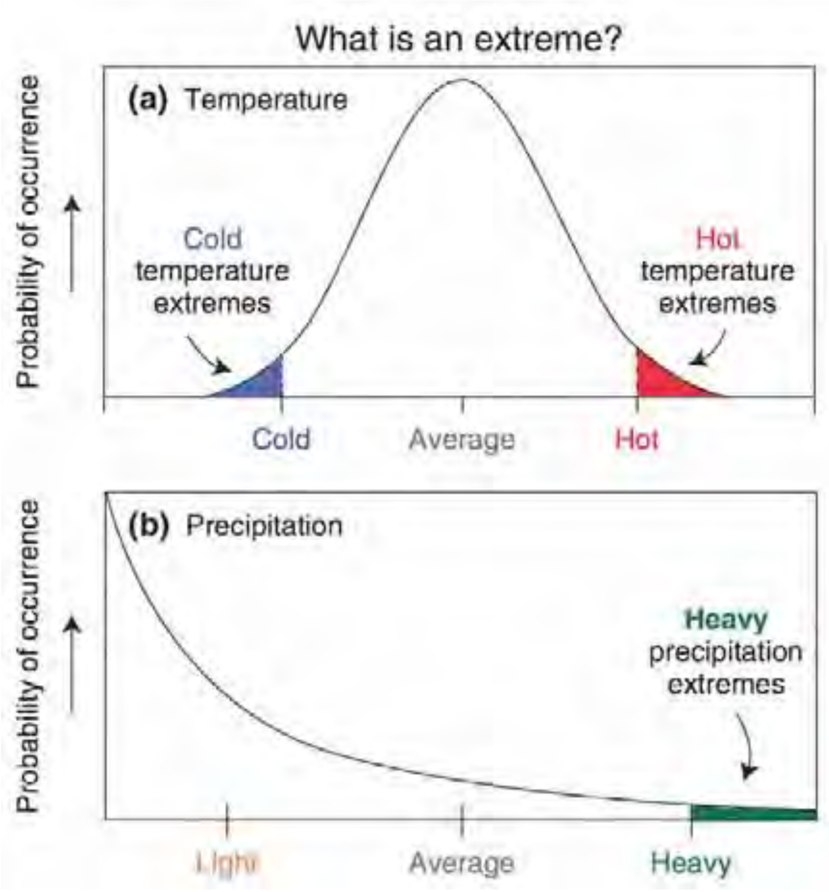

Figure 2-13: The probability distributions of daily temperature and precipitation. The higher the black line, the more often weather with those characteristics occurs. Shaded areas denote extremes (figure 1 of Zhang et al., 2011).

Because large changes in the extremes can occur even with small changes in the average climate, extremes may be the first indication that the climate is changing in a way that can affect humans and the environment. However, while the importance of the societal and economic impacts of extreme climate events is undeniable, the study of climate events (particularly on the global scale) is still in its infancy [*Alexander and Tebaldi*, 2012].

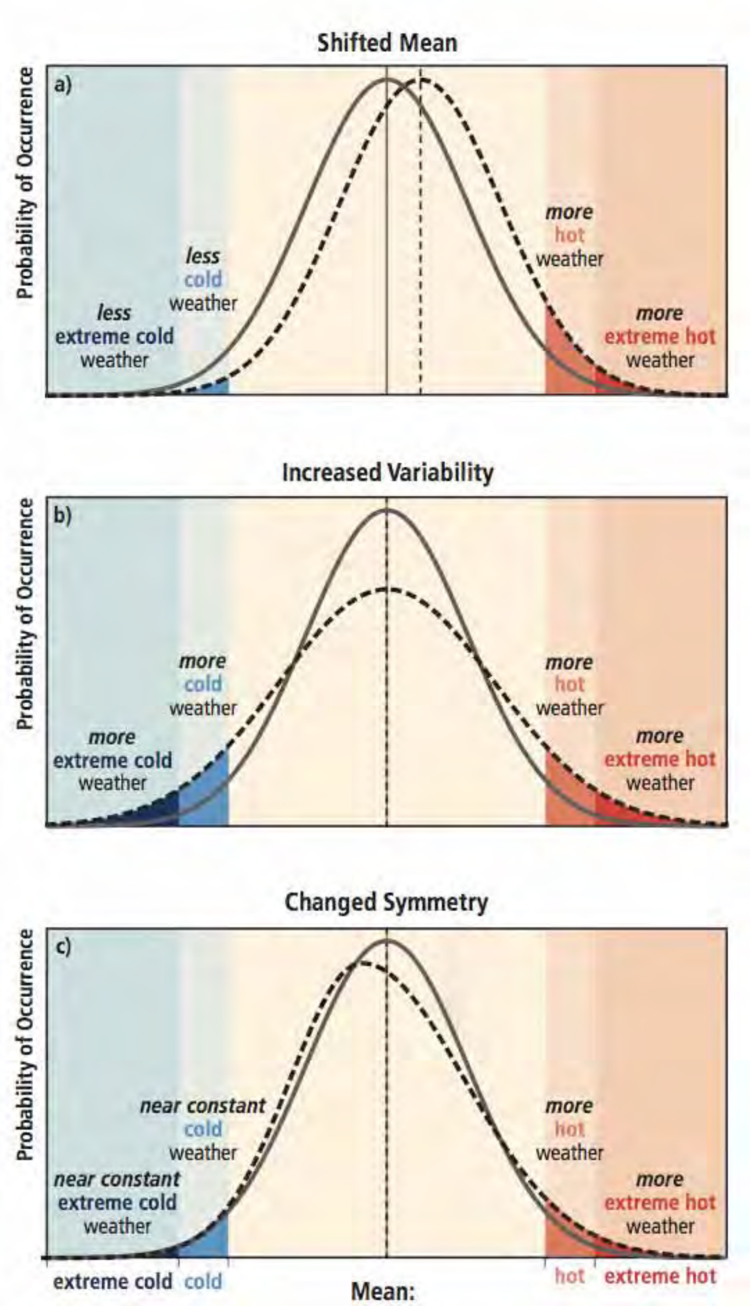

Figure 2-14: The effect of changes in temperature distribution on extremes. Different changes in temperature distributions between present and future climate and their effects on extreme values of the distributions: (a) effects of a simple shift of the entire distribution toward a warmer climate; (b) effects of an increase in temperature variability with no shift in the mean; (c) effects of an altered shape of the distribution, in this example a change in asymmetry toward a hotter part of the distribution (modified figure SPM.3 in IPCC, 2012). The solid line indicates the initial distribution while the dashed line indicates the new distribution.

The first IPCC report did not address the question of weather extremes have changed [*Folland et al.*, 1990; *Folland et al.*, 1992]. In the second assessment report, IPCC attempted to address the question of whether climate had become more variable or extreme [*Nicholls et al.*, 1996] but found no global evidence of change in part because observational data was not comprehensive enough. There were a few regional studies available but the lack of consistency in definition of extremes made it impossible to provide a comprehensive global picture. These challenges led to efforts to improve the analysis of extremes [*Nicholls and Alexander*, 2007] such that by the third and fourth assessment reports in 2001 and 2007, firmer statements could be made about past and future changes in extremes and the attribution of their causes [*Alexander and Tebaldi*, 2012].

With the documented increasing trend (0.13 ± 0.03 °C decade^{-1}) in global mean temperature since 1950 [*Trenberth et al.*, 2007], changes in temperature extremes could be observed. The change in the extremes included a reduction in cool nights and an increase in the intensity of heavy precipitation events [*Trenberth et al.*, 2007]. But while these changes in extremes are consistent with a warmer climate, extensive research demonstrates that changes in the mean may be unreliable indicators of changes in the magnitude of relative extremes which occur within the tails [*Mearns et al.*, 1984; *Katz and Brown*, 1992; *Zwiers and Kharin*, 1998; *Easterling et al.*, 2000a; *Kharin and Zwiers*, 2000; *Kharin et al.*, 2007]. That is, changes in extremes may also be influenced by changes in other parameters of the distribution, such as scale and skewness, which warrant projections of climate extremes to be calculated independently from mean projections [*Perkins*, 2011].

Climate extremes are commonly analysed in terms of return levels [*Kharin et al.*, 2007] or indices [*Frich et al.*, 2002; *Alexander et al.*, 2006]. A return level is the magnitude of an event that occurs once on average during a specified return period [*Coles*, 2001]. For example, a 1-in-20 year precipitation event is said to occur, on average, once every 20 years. The generalized extreme value distribution has also been used extensively in this kind of analysis [e.g. *Zwiers and Kharin*, 1998; *Kharin and Zwiers*, 2000; *Kharin et al.*, 2007; *Rusticucci and Tencer*, 2008; *Perkins*, 2011].

Climate indices are diagnostic tools used for monitoring the climate and are designed to describe changes in the frequency, magnitude and duration of climate extremes. Frich et al. [2002], using a limited set of climate indices to analyse global terrestrial observed data, concluded that a large proportion of the global land area was increasingly affected by a significant change in climatic extremes during the second half of the 20th century, including an increase in rainfall and an increase in warm nights. Alexander et al. [2006] used indices defined by the CCl/CLIVAR/JCOMM Expert Team on Climate Change Detection and Indices [ETCCDI, *Peterson and Manton*, 2008] and a more comprehensive set of global observational data. Their results showed widespread significant changes in temperature extremes associated with warming, especially for indices derived from daily minimum temperature. Daily maximum temperature indices showed similar changes but with smaller magnitudes [*Alexander et al.*, 2006]. Precipitation changes showed widespread and significant increase, but the changes are much less spatially coherent than the changes in temperature [*Alexander et al.*, 2006]. Some of these results are shown in Figures 2-15 to 2-17.

Figure 2-15a shows a significant decrease in the annual occurrence of cold nights while Figure 2-15b shows a significant increase in the annual occurrence of warm nights implying a positive shift in the distribution of daily minimum temperature throughout the globe. A similar shift towards warmer days is seen in daily maximum temperature but at smaller magnitudes (Figure 2-15c and 2-15d). Figure 2-16 shows a decrease in the duration of cold spells (Figure 2-16a), number of frost days (Figure 2-16c), and the extreme temperature range (Figure 2-16d), but an increase in the duration of warm spells (Figure 2-16b). Precipitation indices show increasing trends, which are widespread and significant, but these changes are much less spatially coherent than the temperature trends (Figure 2-17). Comparison between observed and simulated trends at the global scale shows that, despite limitations, models can reasonably simulate trends in temperature extremes but not precipitation extremes [*Tebaldi et al.*, 2006]. Multi-model projections [e.g. *Tebaldi et al.*, 2006; *Kharin et al.*, 2007] have also shown changes in temperature and precipitation extremes consistent with a warmer climate.

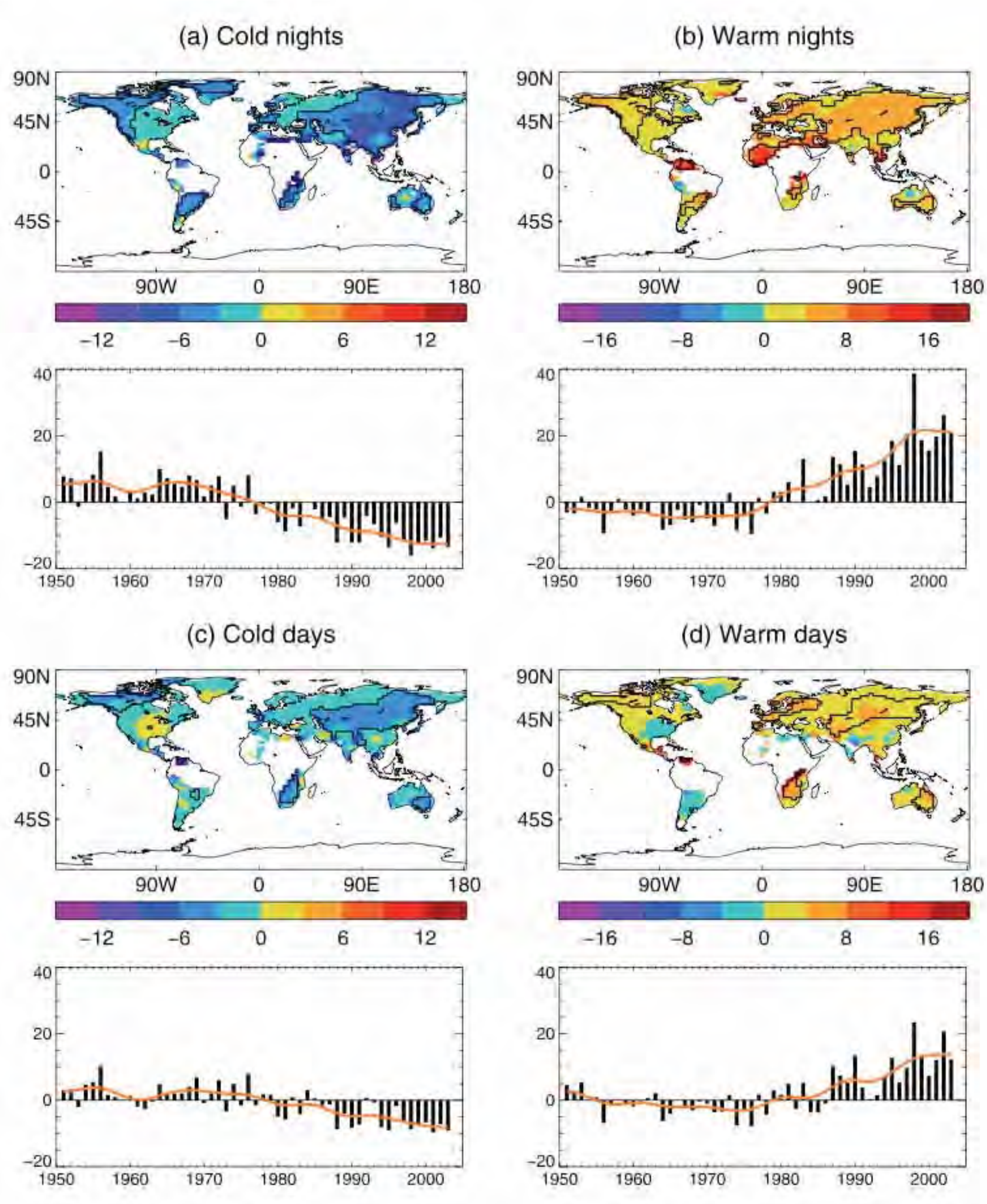

Figure 2-15: Trends (in days per decade, shown as maps) and annual time series anomalies relative to 1961–1990 mean values (shown as plots) for annual series of percentile temperature indices for 1951– 2003 for (a) cold nights (TN10p), (b) warm nights (TN90p), (c) cold days (TX10p), and (d) warm days (TX90p). Trends were calculated only for the grid boxes with sufficient data (at least 40 years of data during the period and the last year of the series is no earlier than 1999). Black lines enclose regions where trends are significant at the 5% level. The red curves on the plots are nonlinear trend estimates obtained by smoothing using a 21-term binomial filter (figure 2 of Alexander et al., 2006).

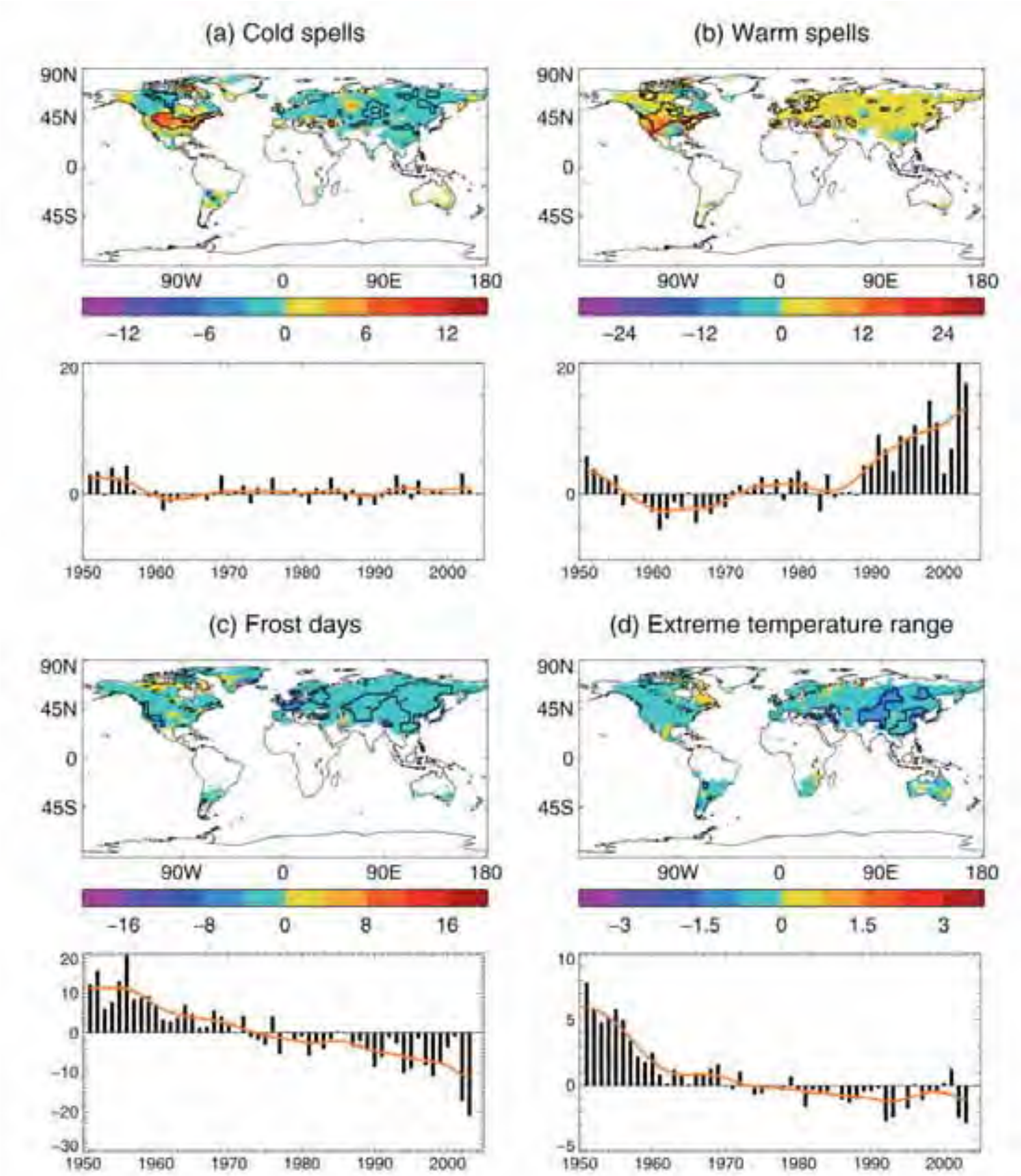

Figure 2-16: As Figure 2-15 but for (a) cold spells (CSDI, in days), (b) warm spells (WSDI, in days), (c) frost days (FD, in days) and (d) extreme temperature range (ETR, i.e. TXx-TNn, in °C) (figure 3 of Alexander et al., 2006).

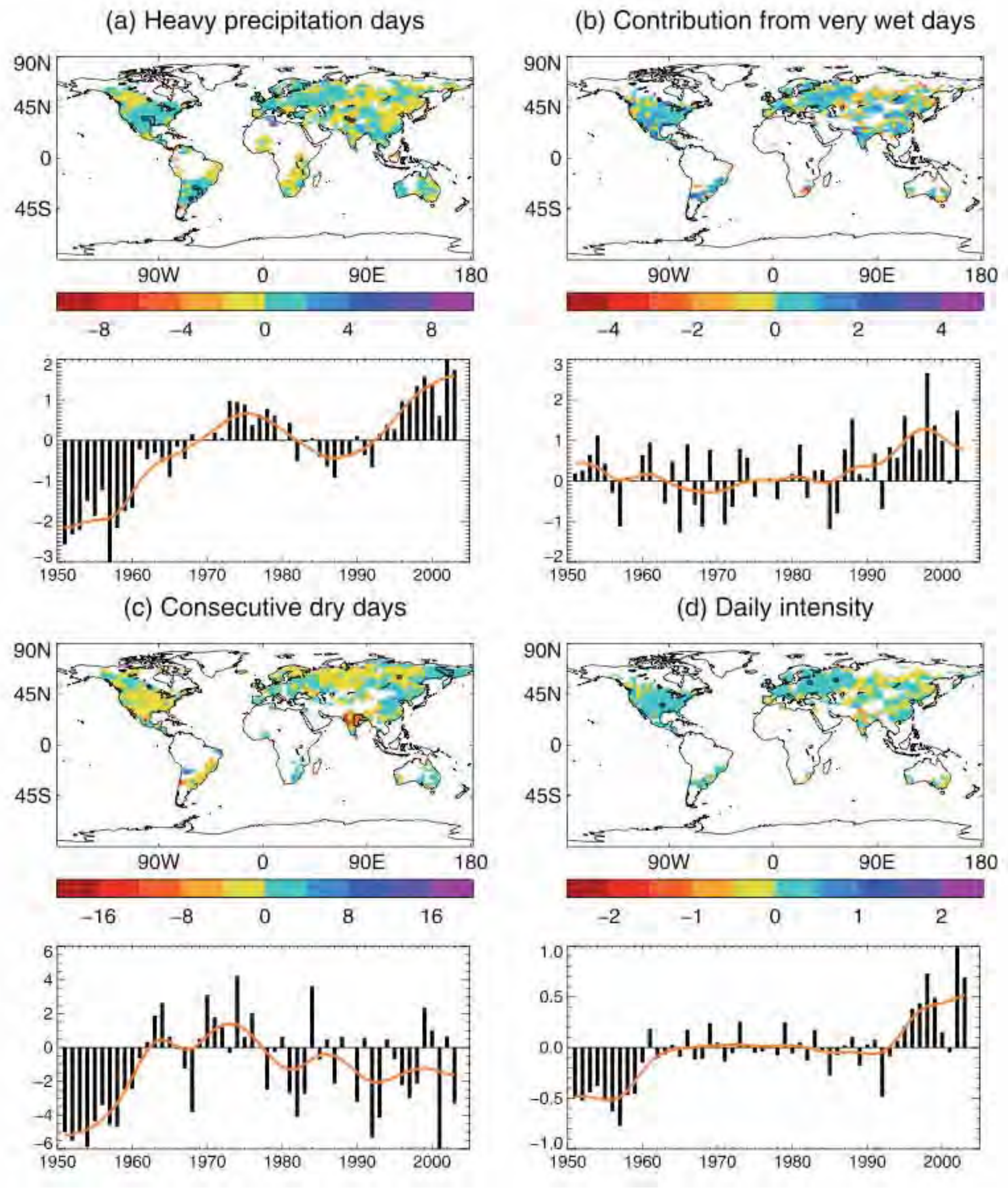

*Figure 2-17: As Figure 2-15 but for precipitation indices (a) heavy precipitation days (R10 in days), (b) contribution from very wet days (R95pT=(R95p/ PRCPTOT)*100 in %), (c) consecutive dry days (CDD in days), and (d) daily precipitation intensity (SDII in mm/day) (figure 6 of Alexander et al., 2006).*

Figure 2-18 shows multi-model average spatial patterns of change of temperature indices at the end of the 20th century (left column) and under the Special Report on Emissions Scenarios [SRES, *Nakićenović et al.*, 2000] A1B (mid-range) scenario (right column). From top to bottom, it shows: (a) total number of frost days, (b) intra-annual temperature range, (c) growing season length, (d) heat wave duration index and (e) warm nights [*Tebaldi et al.*, 2006]. Shades of blue (red) indicate a cooling (warming) trend.

Figure 2-19 shows multi-model average spatial patterns of change of temperature indices at the end of the 20th century (left column) and under the A1B scenario (right column). From top to bottom, it shows: (a) the number of days with precipitation > 10 mm, (b) maximum number of consecutive dry days, (c) maximum 5-day precipitation total, (d) simple daily intensity index and (e) fraction of total precipitation due to events exceeding the 95th percentile of the climatological distribution for wet day amounts [*Tebaldi et al.*, 2006]. Shades of blue (red) indicate a trend towards wetter (drier) climate.

For all indices it is clear that the dominant patterns surfacing with significant strength at the end of the 21st century are the ones already present at the end of the 20th century. This is not surprising and is most evident in the temperature-related indices (Figures 2-18) but is detectable in the precipitation indices (Figure 2-19) as well [*Tebaldi et al.*, 2006].

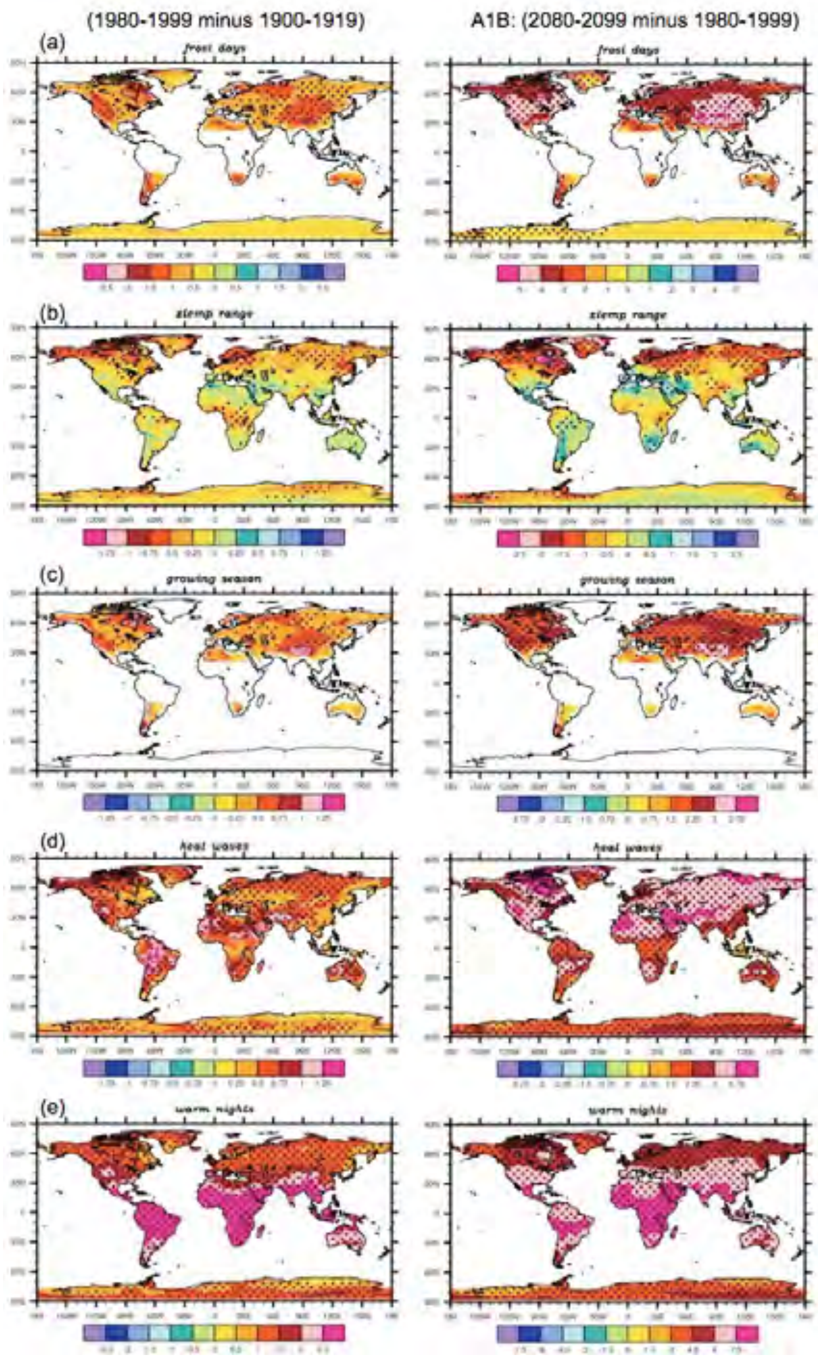

Figure 2-18: Multi-model averages of spatial patterns of change of temperature indices between two twenty-year averages at the end of 20th century (1980–1999 minus 1900–1919, left column) and under A1B (2080–2099 minus 1980–1999, right column). Each grid point value for each model has been standardized first; then a multi-model simple average is computed. Stippled regions correspond to areas where at least five of the nine models concur in determining that the change is statistically significant. Oceans (and subtropical regions for frost days and growing season) are not included in the analysis and are left blank (from figures 3 and 4 of Tebaldi et al., 2006).

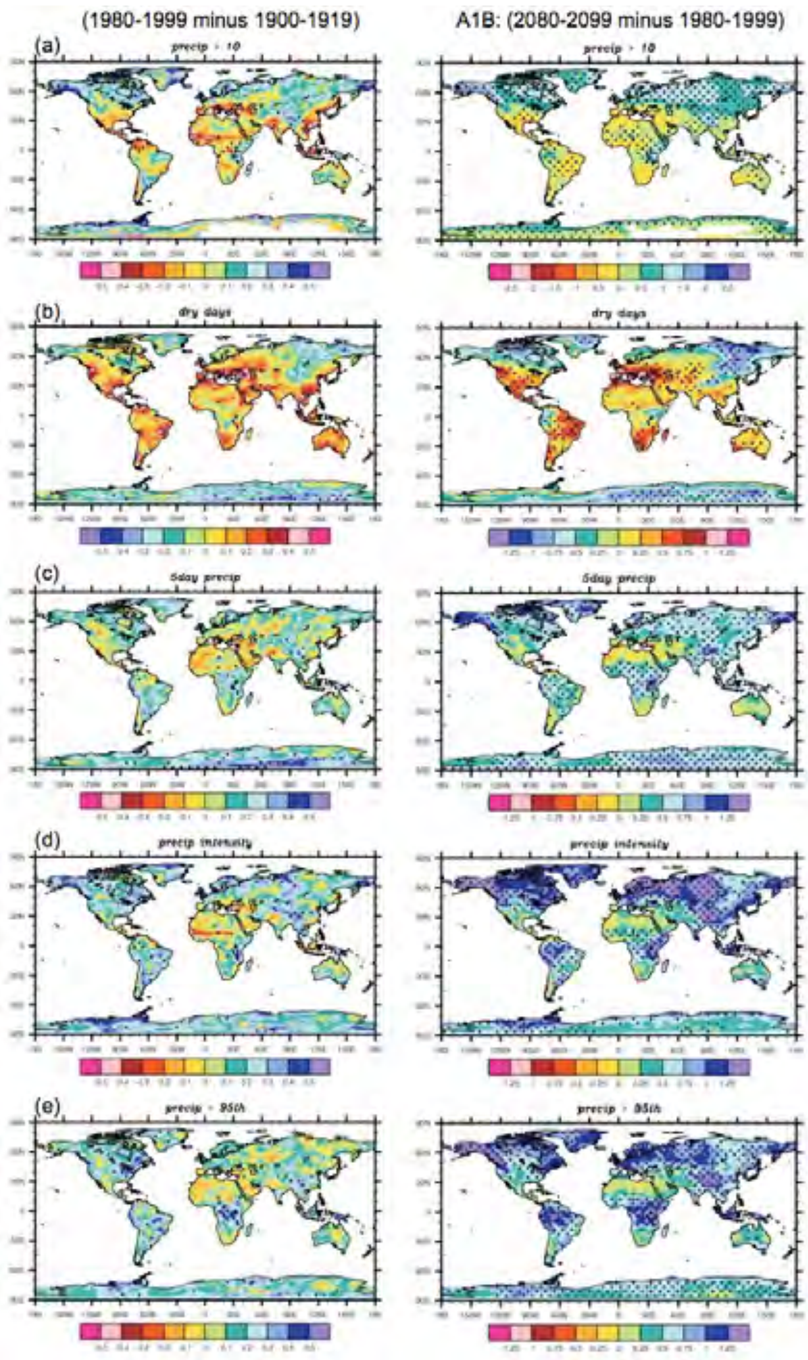

Figure 2-19: As Figure 2-18 but for precipitation indices (from figures 3 and 4 of Tebaldi et al., 2006).

2.5 Drivers of climate extremes

Alexander and Tebaldi [2012] note that natural modes of climate variability such as the El Nino-Southern Oscillation (ENSO), North Atlantic Oscillation (NAO), and the Southern Annular Mode (SAM) have a significant influence on the variability of atmospheric climate. Of these, ENSO has been identified as the most dominant mode of interannual variability that influences mean climate conditions as well as extreme climatic events such as droughts and floods in many parts of the world. However, other contributing factors and processes are also important.

For example, over Australia, Alexander and Arblaster [2009] note that a number of studies have attributed portions of the drying in southwest Australia to anthropogenic forcing [*Cai and Cowan*, 2006; *Hope*, 2006; *Timbal et al.*, 2006], the impact of natural variability [*Cai et al.*, 2005] and land-cover change [*Pitman and Narisma*, 2005; *Timbal and Arblaster*, 2006; *Pitman and de Noblet-Ducoudré*, 2012]. An increase in precipitation and associated cooling in northwest Australia have been variously ascribed to aerosols [*Rotstayn et al.*, 2007] and an enhancement of the Australian monsoon [*Wardle and Smith*, 2004] in addition to other large-scale driving mechanisms which include the decadal variability of the tropical Pacific sea surface temperatures [*Alexander and Arblaster*, 2009].

Mesoscale and regional-scale studies have shown that LULCC can affect extremes. Most recently, Teuling et al. [2010] highlighted how forest and grassland regions of Europe responded differently in terms of heatwaves, identifying a different resilience of the deeply rooted forests compared to grasslands. In fact, once linked with the impact of LULCC on land-atmosphere coupling [*Seneviratne et al.*, 2006a; *Seneviratne et al.*, 2010] and the recognition that the surface energy balance is strongly affected by the nature of the land cover [*Pitman*, 2003; *Bonan*, 2008b; *Levis*, 2010] it is implausible to think that LULCC would not affect extremes to some degree provided it is of a sufficient scale and intensity.

Studies on the role of land surface in suppressing or exacerbating temperatures extremes [*Durre et al.*, 2000; *Seneviratne et al.*, 2006a; *Diffenbaugh et al.*, 2007; *Fischer et al.*, 2007] emphasize the important role of soil-moisture deficit in intensifying or lengthening heatwaves through feedback between temperature, evaporation and precipitation [*Alexander and Tebaldi*, 2012]. In figure 2-20, Alexander [2011] illustrates how the partitioning of the sensible and heat fluxes affects the development of the boundary layer and the hydrological cycle.

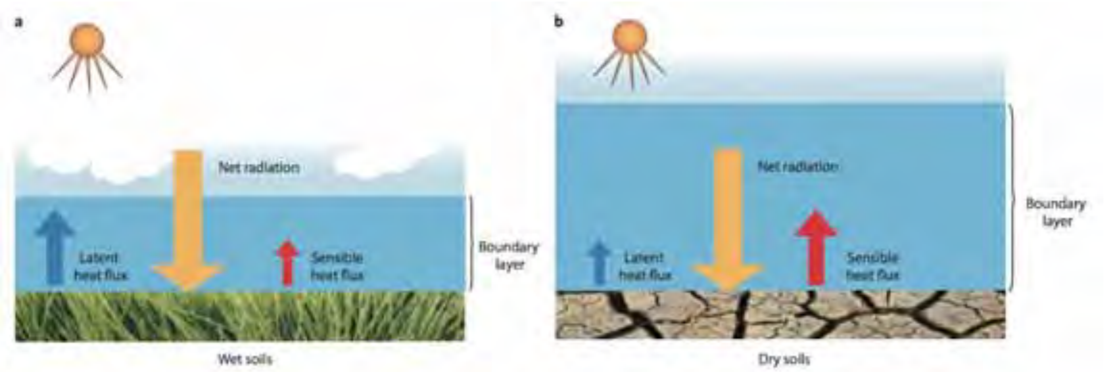

Figure 2-20: Schematic of the net radiation budget at the land surface at (a) areas with high moisture and (b) areas with high soil-moisture deficit (figure 1 of Alexander, 2011).

In areas with high soil moisture (Figure 2-20a), the latent heat flux via evaporation and transpiration dominates, enhancing cloud formation and a tendency for cooling. In contrast, in areas of high soil-moisture deficiency

(Figure 2-20b), the dry soil increases the sensible heat flux, producing a deeper, warmer, drier low-level atmosphere, inhibiting convection and cloud formation and creates a positive feedback loop.

2.6 Summary

This chapter describes the theory of how LULCC can affect climate and presents examples from recent studies to establish the current understanding of the impacts of LULCC on climate in the observed and simulated changes in extremes. Existing studies have established the major role played by LULCC in the climate system [*Pielke et al.*, 2011; *Pitman and de Noblet-Ducoudré*, 2012] and emphasize the need to correctly predict changes in the extremes to ascertain its possibly adverse effects [*Alexander and Tebaldi*, 2012; *IPCC*, 2012]. However, thus far, modelling studies on the role of LULCC have been largely limited to how the mean regional or global climate is affected. Further, studies of how extremes have changed, or might change in the future, have tended to examine the role of increasing greenhouse gases and not examined any role associated with LULCC.

This thesis attempts to combine these separate avenues by examining how LULCC might affect extremes. However, before presenting results on how LULCC affects extremes, the methodology employed in this thesis is presented, followed by an examination of how LULCC affects the mean regional and global climate. The next chapter therefore describes the model used, experiments conducted to simulate LULCC as well as the methods for calculating the changes in the extremes.

Chapter 3
Methodology

To simulate the effect of LULCC on climate extremes, a climate model coupled to a sophisticated land surface model (LSM) capable of simulating the fluxes of energy, water and carbon at the canopy scale is used. The climate model needs to be able to run long enough simulations to allow an equilibrated state to be realized and allow for rigorous statistical testing. This inevitably implies a compromise in terms of the resolution used to resolve spatial scales. Exploring the impact of LULCC on extremes also requires an LSM with sufficient complexity such that any imposed changes in land cover results in a change in surface characteristics that, in turn, affects the simulation of land surface fluxes. This chapter describes the models used, and the modifications implemented, for the LULCC experiments. The methods used to assess changes in the means and extremes are also described.

3.1 The CSIRO Mk3L climate model

The CSIRO Mk3L climate system model is a computationally efficient coupled general circulation model designed primarily for millennial-scale climate simulations and paleoclimate research. It is composed of sub-models that describe the atmosphere, ocean, sea-ice and land surface. A full description of the model is provided by Phipps et al. [2011] and is summarized below.

The atmospheric model is a reduced-resolution version of the atmospheric component of the CSIRO Mk3 model [*Gordon et al.*, 2002] with zonal and meridional grid increments of 5.625° and ~3.18°, respectively. Its hybrid vertical coordinate has 18 vertical levels. Figure 3-1 shows the Mk3L model topography. A cumulus convection scheme [*Gregory and Rowntree*, 1990] and a prognostic stratiform cloud scheme [*Rotstayn*, 1997; 1998; 2000] are both incorporated in the model. The radiation scheme simulates the full annual and diurnal cycles of longwave and shortwave radiation and is able to calculate the cloud radiative forcings [*Lacis and Hansen*, 1974; *Fels and Schwarzkopf*, 1975; 1981; *Schwarzkopf and Fels*, 1985; 1991]. Ozone concentrations are taken from the AMIP II recommended dataset [*Wang et al.*, 1995]. To specify the atmospheric CO_2 concentrations, CO_2 transmission coefficients are generated using utilities provided with the model [*Phipps et al.*, 2011]. The epoch and solar constant, which may be modified for studies on millennial timescales, have been set by default to 0 and 1365 W m^{-2}, respectively [*Phipps et al.*, 2011].

The default land surface model in the CSIRO Mk3L (hereafter referred to as K91) is an enhanced version of the soil-canopy model described by Kowalczyk et al. [1991; 1994]. K91 is replaced by the CSIRO Community Atmosphere Biosphere Land Exchange (CABLE) model for this thesis and is therefore not discussed in further detail.

The CSIRO Mk3L model can be run in three different configurations: (1) the fully coupled climate system model, (2) a stand-alone ocean model, or (3) a stand-alone atmosphere-land-sea ice model. In the stand-alone atmosphere model, which is used in this thesis, four types of surface grid point are employed: land, ocean, mixed-layer ocean and sea-ice. The temperatures of the ocean grid points are determined from prescribed monthly sea surface temperatures. Linear interpolation in time is used to estimate values at each time step. At high latitudes, ocean grid points may be converted to mixed-layer ocean and sea ice grid points [*Phipps et al.*, 2011].

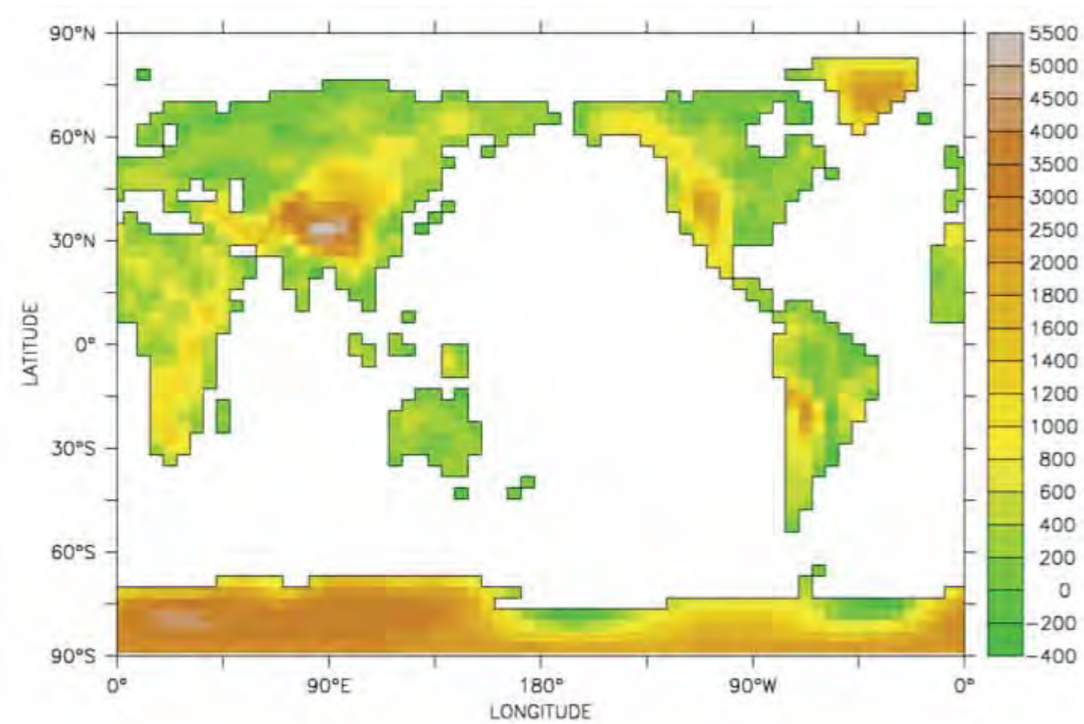

Figure 3-1: The topography of the Mk3L atmosphere model showing the elevation of the land grid points (m) (figure 1 of Phipps et al., 2011).

The sea-ice model includes both ice dynamics and ice thermodynamics [*O'Farrell*, 1998]. Internal resistance to deformation is parameterized using cavitating fluid rheology [*Flato and Hibler III*, 1990; 1992]. The thermodynamic component splits the ice into three layers, one for snow and two for ice [*Semtner*, 1976]. Sea ice grid points are allowed to have fractional ice cover, representing the presence of leads and polynyas.

The oceanic component of Mk3L [*Gordon and O'Farrell*, 1997; *Hirst et al.*, 2000; *Bi*, 2002] is a coarse resolution, z-coordinate general circulation model based on the implementation by Cox [1984] of the primitive equation numerical model of Bryan [1969]. The horizontal grid matches the Gaussian grid of the atmosphere model, and there 21 vertical levels. The prognostic variables are potential temperature, salinity, and the zonal and meridional components of the horizontal velocity. The vertical velocity is diagnosed through the application of the continuity equation.

When fully coupled, the atmospheric and oceanic components exchange fields every hour to ensure consistent simulation of the diurnal cycles of sea surface temperature and salinity. Flux adjustments are usually applied to improve the realism of the control climate and to ensure stability on millennial timescales. However, in this thesis the sea surface temperatures are prescribed, removing the need for flux adjustment, and thus this aspect of the model is not discussed in further detail.

To simulate the impacts of LULCC, the stand-alone atmosphere-land-sea ice model with prescribed sea surface temperature fields is used. This model configuration is commonly used in LULCC experiments [*Pitman et al.*, 2009; *Davin and de Noblet-Ducoudré*, 2010] because it allows the signal due to LULCC to be more clearly isolated against long-term variability induced by coupling to an ocean model. However, there are risks associated with this approach as it has the potential to suppress large-scale teleconnections and reduce the global scale impact of LULCC [*Davin and de Noblet-Ducoudré*, 2010].

In summary, the CSIRO Mk3L climate model's ability to simulate the global climate reasonably combined with its impressive computational efficiency makes it suitable for a large-scale, multi-year study of the impact of LULCC on climate. However, its major weakness is its native land surface model, K91, which lacks the capacity to simulate the feedback from climate change and variability due to changes in the terrestrial carbon balance [*Mao et al.*, 2011]. This limitation could be overcome by replacing the primitive K91 model with a more sophisticated land surface model that couples the fluxes of water and energy and carbon at the canopy scale.

3.2 Mk3L-CABLE

The Community Atmosphere Biosphere Land Exchange (CABLE) land surface model is a "third-generation" land surface model [*Sellers et al.*, 1997] that formally couples the fluxes of energy, water and carbon at the canopy scale. Details of the model have been presented elsewhere [*Wang et al.*, 2011] and only a brief summary is provided here.

CABLE includes several sub-models representing canopy processes, soil, snow and carbon pool dynamics and soil respiration. The major improvements of CABLE over K91 are in the canopy processes and the inclusion of carbon pool dynamics.

CABLE was developed from the soil-canopy atmosphere model (SCAM) by Raupach et al. [1997], which was coupled to an atmosphere model and tested using field measurements by Finkele et al. [2003]. SCAM placed the canopy above the soil surface allowing turbulent transfer between the soil, vegetation and atmosphere and the calculations of canopy aerodynamic properties as a function of canopy height and canopy leaf area index. Wang and Leuning [1998] further improved the model by implementing a one-layer two-leaf canopy model based on the multilayer model of Leuning et al. [1995]. The two-leaf canopy model differentiates between the sunlit and shaded leaves, allowing two sets of physical and physiological parameters to represent the bulk properties of the sunlit and shaded leaves. The one-layer model also included allowance for non-spherical leaf distributions, an improvement of the description of the solar and thermal radiation, and a modification of the stomatal model by Leuning et al. [1995] to include the effects of soil water deficit on photosynthesis and respiration.

The annual plant net primary productivity (NPP) is determined from the annual carbon assimilation corrected for respiratory losses while the seasonal growth and decay of biomass is determined by how carbon is allocated between the leaves, roots and wood. A simple carbon pool model describes the flow of carbon between the soil and vegetation [*Dickinson et al.*, 1998]. CABLE's soil and snow models are similar to that of K91. The multilayer soil model, described in detail by McGregor et al. [1993], simulates soil moisture and temperature, differentiating between liquid water and ice content of the soil [*Kowalczyk et al.*, 2006]. The snow model, computes the temperature, density and thickness of three snowpack layers and the albedo of the snow surface as a function of the age of the top snow layer [*Kowalczyk et al.*, 2006].

3.2.1 Model evaluation

Mao et al. [2011] evaluated the control climatology of the coupled Mk3L-CABLE model and showed that it could simulate atmospheric variables, including near-surface temperature and precipitation, well. The following figures from Mao et al. [2011] show how the simulated temperature (Figure 3-2), precipitation (Figure 3-3) and net radiation (Figure 3-4) from the Mk3L model, coupled to K91 and CABLE, compare to observations. The figures in the left column are for June-July-August (JJA) while those on the left are for December-January-February (DJF). For Figures 3-2 and 3-3, the top row shows the differences between observation and the Mk3L-CABLE simulation, while the second row from the top shows the differences between the observation and the Mk3L-K91 simulation. Only the values over continental surfaces are shown. The bottom row shows the zonally averaged values from the simulations (red line for Mk3L-K91, blue line for Mk3L-CABLE) and the range of available observations (thick grey line).

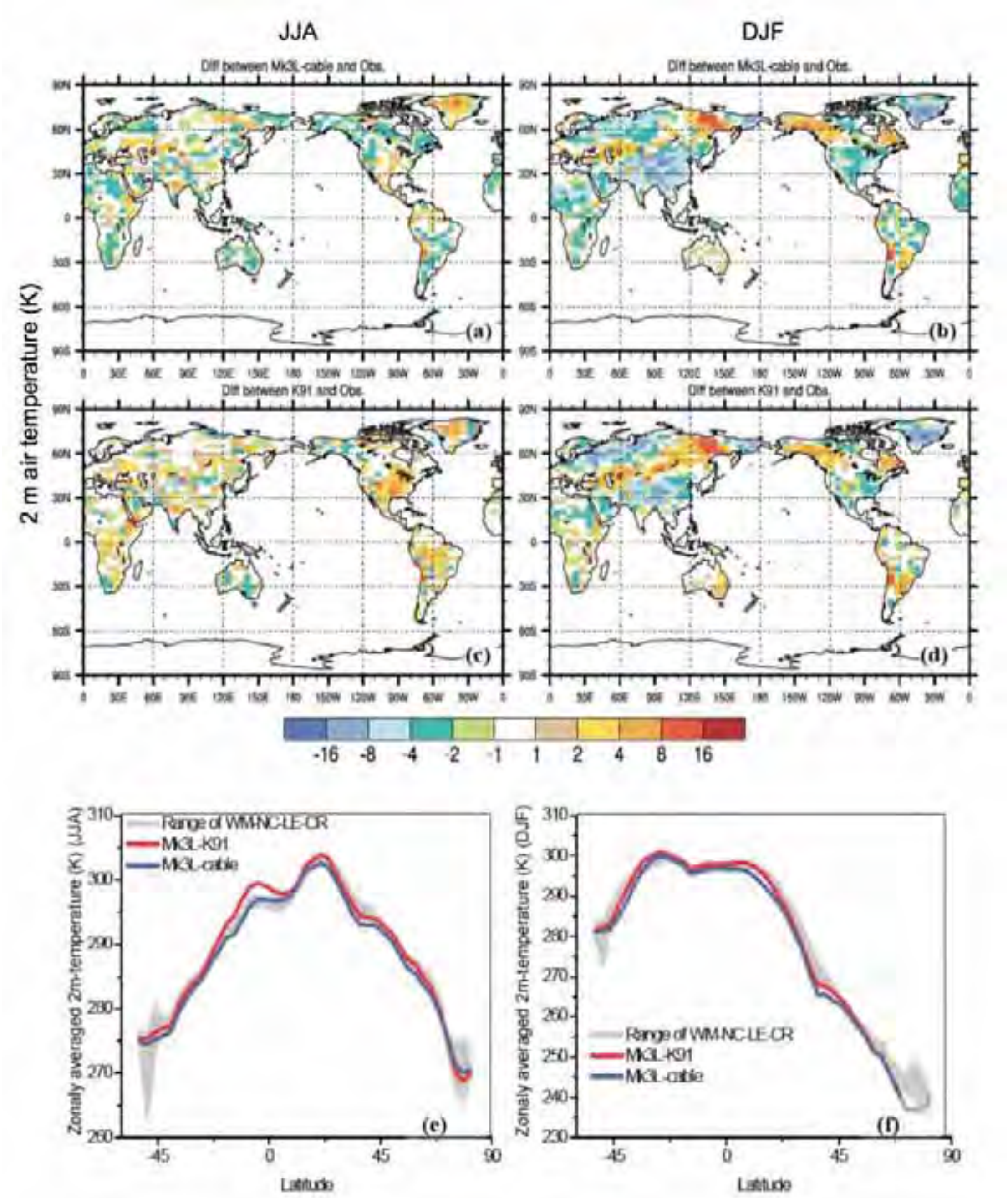

Figure 3-2: The 2 m air temperature differences (K) relative to observations for (a) Mk3L-CABLE for JJA, (b) Mk3L-CABLE for DJF, (c) Mk3L- K91 for JJA and (d) Mk3L-K91 for DJF. In each case the model is differenced from the CRU (New et al., 2000) climatology. In the lower panels the observed range is shown for WM (Willmott and Matsuura, 2001), NC (Kalnay et al., 1996), LE (Legates and Willmott, 1990) and CR (New et al., 2000). Only values over continental surfaces are shown (figure 3 of Mao et al., 2011).

Figure 3-2 shows the difference between the simulated and observed surface air temperature (K). The observed values used in the maps are from CR [*New et al.*, 2000]. The WM [*Willmott and Matsuura*, 2001], NC [*Kalnay et al.*, 1996] and LE [*Legates and Willmott*, 1990] datasets, in addition to the CR, are used in the range of zonally averaged observation plot. The DJF figures are comparable to the differences between the observed and model mean reported for the CMIP1 models [*McAvaney et al.*, 2001]. For example, they show generally similar patterns with a cold bias over northern Eurasia, the Himalayas, China and parts of Africa, and warm bias over North America, eastern Russia and southern Australia [*Mao et al.*, 2011]. The magnitudes of the differences are largely similar and the large-scale biases shows that when simulating the control climatology, Mk3L is insensitive to the LSM used. The zonal average shows that the simulated values are within the range of the observations and that Mk3L can capture the zonal gradients well. Comparison with the results from McAvaney et al. [2001] shows that the model is competitive with those models used in the IPCC Third Assessment Report [TAR, *Mao et al.*, 2011].

Figure 3-3 shows the difference between the simulated and the observed precipitation rate (mm day^{-1}). The observations used in the maps are from CMAP [XA, *Xie and Arkin*, 1997]; the range of values used in the zonal plots includes XA, WM [*Willmott and Matsuura*, 2001], LE [*Legates and Willmott*, 1990] and GP [*Huffman et al.*, 1997]. The DJF figures are comparable to the reported difference between observations and the CMIP1 model simulations [*McAvaney et al.*, 2001].

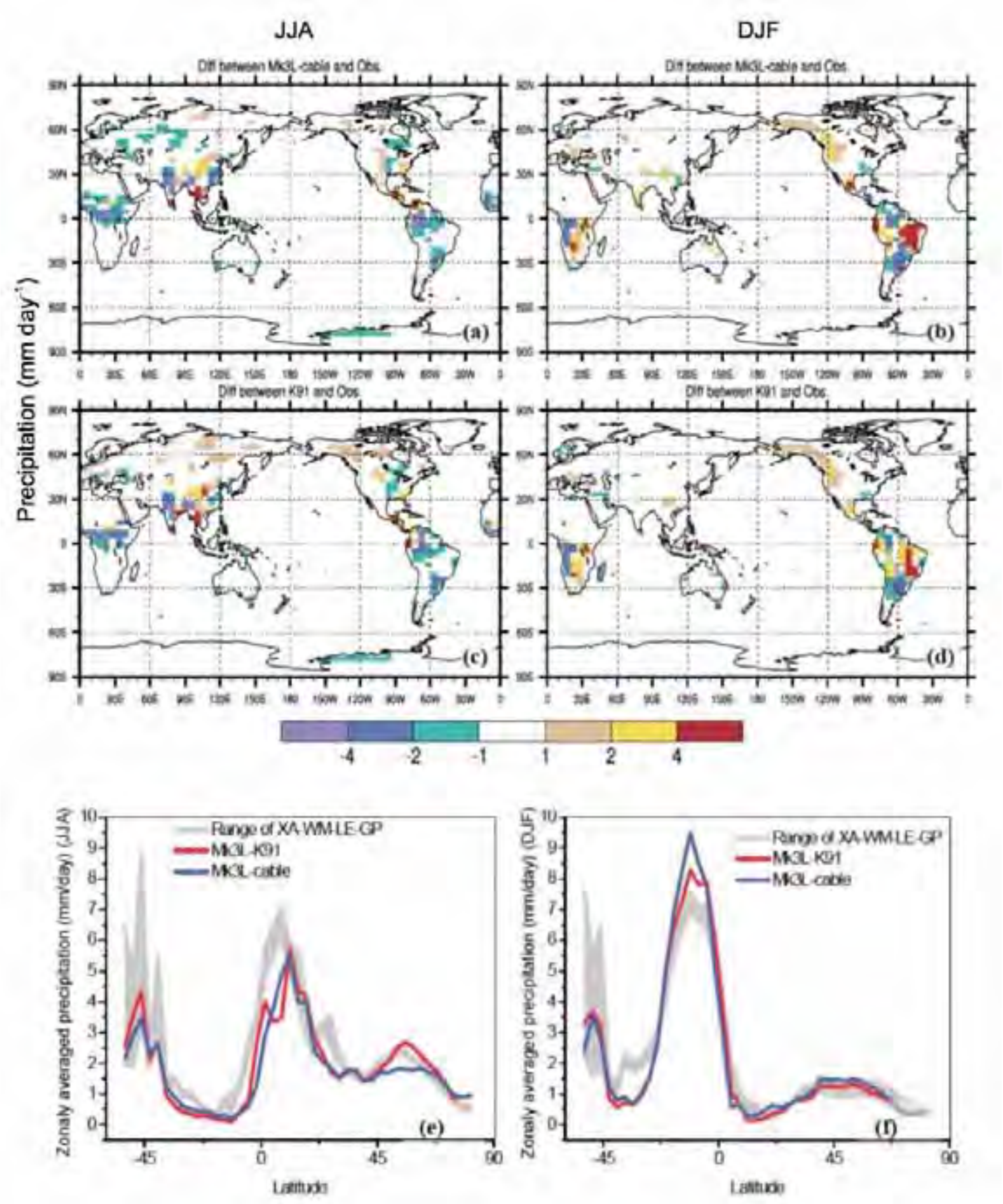

Figure 3-3: As Figure 3-2 but for precipitation (mm day^{-1}) differenced from the CMAP precipitation rate (Xie and Arkin, 1997). In the lower panels the observed range is shown for XA (Xie and Arkin, 1997), WM (Willmott and Matsuura, 2001), LE (Legates and Willmott, 1990) and GP (Huffman et al., 1997). Only values over continental surfaces are shown (figure 4 of Mao et al., 2011).

Both CMIP1 and Mk3L have dry biases over Amazonia although Mk3L's bias is more intense; both have a dry bias over the western edge of North and South America, likely related to a poor representation of the Rockies and the Andes; and both have a wet bias over southern Africa. Overall, Mk3L's precipitation is comparable to the models used in the TAR [*Mao et al.*, 2011].

The zonal averages show that the model captures the zonal variability well but there are clear anomalies. During JJA, the model underestimates the rainfall south of 10°N because of underestimated rainfall over the Amazon and Congo basins; during DJF, the model overestimates the rainfall over the region 0-10°S [*Mao et al.*, 2011]. However, model simulations such as those for CMIP1 have shown that precipitation is a particularly difficult quantity to simulate, especially over the tropics as well as in the region bounded by 30°-40°S, so in this regard, Mk3L may be considered competitive compared to the models used in the TAR [*Mao et al.*, 2011].

Figure 3-4 compares the zonally averaged observed net surface radiation (W $m^{-2,}$ black dots) from ISCCP FD [*Zhang et al.*, 2004] with the model simulation (red line for Mk3L-K91, blue line for Mk3L-CABLE). The model clearly underestimates over the tropics and over the northern hemisphere (JJA) indicating a need to further improve the model's albedo parameterisation to enable net radiation to be simulated with a much higher skill throughout the year [*Mao et al.*, 2011].

Thus, while the control climate described by Mao et al. [2011] was largely reasonable, their evaluation also identified inconsistencies between the model's simulation of net radiation and observed net radiation. While this is not large enough to affect the large-scale simulation of the Earths' climate, it is large enough to be worrisome in terms of using the model for LULCC experiments where changes in net radiation are known to be particularly important [*Davin and de Noblet-Ducoudré*, 2010]. Further, while Mao et al. [2011] presented a good control simulation, the default version of CABLE could not reflect changes in some key vegetation parameters associated with LULCC, including parameters that control how LULCC affects vegetation albedo. Finally, the default version of CABLE used by Pitman et al. [2009] and by de Noblet-Ducoudré et al. [2012] did not use tiling of the surface and therefore tended to impose too large a change due to LULCC. These three problems required some major modifications to CABLE that are explained in Section 3.4.

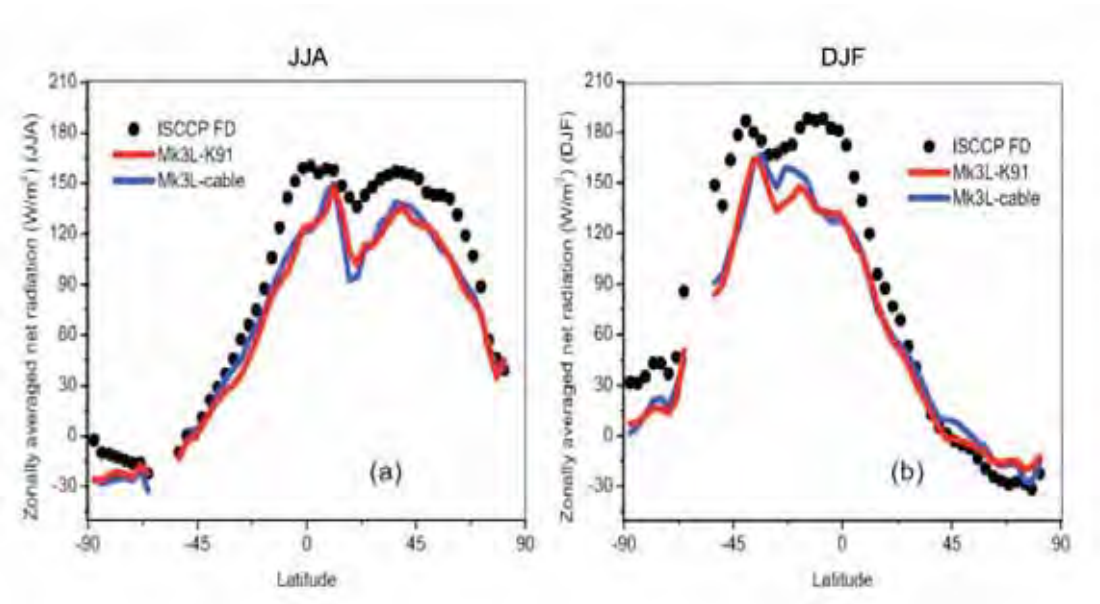

Figure 3-4: Zonal net surface radiation (W m^{-2}) for JJA (left) and DJF (right) for the two Mk3L simulations (observations are ISCCP FD, Zhang et al., 2004; figure 5 of Mao et al., 2011).

3.2.2 Default model set up and configuration

CABLE may be run in two configurations: (1) offline, where the meteorological data are prescribed to the LSM, and (2) coupled, where the LSM is coupled to a host atmospheric model and surface values are exchanged between the models at specified time intervals. For this thesis, CABLE is run in a coupled configuration with Mk3L serving as the host atmospheric model.

The model is run one calendar year at a time and restart files are saved at the end of each run. A script is used to manage the running of the model for multi-year simulations. Initialization files are provided to the model during the first year of simulation. The resulting restart files are then used to provide initial and boundary conditions for the subsequent years. The runtime options for the model are provided via control files. Some of the variables and values used to control Mk3L and CABLE in this study are shown in Tables 3-1 and 3-2.

The soil is represented by six layers with depths of: 0.022, 0.058, 0.154, 0.409, 1.085, 2.872 m from the surface to the bottom, respectively, giving a total depth of 4.6 m [*Gordon et al.*, 2002]. The thermal (specific heat capacity, soil thermal conductivity, etc.) and hydraulic (saturation content, wilting content, field capacity, hydraulic conductivity, etc.) properties are defined for the nine soil types based on Zobler [1986] listed in Table 3-3. The geographical distribution of these soil types is shown in Figure 3-5. In the default configuration of the model, the soil albedo is set to a constant value (0.1) for all land grid points.

The model is setup to simulate the present day climate by default. Thus the CO_2 transmission coefficients are set to 280 ppmv and the prescribed sea surface temperatures (SSTs) are based on the data from NOAA OI V2 dataset [*Reynolds et al.*, 2002] for the period 1982-2001. Likewise, the default vegetation cover (Figure 3-6) and the default leaf area index (Figure 3-7) are configured to reflect present-day conditions. The vegetation types used in the model, based on the IGBP classification, are shown in Table 3-4. Some of the vegetation types marked by asterisk (*) are not used in this thesis.

Table 3-1: Mk3L input parameters defined via the control file

Variable name	Value	Description
`lcouple`	F	Run the model in stand-alone atmosphere mode
`locean`	F	
`qflux`	F	Use prescribed sea surface temperatures
`nsstop`	0	Run model one calendar year at a time
`ndstop`	0	
`lastmonth`	12	
`months`	0	
`bpyear`	0	Epoch (years before present)
`csolar`	1365.0	Solar constant (W m^{-2})
`mstep`	20	Time step (minutes)
`nrad`	6	Call radiation scheme every 6 time steps
`naerosol_d`	0	Do not include indirect sulphate aerosol forcing
`co2_datafile`	co2_data.18l	Name of CO_2 data file
`o3_datafile`	o3_data.18l	Name of O_3 data file
`irfilename`	rest.start	Name of input restart file
`orfilename`	rest.end	Name of output restart file
`filewrflag`	T	Write restart file at end of run
`runtype`		Simulation name; used as prefix of output files
`lsm_type`	cable	Set CABLE as the land surface scheme
`statsflag`	T	Save monthly mean atmosphere variables to file
`savehist`	T	Save model variables every 24 hours (1440 minutes)
`hist_interval`	1440	

Table 3-2: CABLE input parameters

Variable name	**Value**	**Description**
filename%met	Mk3L	Input file
filename%out	out_cable.nc	Output file
filename%log	log_cable.txt	Execution log file
filename%restart_in	restart_out.nc	Restart file to read
filename%restart_out	restart_out.nc	Restart file to write
filename%LAI	LAI_file.nc	Default LAI file
filename%type	gridinfo_file.txt	Default vegetation/soil file
filename%veg	def_veg_params.txt	Vegetation parameters
filename%soil	def_soil_params.txt	Soil parameters
filename%inits	Mk3LsurfClimatology.nc	Initialisation file
output%averaging	tstep	Provide output at this time step (e.g. 'daily','monthly')
numGdpt*	3584	Total number of land grid points

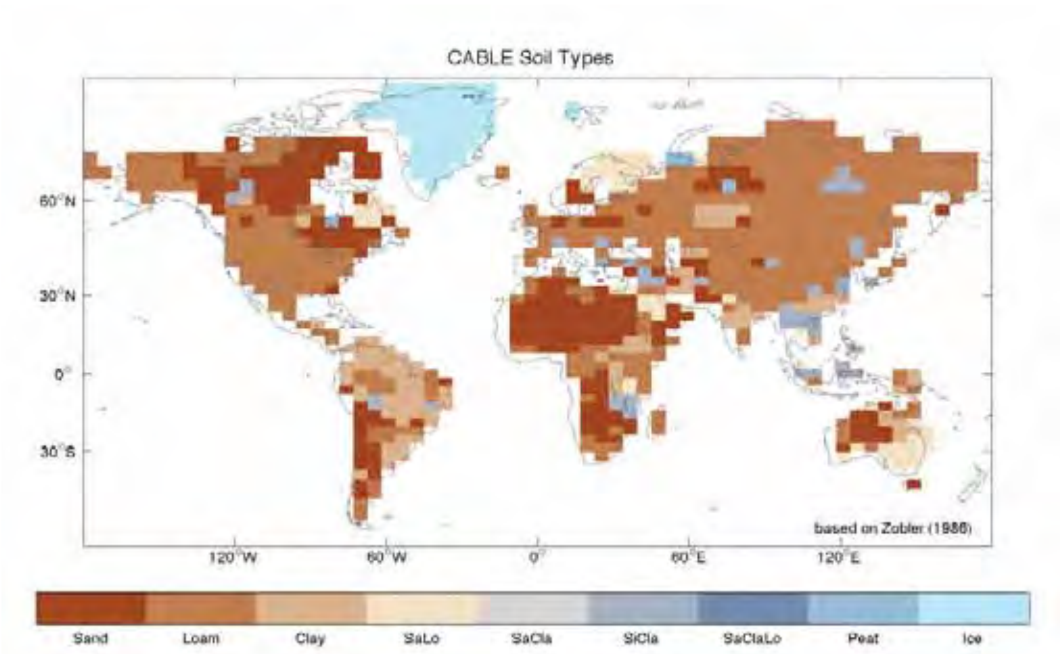

Figure 3-5: The soil types used in CABLE are based on Zobler (1986). Soil characteristics such as the fraction of clay/sand/silt, volume of water at field capacity/saturation/wilting, hydraulic conductivity and soil density are specified as parameters. In the default configuration, soil albedo is set to a global constant (0.1).

Table 3-3: Soil types based on Zobler (1986)

Type	Description	Code
1	Coarse sand/loamy sand	Sand
2	Medium clay loam/silty clay loam/silt loam	Loam
3	Fine clay	Clay
4	Coarse-medium sandy loam/loam	SaLo
5	Coarse-fine sandy clay	SaCla
6	Medium-fine silty clay	SiCla
7	Coarse-medium-fine sandy clay loam	SaClaLo
8	Organic peat	Peat
9	Permanent ice	Ice

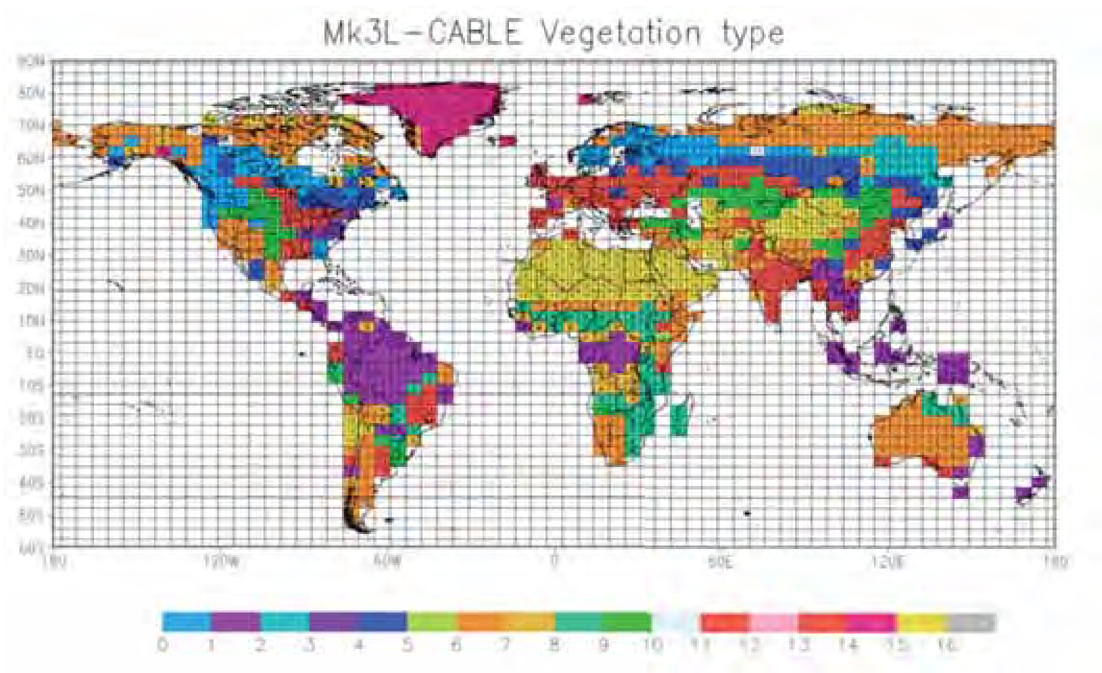

Figure 3-6: The default land cover map provided with Mk3L-CABLE describes present day vegetation. It uses the IGBP vegetation types and is not configured for tiling (i.e. only one vegetation type is defined to occupy each grid cell).

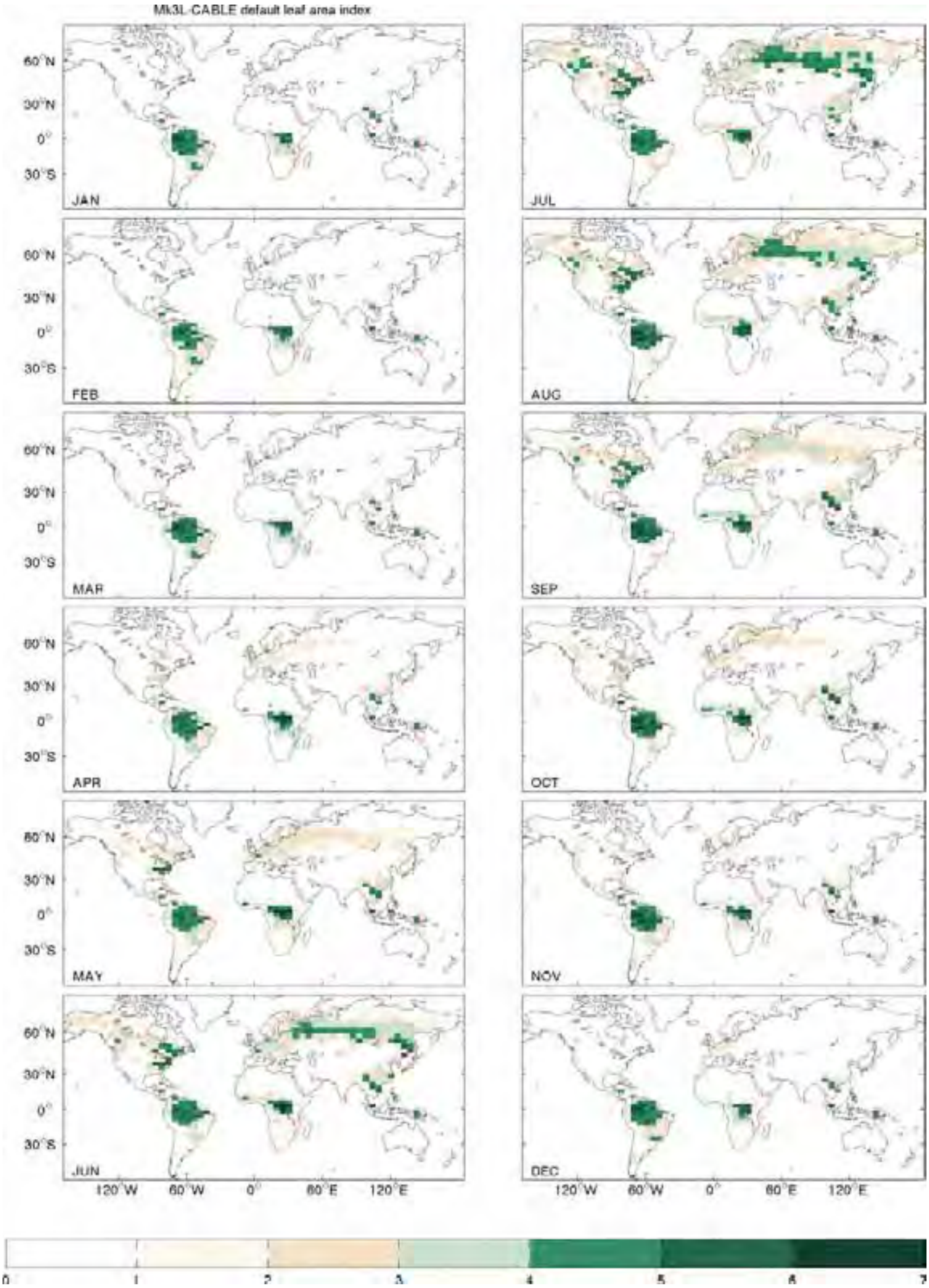

Figure 3-7: The default leaf area index provided with Mk3L-CABLE corresponding to the present-day vegetation cover map.

Table 3-4: IGBP vegetation types.

Type	**Description**	**Code**
1	Evergreen Needleleaf Forests	EveN
2	Evergreen Broadleaf Forests	EveB
3	Deciduous Needleleaf Forests	DecN
4	Deciduous Broadleaf Forests	DecB
5	Mixed Forests	MixF
6*	Closed Shrublands	CShr
7	Open Shrublands	OShr
8	Woody Savannah	WSav
9	Savannas	Sav
10	Grasslands	Gras
11*	Permanent wetlands	Wetl
12	Cropland	Crop
13*	Urban and Built-up	Urb
14*	Cropland/Natural Vegetation Mosaics	Mos
15	Snow and Ice	Sno
16	Barren	Barr
17*	Land-ice	Ice

3.3 Design of numerical experiments

The experiments were designed to simulate LULCC in the form of deforestation at different ambient CO_2 concentrations. To simulate changes in the land surface characteristics, two vegetation maps representing the natural and perturbed land surface were created. CO_2 transmission coefficients and sea surface temperature fields at pre-industrial (280 ppmv) and double pre-industrial (560 ppmv) CO_2 levels were also created to specify the CO_2 forcing. The four experiments conducted for this thesis are listed in Table 3-5.

The atmospheric CO_2 concentration is specified by CO_2 transmission coefficients generated using utilities (***pset*** and ***radint***) provided with the model [*Phipps et al.*, 2011]. Seasonally-varying SST fields corresponding to 1 x CO_2 and 2 x CO_2

levels are prescribed from climatological means derived from the last 1000 years of 7000-year long equilibrium simulations of the CSIRO Mk3L model. Figure 3-8 shows a schematic diagram of the atmospheric CO_2 concentration of two equilibrium runs of the fully coupled ocean-atmosphere Mk3L model from where the SST fields were derived.

Table 3-5: Experiments conducted

Experiment name	Vegetation cover		CO_2 concentration		Sea Surface Temperature
	Code	Description	Code	ppmv	
FOREST1x	Natural	Potential vegetation	1 x CO_2	280	Mk3L-i04
CROP1x	Perturbed	Year 2000	1 x CO_2	280	Mk3L-i04
FOREST2x	Natural	Potential vegetation	2 x CO_2	560	Mk3L-i40
CROP2x	Perturbed	Year 2000	2 x CO_2	560	Mk3L-i40

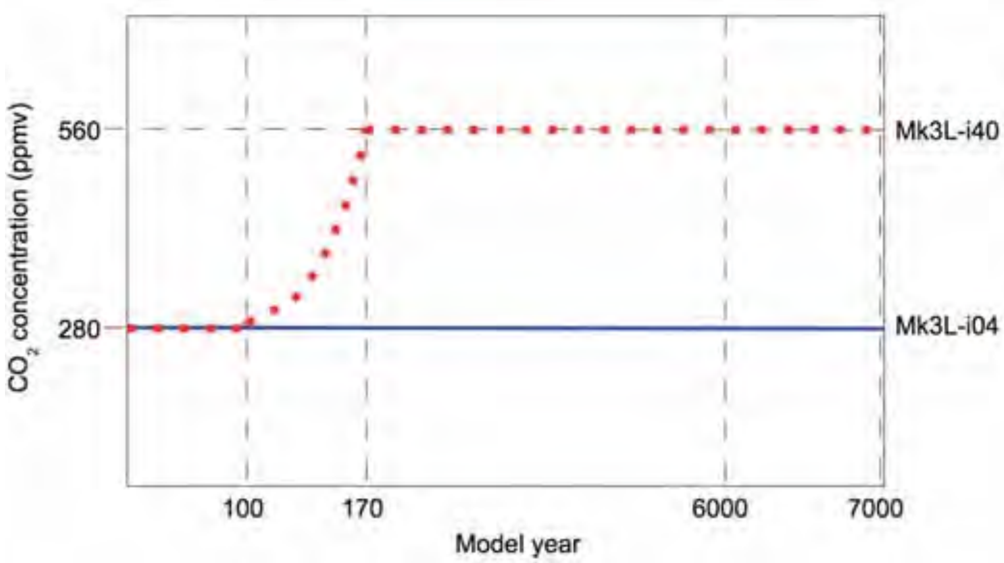

Figure 3-8: Schematic diagram of the atmospheric CO_2 concentrations of the CSIRO Mk3L control simulations that provided the climatological SSTs used in this thesis. The model was run at the fully coupled ocean-atmosphere configuration for 7000 years. The atmospheric CO_2 concentration was maintained at 280 ppmv for the Mk3L-i04 simulation (blue). However, for the Mk3L-i40 simulation (red), the atmospheric CO_2 concentration was increased by 1% per annum starting at simulation year 100 until it reached 560 ppmv at around year 170. It was held at that level until year 7000.

Mk3L-i04 represents the equilibrium run at constant pre-industrial (280 ppmv) CO_2 concentration. Similarly, Mk3L-i40 started with pre-industrial CO_2 level but when it reached model year 100, the CO_2 concentration was increased by 1% per annum until it reached the 560 ppmv level at around model year 170. This atmospheric CO_2 concentration is then maintained until the end of the 7000-year run. The simulated SSTs during model years 6001-7000 of Mk3L-i04 and Mk3L-i40 were used to create the 12-monthly SST datasets for the 1 x CO_2 and 2 x CO_2 conditions, respectively. A time series of the simulated mean annual sea surface temperatures shows that Mk3L-i40 stabilizes at approximately 5000 model years (Figure 3-9).

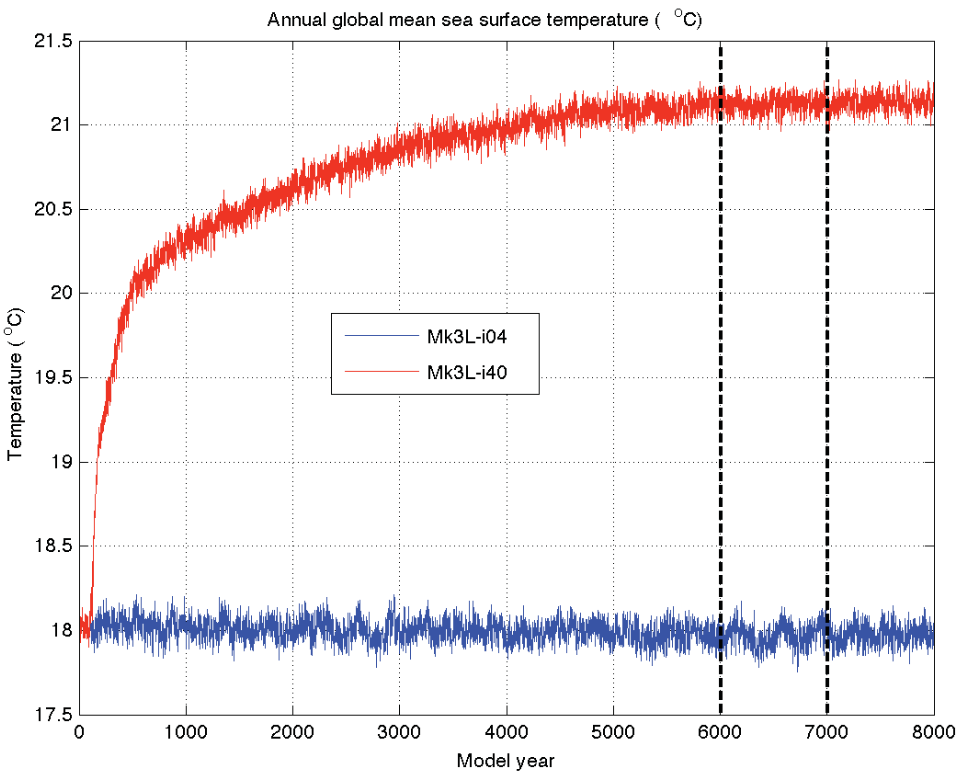

Figure 3-9: Annual global mean sea surface temperature for Mk3L-i04 and Mk3L-i40. Data from model years 6001-7000 of the Mk3L-i04 and Mk3L-i40 simulations are used to create the climatological SST for the 1 x CO_2 and 2 x CO_2 experiments, respectively.

3.4 Modifications to the model and related datasets

While the default configuration of the model can adequately simulate the control climate, it requires some modifications before it can be used to simulate LULCC. A map of the datasets created for the experiments and the related changes in the model is shown in Figure 3-10. The prescribed sea surface temperature and CO_2 transmission coefficients did not require changes in the model and are described in the previous section (Section 3.3). The first modification to the model allowed it to read-in data from a user-defined grid (Section 3.4.1) while the second modification implemented tiling (Section 3.4.2). Section 3.4.3 provides a detailed description of the development of the vegetation cover maps: starting from the high resolution potential vegetation and crop and pasture maps, until the creation of the actual input vegetation maps and related LAI maps. Preliminary simulations using the default configuration (Section 3.2.2), new data (Sections 3.3 and 3.4.3) and modified model (Sections 3.4.1 and 3.4.2) showed discrepancies in the simulated albedo that required the modification of the soil albedo (Section 3.4.4) and leaf reflectance and transmittance parameters (3.4.5).

3.4.1 Modification to facilitate the use of new datasets

The default Mk3L-CABLE coupled model is configured to read input data from a fixed number of land grid points. A fixed value of land grid points has been specified in CABLE to correspond with the Conformal Cubic Atmosphere Model [CCAM, *McGregor and Dix*, 2001] grid and is therefore only appropriate if the atmospheric model being used is CCAM or if the input values are not modified. To allow CABLE to be compatible with any grid format with any number of land grid points (in this case, the land grid points defined in the latitude-longitude grid used by Mk3L) and facilitate the use of new input data, the number of land grid points (**`numGdpt`**) was set as a variable in the CABLE control file. This allows CABLE to be more flexible with regards to the number of land grid points specified in the input file.

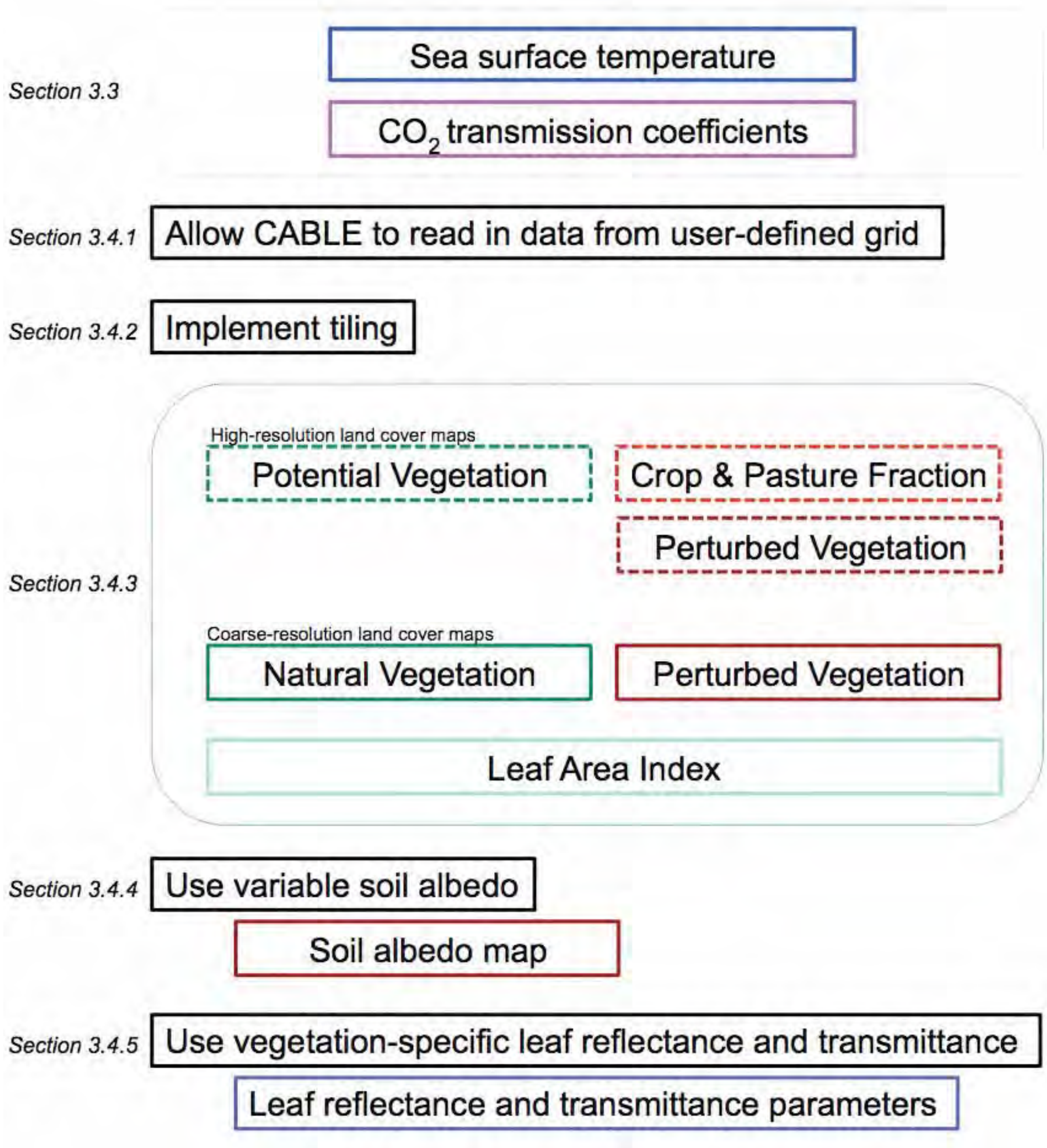

Figure 3-10: A map of the input datasets created for the experiments (colour boxes) and the modifications done to the model (black boxes) and their corresponding sections in this thesis.

3.4.2 Use of vegetation patches

Tiling was not fully implemented in the default version of the model. Thus, there is only one type of vegetation defined for each grid point. However, vegetation types within land grids are typically not homogeneous. To achieve a more realistic description of the land surface, models must be able to account for this heterogeneity. One way of introducing variety within the model grid is to use tiling [e.g. *Avissar*, 1992; *Koster and Suarez*, 1992]. This involves subdividing a grid cell into any number of tiles, with each tile containing a single land cover type [*Dai et al.*, 2003]. The terms patch and tile are used interchangeably in this thesis to refer to such grid cell subdivisions. Figure 3-11 illustrates how tiling can describe the surface characteristics more accurately by allowing several vegetation types to represent a grid cell.

In this thesis, the maximum number of patches within a grid cell (**`patches_in_parfile`**) is set to 4 in the CABLE parameter file. This change requires input parameters related to vegetation to be configured in a tiled format. The development of these datasets is described in the next section.

3.4.3 Development of land cover maps

This section describes the procedure for creating the land cover maps required by the model. It is divided into two sub-sections: high resolution (3.4.3.1) and low resolution (3.4.3.2), to describe the conversion of the different high resolution datasets used to create the model input dataset.

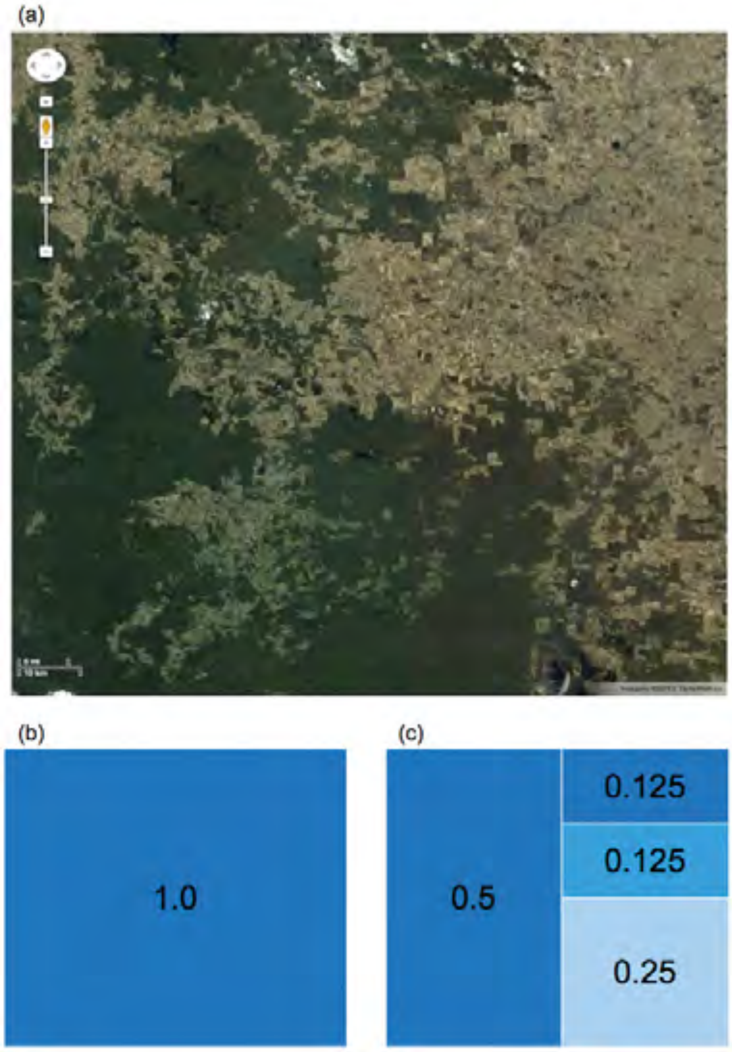

Figure 3-11: Tiling can represent the heterogeneity of vegetation within a grid cell. For example, the sample grid cell in (a) is composed of several vegetation types with the light-coloured area indicating agricultural regions and dark green areas indicating forests. It may be described simply, using a single vegetation type (b), or more realistically, using several vegetation types (b), with the vegetation fraction distributed among the existing vegetation types within the grid cell.

3.4.3.1 High resolution land cover maps

Potential vegetation

The natural vegetation map is based on the Ramankutty and Foley [1999, hereafter RF99] potential vegetation dataset, which describes the state of the global land cover before alteration by humans. The dataset has a grid increment of 0.5° x 0.5° and there are 16 vegetation classes. These vegetation types were mapped to the IGBP vegetation types [*Townshend*, 1992] to make them compatible with CABLE as shown in Table 3-6.

Table 3-6: Mapping of RF99 to the IGBP vegetation classes.

Rammankutty and Foley (1999)		**IGBP**		**Code**
1	Tropical Evergreen Forest/Woodland	2	Evergreen Broadleaf Forests	EveB
3	Temperate Broadleaf Evergreen Forest/Woodland	2	Evergreen Broadleaf Forests	EveB
2	Tropical Deciduous Forest/Woodland	4	Deciduous Broadleaf Forests	DecB
5	Temperate Deciduous Forest/Woodland	4	Deciduous Broadleaf Forests	DecB
8	Evergreen/Deciduous Mixed Forest	5	Mixed Forests	MixF
4	Temperate Needleleaf Evergreen Forest / Woodland	1	Evergreen Needleleaf Forests	EveN
6	Boreal Evergreen Forest/Woodland	1	Evergreen Needleleaf Forests	EveN
7	Boreal Deciduous Forest/Woodland	3	Deciduous Needleleaf Forests	DecN
9	Savanna	9	Savannas	Sav
10	Grassland/Steppe	10	Grasslands	Gras
11	Dense Shrubland	6	Closed Shrublands	CShr
14	Desert	16	Barren	Barr
13	Tundra	8	Woody Savannah	WSav
12	Open Shrubland	7	Open Shrublands	OShr
15	Polar Desert/Rock/Ice	15	Snow and Ice	Sno
16	No Data	15	Snow and Ice	Sno
		11	Permanent wetlands	Wetl
		12	Cropland	Crop
		13	Urban and Built-up	Urb
		14	Cropland/Natural Vegetation Mosaics	Mos
		17	Water bodies	

The RF99 potential vegetation data serves as the baseline vegetation cover for the LULCC experiments. It is thus necessary to properly map the RF99 data to the IGBP vegetation type because the vegetation-specific properties determine how these vegetation types would affect the local climate. Incorrectly mapping the vegetation (e.g. putting tropical forest types in the temperate zones, or deserts in croplands) could potentially create unexpected errors in the simulations or simply stop the model from running. The RF99 potential vegetation data, mapped using the IGBP vegetation types, is shown in Figure 3-12.

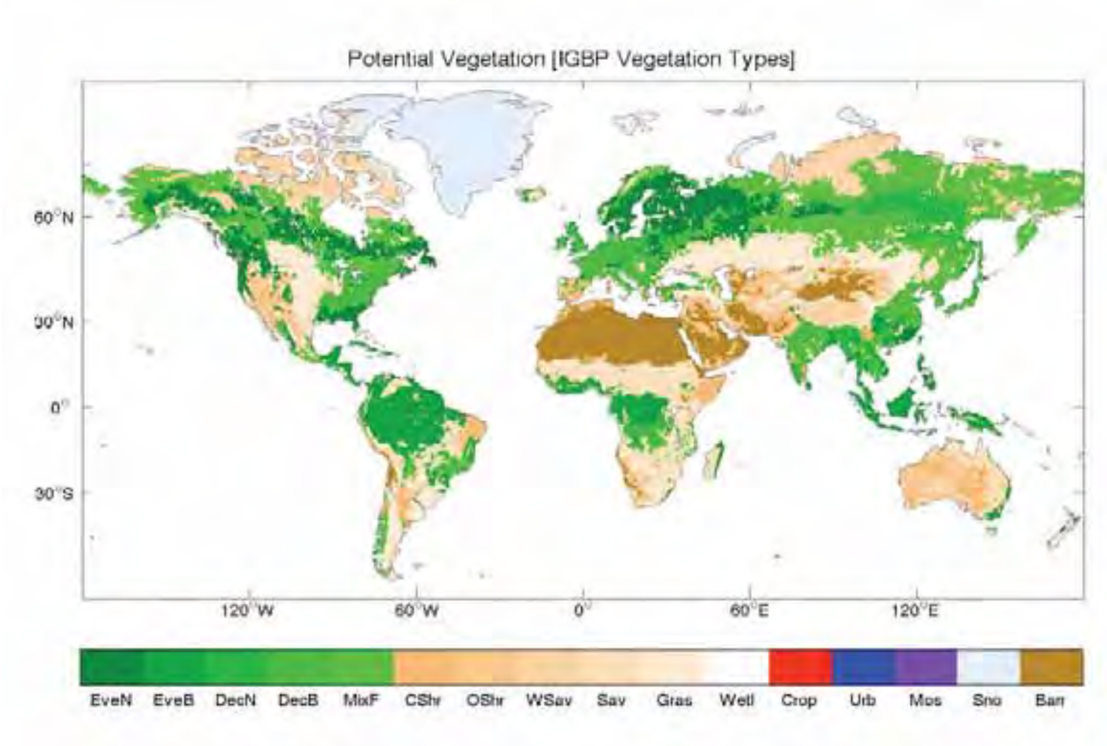

Figure 3-12: The Rammankutty and Foley (1999) potential vegetation data presented in terms of IGBP vegetation types.

<u>Cropland</u>

The cropland map was developed from the Land Use Harmonization dataset [*Hurtt et al.*, 2006] by combining high resolution (0.5° x 0.5° grid increment) crop and pasture fraction data for year 2000 to create a crop fraction map (Figure 3-13). The cropland map specifies the extent of the LULCC in the experiments (i.e. the amount of forests in the potential vegetation map converted to cropland). This closely follows the protocol used by LUCID [*Pitman et al.*, 2009; *de Noblet-Ducoudré et al.*, 2012] in creating crop fraction maps for 1870 and 1992, using crop data from Rammankutty and Foley [1999] and pasture data from Goldewijk [2001].

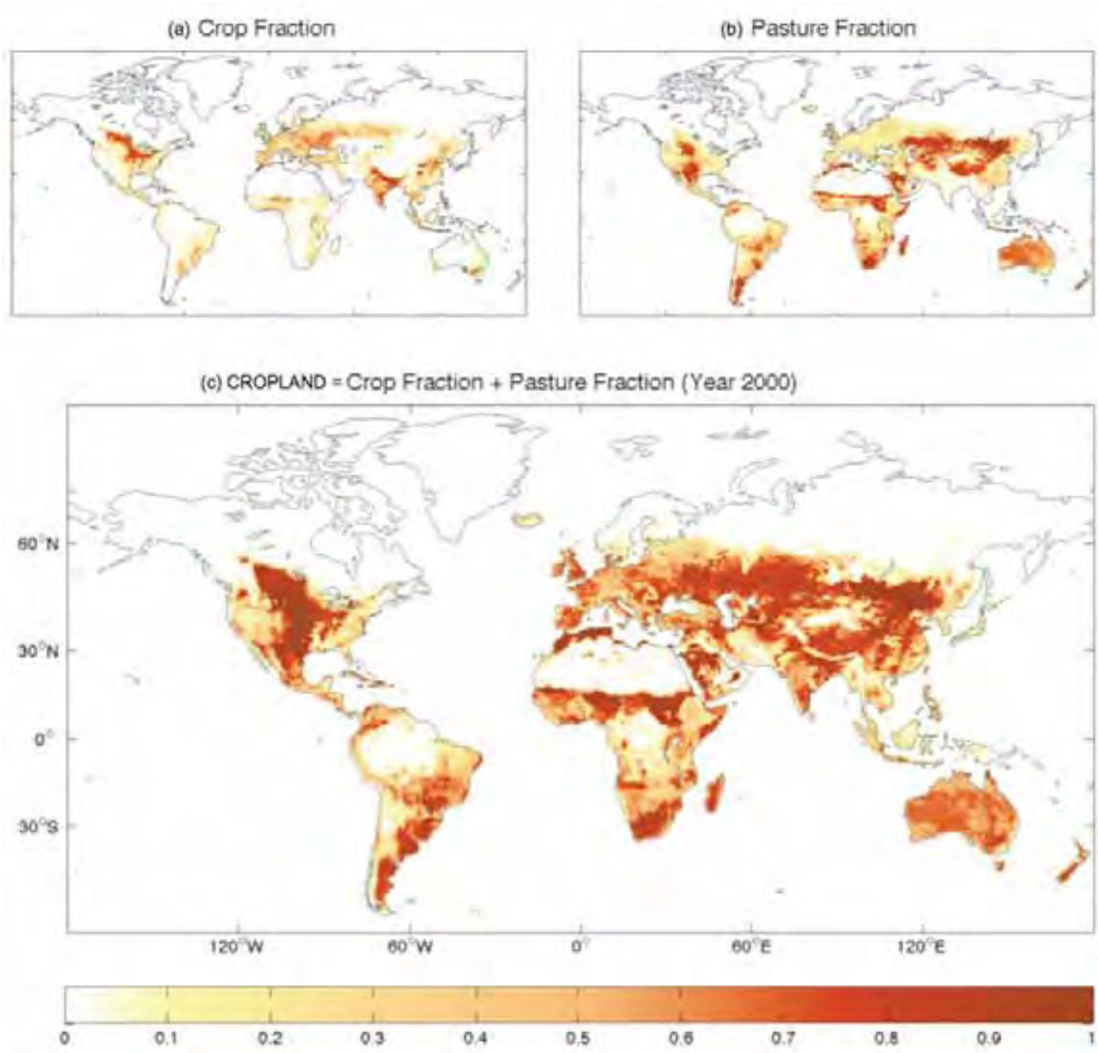

Figure 3-13: The (a) crop and (b) pasture fractions for the year 2000 are combined to create the cropland map (c). The cropland map is used to determine extent of LULCC. These maps were created from the LUH (Hurtt et al., 2006) dataset.

Perturbed vegetation

To create the perturbed vegetation map, the cropland map is applied to the potential vegetation map. This statement seems straightforward. However, the actual procedure on how the cropland map is implement varies considerably. For example, in the LUCID experiments [*Pitman et al.*, 2009; *de Noblet-Ducoudré et al.*, 2012], despite specifying exactly the same potential vegetation and crop and pasture maps, the various modelling groups implemented the LULCC differently. For example, while the CCAM-CABLE group converted the existing vegetation to cropland if the sum of the crop and pasture exceeded 51%, the other modelling groups reduced the existing vegetation in proportion to the crop fraction, while treating pasture as grassland in varying configurations.

In this thesis, a threshold level was used to determine whether a particular forest grid point would be converted to cropland. A forest grid point in the potential vegetation map is fully converted to cropland vegetation type if its cropland fraction (crop + pasture) exceeds 10%. Other existing vegetation types are left as is. The 10% threshold level was chosen after considering the extent of LULCC that will actually be imposed on the model using different threshold levels (Figure 3-14). The next section describes how these maps were derived.

3.4.3.2 Coarse resolution land cover maps

Figure 3-15 illustrates of how a group of high resolution grid points are aggregated to the model's coarse resolution grid point. Given a group of 16 high resolution grid points (Figure 3-15a), each of which are fully covered either by forest or grass, and the corresponding crop fractions (Figure 3-15b), applying a threshold of 10% would result in the converted land use map (Figure 3-15c) composed of 6 grid points fully covered with cropland, 6 grid points fully covered with forests and 4 grid points fully covered with grassland. Note that because only the forests are converted to cropland, the grasslands are kept intact even when the crop fraction exceeds 10%. When aggregated to the coarse resolution grid, it would result in the vegetation types and fractions shown in (Figure 3-15d).

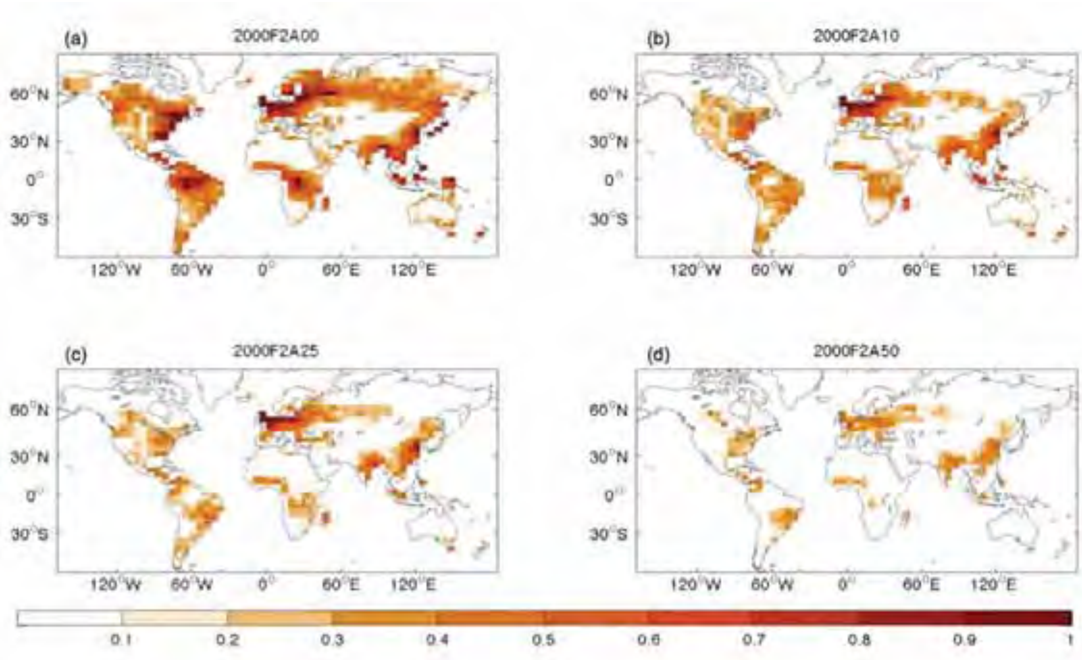

Figure 3-14: Total crop fraction imposed on the model when different threshold levels: (a) 0%, (b) 10%, (c) 25% and (d) 50% are used.

Total crop fraction

Applying the year 2000 cropland map (Figure 3-13c) to the potential vegetation map (Figure 3-12) and aggregating to the Mk3L-CABLE grid results in the total crop fraction maps shown in Figure 3-14. These total crop fraction maps show that using a very low threshold results in an extremely strong LULCC forcing

(Figure 3-14a). On the other hand, using a high threshold level results in a weak LULCC forcing (Figure 3-14d). Because a stronger LULCC forcing is expected to provide a stronger climate change signal, if it does exist, the 10% threshold (Figure 3-14b) was chosen over the 25% threshold (Figure 3-14c).

Figure 3-15: Schematic diagram showing how a group of high resolution grid points of various vegetation types (a) are converted to cropland based on the cropland map (b). In this example, all forest points where the cropland fraction exceeds 10% threshold level are converted to cropland (c). Combining the vegetation fractions of similar vegetation types results in a coarse resolution grid with 3 tiles with the corresponding vegetation fractions (d). Following the colour scheme used in Figure 3-12 for the vegetation types, green, red and tan boxes indicate forests, cropland and grassland, respectively, in (a,c,d). Following the colour scheme used in Figure 3-14, dark (light) colours indicate higher (lower) cropland fractions in (b).

Dominant vegetation types

From the coarse resolution grid points such as that shown in Figure 3-15d, it is possible to identify the dominant vegetation types by ranking the fraction of each vegetation type. In this example, the most dominant vegetation types are forest (37.5%), cropland (37.5%) and grassland (25%). These 3 dominant vegetation types may then be assigned to three patches, each describing the characteristics of their particular vegetation type. In cases where the number of vegetation types is less than the number of patches, the remaining patches are assigned patch fraction of zero.

Vegetation patches

Applying the method described in Figure 3-15 to the high resolution potential vegetation (Figure 3-12) and cropland (Figure 3-13c) maps results in tiled, coarse resolution natural (Figure 3-16a) and perturbed (Figure 3-16b) vegetation maps. Each vegetation type in each patch has a corresponding vegetation fraction such that the total vegetation fraction from the four patches equals unity. Some grid points are more homogeneous and occupy less than 4 of the patches.

Leaf area index

The leaf area index (LAI) describes the amount of leaf area of the canopy. Specifically, it describes the projected area of leaves per unit of ground and is therefore is dependent on the shape and orientation of the leaves, which are in turn dependent on the species of the vegetation [*Bonan*, 2008a]. LAI also varies with time as the presence and absence of leaves vary with vegetation growth through the seasons.

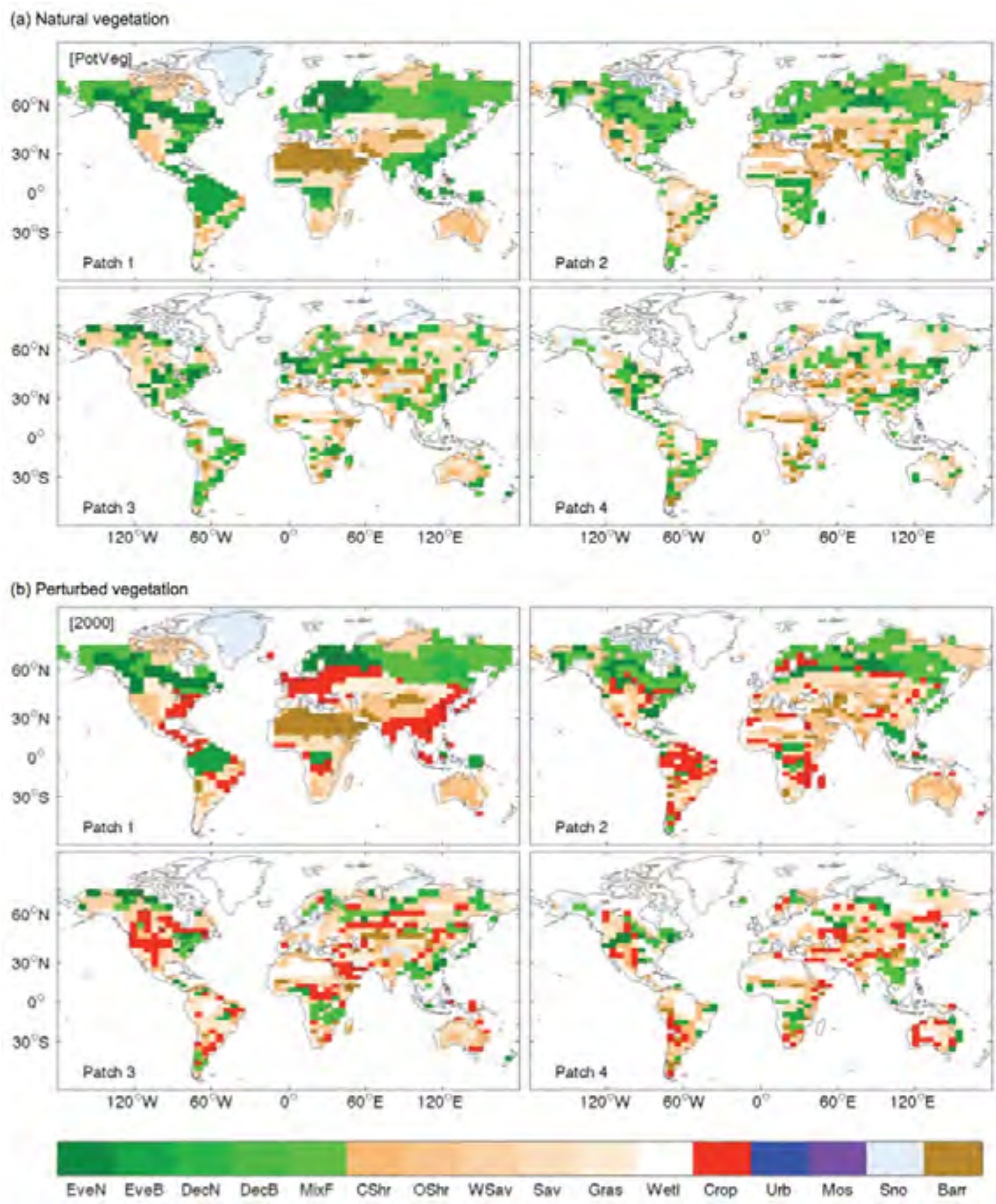

Figure 3-16: The vegetation type maps for the (a) natural and (b) perturbed vegetation types. The most dominant types are assigned to Patch 1 while the next dominant types are assigned to the subsequent patches (maximum of 4).

In the default configuration of the model, the LAI is available as a 12-monthly map based on MODIS data from years 2000-2003 and describes the LAI of the present day vegetation cover (Figure 3-7). To properly represent the LAI corresponding to the natural and perturbed vegetation surface required for this thesis, simplified LAI profiles similar to those developed by Bonan [1996] were derived from the existing LAI map and tiled 12-monthly maps such as that shown in Figure 3-17 for the natural vegetation cover are created as input to the model. Figure 3-18 shows the difference between the LAI of the natural and perturbed vegetation cover. This simple method of creating LAI maps may certainly be improved by incorporating various generalized [*Bonan*, 1996], in-situ [*Scurlock et al.*, 2001] and satellite-derived [e.g. *Liu and Liu*, 2011; *Yuan et al.*, 2011] datasets. However, these simplified LAI maps are appropriate for the LULCC experiments in this thesis.

3.4.4 Improvement of soil albedo parameters

The net radiation discrepancy (Figure 3-4) in the default model configuration found by Mao et al. [2011] is directly related to errors in the simulated surface albedo. Therefore, it is very important to calibrate the model such that it properly calculates the surface albedo at each time step.

Figures 3-19a and 3-19b show the difference between the observed and simulated albedo, for JJA and DJF, from the default model configuration. The MODIS data is from years 2000-2003 and the simulation is for the present day conditions. The discrepancy in albedo over the northern hemisphere during DJF is expected because of the expected differences in albedo due to snow. However, the discrepancy over the deserts of northern Africa and western Asia, during both JJA and DJF, is unexpected.

The vertical profile of the leaf area in the canopy affects the distribution of the radiation in the canopy and the absorption of radiation by leaves [*Bonan*, 2008a]. In regions of low LAI, plants absorb less of the solar radiation and the overall surface albedo is largely that of the soil [*Bonan*, 2008a]. The discrepancy in surface albedo over the desert regions in Figure 3-19a could thus be due to errors in the soil albedo, which is set to a constant value of 0.1 in the default version of CABLE.

Since actual global soil albedo datasets do not exist, a soil albedo map was constructed from the MODIS broadband albedo dataset. The snow-free broadband albedo maps from each hemisphere -- JJA for the North Hemisphere (Figure 3-20a) and DJF for the Southern Hemisphere (Figure 3-20b) -- are combined to create one albedo map (Figure 3-20c), which is then provided to the model via the CABLE surface initialization file (***Mk3LsurfClimatology.nc***).

This modification of the soil albedo parameter resulted in substantially improved albedo maps for the control climate especially over the desert areas (Figure 3-19c and 3-19d). The zonally average surface albedo (Figure 3-19e and 3-19f) show marked improvements, particularly over 0°-45°N, due to the modification of soil albedo.

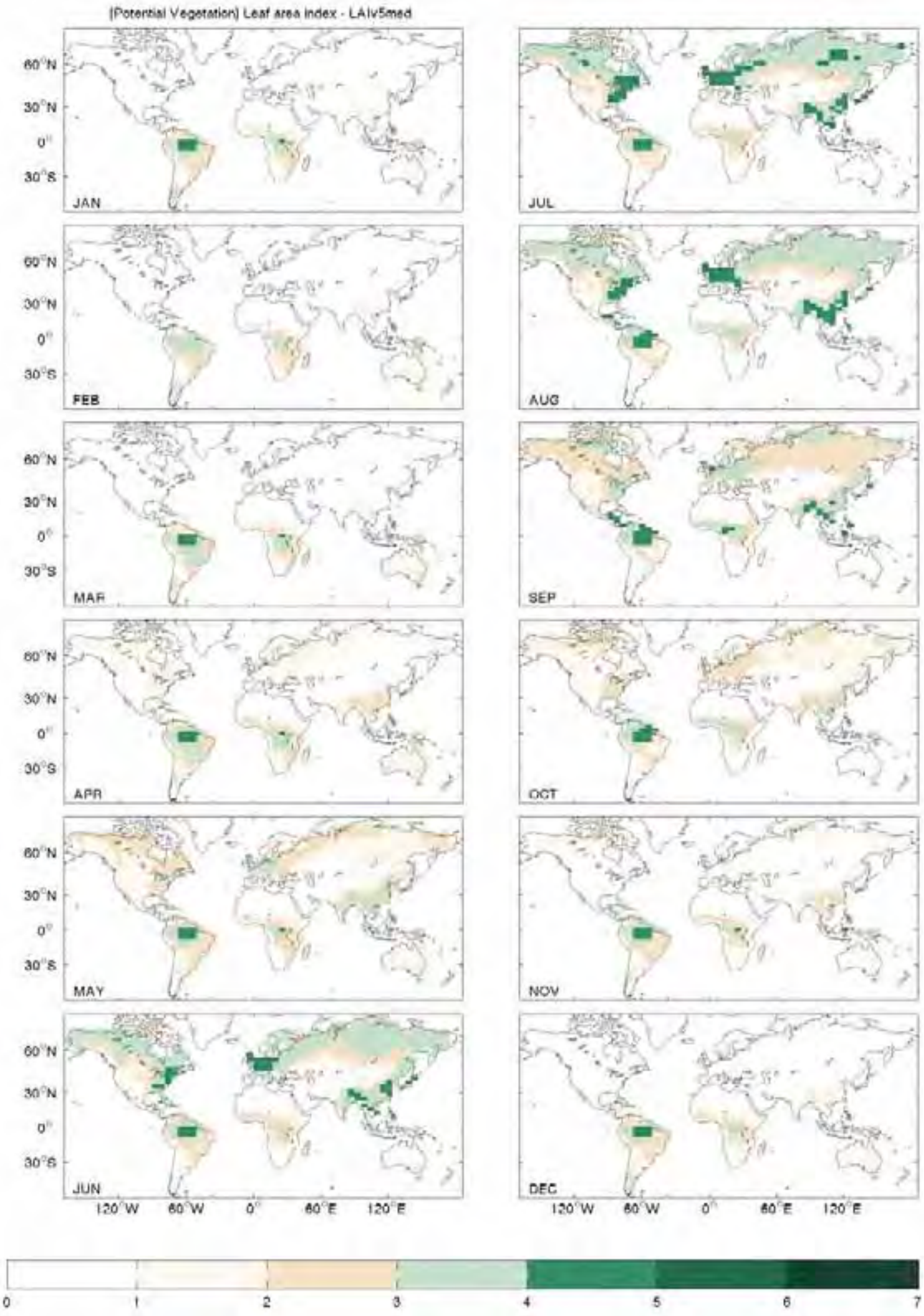

Figure 3-17: Monthly leaf area index for the natural vegetation cover. Regions with evergreen vegetation such as the Amazon maintain high levels of LAI throughout the year while most regions indicate monthly variations in the LAI consistent with the development of the vegetation throughout the year (e.g. emergence of new leaves in spring and leaf-fall in autumn).

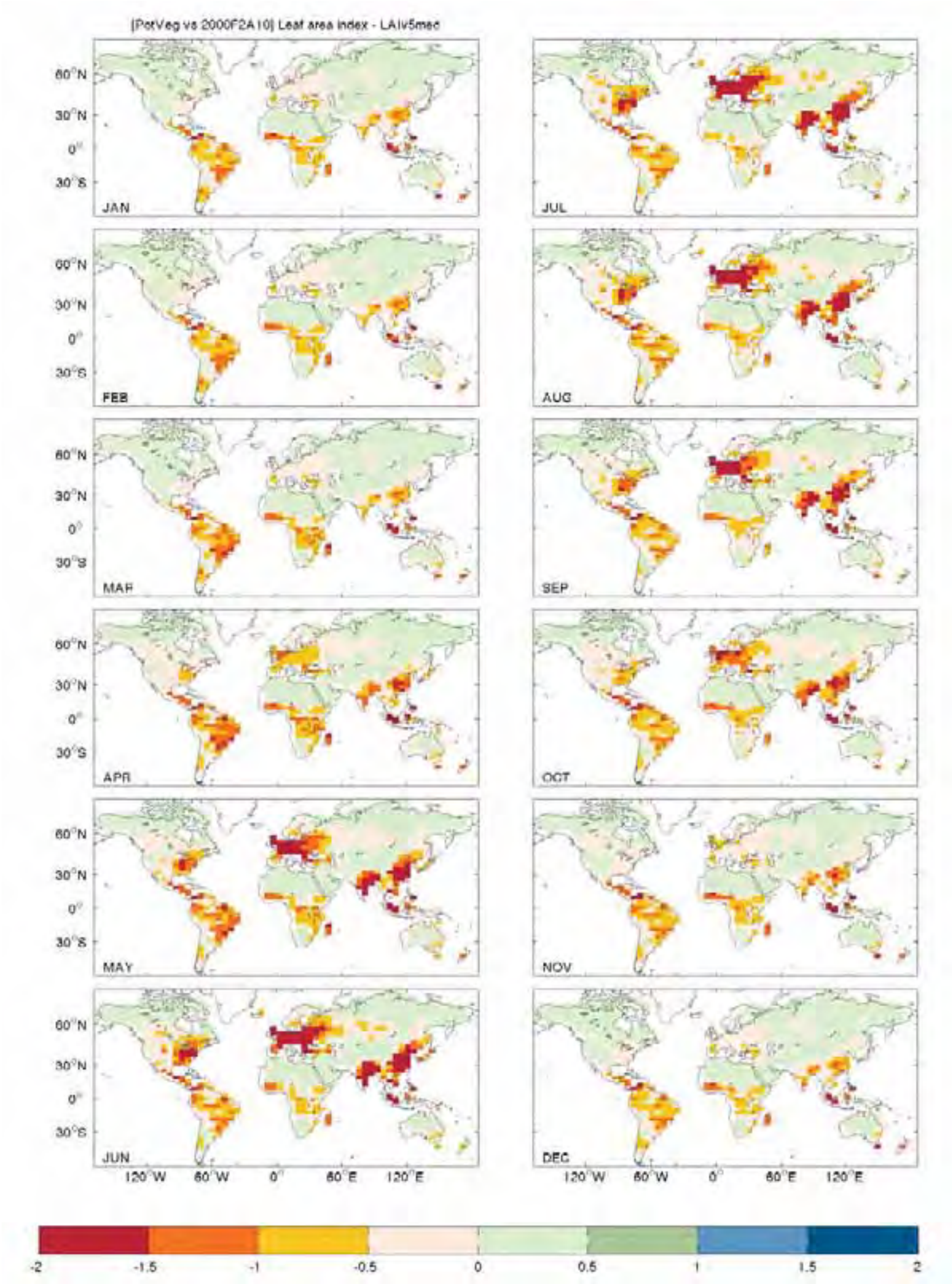

Figure 3-18: Difference in the monthly leaf area index of the perturbed and natural vegetation cover. The decrease in LAI is evident over the regions of LULCC and is particularly large during the non-winter months.

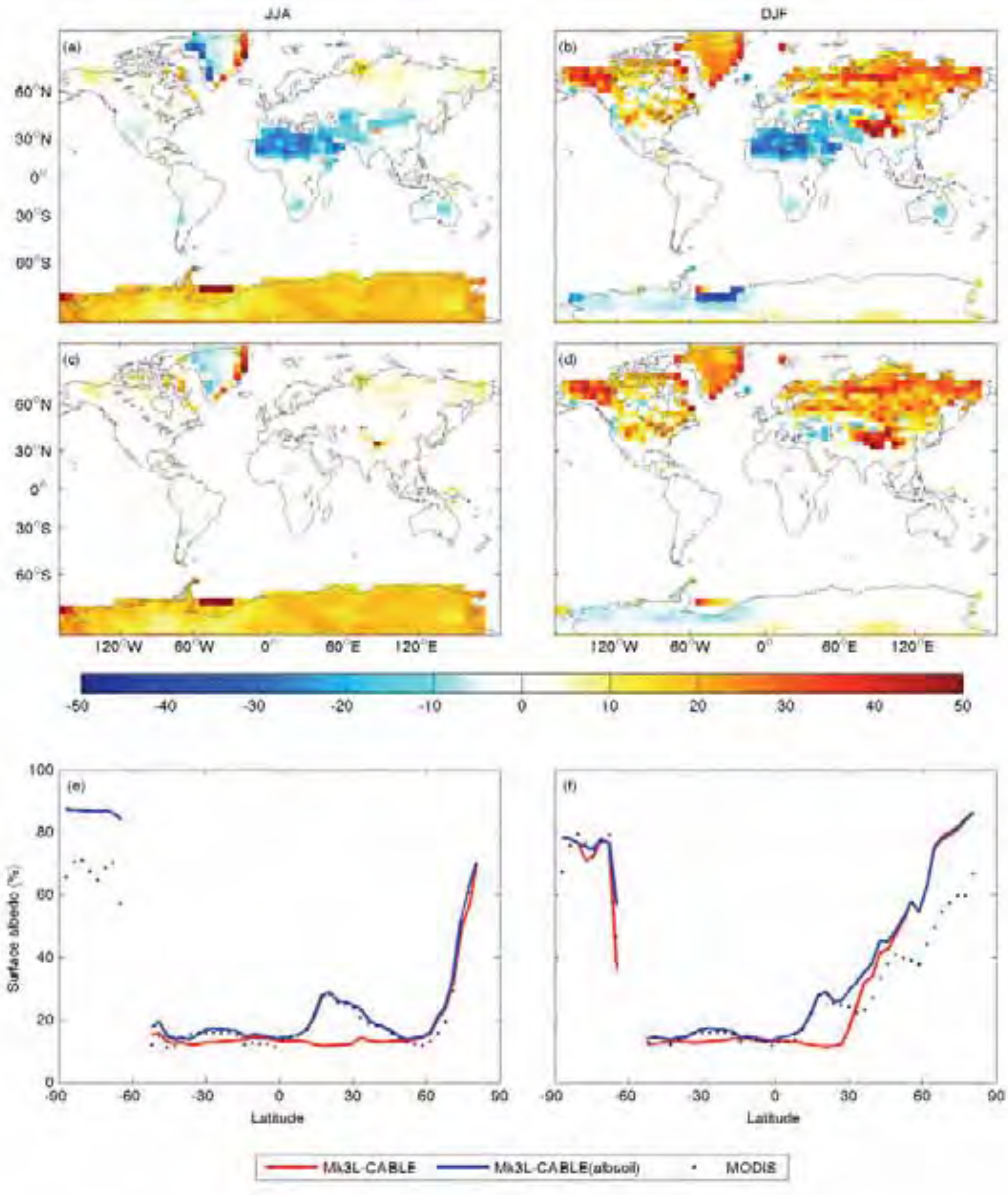

Figure 3-19: Comparison of present day Mk3L-CABLE surface albedo with MODIS data for JJA (left column) and DJF (right column). The default CABLE configuration using a constant soil albedo results in the surface albedo discrepancy shown in (a, b). While the discrepancy over the northern hemisphere during winter is expected because of changes in snow cover, the discrepancy over the deserts of northern Africa and western Asia is unexpected. Applying a spatially varying soil albedo results in a surface albedo discrepancy shown in (c, d). The zonally averaged surface albedo for the default and soil albedo-corrected CABLE configurations and MODIS are shown in (e, f). Note that albedo values here are have been multiplied by 100.

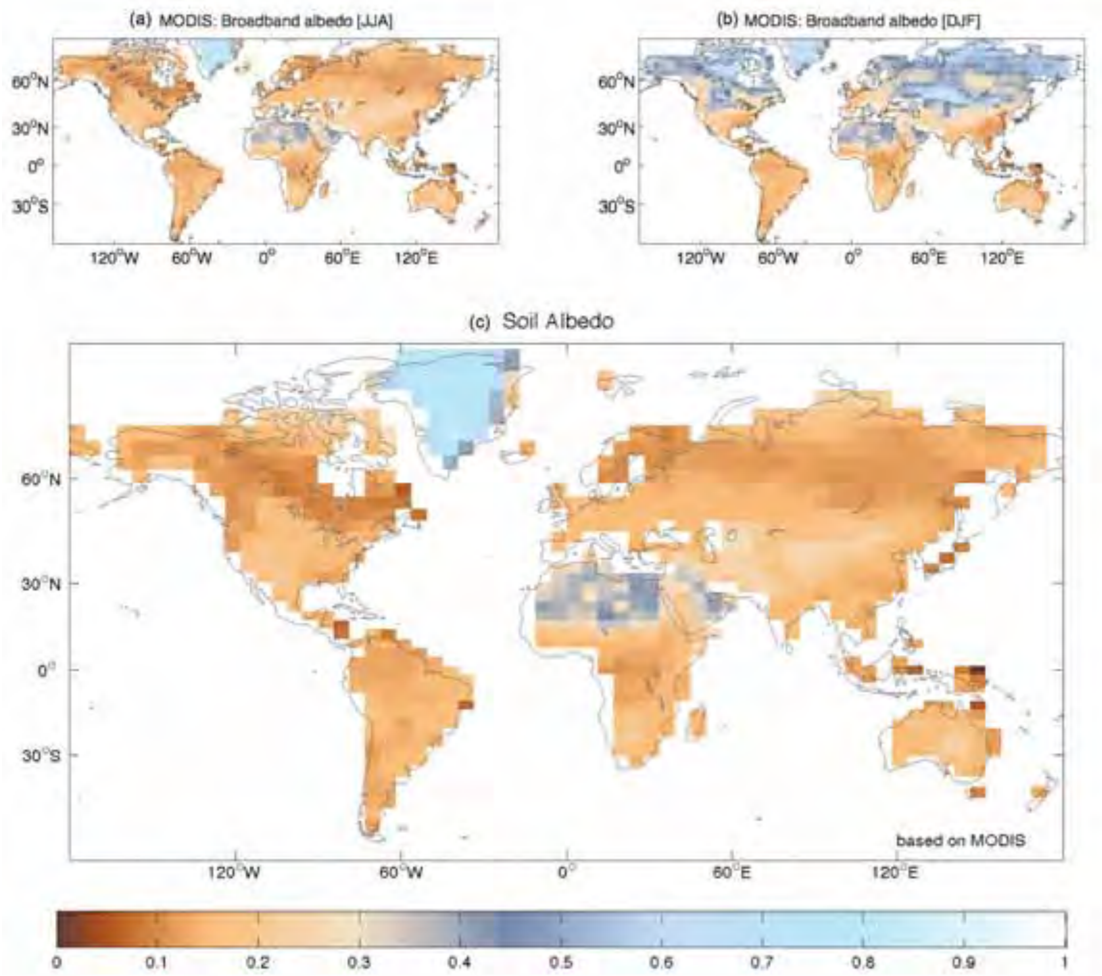

Figure 3-20: The snow-free MODIS broadband albedo during (a) JJA and (b) DJF are combined to create the soil albedo map (c). Most land areas have values that are close to 0.1 but some desert (e.g. Sahara) and permanent ice regions (e.g. Greenland) have relatively higher albedo.

3.4.5 Improvement of leaf reflectance and transmittance parameters

Different types of vegetation have different leaf orientation and optical characteristics (see Table 2-1). The overall surface albedo for a plant canopy is the combined reflection of all plant material (leaves and stems) and the underlying ground surface. With low LAI, plants absorb little solar radiation and the overall albedo is that of soil. However, as the LAI increases, the surface albedo responds more to the optical properties of foliage [*Bonan*, 2008a]. In the absence of snow, dark-coloured forests would have lower albedo than light-coloured crops; replacing forests with crops should therefore result in increased albedo. However, results from preliminary experiments show no change over regions of LULCC (Figure 3-21) during the summer months (Figure 3-22) indicating that the model is not properly simulating the LULCC-induced change in albedo.

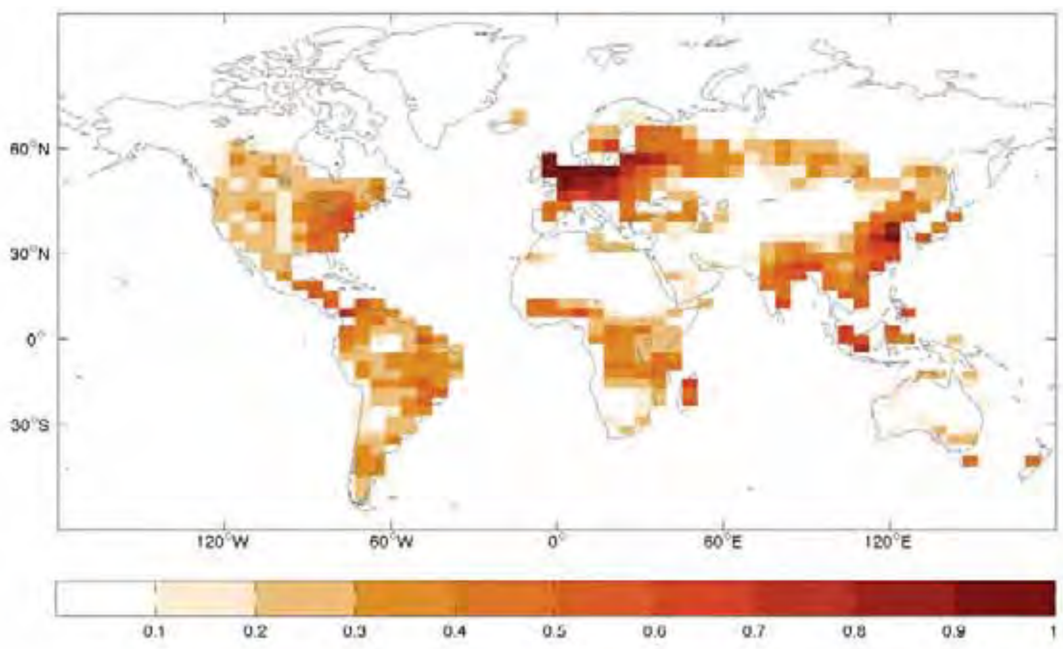

Figure 3-21: Regions of LULCC shown in terms of total crop fraction (same as Figure 3-16b).

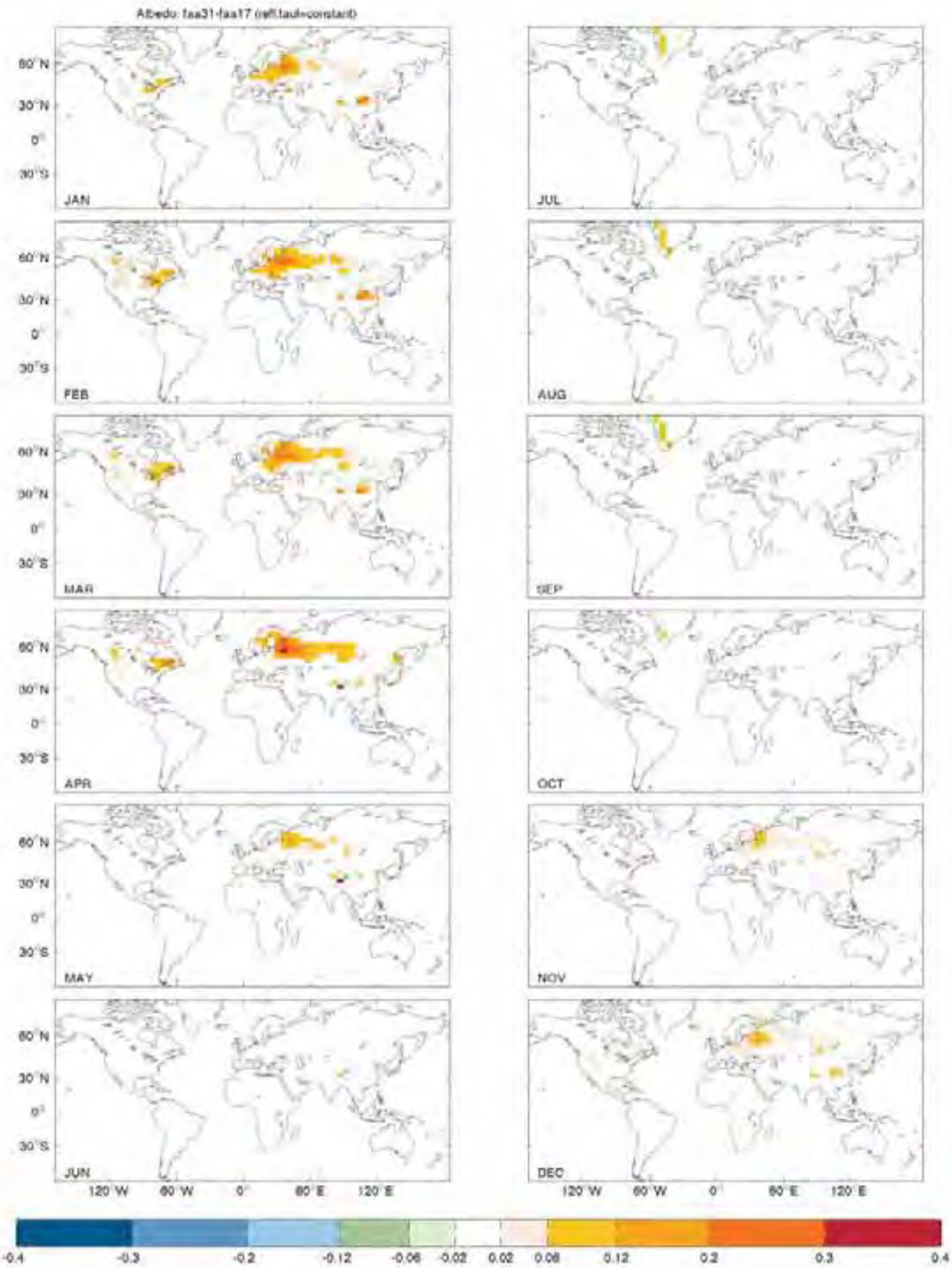

Figure 3-22: Comparison of monthly albedo from two simulations using different land cover maps (natural and perturbed) show negligible difference over regions of LULCC especially during JJA. This indicates that the model is not simulating differences in albedo due to LULCC. Changes in albedo due to changes in snow cover are evident during winter and spring seasons.

In the default version of CABLE, the leaf reflectance and transmittance parameters have been set to a constant value (specifically 0.1, 0.4, and 0.02 for the visible, near IR and thermal bands, respectively) for all vegetation types. These are adequate for simulating a control climate, but cannot capture the impact of a change in the vegetation. This simplification contributed to the errors in the calculation of the change in surface albedo due to LULCC (Figure 3-22). To allow a change in surface albedo due to the change in vegetation, the leaf reflectance and transmittance data have to be specified for each vegetation type.

To adapt CABLE to reflect this functionality, the leaf reflectance (**`rholeaf`**) and transmittance (**`tauleaf`**) were included as vegetation parameters. Initial values were adapted from Dorman and Sellers [1989, hereafter DS89] and then adjusted via an iterative process such that: (1) the albedo simulated for the perturbed vegetation closely approximates to the MODIS broadband albedo and (2) the difference between the simulated surface albedo of the natural and perturbed vegetation experiments over regions of LULCC is not negligible, especially during JJA. The leaf reflectance and transmittance values for the visible (VIS) and near IR (NIR) bands from DS89 and the modified values are shown in Table 3-7.

The difference between observations and the simulated albedo for the perturbed vegetation, using the DS89 parameters (Figure 3-23) shows large discrepancies in the albedo over regions of Africa, Australia, Middle East, China, and Western United States. These regions are either mapped as “Barren” or a combination of various “Shrubs” and “Savannas” (Figure 3-16b) indicating the need to modify the optical characteristics of these vegetation types. Smaller discrepancies over the northern mid-latitudes and tropics where forests are located (Figure 3-16b) also indicate the need to make subtle changes in the optical characteristics of the forest vegetation types.

The difference between observations and the simulated albedo for the perturbed vegetation, using the modified DS89 parameters, some intermediate values and the final set of **`rholeaf`** and **`tauleaf`** parameters, are shown in Figures 3-23, to 3-26. The differences in surface albedo using the DS89 parameters are shown in Figure 3-27. Multiple adjustments eventually managed to get the simulated value closer to observation resulting in a change in albedo during JJA that is discernable over regions of LULCC (Figure 3-28).

Table 3-7: Adjusted leaf reflectance and transmittance values

		Dorman and Sellers (1989)				**Modified**			
		Reflectance		**Transmittance**		**Reflectance**		**Transmittance**	
		VIS	**NIR**	**VIS**	**NIR**	**VIS**	**NIR**	**VIS**	**NIR**
Default		0.1	0.4	0.1	0.4	0.1	0.4	0.1	0.4
1	EveN	0.070	0.350	0.050	0.100	0.080	0.350	0.050	0.250
2	EveB	0.100	0.450	0.050	0.250	0.200	0.450	0.050	0.250
3	DecN	0.070	0.350	0.050	0.100	0.080	0.350	0.050	0.250
4	DecB	0.100	0.450	0.050	0.250	0.060	0.450	0.050	0.250
5	MixF	0.070	0.400	0.050	0.150	0.130	0.400	0.050	0.250
6	CShr	0.100	0.450	0.050	0.250	0.090	0.450	0.100	0.250
7	OShr	0.001	0.001	0.001	0.001	0.500	0.500	0.100	0.250
8	WSav	0.100	0.450	0.050	0.250	0.500	0.500	0.100	0.250
9	Sav	0.100	0.450	0.070	0.250	0.300	0.500	0.100	0.250
10	Gras	0.110	0.580	0.070	0.250	0.500	0.500	0.100	0.250
11	Wetl	0.107	0.469	0.070	0.250	0.107	0.469	0.100	0.250
12	Crop	0.110	0.580	0.070	0.250	0.170	0.580	0.100	0.250
13	Urb	0.097	0.396	0.062	0.232	0.097	0.396	0.100	0.250
14	Mos	0.101	0.399	0.067	0.250	0.101	0.399	0.100	0.250
15	Sno	0.159	0.305	0.026	0.126	0.159	0.305	0.100	0.250
16	Barr	0.100	0.450	0.050	0.250	0.420	0.450	0.100	0.250
17	Ice	0.159	0.305	0.026	0.126	0.159	0.305	0.100	0.250

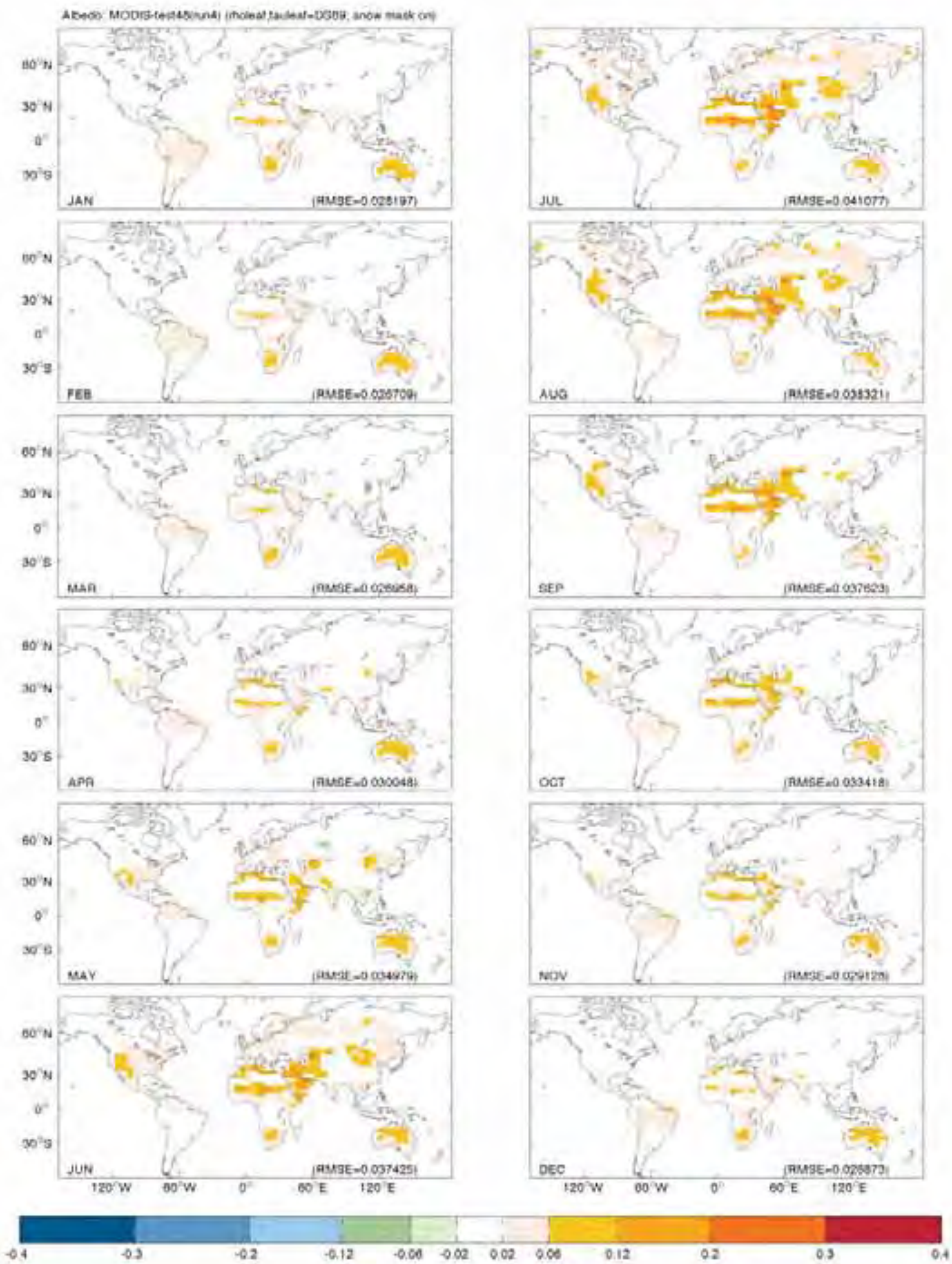

Figure 3-23: Comparison between observed (MODIS) and simulated albedo where the leaf reflectance and transmittance parameters are set to the DS89 values.

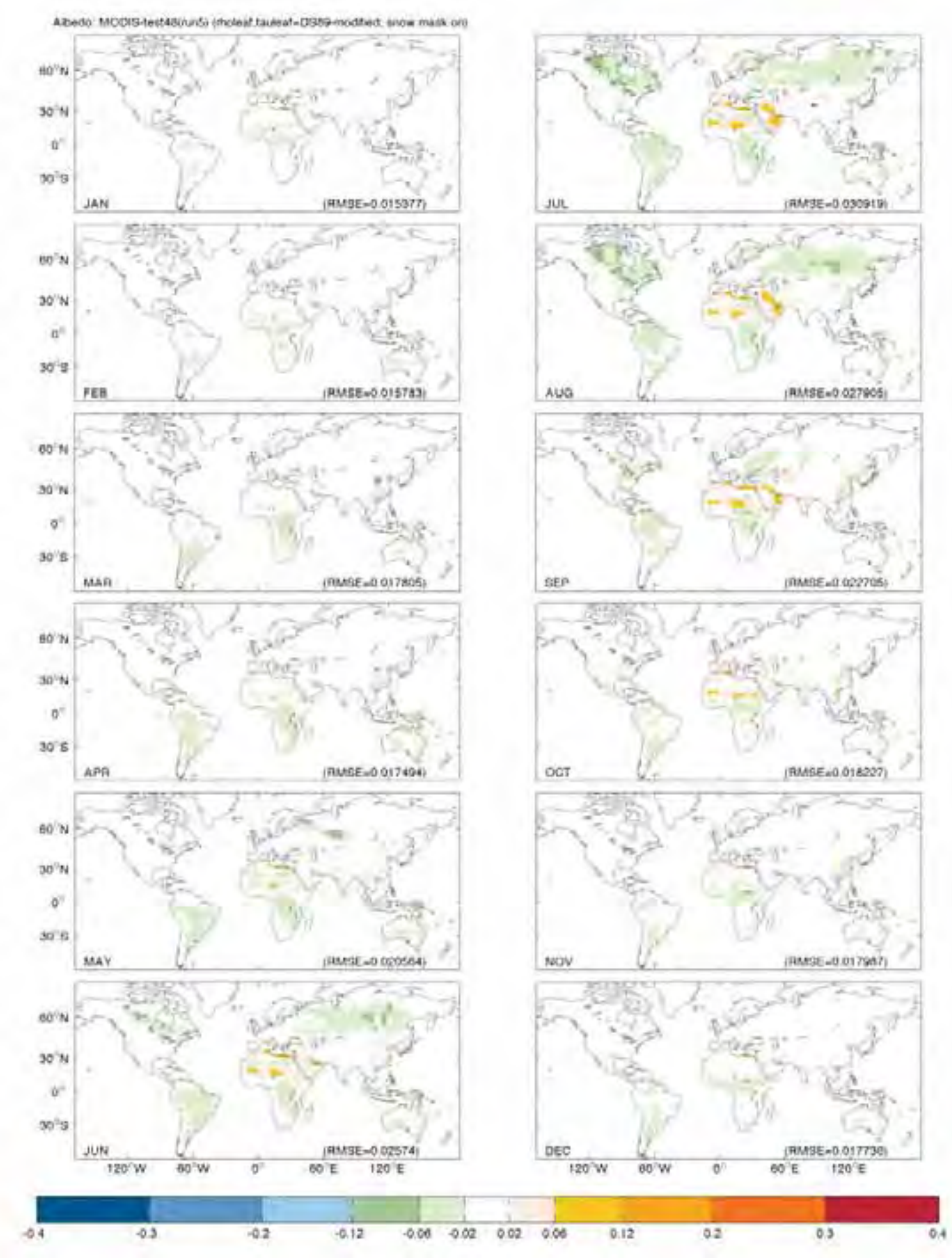

Figure 3-24: As Figure 3-23 but with rholeaf and tauleaf adjusted once.

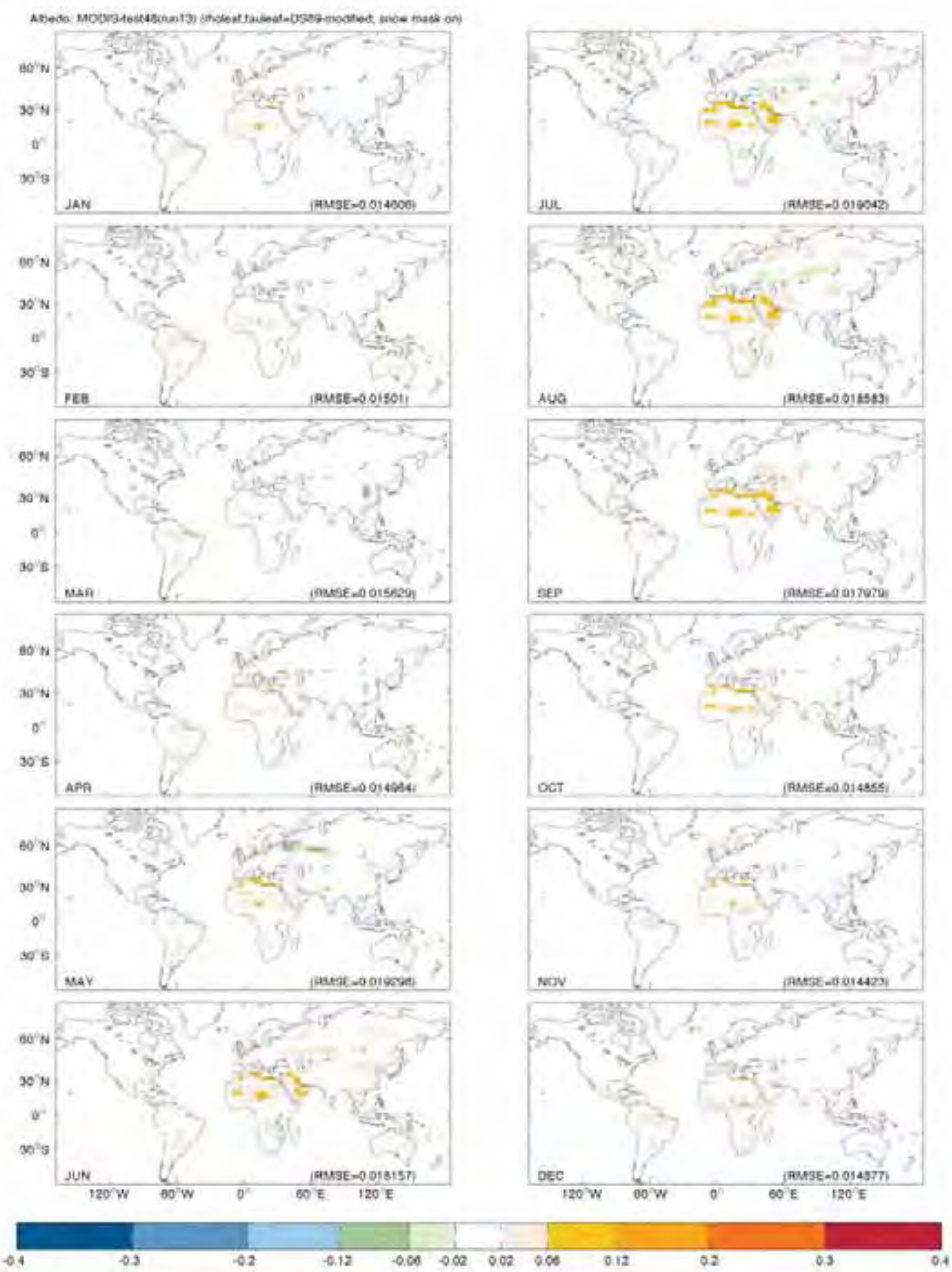

Figure 3-25: As Figure 3-23 but with rholeaf and tauleaf adjusted several times.

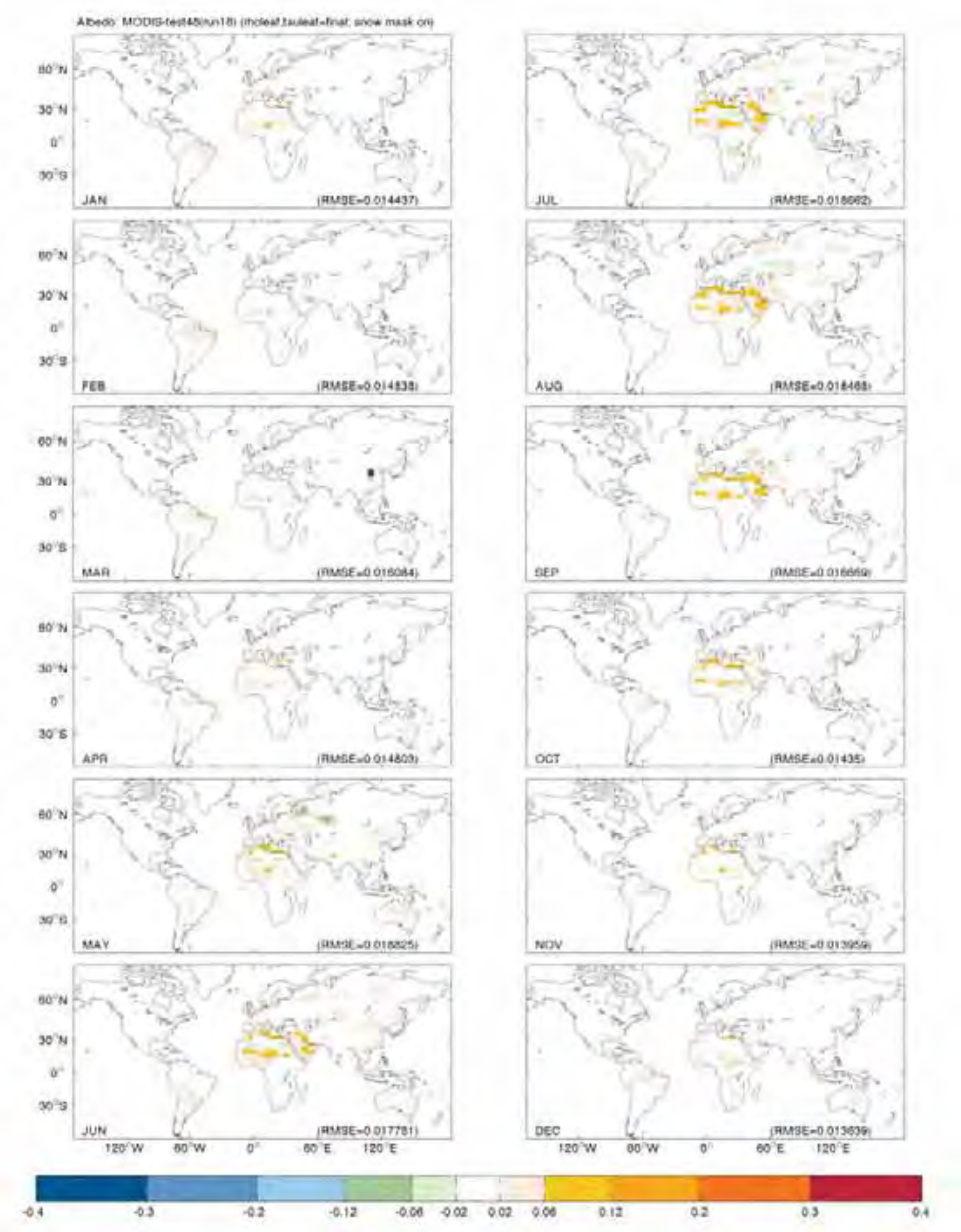

Figure 3-26: As Figure 3-23 but with the final version of rholeaf and tauleaf.

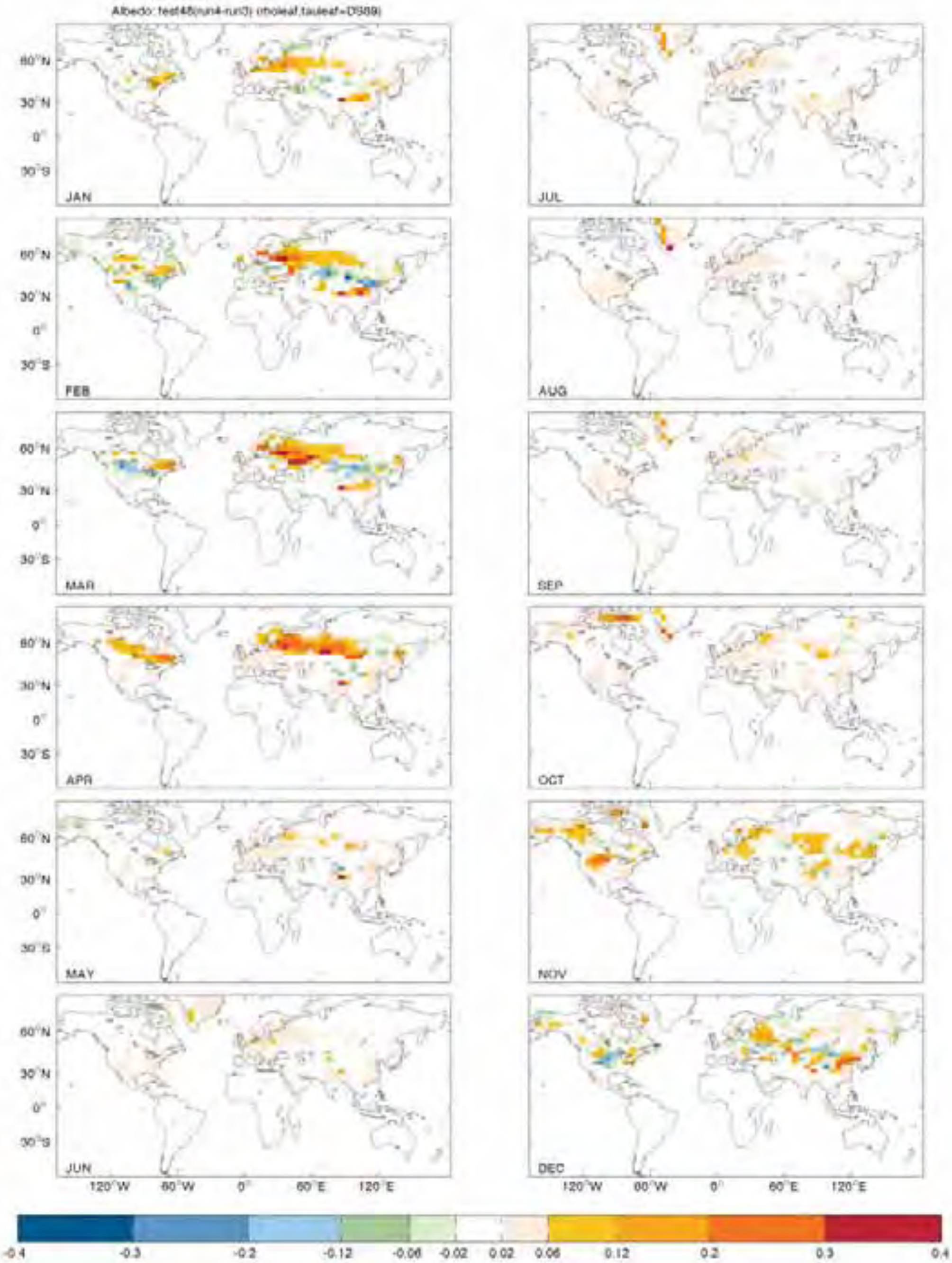

Figure 3-27: As Figure 3-22 (change in surface albedo due to LULCC) but with rholeaf, tauleaf set to DS89.

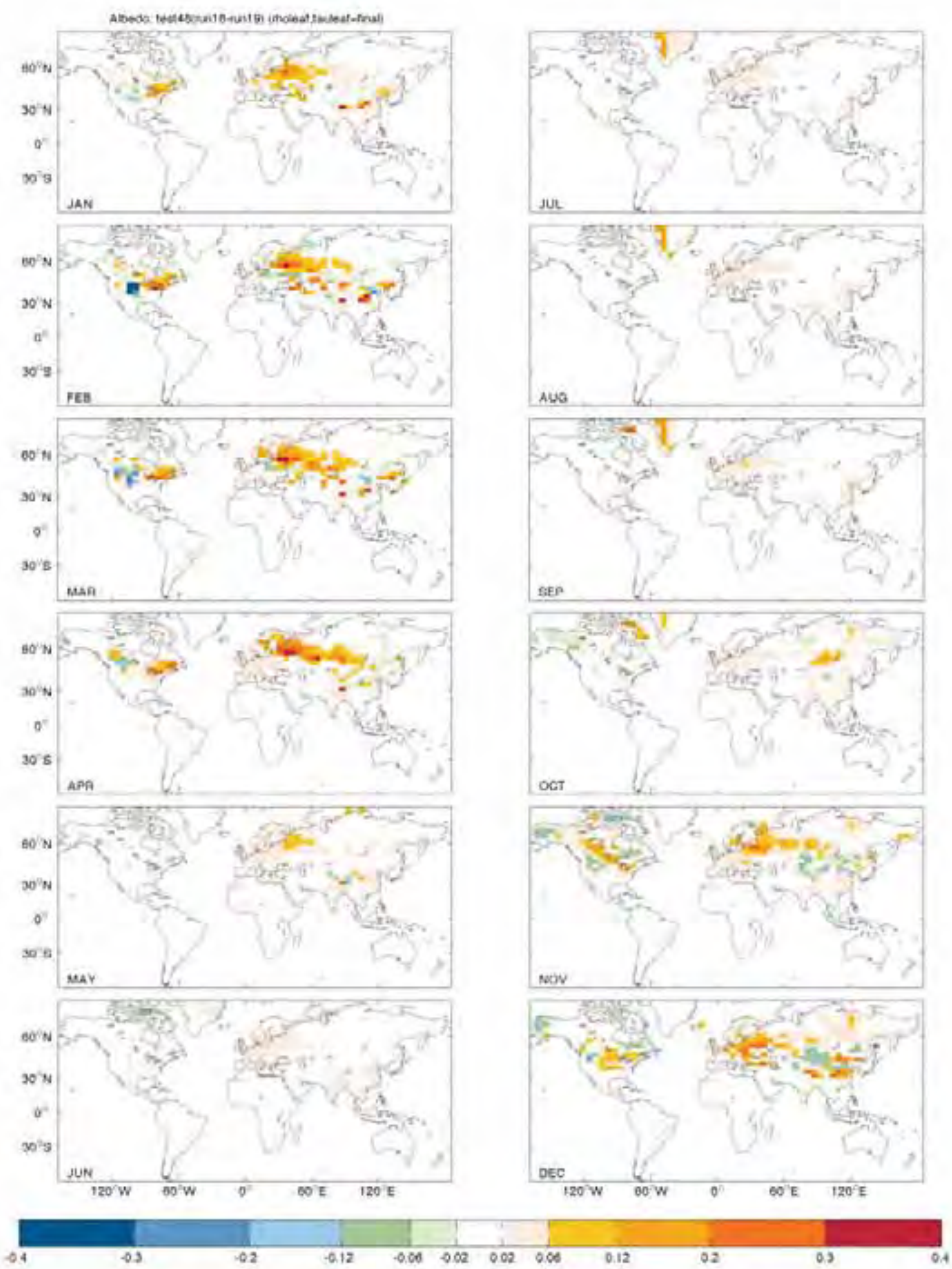

Figure 3-28: As Figure 3-22 (change in surface albedo due to LULCC) but with rholeaf, tauleaf set to the final version.

Figure 3-29 shows the root mean square error (averaged over all land grid points for each month) of the simulated albedo compared to the observation. Using the constant leaf optical properties (black line), large discrepancies are evident during May to September. Using the DS89 data actually increased the error (solid blue line) but subsequent adjustments eventually decreased the error to less than that of the original configuration (red line). While errors still exist and the values of the leaf reflectance and transmittance values may not match that of DS89, and in some cases the values are actually constant across some vegetation types (Table 3-7), these modifications did achieve the goal of allowing the model to reflect the changes in surface albedo due to LULCC (Figure 3-28).

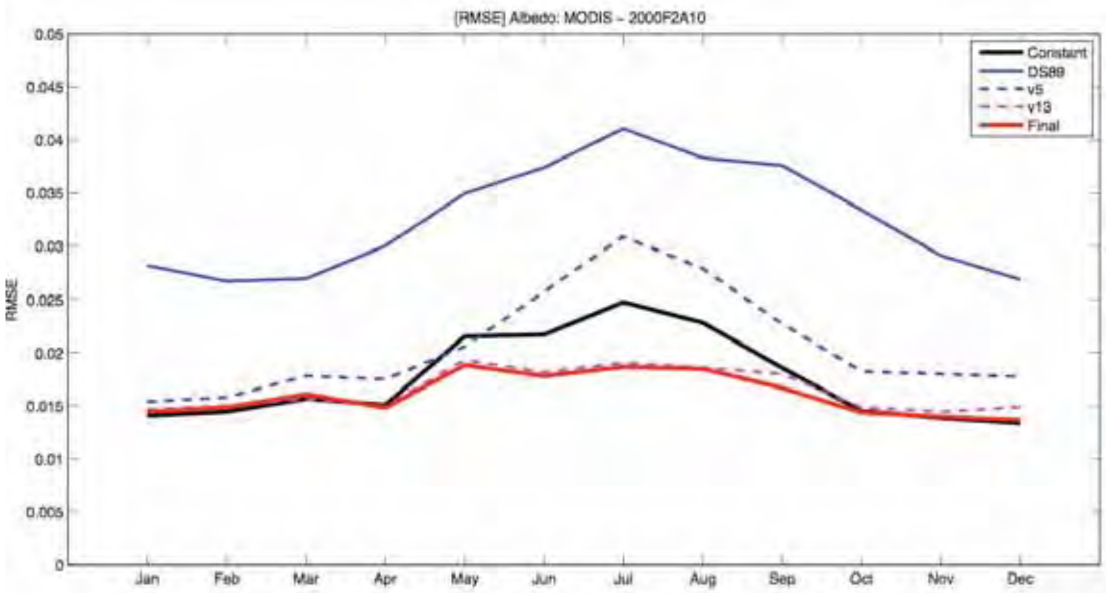

Figure 3-29: Root mean square error of the simulated monthly albedo compared to observations. In this case, error is defined as the absolute difference between the observed and simulated value, averaged over all the land grid points. Each line indicates the RMSE of the simulations shown in Figures 3-22 to 3-28, with the default and final configurations shown in black and red, respectively. To facilitate visualization, results from the intermediate simulations were not included in the plot.

3.5 Climate extreme indices

To assess changes in climate extremes, indices recommended by the CCl/CLIVAR/JCOMM Expert Team on Climate Change Detection and Indices [ETCCDI, *Alexander et al.*, 2006; *Peterson and Manton*, 2008] are used. These indices are calculated from daily precipitation and daily maximum (Tmax) and minimum (Tmin) temperature and have been developed to assess changes in intensity, duration and frequency of extreme climate events. The complete set of the ETCCDI indices are listed in Table 3-8. Precise definitions are available in the appendix or at http://cccma.seos.uvic.ca/ETCCDI/list_27_indices.shtml. Two derived indices (ETR and R95pT), defined by Alexandar et al. [2006], are also included in the table. Only a subset of these indices is used in this thesis.

For each simulation, the indices were calculated using the software package FClimdex developed by the ETCCDI and available online at http://cccma.seos.uvic.ca/ETCCDI/software.shtml [*Alexander et al.*, 2006]. The particular version of FClimdex used for this thesis did not process netCDF format files and therefore required the preparation of input data files for each land grid point in ASCII text format. It was also designed to use thresholds that are already embedded within the input data. In this study however, a specific experiment (e.g. FOREST1x) is designated as the control simulation and thus indices that require a threshold for calculation (e.g. TX10p, TN10p, TX90p, TN90p, WSDI and CSDI) have to refer to the values from the designated control simulation. To implement this, FClimdex was modified so that when the control simulation is processed, the 10th and 90th percentile values of the temperature are saved in files and when the other simulations are processed, these saved percentile values are read as input data and used as the threshold for determining the extreme indices.

Annual extremes are calculated for all indices but for some indices (TXn, TNn, TXx, TNx, TX10p, TN10p, TX90p, TN90p, DTR, RX1day and RX5day) the monthly extremes are also calculated. Whenever possible, the seasonal extremes (i.e. extreme value among three monthly extremes for the seasons: DJF, MAM, JJA, SON) are presented in the results.

Table 3-8: The complete list of 27 ETCCDI-recommended temperature and precipitation indices and two derived+ indices (ETR and R95pT) defined by Alexander et al. (2006). Indices that are not used are in this thesis are marked by an asterisk (*). Note that, in this thesis, the temperature frequency indices (TX10p, TN10p, TX90p and TN90p) are expressed in terms of number of days while ETCCDI uses percentages.

Index		**Definition**	**Unit**
	A. Temperature		
	Intensity		
TXn	Min Tmax	Coldest seasonal daily maximum temperature	°C
TNn	Min Tmin	Coldest seasonal daily minimum temperature	°C
TXx	Max Tmax	Warmest seasonal daily maximum temperature	°C
TNx	Max Tmin	Warmest seasonal daily minimum temperature	°C
DTR	Diurnal temperature range	Mean difference between daily Tmax and Tmin	°C
ETR*+	Extreme temperature range	TXx - TNn	°C
	Duration		
GSL	Growing season length	Annual number of days between the first occurrence of 6 consecutive days with T > 5°C and first occurrence of consecutive 6 days with T < 5°C. For the Northern	Days per year

Index		Definition	Unit
		Hemisphere this is calculated from 1 January to 31 December while for the Southern Hemisphere it is calculated from 1 July to 31 June.	
CSDI	Cold spell duration indicator	Annual number of days with at least 6 consecutive days when Tmin < 10^{th} percentile	Days per year
WSDI	Warm spell duration indicator	Annual number of days with at least 6 consecutive days when Tmax > 90^{th} percentile	Days per year
ID0*	Ice days	Annual count when daily maximum temperature < 0°C	Days per year
FD0*	Frost days	Annual count when daily minimum temperature ≤ 0°C	Days per year
SU25*	Summer days	Annual count when daily maximum temperature > 25°C	Days per year
TR20*	Tropical nights	Annual count when daily minimum temperature > 20°C	Days per year
	Frequency		
TX10p	Cool days	Number of days when Tmax < 10^{th} percentile	Days per season
TN10p	Cool nights	Number of days when Tmin < 10^{th} percentile	Days per season
TX90p	Warm days	Number of days when Tmax > 90^{th} percentile	Days per season
TN90p	Warm nights	Number of days when Tmin > 90^{th} percentile	Days per season
	B. Precipitation		
	Intensity		
RX1day	Max 1-day precipitation	Seasonal maximum 1-day precipitation	mm
RX5day	Max 5-day precipitation	Seasonal maximum 5-day precipitation	mm
PCRPTOT*	Annual total wet-day precipitation	Annual total precipitation from wet days (i.e. when precipitation ≥ 1.0 mm)	mm
SDII	Simple daily intensity index	Annual total precipitation divided by the number of wet days (i.e. when precipitation ≥ 1.0 mm)	mm/day
R95p*	Very wet days	Annual total precipitation from very	mm

Index		Definition	Unit
		wet days (i.e. when precipitation > 95^{th} percentile)	
R99p*	Extremely wet days	Annual total precipitation from extremely wet days (i.e. when precipitation > 99^{th} percentile)	Mm
R95pT+	Annual contribution from very wet days	(annual total precipitation > 95^{th} percentile)/ (annual total precipitation))*100	%
	Duration		
CWD	Consecutive wet days	Maximum annual number of consecutive wet days (i.e. when precipitation ≥ 1.0 mm)	Days
CDD	Consecutive dry days	Maximum annual number of consecutive dry days (i.e. when precipitation < 1.0 mm)	Days
	Frequency		
R10mm	Heavy precipitation days	Annual number of days when precipitation ≥ 10 mm	Days
R20mm*	Very heavy precipitation days	Annual number of days when precipitation ≥ 20 mm	Days
Rnnmm*	User defined precipitation threshold	Annual number of days when precipitation ≥ nn, where nn is a user defined threshold	Days

Alexander et al. [2006] divided these indices into five different categories: (1) absolute indices (TXn, TNn, TXx, TNx, RX1day and RX5day) which represent the maximum and minimum values within a season or year and are the key indicators of changes in the extremes; (2) percentile-based temperature indices (TX10p, TN10p, TX90p, TN90p, R95p, R99p) which sample the coldest and warmest deciles, allowing the evaluation of the extent to which extremes are changing; (3) threshold indices (ID0, FD0, SU25, TR20, R10mm and R20mm) which are defined as the number of days when temperature or precipitation falls below or above a fixed threshold; (4) duration indices which define periods of excessive warmth (WSDI), cold (CSDI), wetness (CWD), dryness (CDD) or mildness (GSL); and (5) other indices which do not fall into the other categories but whose changes could have significant societal impacts (DTR, SDII, ETR and R95pT). Indices defined to exceed fixed thresholds that are not applicable to most regions of the globe are not used in this thesis.

3.6 Statistical methods

In most figures in the results section, only the grid points with statistically significant difference are shown to emphasize the significant change. In cases where the coastlines are shown, grid points with negligible change are shown as white spaces. However, in some cases when coastlines are not suitable, grey dots are used to indicate the land grid points that are not statistically significant.

3.6.1 Difference between means

To test the statistically significant difference between means, the modified *t* test, following the methodology described by Zwiers and Von Storch [1995] and Von Storch and Zwiers [1999], is used in place of the Student's *t* test to account for time-dependence within the data. This test is more rigorous than the standard *t* test and has been used by Findell et al. [2006; 2007; 2009] in several land cover change studies.

A critical assumption of a standard *t* test is independence of samples from different points in the time series. This assumption is not valid for an autocorrelated time series and the effective number of degrees of freedom is smaller than the total number of points in time in the overall sample. In general, the variance of an autocorrelated series is smaller than that of an uncorrelated series. Thus, using the standard *t* test for an autocorrelated series would result in an overestimation of the *t* statistic and a more frequent rejection of the null hypothesis (i.e., that there is no significant difference between the means of the two samples) and would result in a bias towards detection of significant change.

The modified *t* test accounts for autocorrelation within the time series by comparing the standard *t* statistic to an alternative critical *t* value that has been determined from a Monte Carlo experiment where random time series for autoregressive processes of first order with a specified lag-1 autocorrelation were generated. This comparison to an alternative critical value (instead of simply using the standard *t* statistic) reduces the number of false rejections of the null hypothesis and results in a more reliable statistical test.

3.6.2 Difference between distributions

Since the distribution of many climate variables is not necessarily Gaussian, a parametric test such as the *t* test may be inappropriate for testing the null hypothesis that there is no statistically significant difference between two distributions. In such cases, a non-parametric test that makes no assumptions about the distribution of the data, such as the two-tailed Kolmogorov-Smirnov (KS) test, is used. The KS test has been used by *Deo et al.* [2009] in a regional study of climate extreme indices.

3.6.3 Accounting for spatial correlation

Neither the modified *t* test nor the KS test accounts for spatial correlation within fields. Because data from adjacent grid points are not independent, the effective number of spatial degrees of freedom is much smaller than the number of grid points. Thus, the collective significance of statistical tests in a finite number of interdependent time series needs to be much larger than the nominal level [*Livezey and Chen*, 1983]. That is, if testing at a 95% confidence level, much greater than 5% of the continental surfaces should appear statistically significant to indicate field significance.

As the threshold over which results may be classified as field significant differs between variables and indices, a bootstrapping method, following Kiktev et al. [2003] and Alexander et al. [2006], is used. This involves using a moving block re-sampling technique [*Wilks*, 1997] to create 1000 sets of 20-year samples by randomly taking two consecutive years of data at a time for each index and experiment. To maintain spatial dependence, all grid points were re-sampled in the same order for each experiment. For each pair of 20-year bootstrapped samples, the two-tailed KS test was applied to determine the grid points with statistically significant difference and, for each field, the percentage of significant grid points were then calculated. This resulted in 1000 percentage values for each index. The 5th percentile of these percentages is defined as the field significance threshold level to which the percentage of significant grid points of the non-bootstrapped data is then compared. The variable or index is field significant if the percentage of significant grid points in the non-bootstrapped data exceeds the threshold level.

3.6.4 Regression method

Regression analysis is used to understand how the typical value of dependent variable varies with respect to one of the independent variables when the other independent variables are held fixed. The least squares method is commonly used in data fitting, i.e. to construct a mathematical function from a set of data points. The best fit, in terms of "least squares", means that sum of the squared residuals (i.e. errors between the observed and fitted value provided by the model) is minimized. The ordinary or linear least squares regression method considers only the errors in one direction (usually in the ordinate or y-axis) and this is applicable in the common cases where the variables being compared are dependent and independent. However, in cases where two dependent variables are being compared, the total least squares (TLS) regression method [*Lybanon*, 1984; *Allen and Stott*, 2003] is used to account for errors on both the ordinate and abscissa (x-axis). This method has been used by Stott et al. [2003] to detect evidence of solar influence on surface temperature changes and by Min et al. [2011] to investigate the anthropogenic impact on precipitation extremes.

The TLS regression method is used instead of the ordinary least squares regression in later chapters to explore the relationship between the mean changes in the surface variables and the extreme indices.

3.7 Summary

This chapter describes how CSIRO Mk3L, a computationally efficient global climate model, was coupled to CABLE, a sophisticated land surface model, to investigate the effect of LULCC on climate extremes. While the default model configuration could reasonably simulate present day climate, it required modification in order to properly reflect LULCC. These modifications include changes in the model itself as well as changes in the input parameters. Datasets reflecting the change in surface vegetation and CO_2 concentrations were also developed. State-of-the-art indices and statistics used to assess changes in the surface variable and climate extremes were also described. Results from the experiments described here will be presented in the succeeding chapters.

Chapter 4
Changes in the mean climate

The impacts of LULCC on the mean climate are presented in this chapter because these changes will be important in explaining the changes in the extremes. Since LULCC is expected to affect the surface energy and water balance, changes in net radiation, sensible and latent heat fluxes as well as changes in precipitation and snow depth are explored. For comparison, simulated changes in these surface variables due to the increase in CO_2 alone are also presented to help place simulated impacts due to LULCC into a broader context. It should be emphasized that the changes due to CO_2 were conducted at equilibrium conditions and are not comparable to the changes due to CO_2 from observations and simulations where the atmospheric CO_2 varies in time.

Some of the results, in particular those in Section 4.3, have been included in a previous publication by Pitman et al. [2011] but substantial additional material that extends the original publication have been included in this chapter.

Candidate's contributions to this work

The idea to explore the impacts of LULCC came from my supervisor, Professor Andy Pitman but we discussed the details of the project together over the first year of the project. Dr. Steven Phipps and Dr. Gab Abramowitz provided guidance in the use of the CSIRO Mk3L and CABLE models. Together, we worked to modify and test the coupled model and design the numerical experiments. I prepared the input datasets, conducted the experiments and processed the results. I also examined how best to modify CABLE to undertake the experiments following the identification that the model could not appropriately capture the impact of land cover change. I sourced appropriate methodologies from the literature and implemented these into CABLE. Professor Pitman, Dr. Abramowitz, Dr. Ying Ping Wang, Dr. Phipps and Dr. de Noblet-Ducoudré and I contributed jointly to the analysis and writing of the original Pitman et al. [2011] paper. Section 4.3 builds extensively on this paper, including significant new and more detailed material.

4.1 Data description

Monthly data from four experiments (Table 3-5) with natural and perturbed vegetation cover at CO_2 concentrations of 280 ppmv (1 x CO_2) and 560 ppmv (2 x CO_2) are used in this analysis. The change due to LULCC at 280 ppmv is defined as the difference between FOREST1x and CROP1x (CROP1x – FOREST1x). For brevity, this quantity will also be referred to as dLCC@280. In the same manner, the change due to LULCC at 560 ppmv is the difference between FOREST2x and CROP2x (CROP2x – FOREST2x) and will be referred to as dLCC@560. The change due to the increase in CO_2 alone is calculated as the difference between FOREST1x and FOREST2x (FOREST2x – FOREST1x) and will be referred to as dCO2.

Each experiment is integrated for 300 years using the CSIRO Mk3L model coupled to the CABLE land surface model (see Chapter 3). Data from simulation years 101 to 300, when the model has reached equilibrium, are evaluated. Monthly means are defined as the average of monthly values over this 200-year period. Seasonal means indicate averages over the following 3-month periods: December-January-February (DJF), March-April-May (MAM), June-July-August (JJA), and September-October-November (SON). The corresponding terms: winter, spring, summer and autumn, refer to the Northern Hemisphere seasons, unless otherwise specified. The regions of interest (Eurasia: ~40°-65°N, ~0°-112°E, North America: ~30°-55°N, ~60°-123°W and South East Asia: ~11°-40°N, ~73°-124°E) are selected to coincide with areas of intense LULCC (Figure 4-1). Regional averages are calculated over the land grid points bounded by the boxes in the figure. Global averages include all land grid points excluding Antarctica and Greenland. In most of the maps presented in this chapter, only the grid points with statistically significant difference at the 99% level using the modified *t* test (see Section 3.6.1) are shown.

4.2 Changes due to LULCC compared to CO_2 doubling

Figure 4-2 shows the simulated annual global mean of the surface variables from the four experiments over land grid points excluding Antarctica and Greenland. The simulated net radiation, surface temperature, precipitation and snow depth stabilizes within a few years from model initialization but other variables such as latent heat flux (Figure 4-2c) stabilizes much later, at around simulation year 80. Results prior to year 80 are therefore omitted to avoid problems related to spin-up.

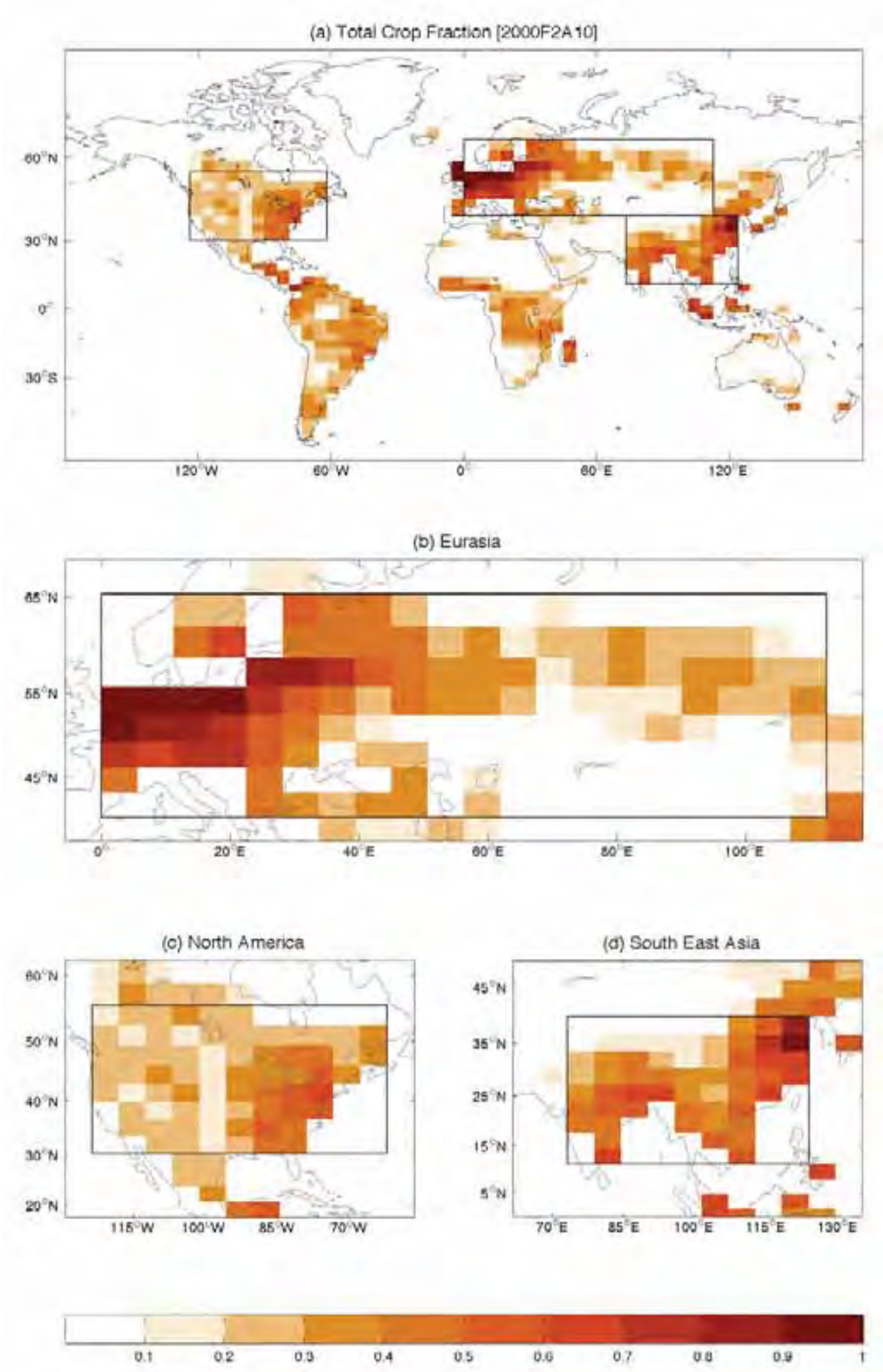

Figure 4-1: Total crop fraction map with the regions of interest in this chapter indicated by boxes (a) and shown in the sub-plots: (b) Eurasia (~40°-65°N, ~0°-112°E), (c) North America (~30°-55°N, ~60°-123°W) and (d) South East Asia (~11°-40°N, ~73°-124°E).

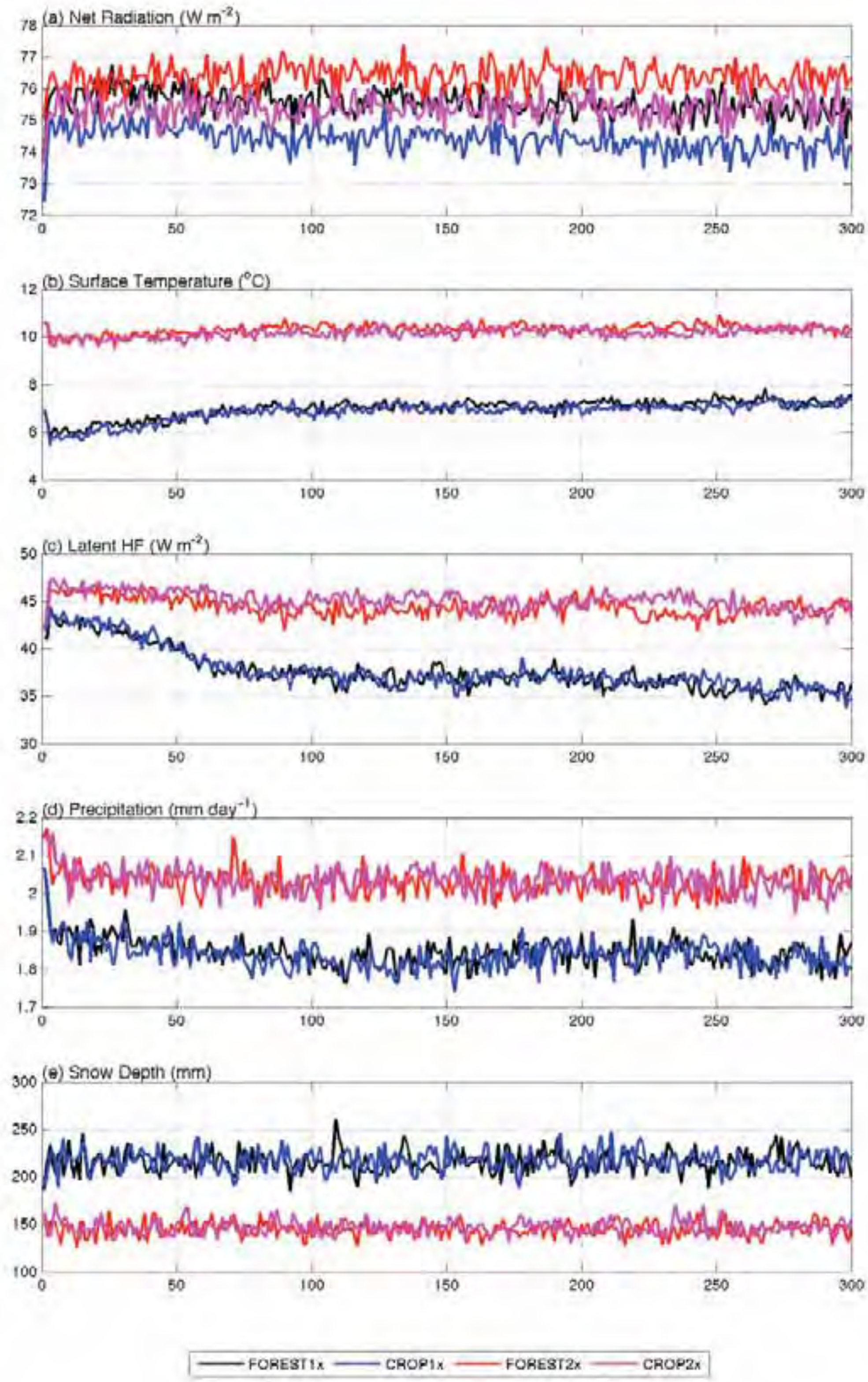

Figure 4-2: Annual global mean of simulated (a) net radiation (W m^{-2}), (b) surface temperature (°C), (c) latent heat flux (W m^{-2}), (d) precipitation (mm day^{-1}) and (e) snow depth (mm) over land grid points excluding Antarctica and Greenland. The x-axis indicates the simulation year.

Figure 4-2 also shows that simulations at the same CO_2 concentration (i.e. FOREST1x and CROP1x, or FOREST2X and CROP2x) differ little relative to the change caused by doubling CO_2 (i.e. between FOREST1x and FOREST2x or between CROP1x and CROP2x). That is, in terms of global averages, the changes due to LULCC are generally much smaller than those due to CO_2. The experiments at higher CO_2 levels (FOREST2x and CROP2x) simulate higher surface temperature (Figure 4-2b), higher latent heat flux (Figure 4-2c), more precipitation (Figure 4-2d) and less snow (Figure 4-2e) than the experiments at lower CO_2 levels (FOREST1x and CROP1x). However, in terms of net radiation (Figure 4-2a), there is a marked difference between the experiments with different vegetation cover (i.e. between FOREST1x and CROP1x; and between FOREST2x and CROP2x), with LULCC inducing decreased net radiation over the global land points. This LULCC-induced change is opposite to that of increased CO_2, which increases the global net radiation.

Figures 4-3 and 4-4 show the zonal mean of the surface variables during DJF and MAM (Figure 4-3) and JJA and SON (Figure 4-4). Again the difference between the 1 x CO_2 and 2 x CO_2 experiments are evident, while the difference between the natural and perturbed vegetation cover experiments are only clear for latent heat flux. Increased CO_2 induces slightly higher net radiation over the tropics (~30°S-30°N) during DJF, JJA and SON but lower net radiation over the northern high-latitudes (~60°-75°N) during MAM (Figures 4-3a and 4-4a). It also induces generally higher surface temperature throughout the year (Figures 4-3b and 4-4b); decreased snow cover during DJF, MAM and SON (Figures 4-3e and 4-4e) over the northern mid-latitudes (~30°-75°N); and increased precipitation

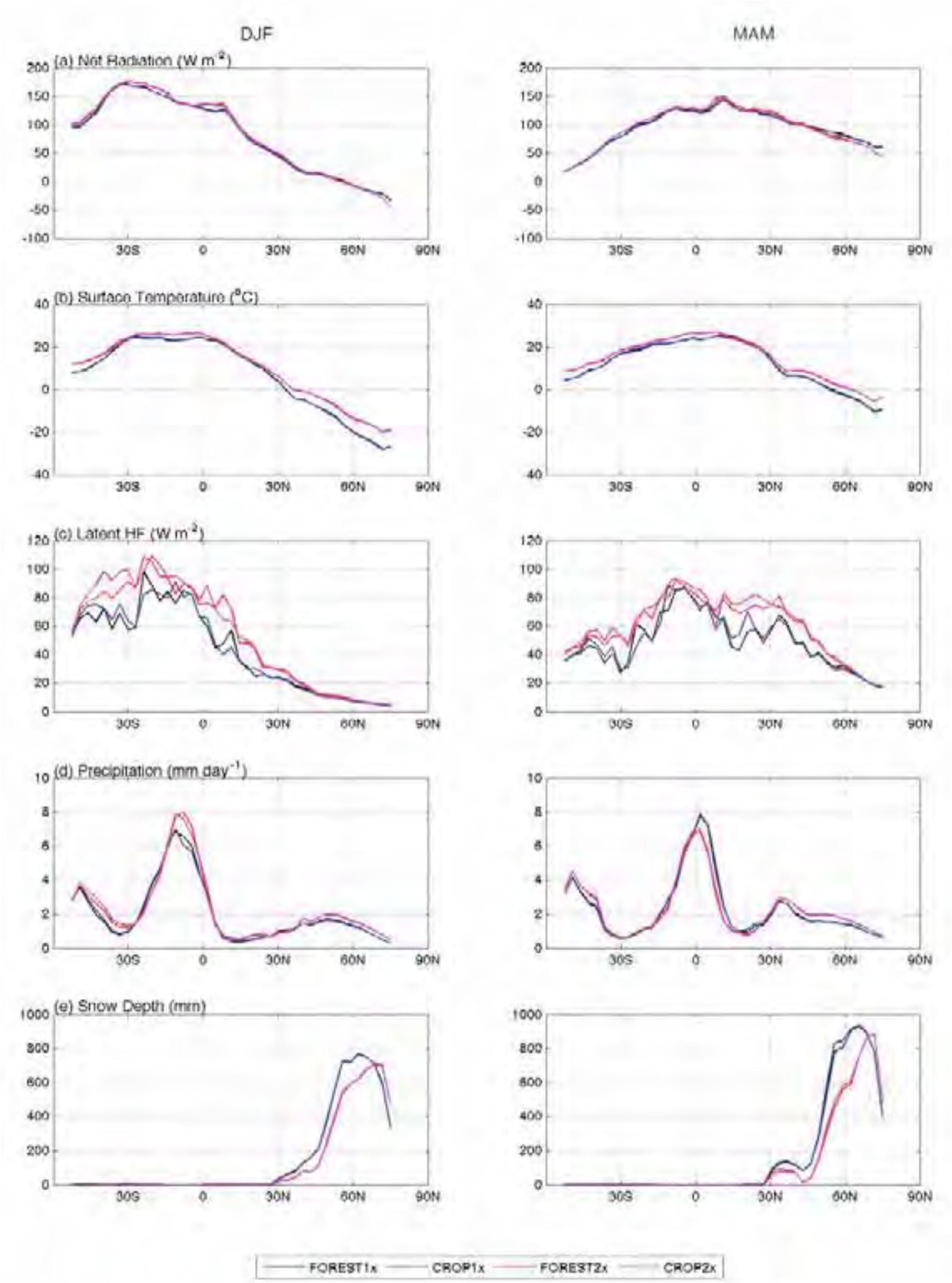

Figure 4-3: Zonal mean of simulated (a) net radiation (W m^{-2}), (b) surface temperature (°C), (c) latent heat flux (W m^{-2}), (d) precipitation (mm day^{-1}) and (e) snow depth (mm) for DJF (left column) and MAM (right column) over land grid points excluding Antarctica and Greenland. The x-axis indicates the latitudes (from 60°S to 90°N).

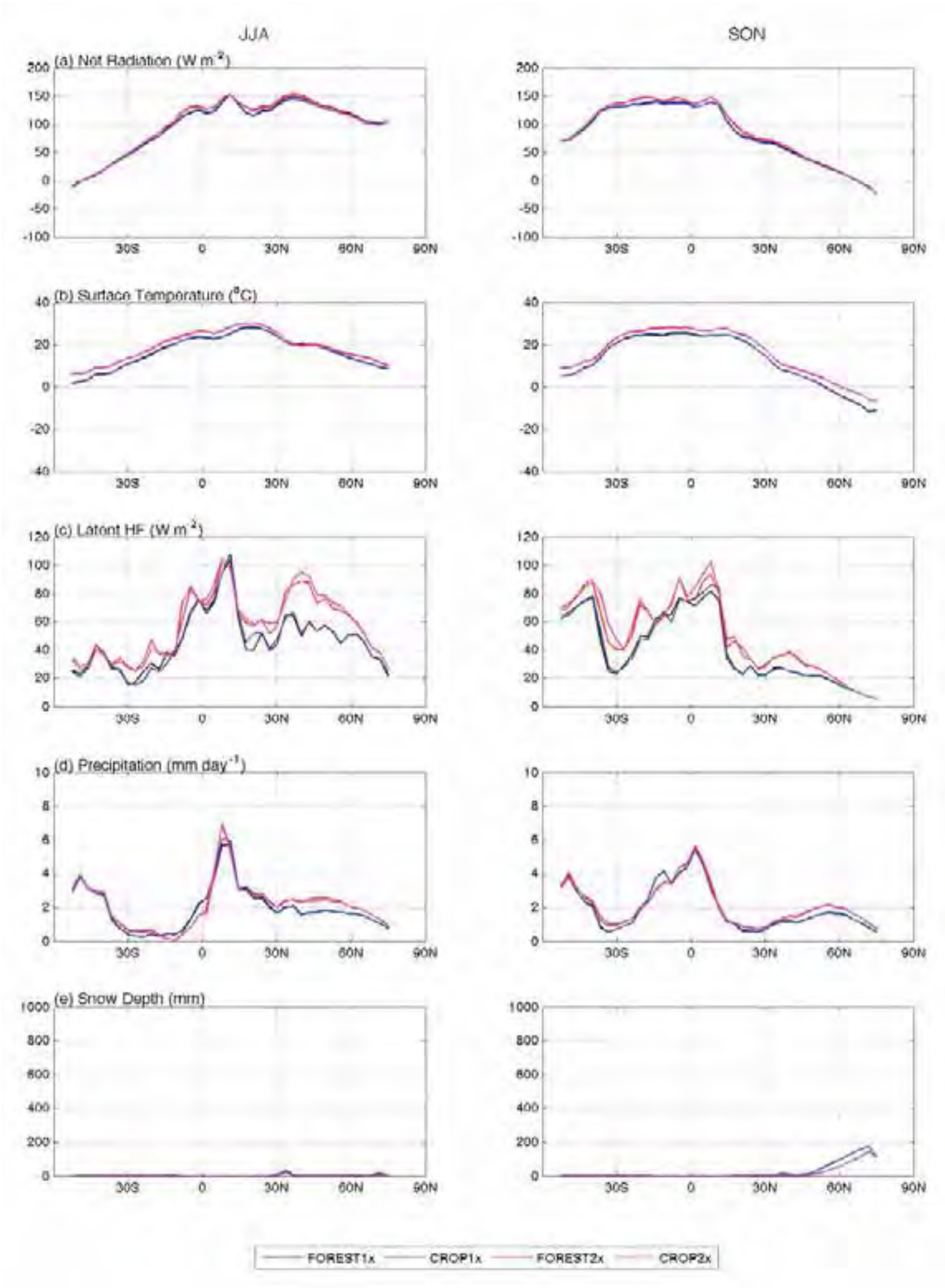

Figure 4-4: As Figure 4-3 but for JJA (left column) and SON (right column).

throughout the year over the mid-latitudes (~30°-60°S and ~30°-75°N) (Figures 4-3d and 4-4d). Over the tropics (~30°S-30°N), the impact of increased CO_2 on precipitation is more complex, varying through the seasons and according to geographical location (Figures 4-3d and 4-4d).

Increased CO_2 also induces increases in latent heat flux throughout the year (Figures 4-3d and 4-4d). However, LULCC also induces interesting changes, which, in some cases, are almost as large as that due to increased CO_2. For example, over the tropics (30°S-30°N) during most of the year, and during the summer over the mid-latitudes: DJF at (~30°-60°S) and JJA at (~30° -60°N).

These results motivate the exploration of changes in the monthly mean and further analysis over LULCC regions. Figure 4-5 shows the change in the monthly surface variables due to LULCC at 280 ppmv (blue) and at 560 ppmv (red). The global average is shown on the left-most column while the averages over Eurasia, North America and South East Asia are shown in the second, third and fourth columns from the left. As expected, the global average is much smaller compared to the regional averages. Globally, the change in net radiation (Figure 4-5a) ranges from -2.0 to 0.0 W m^{-2}; surface temperature (Figure 4-5b) from -0.3 to 0.0 °C; latent heat flux (Figure 4-5c) from -1.0 to 1.0 W m^{-2}; precipitation (Figure 4-5d) from -0.05 to 0.05 mm day^{-1}; and snow depth (Figure 4-5e) by less than 10 mm. Considering that the globally averaged monthly standard deviations are as much as 2 W m^{-2} for the net radiation, 0.6 °C for the surface temperature, 2 W m^{-2} for the latent heat flux, 0.11 mm day^{-1} for precipitation and 40 mm for snow depth, these changes are very small.

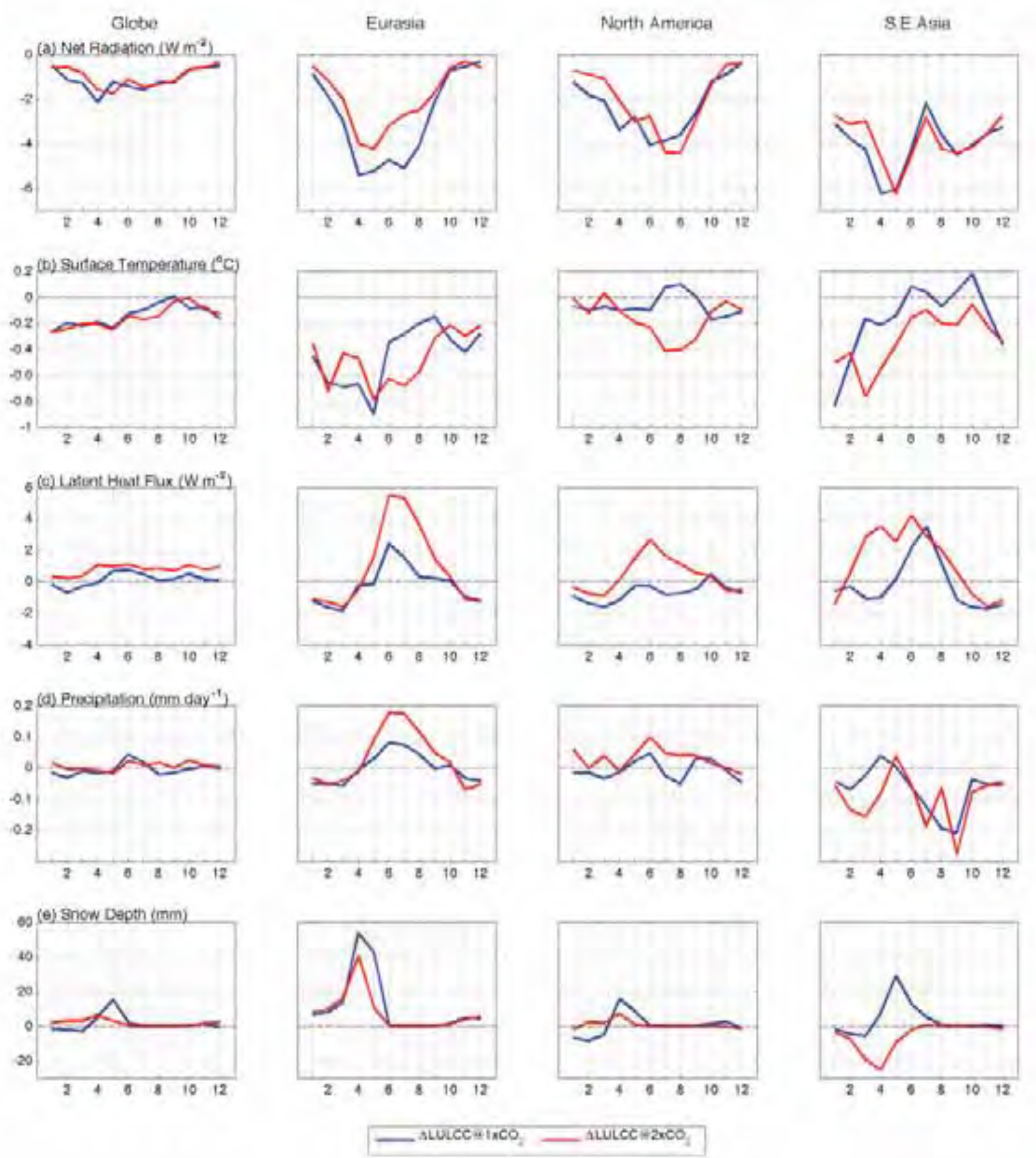

Figure 4-5: Changes due to LULCC in the monthly surface variables over the globe, Eurasia, Asia and Eastern US: (a) net radiation (W m^{-2}), (b) surface temperature (°C), (c) latent heat flux (W m^{-2}), (d) precipitation (mm day^{-1}) and (e) snow depth (mm). The blue lines indicate changes due to LULCC at 280 ppmv while the red lines indicate changes due to LULCC at 560 ppmv. The x-axis indicates the month.

In contrast, large changes in surface variables are evident within the regions of intense LULCC, suggesting that while LULCC does not induce significant change on the global climate, it does significantly affect regional climate.

Figures 4-6 to 4-9 show global maps of the changes due to LULCC at 280 ppmv (a, left column) and due to increased CO_2 (b, right column) for DJF (top row), MAM (second row from the top), JJA (third row from the top) and SON (bottom row). Only grid points that are statistically significant at the 99% level using the modified *t* test are shown.

Figure 4-6a shows a general decrease in net radiation throughout the year especially over areas of LULCC. Figure 4-6b on the other hand displays a more widespread change due to increased CO_2; increases are evident over the tropics and Southern Hemisphere while decreases are visible over the mid-latitudes.

Figure 4-7a shows a marked decrease in surface temperature over Eurasia especially during DJF and MAM, and over parts of northern Africa and Asia during most of the year. Increased surface temperature over the parts of the tropics is also evident. CO_2 doubling on the other hand (Figure 4-7b) induces intense (> 2°C) and widespread surface warming throughout the year with slight cooling over northern Africa during DJF, MAM and JJA and over parts of North America during JJA.

Figure 4-8a shows quite large (-10 to 10 W m^{-2}) regional changes due to LULCC especially during MAM and JJA while Figure 4-8b shows large (> 30 W m^{-2}) increases in latent heat flux during the same period.

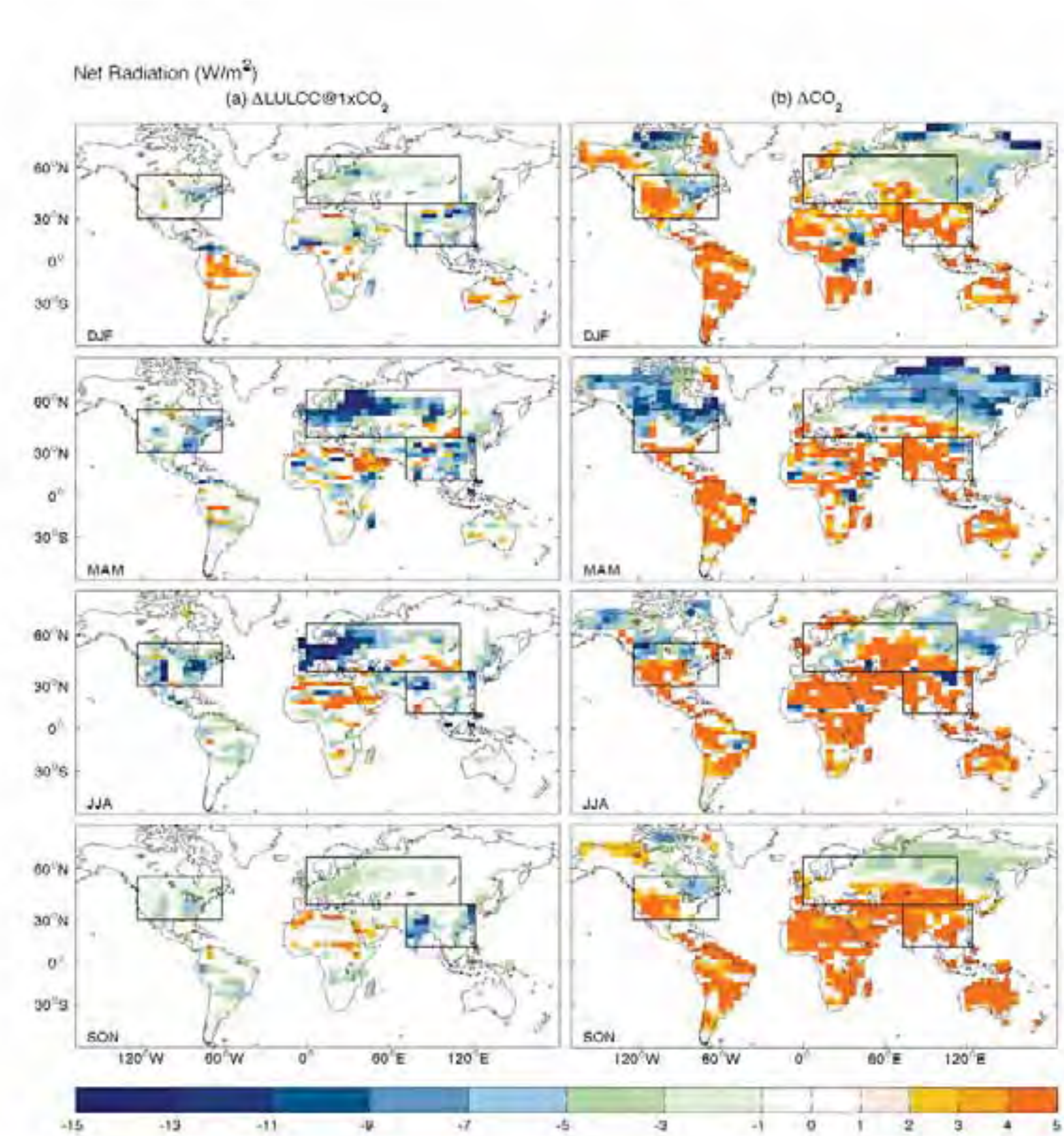

Figure 4-6: Mean seasonal change in net radiation (W m^{-2}) due to (a) LULCC at 280 ppmv and (b) CO_2 doubling only. Only grid points with statistically significant difference at the 99% level using the modified t test are shown. From top to bottom: DJF, MAM, JJA and SON.

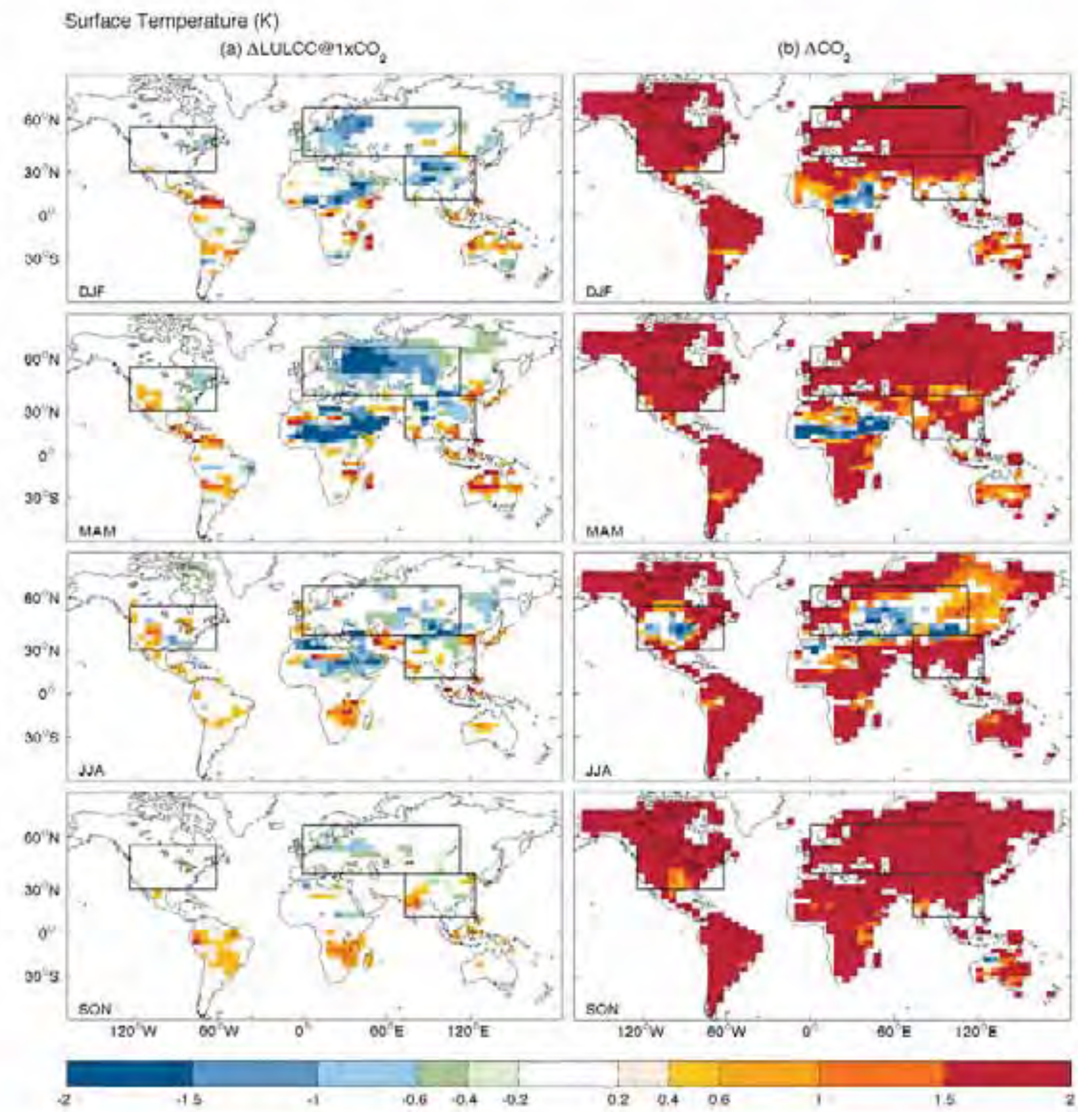

Figure 4-7: As Figure 4-6 but for surface temperature (°C). Values > 2°C are masked in the dCO2 simulations to preserve a wide enough range of values to show the impact due to LULCC.

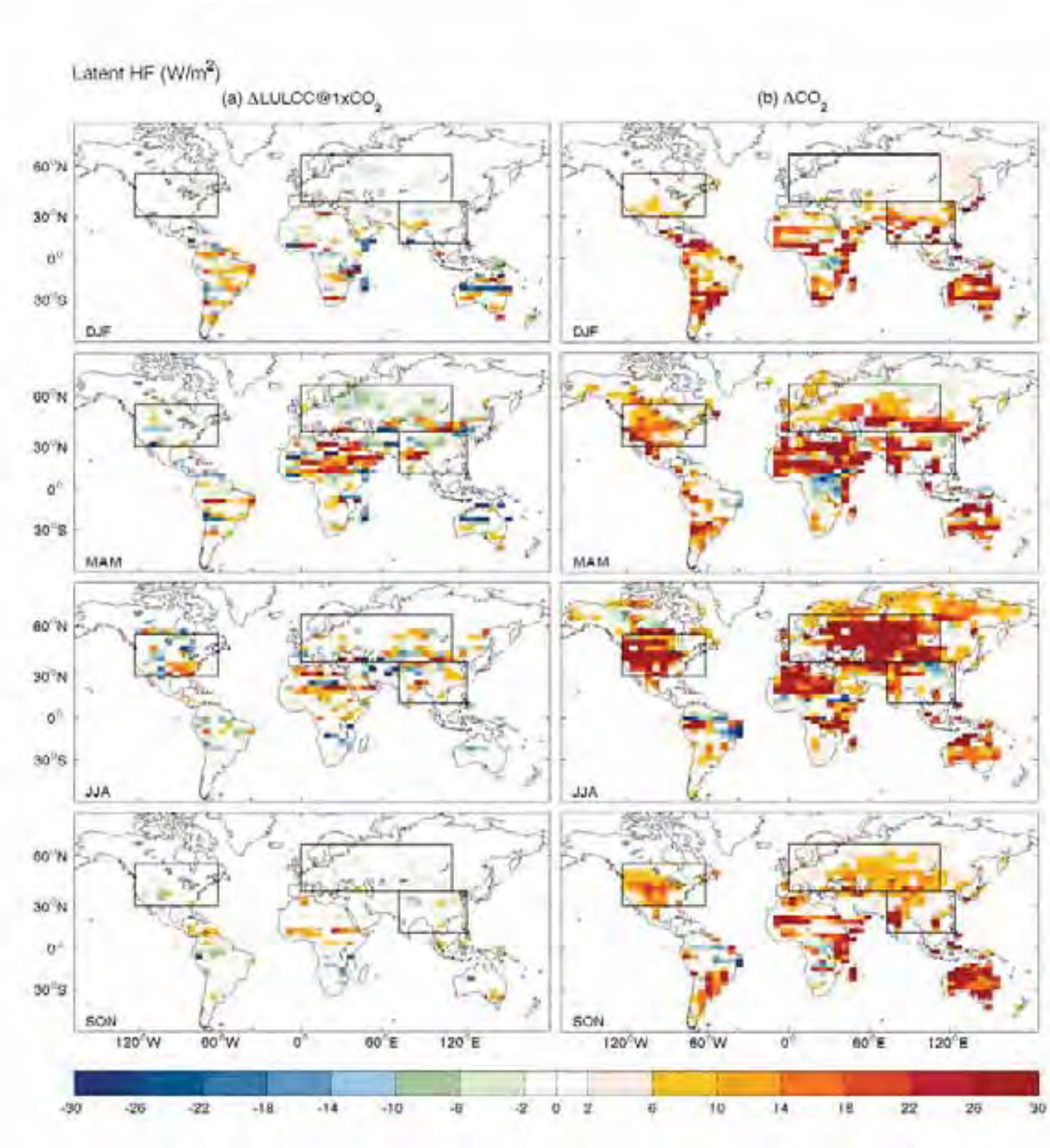

Figure 4-8: As Figure 4-6 but for latent heat flux (W m^{-2})

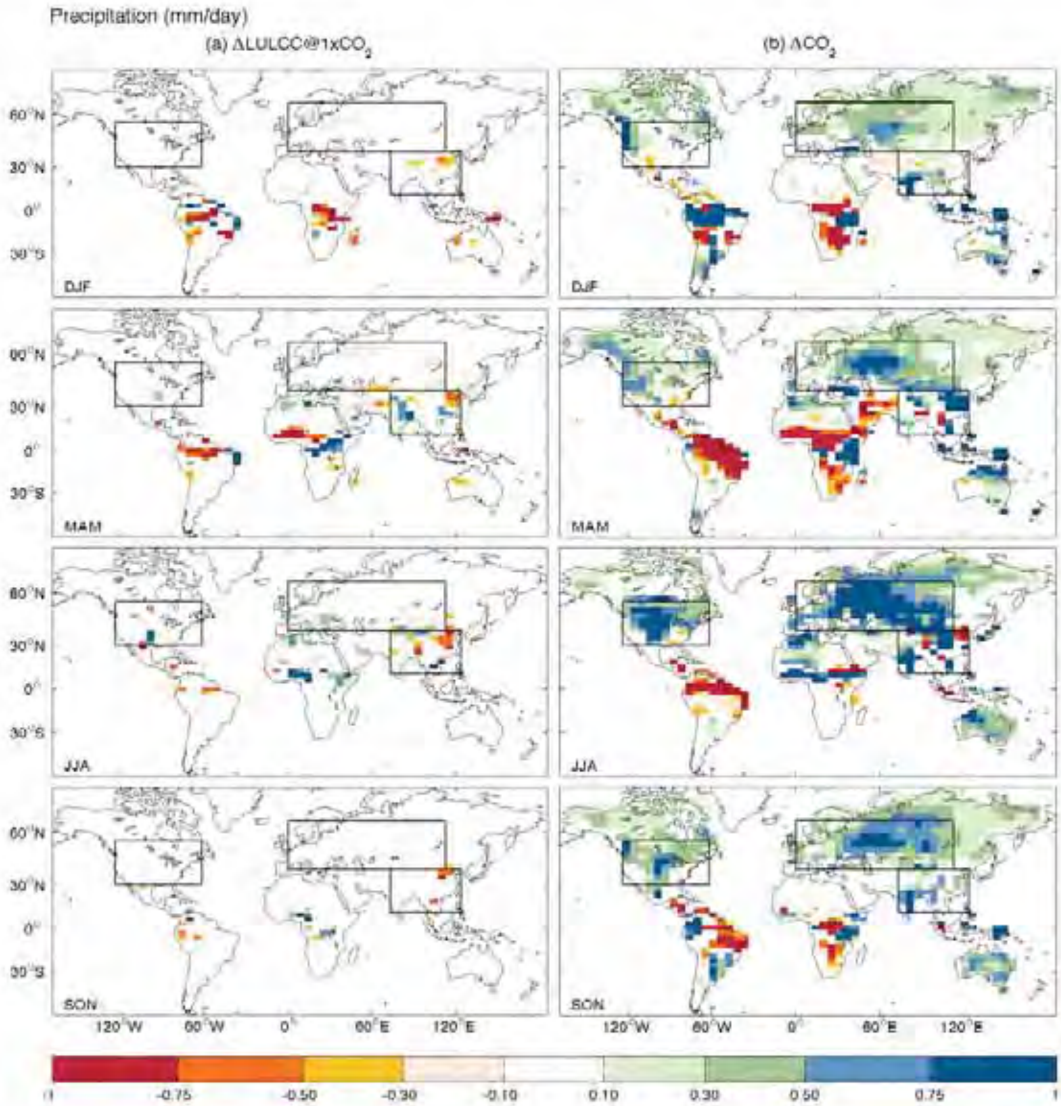

Figure 4-9: As Figure 4-6 but for precipitation (mm day $^{-1}$).

Figure 4-9a shows negligible change in seasonal precipitation due to LULCC while increased CO_2 induces widespread and intense (> 1 mm day^{-1}) increases over the Northern Hemisphere (Figure 4-9b). Quite large decreases (> 1 mm day^{-1}) are also evident over the tropics and Southern Hemisphere.

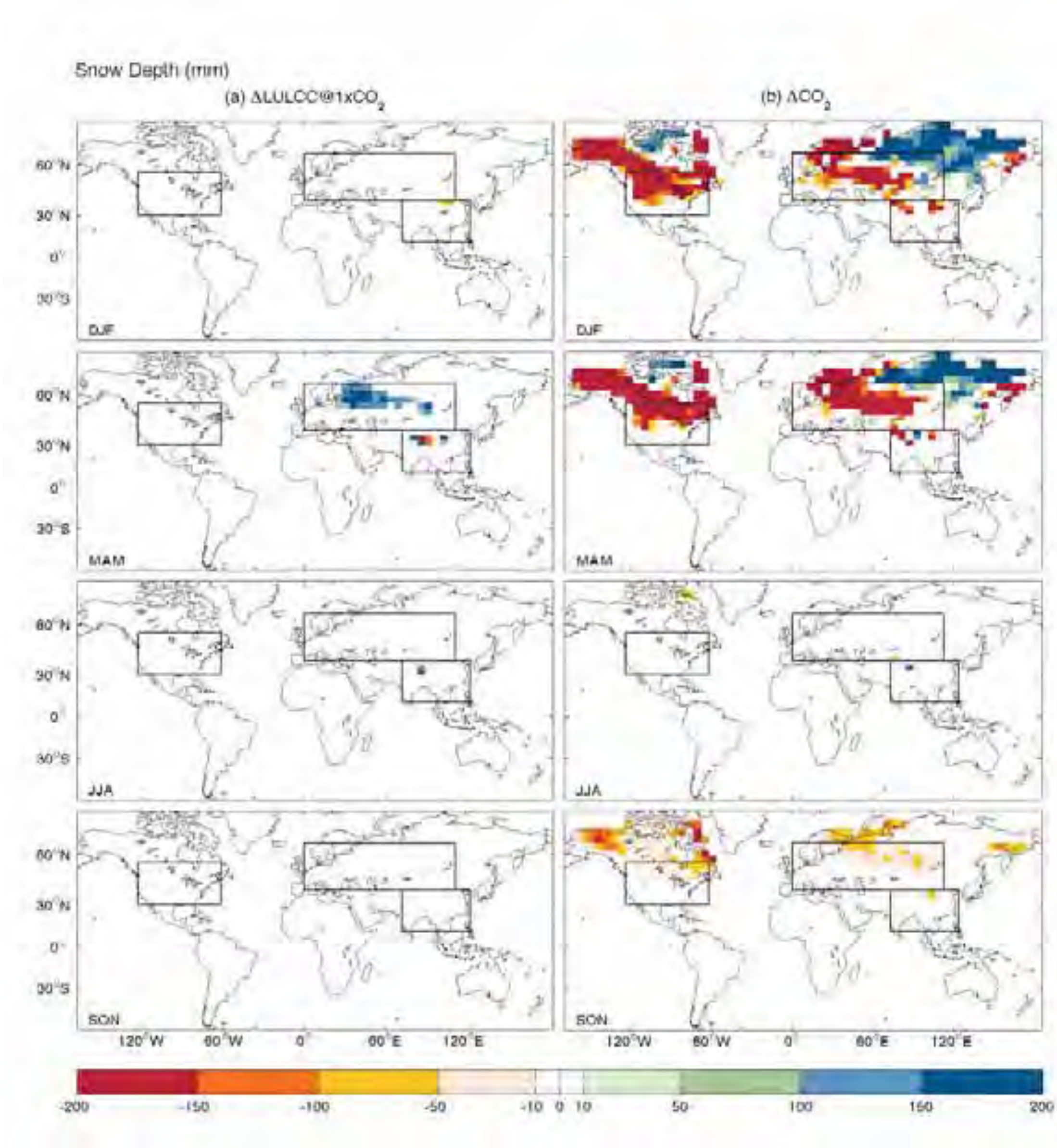

Figure 4-10: As Figure 4-6 but for snow depth (mm).

Figure 4-10 shows the change in snow depth. The increase in snow depth due to LULCC during MAM over Eurasia is evident in Figure 4-10a. On the other hand, increased CO_2 causes widespread decrease in snow depth over the northern high-latitudes (North America and Western Europe) during DJF, MAM and SON as well as widespread increase in snow depth over the northern high latitudes during DJF and MAM are shown in Figure 4-10b.

Figures 4-6 to 4-10 show that LULCC significantly affects the seasonal means of surface variables in the regional-scale while CO_2 doubling causes more widespread, in most cases global-scale, change. The magnitude of the change due to LULCC is also generally smaller than due to CO_2 doubling. However, during some seasons and over regions of LULCC, the magnitude of change due to LULCC can be as large as that of CO_2 doubling. The change due to LULCC may be of the same or opposite sign to the change due to CO_2 doubling indicating the possibility of either enhancing or cancelling their impacts, depending on the time of year, variable and region.

While most of the change due to LULCC coincide with the regions of LULCC, some of the significant changes also occur over areas where no LULCC have been imposed suggesting the possibility of remote impacts due to LULCC. However, because the SSTs prescribed in the model simulations do not vary interannually it is not legitimate to explore teleconnections with the current set of experiments.

In terms of the negligible change in mean rainfall due to LULCC, it should be noted that the model used here has a coarse resolution which could not be expected to capture the mesoscale and sub-grid processes which are very important in simulating complex rainfall processes. The changes in rainfall are therefore likely indicative of the sign of the change due to LULCC but likely not the magnitude of the change.

Since the changes due to LULCC occur at regional scale, the next section explores the changes within these regions of intense LULCC and compares the changes due to LULCC at different CO_2 levels.

4.3 Changes due to LULCC at different CO_2 levels

The cooling over mid- and high-latitudes, and warming over the tropics and sub-tropics due to LULCC, particularly in the winter and spring (Figure 4-7), are not unexpected [*Davin and de Noblet-Ducoudré*, 2010]. This biophysical impact of LULCC is realized through three mechanisms: (a) an increased albedo and hence a reduction in net radiation [*Forster et al.*, 2007] (crops are commonly more reflective than forests); (b) an amplification of the positive snow-albedo feedback (forests mask snow on the ground more effectively than crops and pasture) [*Betts*, 2000]; and (c) a change in how net radiation is partitioned between latent heat and sensible heat fluxes (crops and pasture have less capacity to sustain high latent heat fluxes compared to forests when evaporative demand is high). LULCC in mid- and high-latitudes tends to cool because mechanisms (a) and (b) dominate in winter and spring due to the presence of snow. In summer, in the absence of snow, mechanism (c) can be significant if moisture limits evaporation. In the tropics, LULCC tends to be associated with warming and drying because mechanism (c) dominates and sensible heat fluxes increase, warming the atmosphere [*Davin and de Noblet-Ducoudré*, 2010]. The relative dominance of these mechanisms depends on the amount of snow and the amount and seasonality of precipitation. Less snow in a warmer world would weaken the positive snow-albedo feedback, reduce the influence of mechanism

(b) and partially negate cooling from LULCC at high latitudes. In all regions, mechanism (c) can be masked by higher precipitation since this would reduce the likelihood of moisture stress limiting the latent heat flux, tending to minimize increases in sensible heat fluxes [*Pitman et al.*, 2011].

The following figures help illustrate how these mechanisms result in the simulated changes due to LULCC over three regions: Eurasia, North America and South East Asia.

The absolute change in temperature and precipitation due to LULCC at 1 x CO_2 relative to the change due to LULCC at 2 x CO_2 (dLCC@280 / dLCC@560) are shown in Figures 4-11 and 4-17, respectively. Where there is negligible difference between the change at 1 x CO_2 and 2 x CO_2, grid points are shown in white. Grid points where the absolute change at 2 x CO_2 is greater than at 1 x CO_2 are shown in red; and where the absolute change at 1 x CO_2 is greater than at 2 x CO_2, grid points are shown in blue. A value of 1 means the change at 1 x CO_2 is double the change at 2 x CO_2; a value of -0.5 means the change at 2 x CO_2 is double the change at 1 x CO_2.

Figures 4-12 and 4-13 show regional averages of the changes due to LULCC in the surface variables during DJF and MAM (Figure 4-12) and JJA and SON (Figure 4-13). Changes in net radiation (square boxes) and latent heat flux (square boxes), combined with the actual snow, precipitation and temperature values (circles) result in the simulated changes in surface temperature (hexagons, red for warming and blue for cooling).

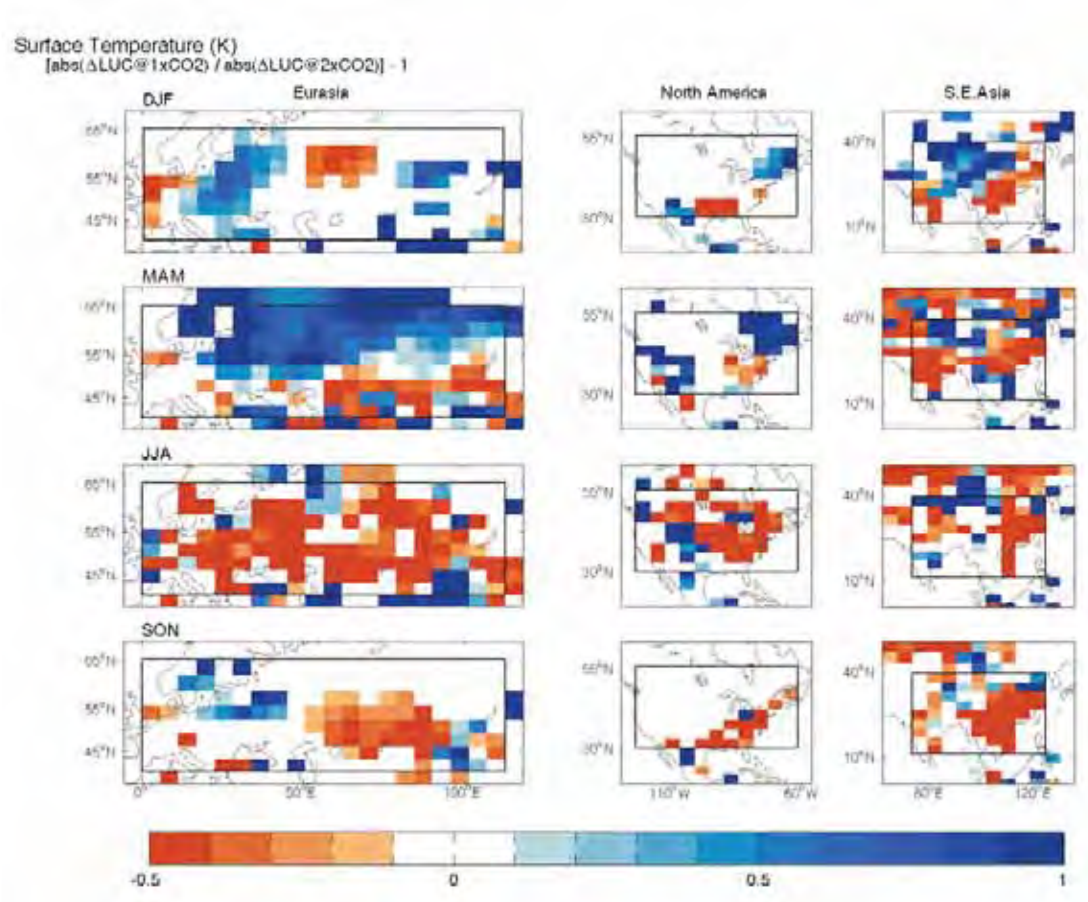

Figure 4-11: The ratio of the absolute change in surface air temperature for each season due to LULCC at 1 x CO_2 to the absolute change at 2 x CO_2. Three regions are shown: Eurasia, North America and South East Asia. A value of 0 is where the changes are identical while -0.5 is where the change at 2 x CO_2 is double the impact at 1 x CO_2. Only points that are statistically significant at a 99% confidence level are shown. Note negative values occur due to the subtraction of 1.0 from the ratio to centre "no change" on zero.

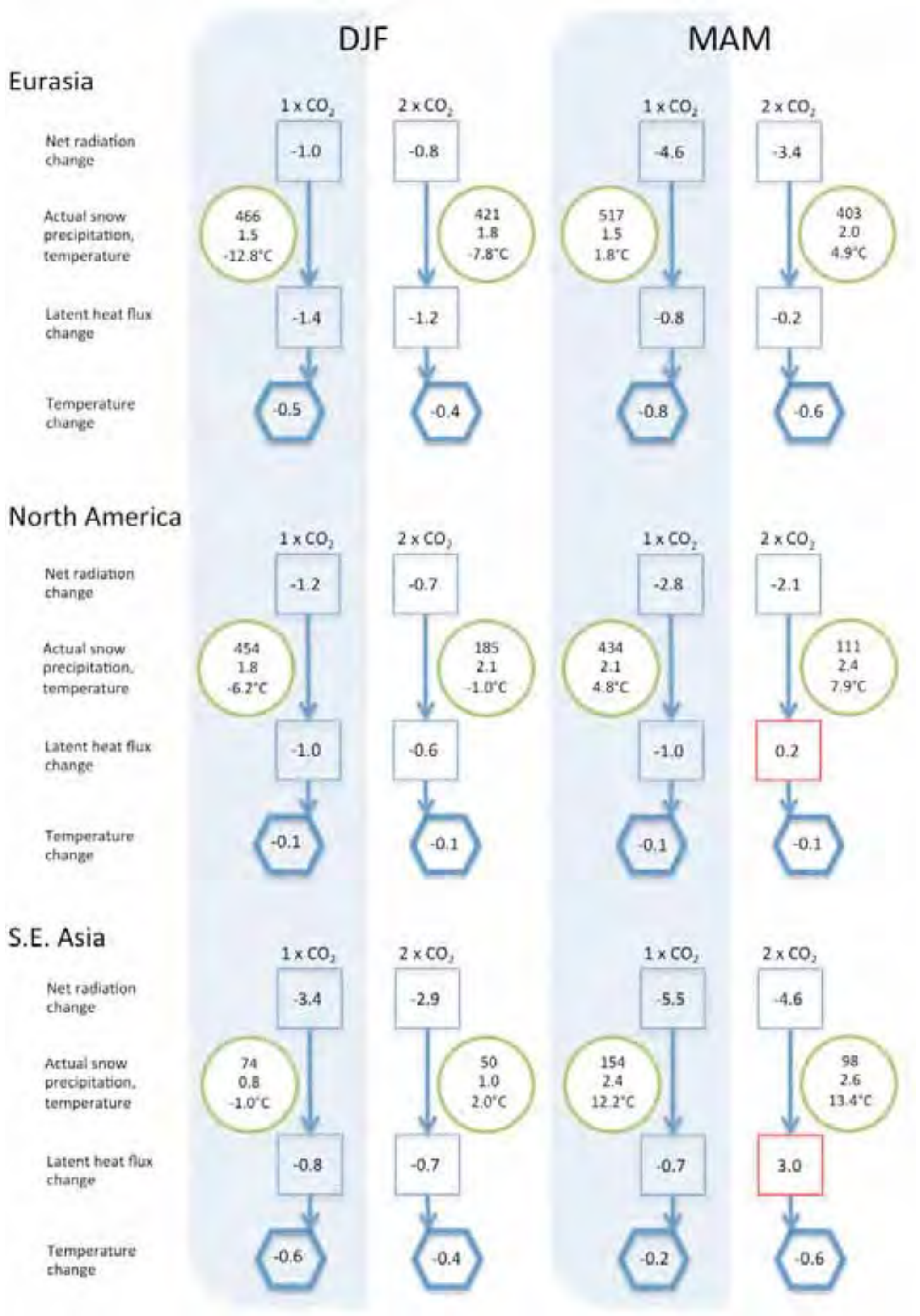

Figure 4-12: How LULCC affects key near-surface and surface variables at 1 x CO_2 and 2 x CO_2: LULCC-induced changes during DJF (left column) and MAM (right column) in Eurasia, North America and S.E. Asia are shown. The mean change in net radiation (W m^{-2}), latent heat flux (W m^{-2}) and temperature (°C) are in boxes. The actual depth of snow (mm of snow), mean climatological precipitation (mm day^{-1}) and mean temperatures (°C) at both 1 x CO_2 and 2 x CO_2 for LULCC simulations are shown in circles. Blue boxes indicate decreases and red boxes indicate increases in each quantity.

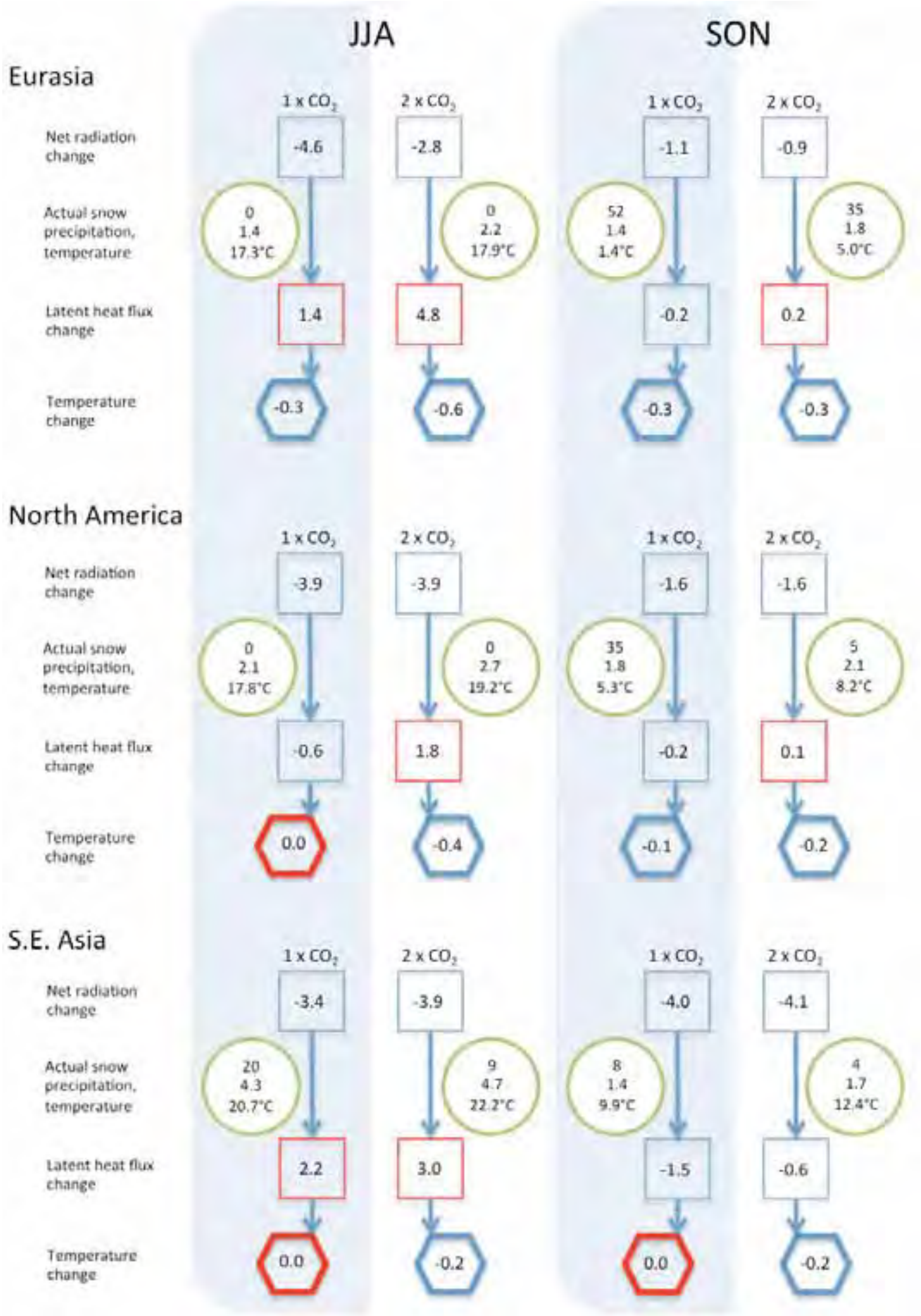

Figure 4-13: As Figure 4-12 but for JJA (left column) and SON (right column).

The succeeding figures show the change due to LULCC at two CO_2 levels for surface air temperature (Figure 4-14), net radiation (Figure 4-15), snow depth (Figure 4-16), precipitation (Figure 4-18), and latent heat flux (Figure 4-19). Except for Figure 4-16, the top four rows of these figures show the changes at 1 x CO_2 (dLCC@280) and are the regional versions of the changes shown in Figures 4-6 to 4-10; the bottom four rows show the changes at 2 x CO_2 (dLCC@560). For the snow depth (Figure 4-16), only the values for MAM are shown because there are no significant changes during the rest of the year (see Figure 4-10). The color scales used for the global and regional maps are identical.

4.3.1 Eurasia

Over Eurasia, dLCC@280 dominates during MAM, and dLCC@560 dominates during JJA. During DJF and SON, the magnitude of changes over most of the region is similar at 1 x CO_2 and at 2 x CO_2 conditions. However, this similarity is not uniform throughout the region as shown by the isolated patches of color in the map for DJF and SON: in some areas, dLCC@280 dominates while dLCC@560 dominates in other areas.

The actual change in the region is shown in Figure 4-14 and summarized as regional averages in Figures 4-12 and 4-13. As shown in Figure 4-14, during MAM, the cooling due to LULCC at 1 x CO_2 (-0.8°C) for most of Eurasia is much larger than that at 2 x CO_2 (-0.6°C). The opposite is true during JJA, where the slight cooling at 1 x CO_2 (-0.3°C) intensifies at 2 x CO_2 (-0.6°C). During DJF, the region of cooling shifts from west and east to the center of the region but the magnitude of the cooling varies only slightly (from -0.5°C to -0.4°C), resulting in the spatial variation shown in Figure 4-11. A similar change can be seen during SON where the slight cooling west of the region (-0.3°C) spreads towards center of the region (-0.3°C).

The substantial reduction in the impact of LULCC on surface air temperature over Eurasia in MAM under 2 x CO_2 relative to 1 x CO_2 (Figure 4-11) is due to a much smaller change in net radiation under 2 x CO_2 (Figure 4-15). The warmer temperatures at 2 x CO_2 (Figure 4-12) result in decreased snow depth (Figure 4-16) and weaken the positive snow-albedo feedback. At 1 x CO_2, LULCC causes cooling across Eurasia of -1.0°C to -2.0°C; this is reduced to -0.6°C to -1.5°C under 2 x CO_2 (Figure 4-14). Over the eastern US, cooling of -0.4°C to -1.0°C at 1 x CO_2 is reduced to -0.2°C to -0.6°C under 2 x CO_2. A similar mechanism occurs for DJF and SON, although during these seasons the difference in net radiation at 1 x CO_2 and 2 x CO_2 is much smaller (Figure 4-12) compared to during MAM.

During JJA, in the absence of snow, the mechanisms that explain the impact of LULCC are fundamentally different and are dominated by changes in precipitation (Figure 4-18) caused by the increase in CO_2. Over Eurasia, LULCC has a larger cooling effect at 2 x CO_2 (Figure 4-14) which attenuates the warming due to the elevated CO_2. This larger cooling is due to a *higher* latent (Figure 4-19) and lower sensible heat flux under 2 x CO_2 despite the change in the nature of the vegetation and the decrease in net radiation (Figure 4-15). This is caused by an increase in summer precipitation from 1.4 mm day^{-1} (1 x CO_2) to 2.2 mm day^{-1} (2 x CO_2) and consequently LULCC is imposed in a less moisture-limited environment. While LULCC in isolation tends to decrease the latent heat flux

[*Pitman et al.*, 2009; *Lawrence and Chase*, 2010] this is counteracted by the CO_2-induced increase in rainfall (Figure 4-18) that enables a higher latent heat flux (Figure 4-19) and therefore stronger cooling (Figures 4-14).

4.3.2 North America

Over North America, the magnitude of the change at 2 x CO_2 dominates during JJA. During the rest of the year, the magnitude of the change at 1 x CO_2 and 2 x CO_2 are similar throughout most of the region although dLCCC@280 dominates small areas during DJF and MAM; and dLCC@560 dominates over small areas during SON.

During JJA, the slight cooling of eastern US and slight warming of western US at 1 x CO_2 (0.0°C) intensifies to a cooling over eastern US and a decreased warming over western US during 2 x CO_2 (-0.4°C). Small and localized changes (-0.2°C to -0.1°C) resulted in localized but differences along the west and east coasts of North America.

While snow-albedo feedback also occurs over North America, and there is substantial snow cover during the non-summer months, there appears to be no widespread significant difference between the magnitudes of the change due to LULCC at 1 x CO_2 and at 2 x CO_2 for snow depth (Figure 4-16), net radiation (Figure 4-15) and surface temperature (Figure 4-14).

During JJA, as with Eurasia, the differences surface temperature between 1 x $C0_2$ and 2 x CO_2 (Figure 4-14) are due to differences in the change in latent heat flux (Figure 4-19) and precipitation (Figure 4-18).

4.3.3 South East Asia

The magnitude of the change at 2 x CO_2 dominates most of South East Asia during MAM, JJA and SON and the tropics during DJF; the change at 1 x CO_2 dominates sub-tropical South East Asia during DJF.

The significant, but spatially varied, changes over South East Asia during 1 x CO_2 actually intensified at 2 x CO_2; with the cool regions (sub-tropics and tropical east) generally becoming cooler and the warm regions (tropical west) becoming warmer. However, these changes vary between seasons. And the complex patterns of changes with opposing signs, despite having large magnitudes, result in small regional averages.

During DJF, cooling which is concentrated on the northwest of the region at 1 x CO_2 (-0.6°C) spreads out towards the south of the region at 2 x CO_2 (-0.4°C). During MAM, the north-south pattern and cooling and warming at 1 x CO2 (-0.2°C) becomes a widespread cooling at 2 x CO_2 (-0.6°C). During JJA and SON, the localized warming in the south and cooling in the north at 1 x CO_2 (0.0°C) intensifies to a warming of the western region and cooling of the eastern region at 2 x CO_2 (-0.2°C).

Snow cover over this region is limited to a few grid points over the high altitude regions of the Tibetan Plateau. It is therefore reasonable to expect that changes in net radiation (Figure 4-15) in this region would be driven by mechanisms other than the snow-albedo feedback.

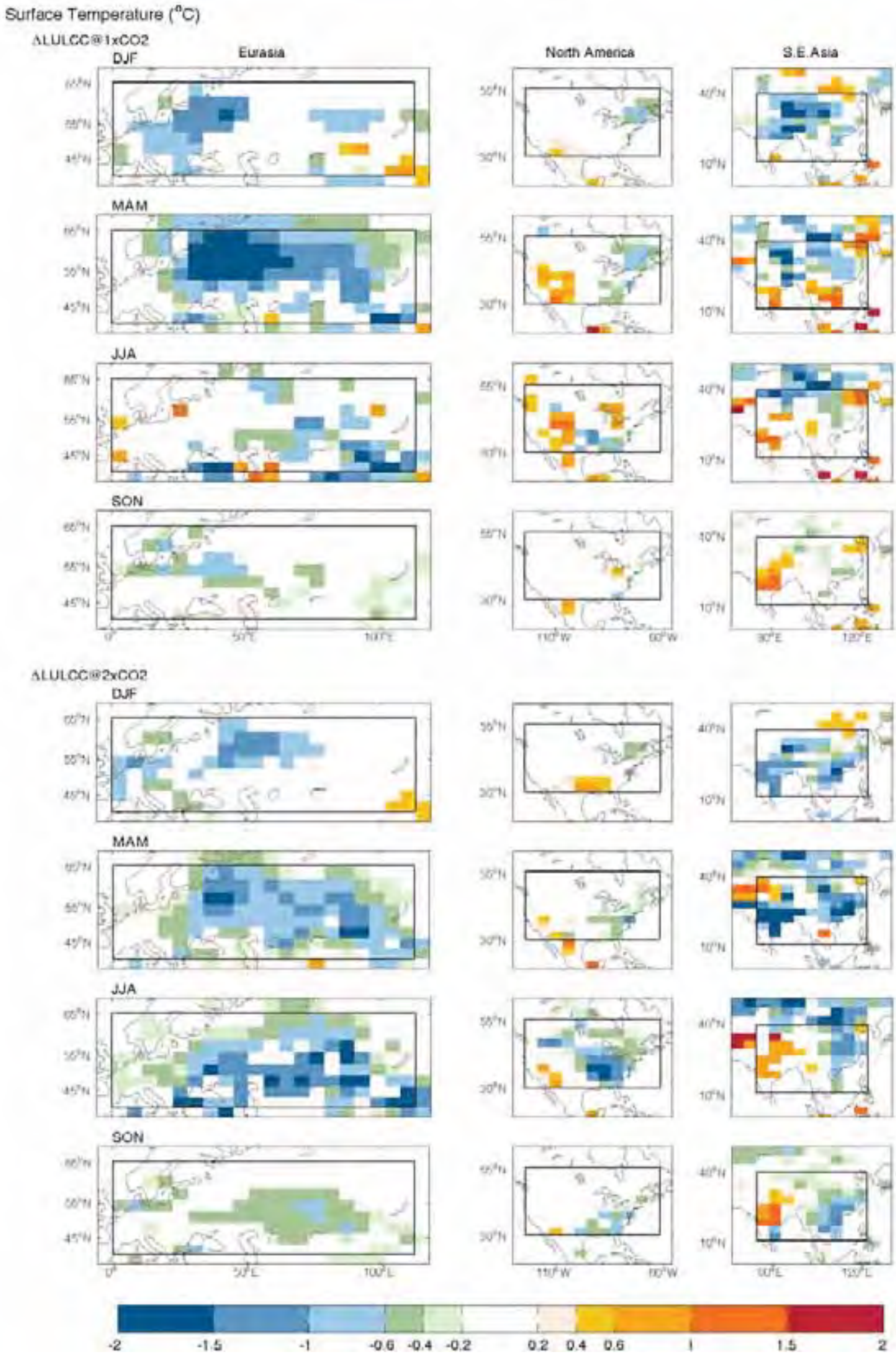

Figure 4-14: Change in surface air temperature (°C) for each season due to LULCC at 1 x CO_2 (top four rows) and 2 x CO_2 (bottom four rows) over Eurasia (left), North America (middle) and South East Asia (right). Only points that are statistically significant at a 99% confidence level using the modified t test are shown.

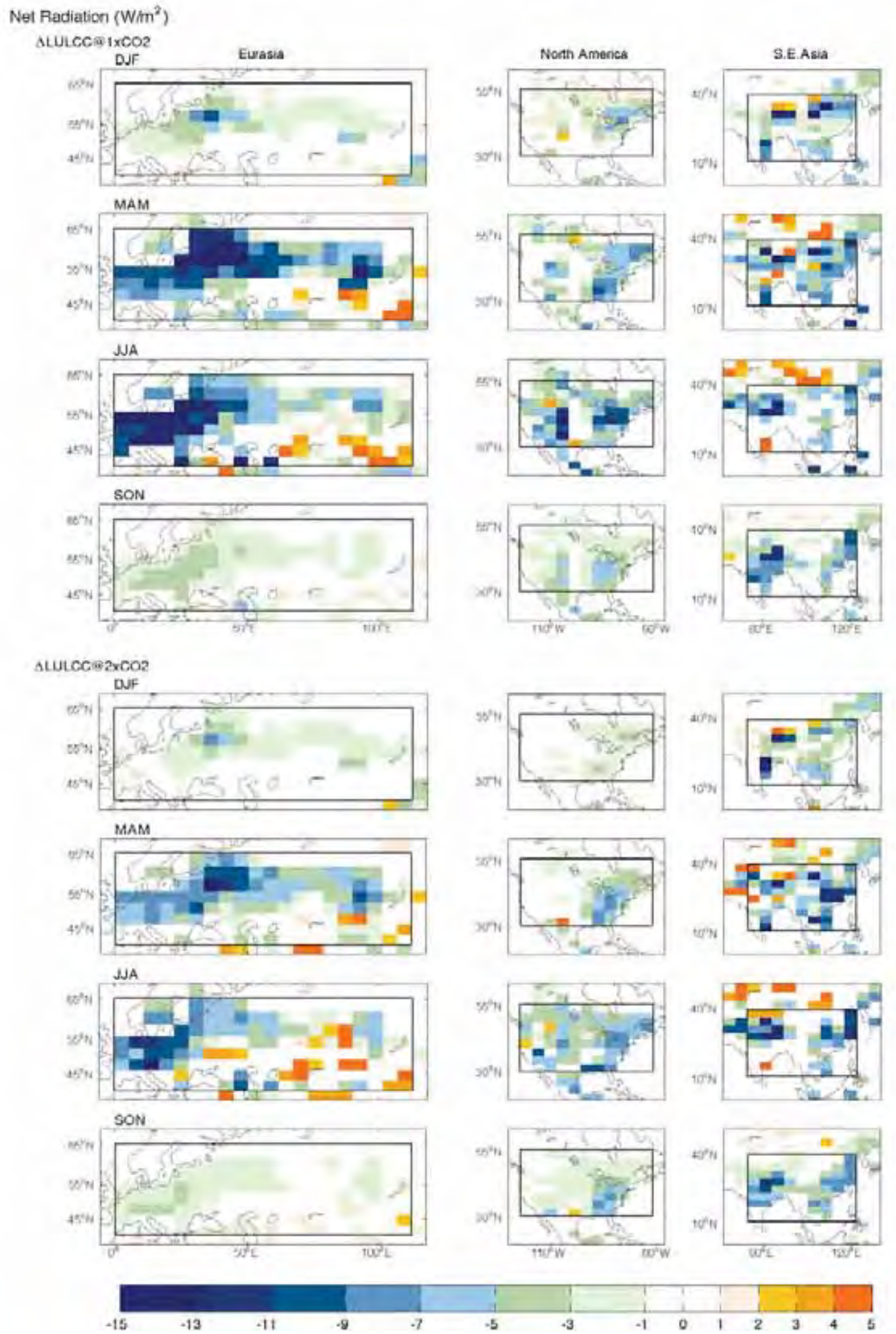

Figure 4-15: As Figure 4-14 but for net radiation (W m⁻²).

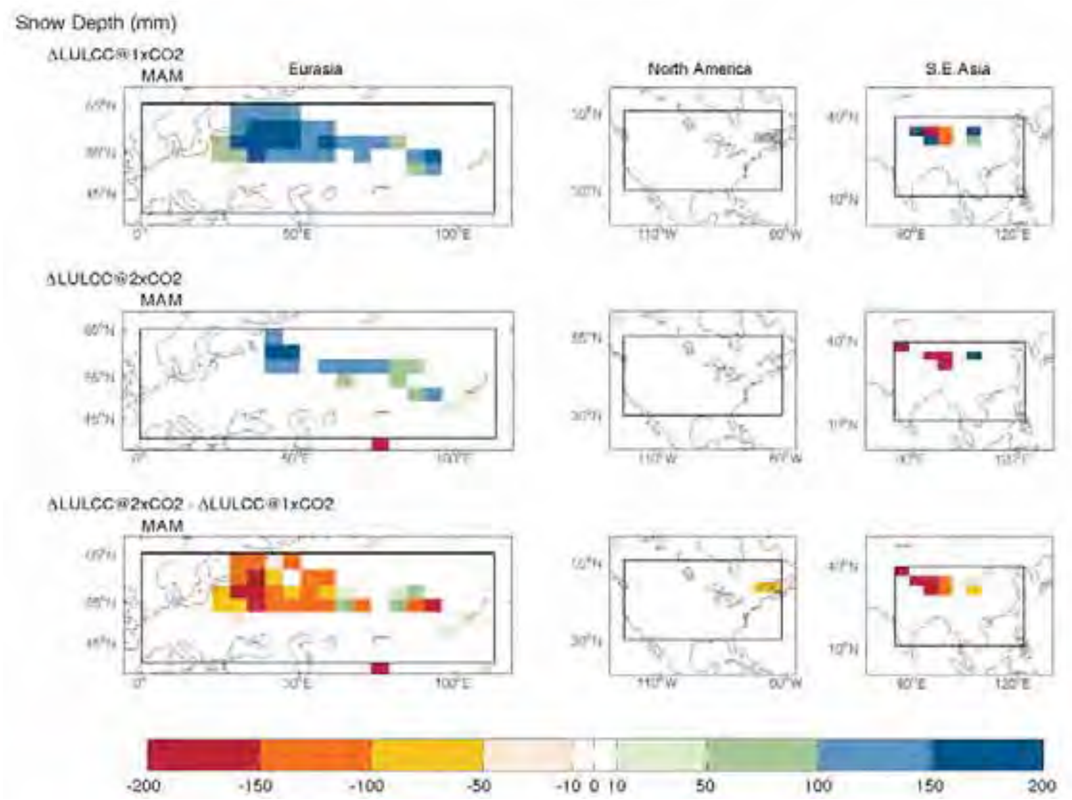

Figure 4-16: Snow depth (mm) in March-April-May for the three regions at (a) 1 x CO_2; (b) 2 x CO_2; and (c) the difference between them (2 x CO_2 minus 1 x CO_2). Only points that are statistically significant at a 99% confidence level using the modified t test are shown.

4.4 Summary

In this chapter the Mk3L-CABLE model was used to simulate 4 LULCC experiments at two CO_2 levels: pre-industrial (1 x CO_2, 280 ppmv) and 2 x CO_2 (560 ppmv). Each experiment either had natural vegetation cover (FOREST, representing potential vegetation) or perturbed vegetation cover (CROP, where forests are converted to cropland based on the year 2000 crop and pasture fraction from the LUH dataset). Sea surface temperatures corresponding to a climate in equilibrium with atmospheric CO_2 concentrations at 280 ppmv and 560 ppmv were prescribed. Monthly output from years 101-300 of a 300-year simulation were used in the analysis which focused on the key variables affected by LULCC: net radiation, surface temperature, latent heat flux, precipitation and snow depth. The impact of LULCC at 280 ppmv was defined as the difference of FOREST1x and CROP1x; the impact of LULCC at 560 ppmv is defined as the difference of FOREST2x and CROP2x; and the impact of doubling CO_2 is defined as the difference between FOREST1x and FOREST2x.

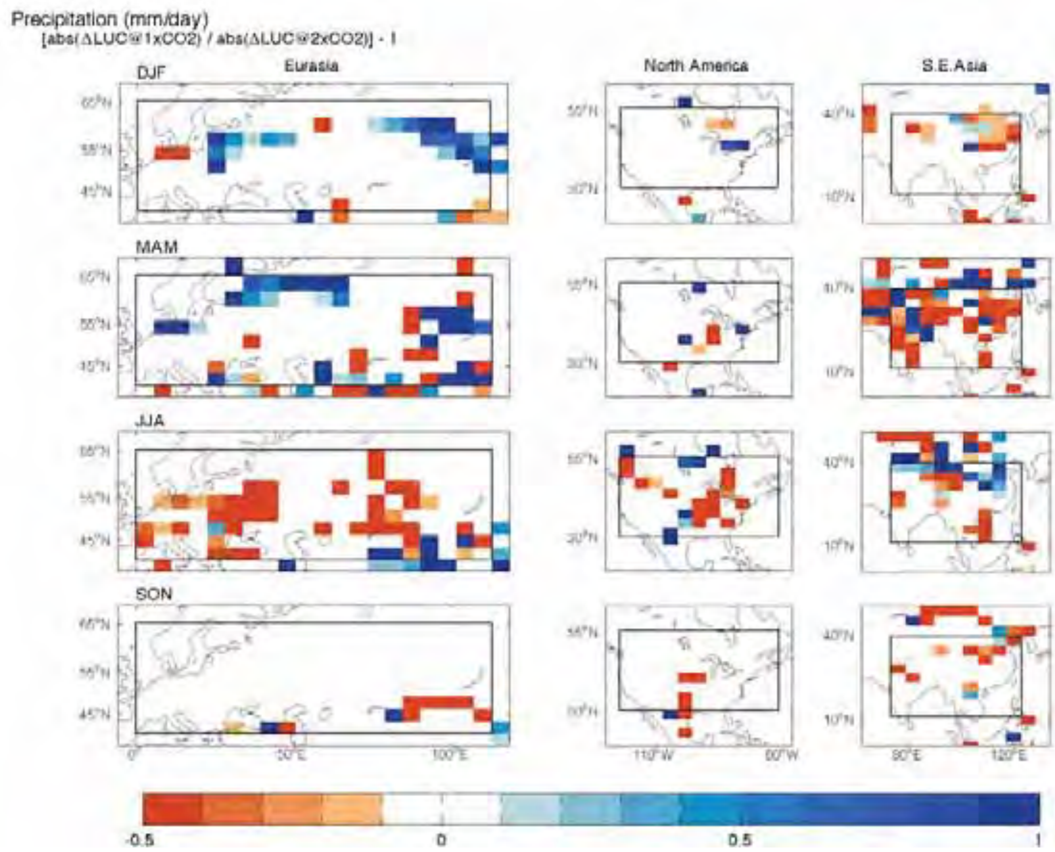

Figure 4-17: As Figure 4-11 but for precipitation (mm day^{-1}).

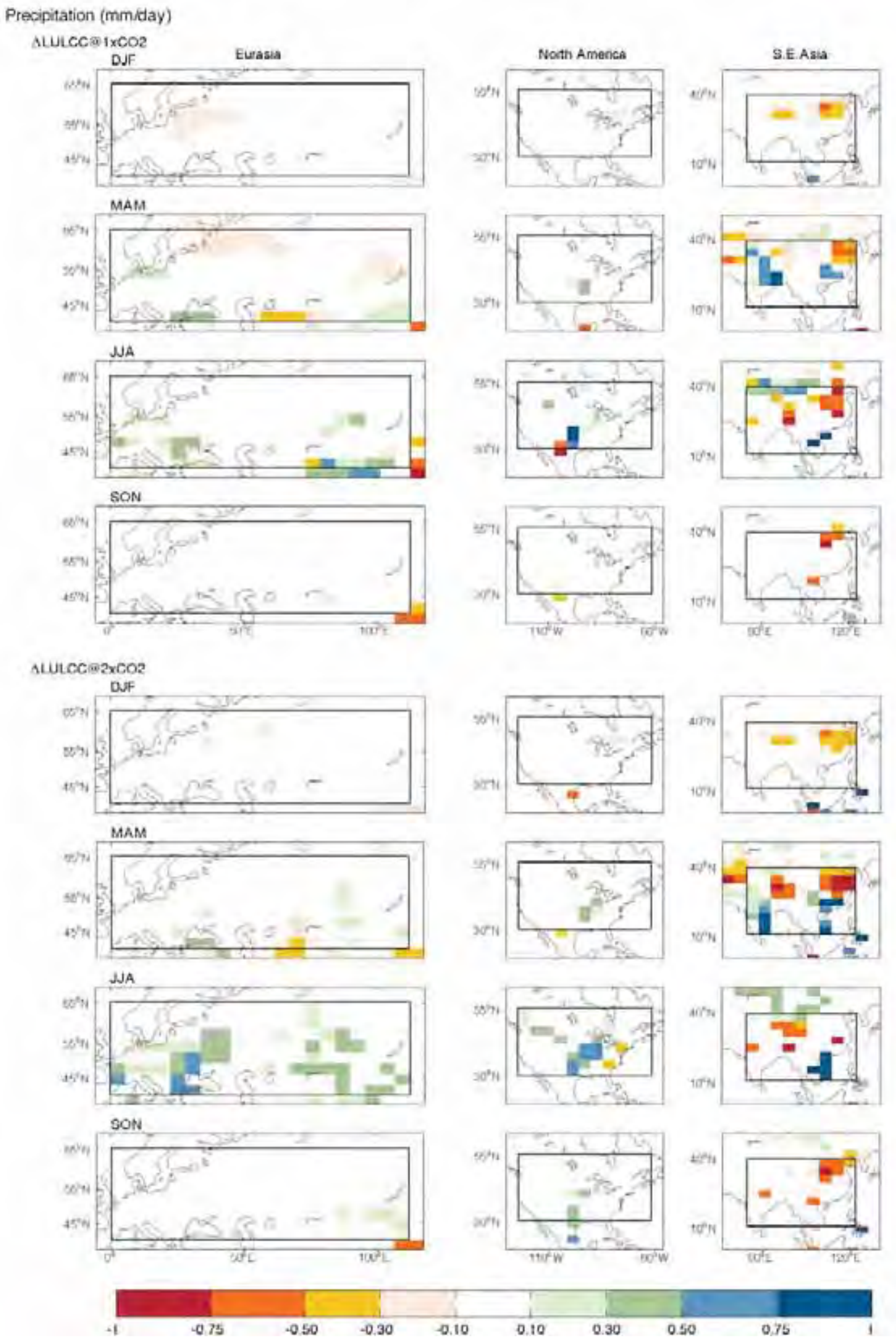

Figure 4-18: As Figure 4-14 but for precipitation (mm day⁻¹).

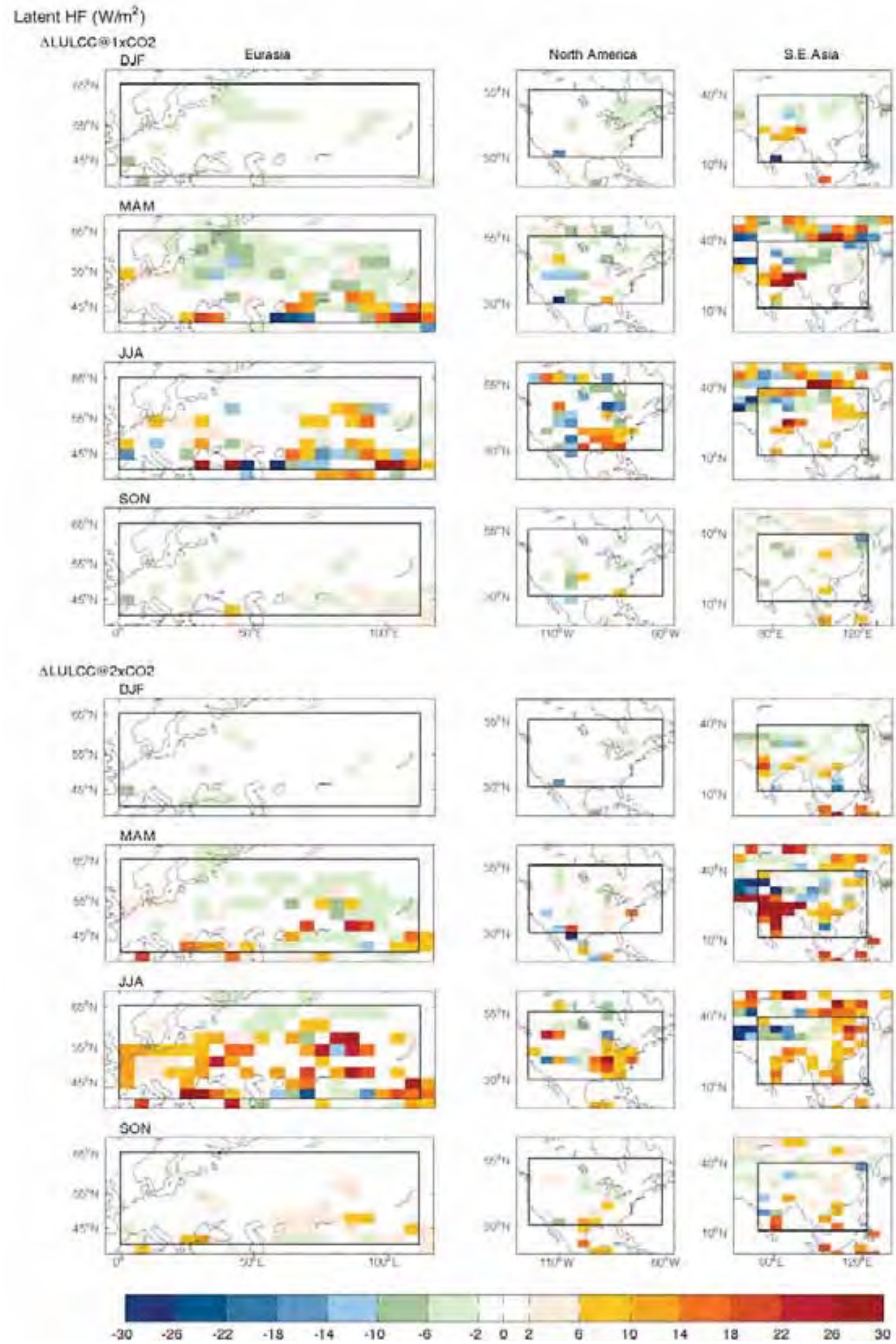

Figure 4-19: As Figure 4-14 but for the latent heat flux (W m^{-2}).

The globally averaged annual time series generally showed small difference between experiments with different vegetation cover, but large difference between experiments at different CO_2 levels for most of the key variables. However, net radiation showed clear difference due to LULCC. Zonal averaging showed small differences due to LULCC and larger difference due to CO_2 for most variables except latent heat flux, which showed large changes due to LULCC over the tropics and sub-tropics. These results motivated a regional focus on areas of intense LULCC (Eurasia, North America and South East Asia) where the monthly mean difference showed large differences due to LULCC throughout the year, with variables showing different seasonal patterns and differences between the impact of LULCC at 280 ppmv and at 560 ppmv are clearly visible. These results, in turn, lead towards two comparisons: 1) between the impacts of LULCC and CO_2, and 2) between the impacts of LULCC at 280 ppmv and at 560 ppmv.

Comparing the impacts of LULCC and CO_2, it is clear that the impact of LULCC is regional-scale while that of CO_2 is global-scale. The impact of LULCC varies with season but is generally more intense during MAM and JJA. LULCC induces cooling in the mid-latitudes and warming in the tropics while CO_2 induces widespread warming.

Comparing the impact of LULCC at different CO_2 levels, it is found that the impact of LULCC varies regionally and seasonally, depending on the CO_2 levels. During MAM, cooling decreases at 2 x CO_2 over Eurasia; over North America, the warming over western US decreases, and cooling of eastern US decrease at 2 x CO_2; cooling increases over northern S.E. Asia; and the warming over southern

Asia switches to cooling at 2 x CO_2. The change during MAM coincides with a decrease in snow depth at 2 x CO_2 with less snow resulting in decreased surface albedo and increased net radiation resulting in increased warming, decreasing the cooling induced by LULCC. During JJA, cooling increases at 2 x CO_2 over Eurasia; over North America, the warming over western US decreases and cooling of eastern US increases at 2 x CO_2; over Asia, the warming over India and cooling over China increases at 2 x CO_2. The change during JJA coincides with a general increase in latent heat flux, which leads to increased precipitation and surface cooling. Despite these changes, regional changes can still appear to be quite small because the averaging over relatively large regions masks the localized cooling and warming within the regions of interest (e.g. over eastern and western US, and over eastern and western Asia).

These results show that:

- Mk3L-CABLE is able to simulate the impact of LULCC similarly to existing literature
- The impact of LULCC is regional compared to the global-scale impact of CO_2
- LULCC warms the tropics and cools the mid-latitudes
- The impact of LULCC varies regionally, seasonally and depends on CO_2 levels
- The difference in the LULCC impact at different CO_2 levels is controlled, in part, by snow depth during MAM and by the latent heat flux during JJA,

with decreasing snow depth inducing decreased cooling and increased latent heat flux associated with increased precipitation increasing surface cooling.

While the results presented in this chapter are useful as they help confirm earlier results with other climate models, they have a more important implication. Since the model is broadly consistent with other simulations of the mean impact of LULCC and since the model simulates the mean climate well (Chapter 3), this provides an opportunity to use the model to explore how LULCC affects climate extremes, as distinct from climate means. This is the subject of Chapter 5.

Chapter 5
Changes in climate extremes

This chapter explores how LULCC, specifically in the form of deforestation, changes the ETCCDI extremes indices. Parts of this chapter, in particular the temperature extremes (Sections 5.3 to 5.5), have been previously published by Avila et al. [2012].

<u>Candidate's contributions to this work</u>

The idea to explore the impacts of LULCC on climate extremes came from extensive discussions between my supervisor and myself. I extended the simulations performed for the previous chapter for another 100 years to output the daily data required to calculate the extremes indices. I undertook the calculation of extremes using software provided by Dr. Lisa Alexander and Dr. Markus Donat, who also provided guidance in the use of the ETCCDI indices and FClimDex software. I chose the detailed methodologies, statistical methods and undertook the first-order analysis of the results. I led the analysis and writing of original Avila et al. [2012] paper, supported by the co-authors. Some of this material has been included in Sections 5.3 to 5.5 but it is significantly revised and expanded from the original paper.

5.1 Introduction

Extreme weather and climate events can cause loss of life, severe damage to the environment, economy and society. As such, climate extremes, together with environmental and human factors that can lead to impacts and disasters are at the core of disaster risk management and climate change adaptation. The adverse impacts of climate extremes are considered disasters when they produce widespread damage and cause severe alterations in the normal functioning of communities and societies [*IPCC*, 2012]. The goal of disaster risk management and climate change adaptation is to minimize risk by minimizing exposure and vulnerability and increasing resilience to the potential adverse impacts of climate extremes [*Pielke and Bravo de Guenni*, 2004; *IPCC*, 2012]. Understanding climate extremes, which could be due to natural variability, anthropogenic climate change or LULCC, and their implication on society and social development is therefore of primary importance.

The impacts of extreme events are usually determined by the exposure and vulnerability of the affected communities [*IPCC*, 2012]. For example, the impact of a tropical cyclone (TC) differs depending on when and where it makes landfall, whether the region of landfall is populated or unpopulated (exposure); whether it is a developed or a developing economy (vulnerability). The characteristics of the climate extreme also affect its impact. How intense is the TC, how long does it last (duration) and how frequent is it? The changes in the intensity, duration and frequency of climate extremes due to LULCC are explored in this chapter. Due to model data availability, analysis will be limited to changes in temperature and precipitation extremes. Changes in tropical cyclones, droughts, floods and other events (e.g. small-scale weather extremes) resulting from LULCC will not be discussed although, at least for cyclones, it is hard to imagine a link between LULCC and their characteristics.

Evidence from observations gathered since 1950 indicate change in some extremes, although confidence depends on the data availability and varies across regions and for different extremes. Relative to the 1961-1990 reference period, there is high to very high confidence in an overall decrease in the number of cold days (TX10p) and nights (TN10p) and an overall increase in the number of warm day (TX90p) and nights (TN90p) at the global scale (i.e. over most land areas with sufficient data) [*IPCC*, 2012]. In many (but not all) regions over the globe with sufficient data, there is a medium confidence that the length or number of warm spells or heat waves has increased [*IPCC*, 2012]. With regards to precipitation, it is likely that more regions have experienced increases than decreases, although there are regional and subregional variations in the trends [*IPCC*, 2012]. Some of these, at least at the global scale, have been attributed to anthropogenic influences. In existing literature, this formal attribution has been made to increases in atmospheric concentrations of greenhouse gases [*IPCC*, 2012].

The aim of this chapter is to address this gap and explore whether LULCC, specifically in the form of deforestation, can cause the changes in the extremes and whether future detection and attribution studies should also account for LULCC. Please note that parts of this chapter, particularly the temperature extremes, have been previously published by Avila et al. [2012].

5.2 Methods

The joint CCl/CLIVAR/JCOMM Expert Team on Climate Change Detection and Indices (ETCCDI) recommended an internationally agreed suite of indices of climate extremes from daily precipitation and temperature data. In order to detect changes in the extremes, the indices were developed to be statistically robust, cover a wide range of climates and have a high signal-to-noise ratio. The internationally agreed indices also allow for comparison of analyses conducted from any part of the world and seamless merging of index data to produce a global picture [*Zhang et al.*, 2011]. A total of 29 indices are defined in Table 3-8 but only 19 indices are used in this study. These indices were chosen because they are applicable across most of the globe and changes in these climate extremes have significant impacts on critical sectors such as water, agriculture and food security, forestry, health and tourism.

Temperature indices, except for those indicating duration, are presented as seasonal extremes. All rainfall indices, except for the maximum 1-day and 5-day precipitation, are presented as annual extremes.

The indices were calculated from 50 years (from simulation years 351 to 400) of daily maximum and minimum temperature and precipitation data from the experiments listed in Table 3-5. For indices that required a threshold for calculation (e.g. TX10p, TN190p, TX90p, TN90p, WSDI, CSDI and R95pT), the FOREST1 experiment is defined as the control simulation. The FClimdex software package was used to calculate the indices (see Section 3.5 for details).

The change due to LULCC is defined as the difference between the FOREST1x and CROP1x experiments (CROP1x – FOREST1x). That is, the difference between natural and perturbed vegetation cover experiments where the equilibrium CO_2 concentrations are kept constant at 280 ppmv. The change due to increased CO_2 is defined as the difference between the FOREST1x and FOREST2x experiments (FOREST2x – FOREST1x) where the CO_2 concentrations are at 280 and 560 ppmv, respectively, and the land cover represents the natural vegetation cover. The differences between the indices of the two experiments with different vegetation covers at 560 ppmv CO_2 levels (CROP2x – FOREST2x) were also analyzed but the results are not shown here.

The results are presented as global bubble maps. This is an efficient way of visualizing the statistical significance, sign and magnitude of changes in the extremes. Colour dots indicate land grid points with statistically significant change at a 95% confidence level using the two-tailed Kolmogorov-Smirnov (KS) test. Grey dots indicate grid points that do not have statistically significant change in extremes. Regions with no LULCC are not shown. Red dots indicate a change towards a warmer or dryer extreme while blue dots indicate a change towards a cooler or wetter extreme. This means that for indices that convey "warm-ness" (TXn TNn, TXx, TNX, DTR, GSL, WSDI, TX90p and TN90p) or "dry-ness" (R95pT and CDD), red dots indicate an increased index value (i.e. more warm, more dry) and blue dots indicate decreases (less warm, less dry). The opposite is true for indices that convey "cold-ness" (CSDI, TX10p and TN10p) and "wet-ness" (RX1day, RX5day, SDII, CWD, R10mm) where the red dots indicate decreased index value (less warm, less dry) and blue dots indicate increased index value (more cold, more wet).

The sizes of the dots indicate the magnitude of change with the range of values indicated by the figure legend. The legends indicate the lower bound of the range being represented by the dot of that particular size (e.g. for Figure 5-1, 0.2 represents changes ranging from 0.2 to 1.99°C; 2=2.0 to 3.99°C; 4=4.0 to 11.99°C and 12 represents values equal to or greater than 12°C). Values less than the smallest value in the range are considered too small and are then indicated by grey dots.

The maps of the changes due to LULCC are shown in the left column while those due to CO_2 are shown on the right. The potential impacts of increased CO_2 on the extreme indices have been well reported in the literature for both historical [e.g. *Kiktev et al.*, 2003; *Kiktev et al.*, 2007; *Christidis et al.*, 2011] and for the future [e.g. *Tebaldi et al.*, 2006; *Kharin et al.*, 2007; *Meehl et al.*, 2007; *Sillmann and Roeckner*, 2008; *Alexander and Arblaster*, 2009; *Russo and Sterl*, 2011]. Models have also been extensively used to project substantial warming in temperature extremes by the end of the 21st century, as well a likely increase in the frequency of heavy precipitation or the proportion of total rainfall from heavy rainfall events over many areas of the globe [*IPCC*, 2012].

It should be emphasized that the changes in the extremes due to CO_2 displayed in this thesis were conducted at equilibrium conditions (i.e. CO_2 concentration were maintained at 280 ppm and 560 ppm and not allowed to increase in time as in a real-world scenario). Results are therefore provided only as a point of comparison for the change in LULCC and are not comparable to the changes due to CO_2 from observations and simulations where the atmospheric CO_2 varies in time.

For indices with seasonal values, changes during December-January-February (DJF), March-April-May (MAM), June-July-August (JJA) and September-October-November (SON) are shown in four rows, from top to bottom; while annual indices are shown in a single row, often with other annual indices (e.g. Figure 5-6).

The aim of this chapter is to identify those indices strongly affected by LULCC and those near-continental scale regions where the temperature impact of LULCC is either of the same sign as the impact of increased CO_2, or alternatively acts to mitigate the effect of increased CO_2. To avoid any impression that temperature indices are always affected by LULCC, maps of indices that are negligibly perturbed are also presented.

5.3 Impact of LULCC on temperature intensity extremes

The impact of LULCC and CO_2 doubling on the coldest daily maximum temperature (TXn) is shown in Figure 5-1. While land areas most commonly show statistically significant warming in TXn in all seasons due to doubling CO_2 (Figure 5-1b), and increases reach 12°C in the northern high latitudes in DJF, the impact of LULCC is very small (although locally statistically significant) and most commonly causes cooling of up to 2°C (Figure 5-1a). This cooling in TXn is geographically isolated. The magnitude of changes due to LULCC is almost always small in comparison to CO_2.

The results for the coldest daily minimum temperature (TNn, Figure 5-2) are similar to those for TXn. In DJF and MAM, LULCC induces cooling in TNn of up to 4°C over parts of Eurasia (Figure 5-2a) but elsewhere, where significant changes occur they are almost always limited to 2°C. These are almost always substantially smaller than the impact of 2 x CO_2 on TNn (Figure 5-2b) but tend to counter 2 x CO_2 changes. An interesting increase in TNn occurs in SON over Asia (1-2°C) that is additive to the increase due to 2 x CO_2.

In many regions, LULCC causes changes in the hottest daily maximum temperature (TXx) by up to 4°C (Figure 5-3a). TXx increases by 2-4°C in the tropics and sub-tropics in most seasons and by up to 2°C in the mid- and high-latitudes of the northern hemisphere in JJA. TXx cools due to LULCC by up to 2°C in the mid-latitudes of the northern hemisphere in MAM. It is therefore highly geographically specific whether these changes add to, or counter, changes due to 2 x CO_2 (Figure 5-3b).

In contrast to TXn and TNn, there are some regions where the magnitude of the impact of LULCC on TXx is of a similar magnitude to warming due to 2 x CO_2. However, note that the impact of 2 x CO_2 on TXx is to cool the northern hemisphere mid-latitudes (MAM, JJA and SON). This is associated with a large intensification of the hydrological cycle in the climate model. This tends to increase rainfall, and thereby soil moisture and transpiration [*Seneviratne et al.*, 2010], increasing the probability of evaporative cooling on very hot days.

The general increase in TXx due to LULCC in seasons and regions with large radiation inputs is expected since the aerodynamically smoother surface post deforestation suppresses turbulent energy exchange which tends to warm the surface while the replacement of deeply rooted vegetation with shallow grasses and crops tends to limit evaporative cooling as moisture becomes limited [*Teuling et al.*, 2010].

In contrast, a reduction in TXx over mid- and high latitudes coincident with snow cover is also anticipated since snow will mask crops more efficiently than trees leading to winter cooling [*Betts*, 2000]. As LULCC affects temperatures mainly in terms of albedo and the partitioning of available energy, a large impact on the hottest daily minimum temperature (TNx) would not be anticipated. Indeed, the impact of LULCC on TNx is limited to ~1°C (Figure 5-4a) and is negligible compared to 2 x CO_2 (Figure 5-4b).

The diurnal temperature range (DTR, Figure 5-5) is strongly reduced (commonly by 2-4°C but up to 12°C in JJA) by 2 x CO_2 over most continental areas, and is increased in the tropics in most seasons which is consistent with *Vose et al.* [2005]. LULCC provides a more complex pattern of changes in DTR. LULCC tends to increase DTR over the northern mid- and high-latitudes in DJF and JJA, although mainly by less than 1°C, partially mitigating decreases due to 2 x CO_2. In the tropics and sub-tropics, LULCC tends to increase DTR in all seasons; this is the same direction and magnitude of change as caused by 2 x CO_2. This is particularly clear in all seasons over South America where increases in DTR due to LULCC are of the same magnitude as increases due to 2 x CO_2 suggesting that large-scale LULCC complicates efforts to use DTR in studies of global warming and needs to be taken into account in regions of intense landscape modification.

5.4 Impact of LULCC on temperature duration extremes

The growing season length (GSL, Figure 5-6a) is weakly affected by LULCC. GSL is locally reduced mainly by ~1-5 days per year by LULCC but is increased by a much larger amount (10-50 days per year) by 2 x CO_2. A relatively large increase in GSL (10 days per year) over China is shown in Figure 5-7a due to LULCC, amplifying the impact of 2 x CO_2 in this region.

LULCC tends to increase both the cold spell durations (the number of days with at least 6 consecutive days when the minimum temperature is below the 10^{th} percentile, CSDI, Figure 5-6b) and warm spell durations (the number of days with at least 6 consecutive days when the maximum temperature is above the 90^{th} percentile, WSDI, Figure 5-6c). There are quite large regions where the increase in CSDI exceeds 8 days, which is similar in magnitude to 2 x CO_2. However, while 2 x CO_2 systematically decreases CSDI, LULCC increases this measure thereby tending to mask the impact of 2 x CO_2. This contrasts with WSDI (Figure 5-6c) where the impact of LULCC is additive, and in many regions of similar magnitude, to the impact of 2 x CO_2. This leads to a complexity in the use of these indices with LULCC sometimes countering the CO_2 induced changes (CSDI) and sometimes adding to the CO_2 induced changes (WSDI).

5.5 Impact of LULCC on temperature frequency extremes

The impact of LULCC on the frequencies of the percentile-based temperature extremes is shown in Figures 5-7 to 5-10. Note that the percentiles calculated for FOREST1x are used as the threshold values when calculating these indices.

The impact of LULCC on the number of days when the maximum daily temperature is below the 10^{th} percentile (cool days, TX10p) shows a complex pattern of decreases (more than 10 days per season) principally in the tropics and sub-tropics particularly in DJF, JJA and SON (Figure 5-7a) but increases (mainly up to 50 days per season) in Asia (DJF), over large areas of the northern hemisphere (MAM) and over smaller areas of the northern hemisphere (JJA). The decreases in TX10p over tropical South America are particularly consistent in all seasons. The impact from 2 x CO_2 (Figure 5-7b) show increases in JJA over the northern hemisphere mid-latitudes (mainly 10-50 days per season) but the dominant impacts are decreases over most continental surfaces in all seasons.

Figure 5-8 shows the number of days when the minimum daily temperature is below the 10^{th} percentile (cool nights, TN10p). The results for TN10p (Figure 5-8a) differ from TX10p (Figure 5-7a), including the important difference that TN10p does not change consistently over South America. In general, LULCC has a regionally statistically significant impact on TN10p, and this impact is mostly increasing this measure of extremes. This is particularly apparent in the mid- and high-latitudes of Eurasia in DJF and MAM where LULCC counters the impacts of 2 x CO_2. Elsewhere, relative to the impact of 2 x CO_2, the impacts on TN10p are variable but are similar in magnitude to 2 x CO_2 in some major regions.

LULCC affects the number of days when the maximum temperature exceeds the 90^{th} percentile (warm days, TX90p) mostly by more than 10 days per season (Figure 5-9a). The largest and most coherent changes in TX90p occur over the tropics and sub tropics where in all seasons TX90p increases by up to 50 days per season. This is smaller than the impact of 2 x CO_2 (Figure 5-9b) but is likely additive to the increases from 2 x CO_2. In the mid- and high-latitudes of the northern hemisphere, LULCC tends to decrease TX90p, particularly in DJF (over Eurasia) and MAM (Eurasia and eastern US) by at least 10 days per season. These decreases are of an opposite sign and of a smaller magnitude to the impacts of 2 x CO_2.

The result for the number of days when minimum temperatures exceed the 90th percentile (warm nights TN90p, Figure 5-10) is smaller in terms of geographic area than shown for TX90p. While TN90p tends to increase through the tropics due to LULCC (Figure 5-10a) and cool in the mid- and high-latitudes of the northern hemisphere (particularly in DJF, MAM and JJA) the magnitude of these changes is consistently small compared to the impacts of 2 x CO_2.

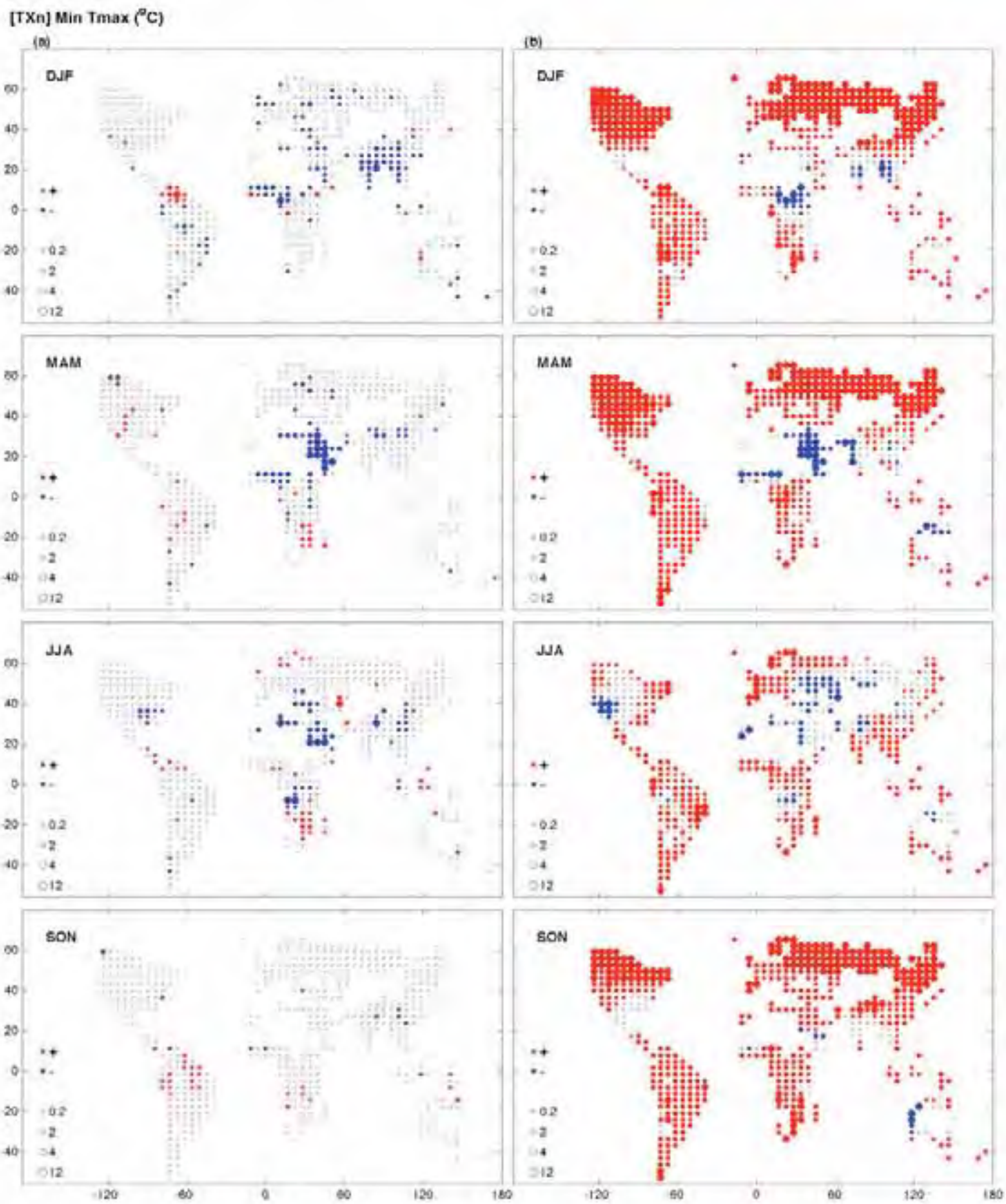

Figure 5-1: Difference between the 50-year mean of (a) CROP1x and FOREST1x and (b) FOREST2x and FOREST1x for the coldest seasonal daily maximum temperature, TXn (°C) during DJF (top row), MAM (second row from the top), JJA (third row, from the top) and SON (bottom row) (figure 2 of Avila et al., 2012).

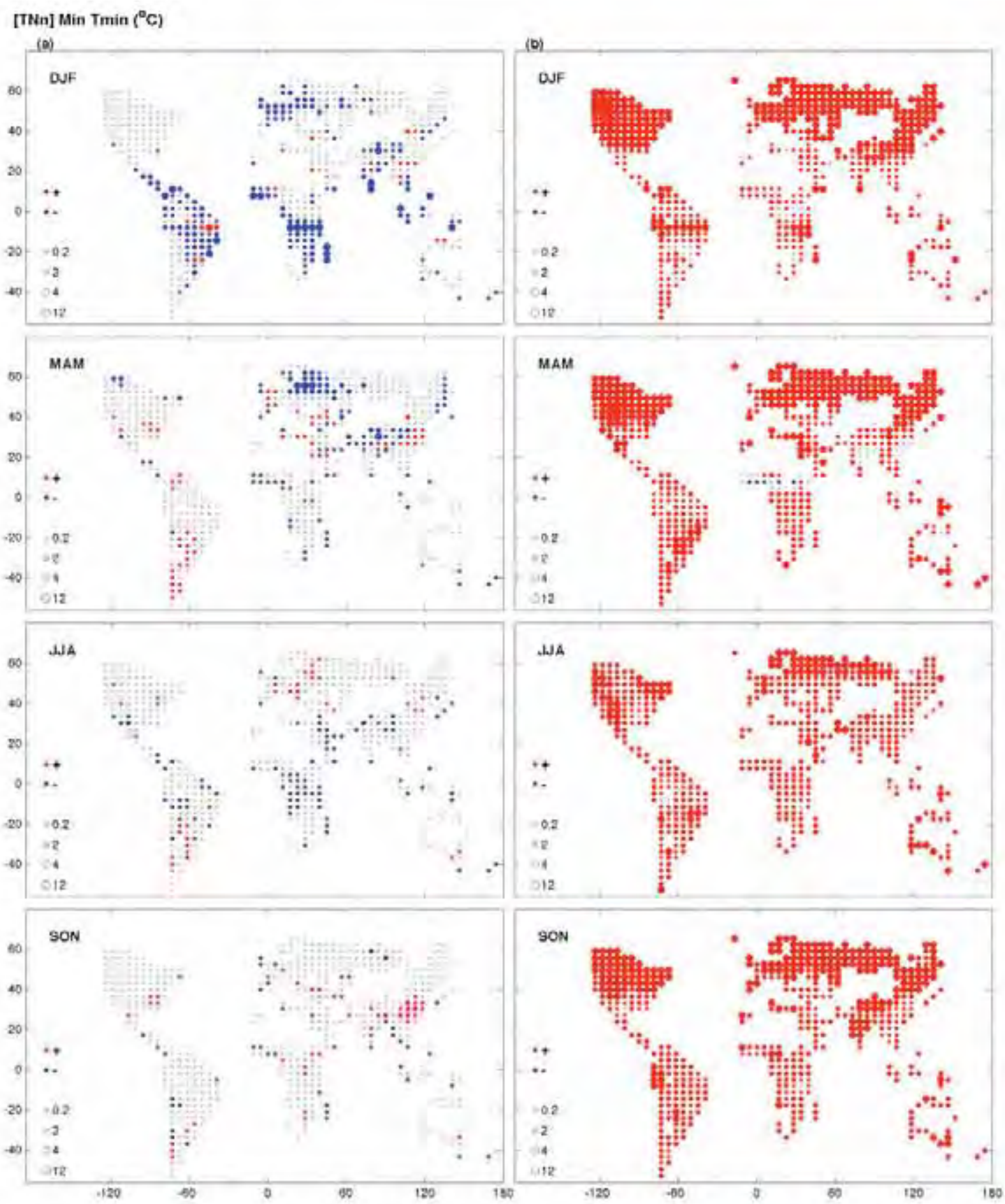

Figure 5-2: As Figure 5-1 but for the coldest seasonal minimum daily temperature, TNn (°C) (figure 3 of Avila et al., 2012).

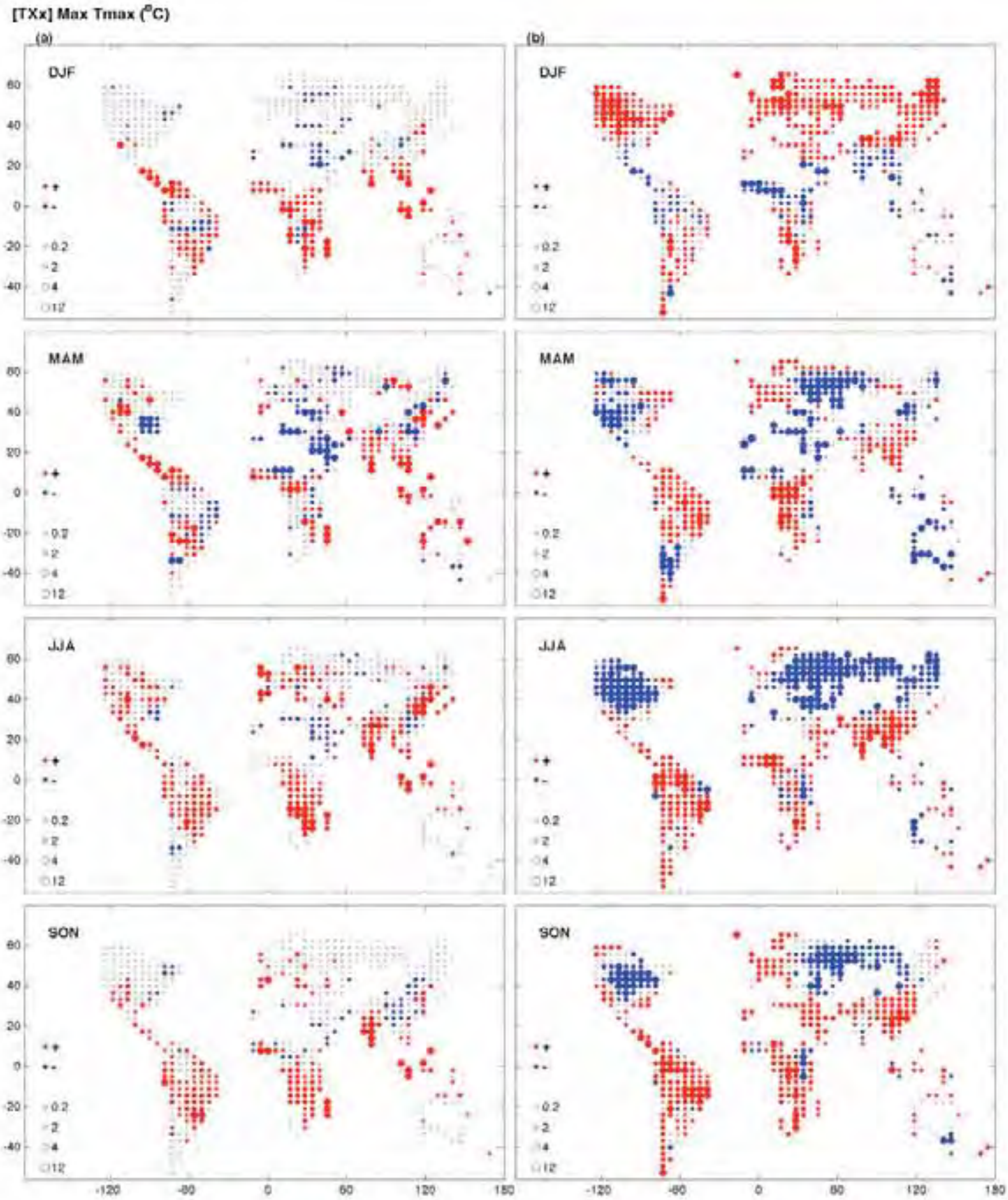

Figure 5-3: As Figure 5-2 but for the warmest seasonal maximum daily temperature, TXx (°C) (figure 4 of Avila et al., 2012).

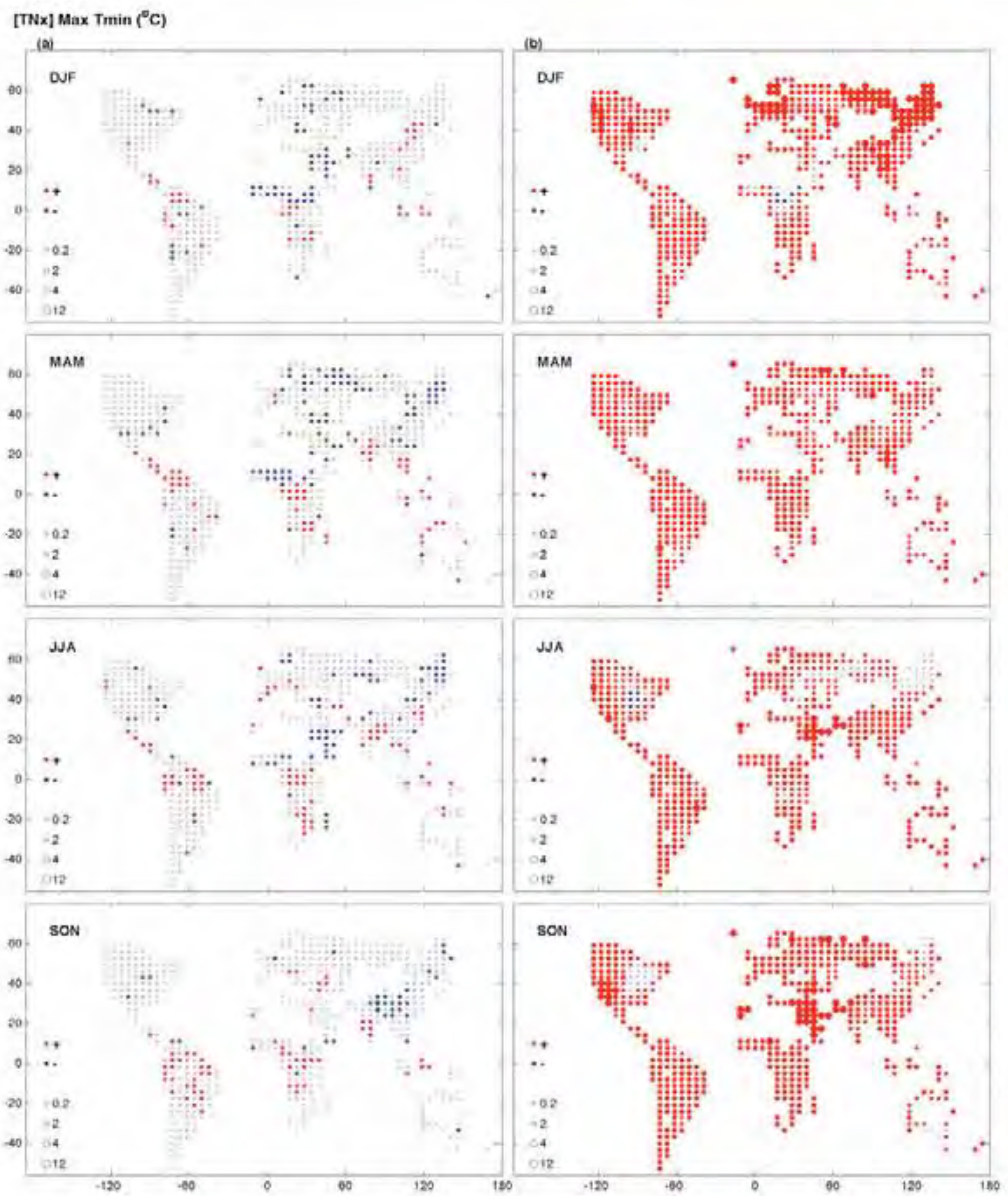

Figure 5-4: As Figure 5-1 but for the warmest seasonal maximum daily temperature, TNx (°C) (figure 5 of Avila et al., 2012).

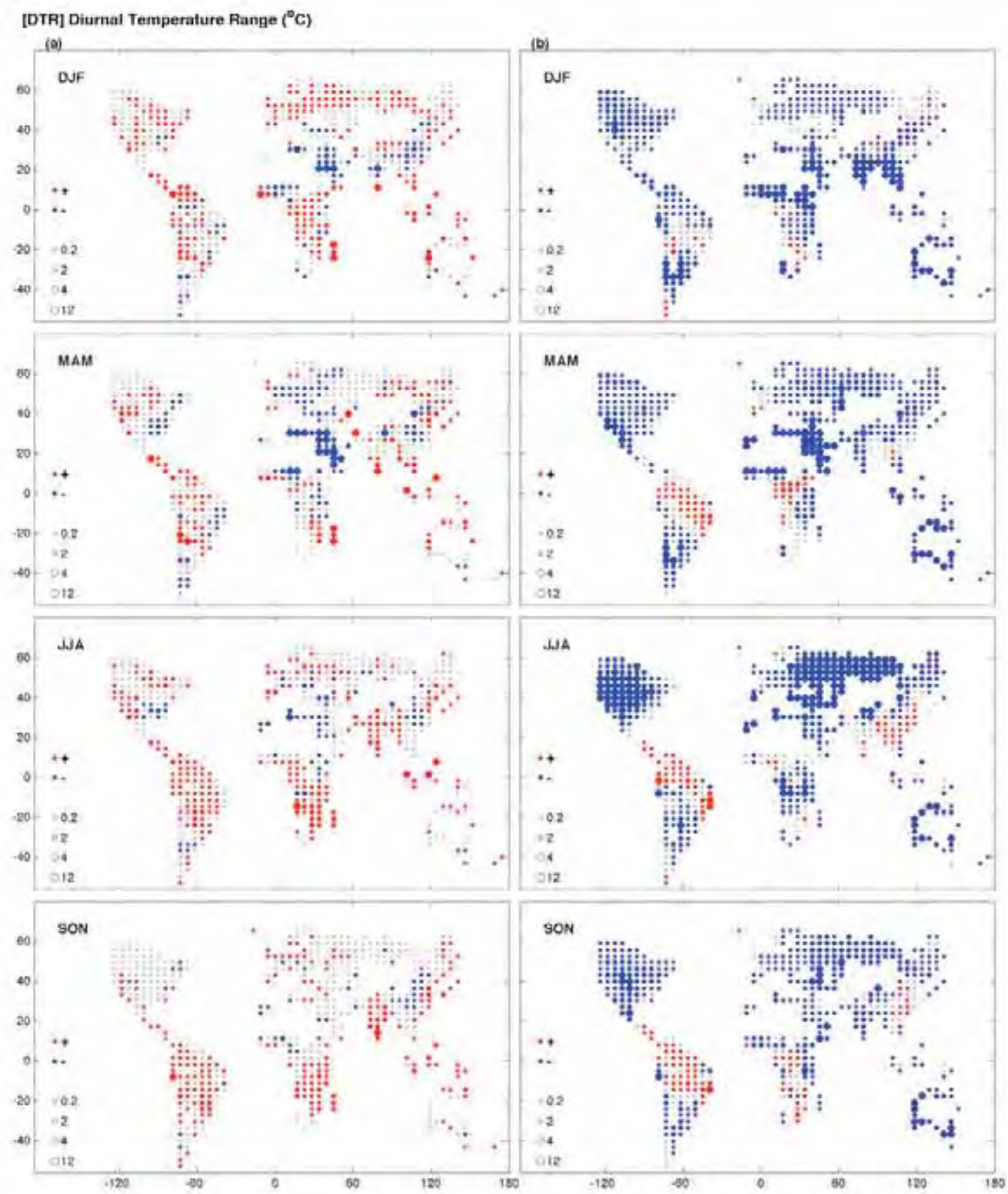

Figure 5-5: As Figure 5-1 but for the diurnal temperature range, DTR (°C) (figure 6 of Avila et al., 2012).

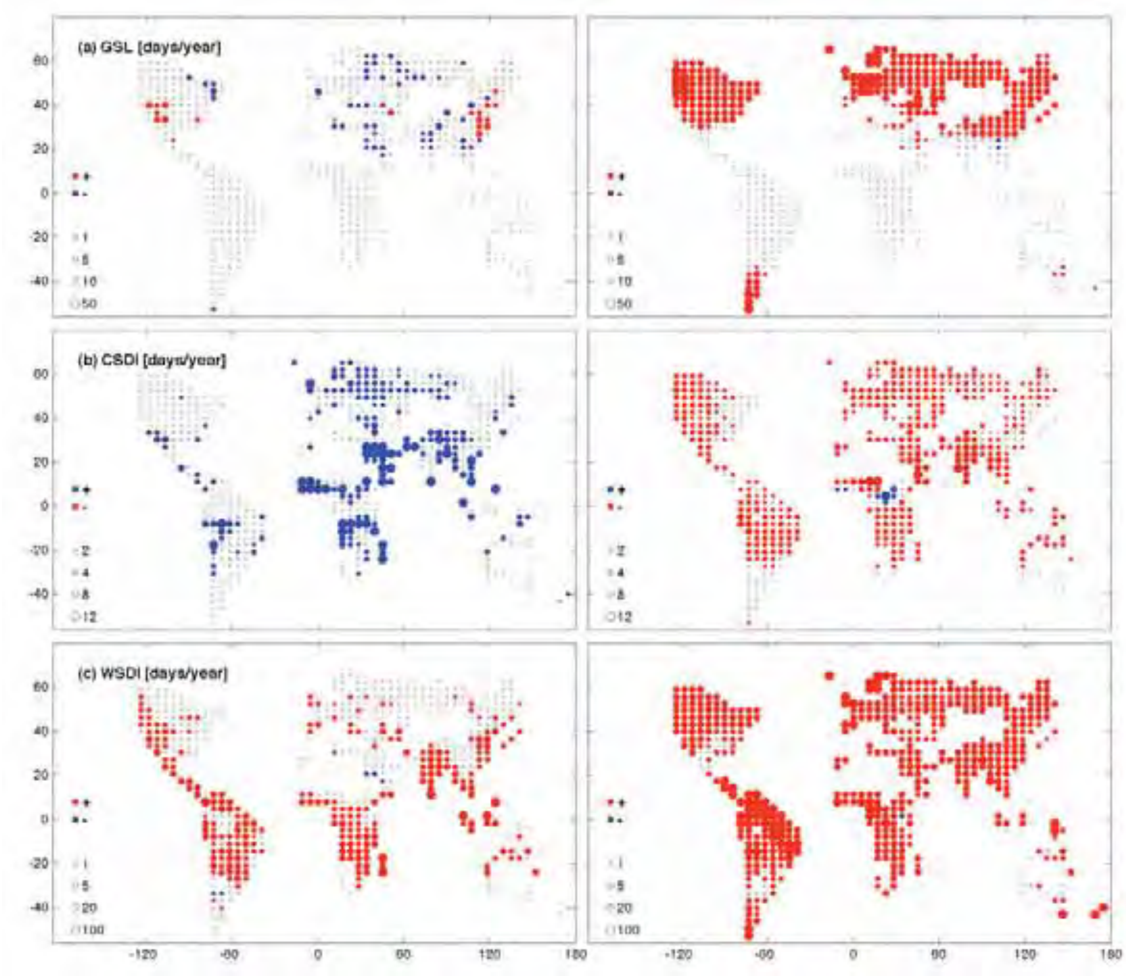

Figure 5-6: As Figure 5-1 but for (a) growing season length, GSL; (b) cold spell duration, CSDI; and (c) warm spell duration, WSDI (all in days per year). Note that blue represents an increase in CSDI and a decrease in GSL and WSDI (figure 7 of Avila et al., 2012).

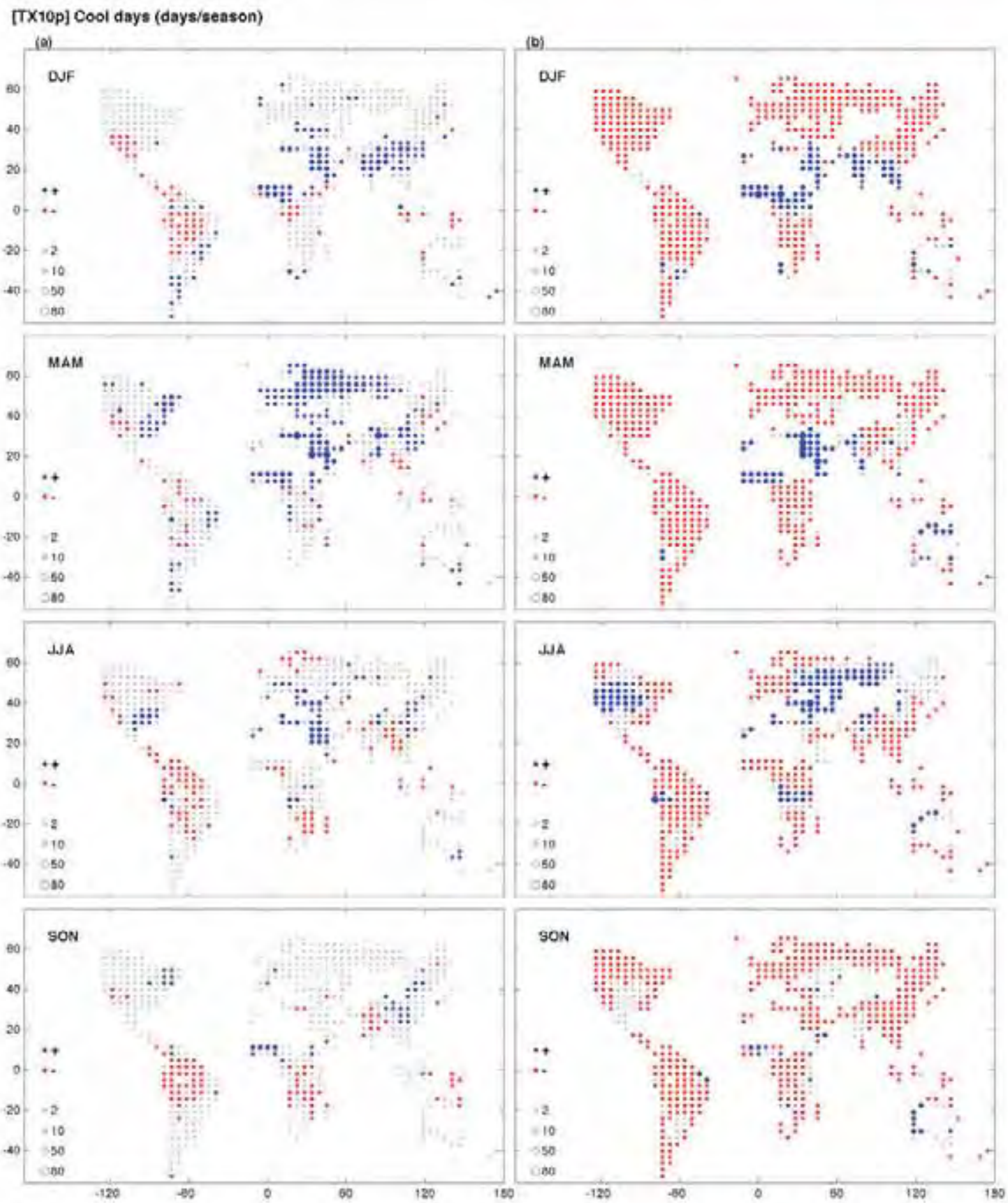

Figure 5-7: As Figure 5-1 but for the number of cool days, TX10p (days per season). Note that blue represents an increase in the number of cool days (figure 8 of Avila et al., 2012).

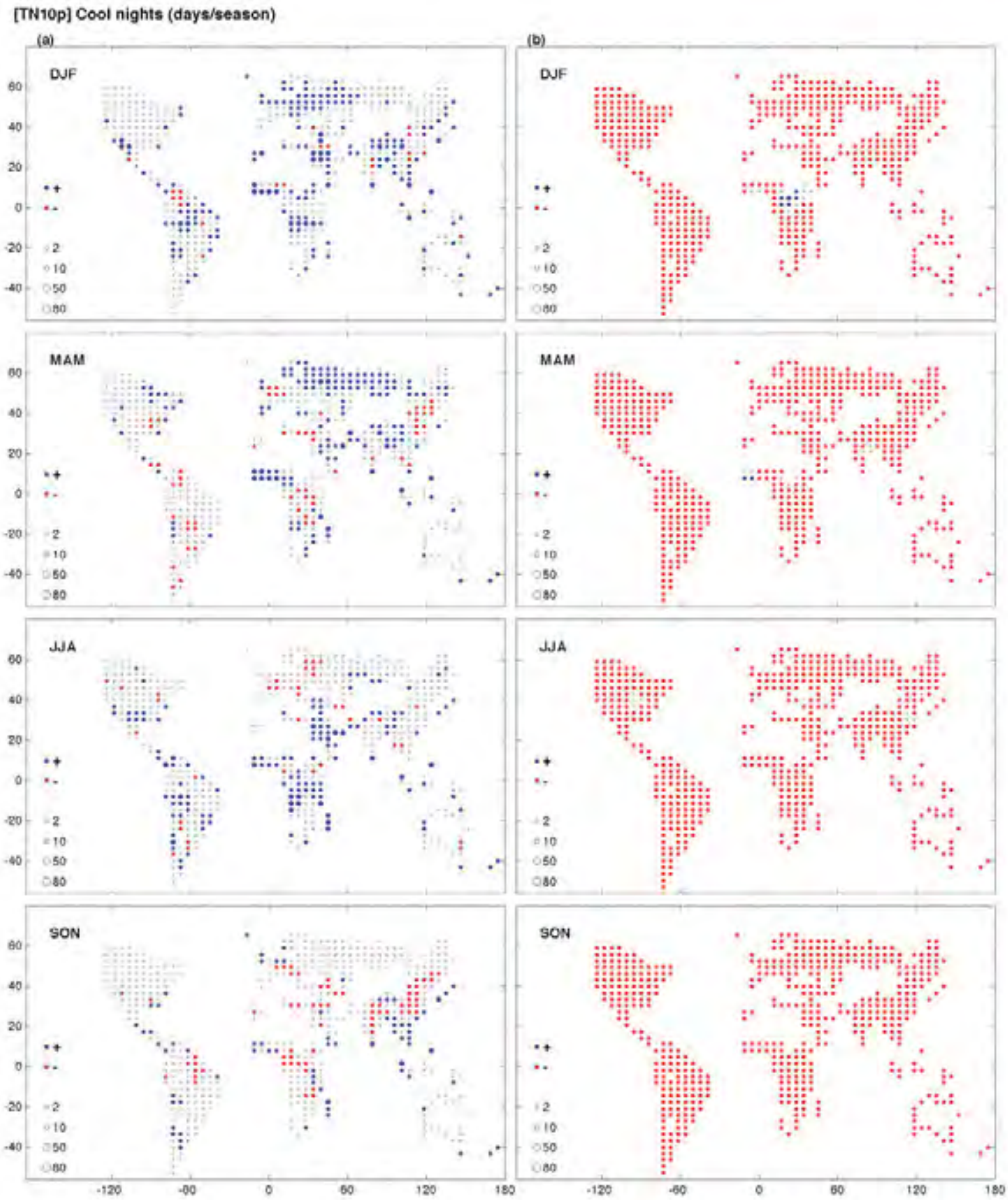

Figure 5-8: As Figure 5-1 but for the number cool nights, TN10p (days per season). Note that blue represents an increase in the number of cool nights (figure 9 of Avila et al., 2012).

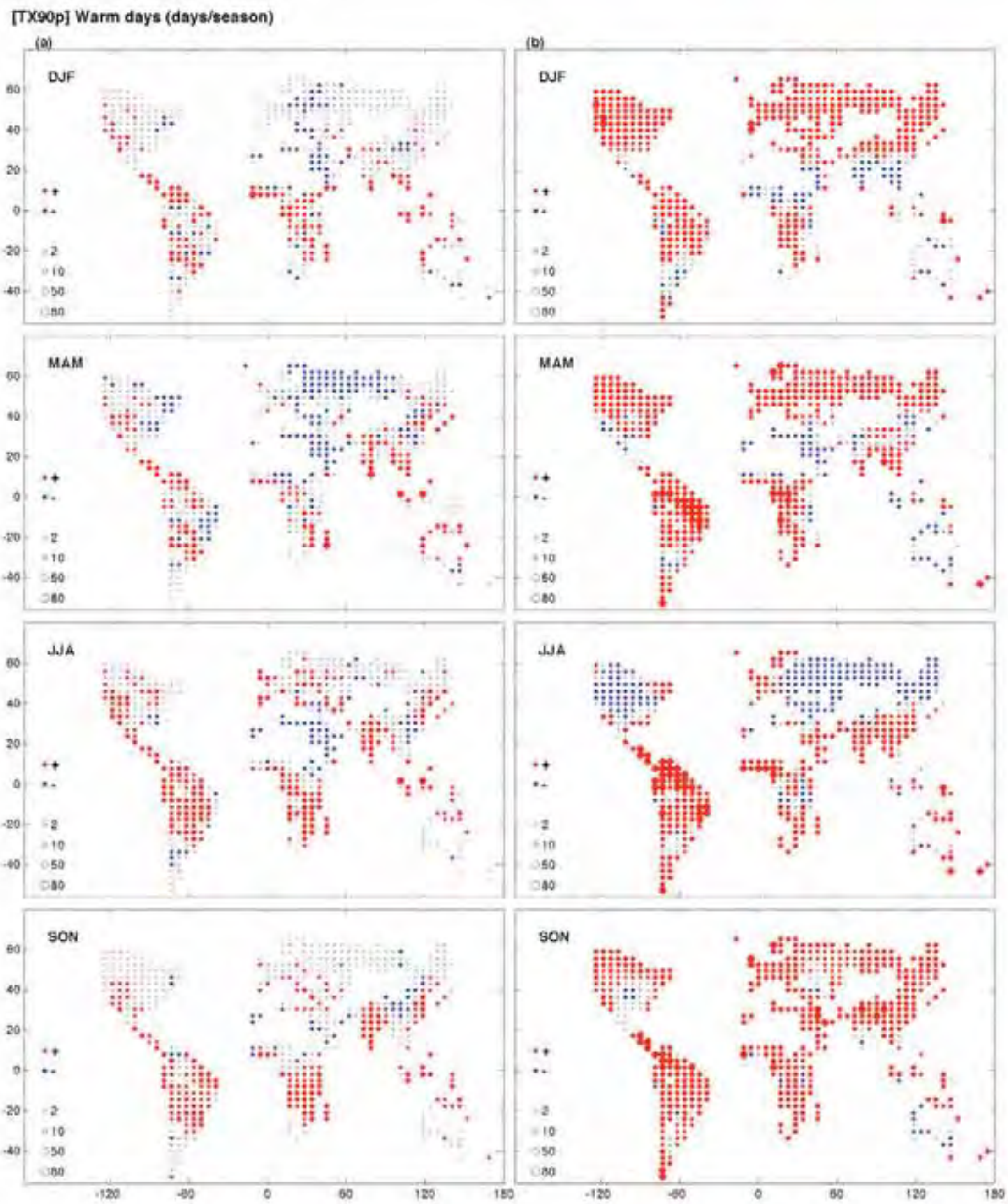

Figure 5-9: As Figure 5-1 but for the number of warm days, TX90p (days per season) (figure 10 of Avila et al., 2012).

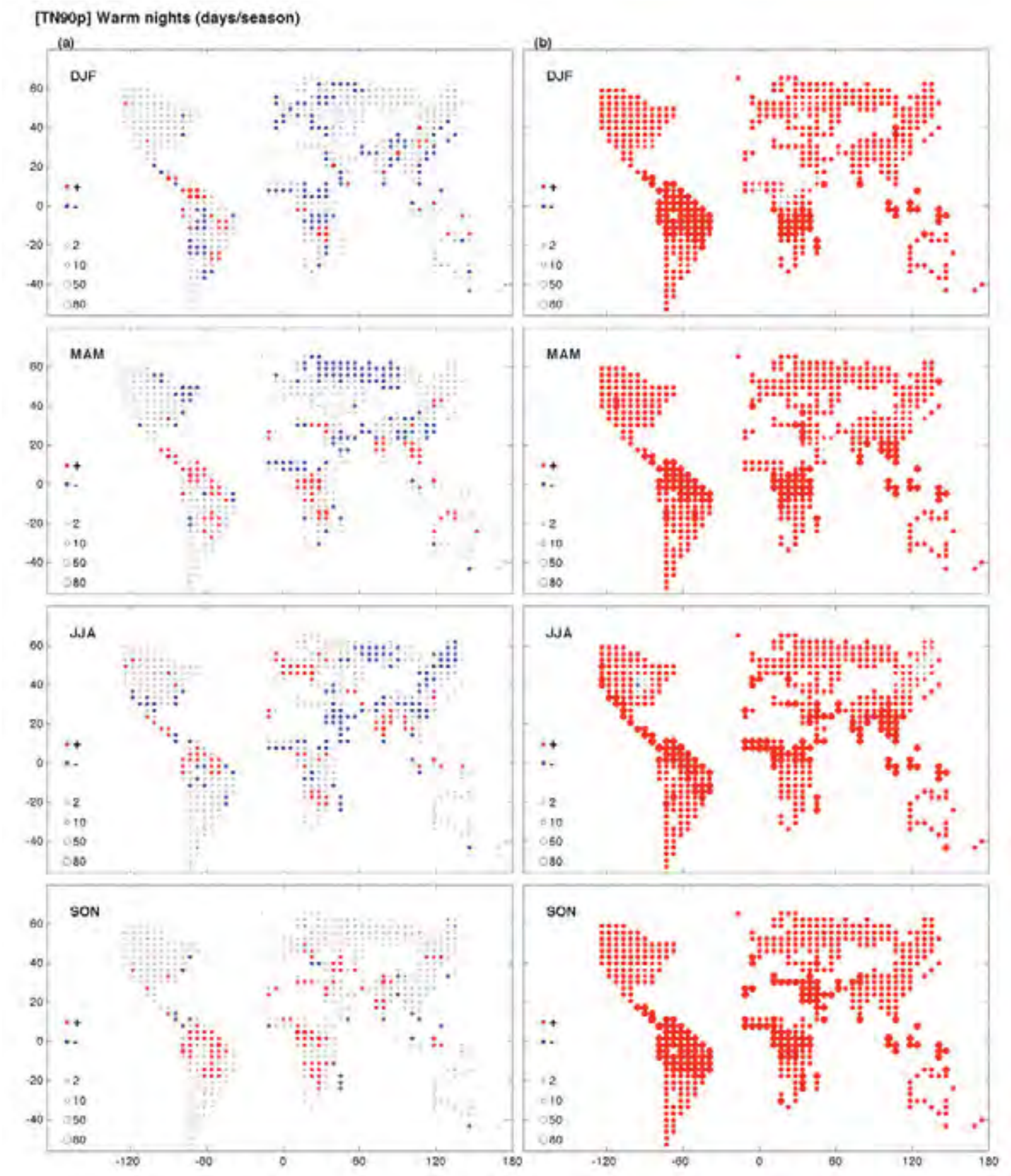

Figure 5-10: As Figure 5-1 but for the number of warm nights, TN90p (days per season) (figure 11 of Avila et al., 2012).

5.6 Impact of LULCC on precipitation extremes

The impact of LULCC on the extreme precipitation indices, such as maximum 1-day and 5-day precipitation (RX1day, RX5day), is generally negligible (Figures 5-11a and 5-12a). In both cases, the scale of impact due to LULCC is small in absolute terms and small relative to 2 x CO_2

Similar results are apparent in the simple daily intensity index (SDII, Figure 5-13a), and the annual contribution from very wet days (R95pT, Figure 5-13b). The impacts on consecutive wet days (CWD, Figure 5-14a), consecutive dry days (CDD, Figure 5-14b) and heavy precipitation days (R10mm, Figure 5-14c) also tend to be very small. Overall, at the continental scale, LULCC does not appear to impact the rainfall indices strongly. Further analysis will be required to determine whether hints of an impact from LULCC over individual regions (e.g. CDD, Figure 5-14b) are real or model noise.

It should be noted however that the model used in this study has very coarse resolution and therefore may not properly capture the small-scale rainfall events (e.g. intense rain storms, tropical cyclones) that could affect rainfall extremes. Thus, the absence of significant changes in the rainfall extremes shown here does not indicate that LULCC does not affect rainfall extremes. It does however highlight the need for climate models to properly simulate rainfall before any assessment of changes in rainfall extremes can be done.

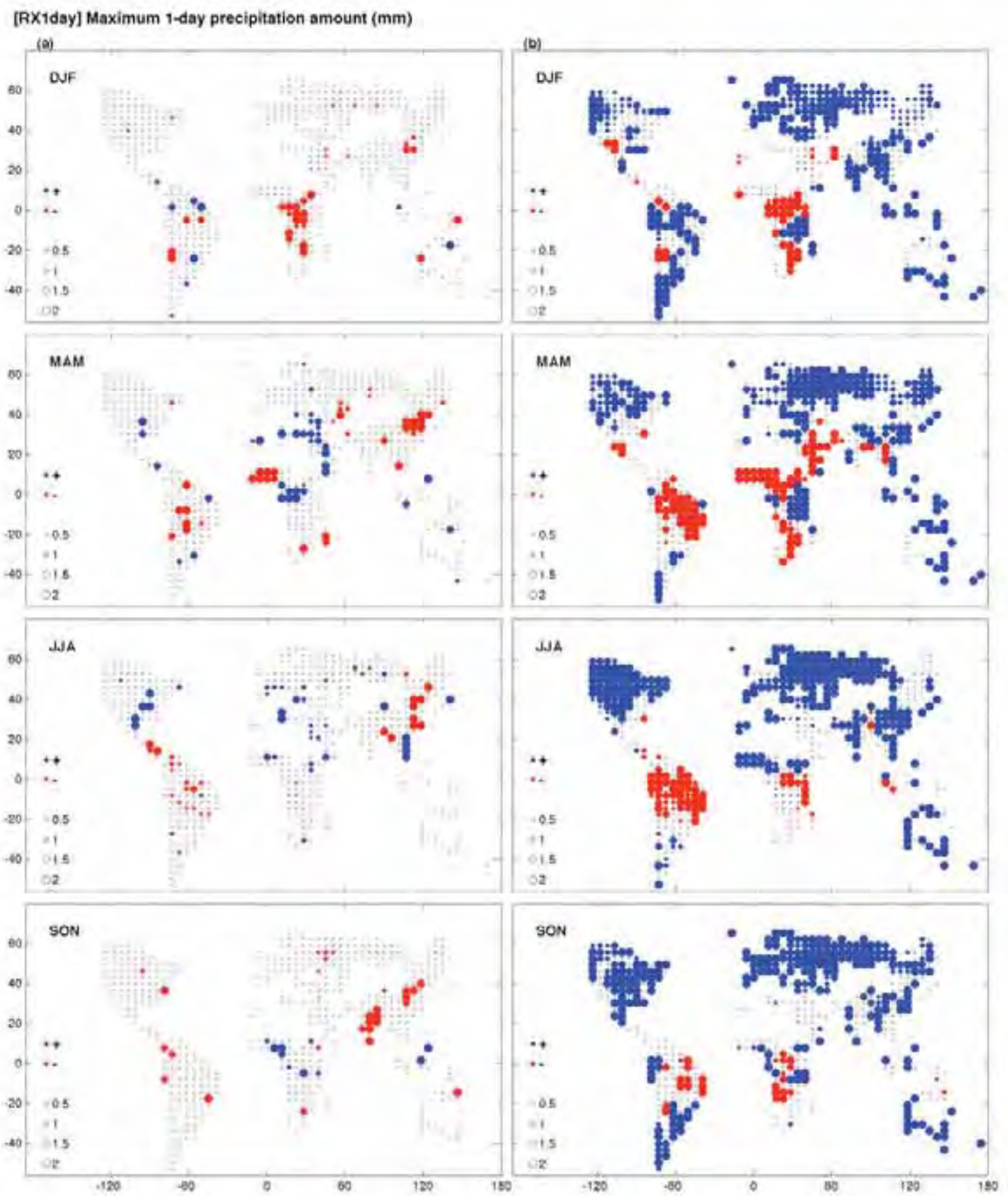

Figure 5-11: As Figure 5-1 but for the seasonal maximum 1-day precipitation, RX1day (mm). Note that blue represents an increase in rainfall.

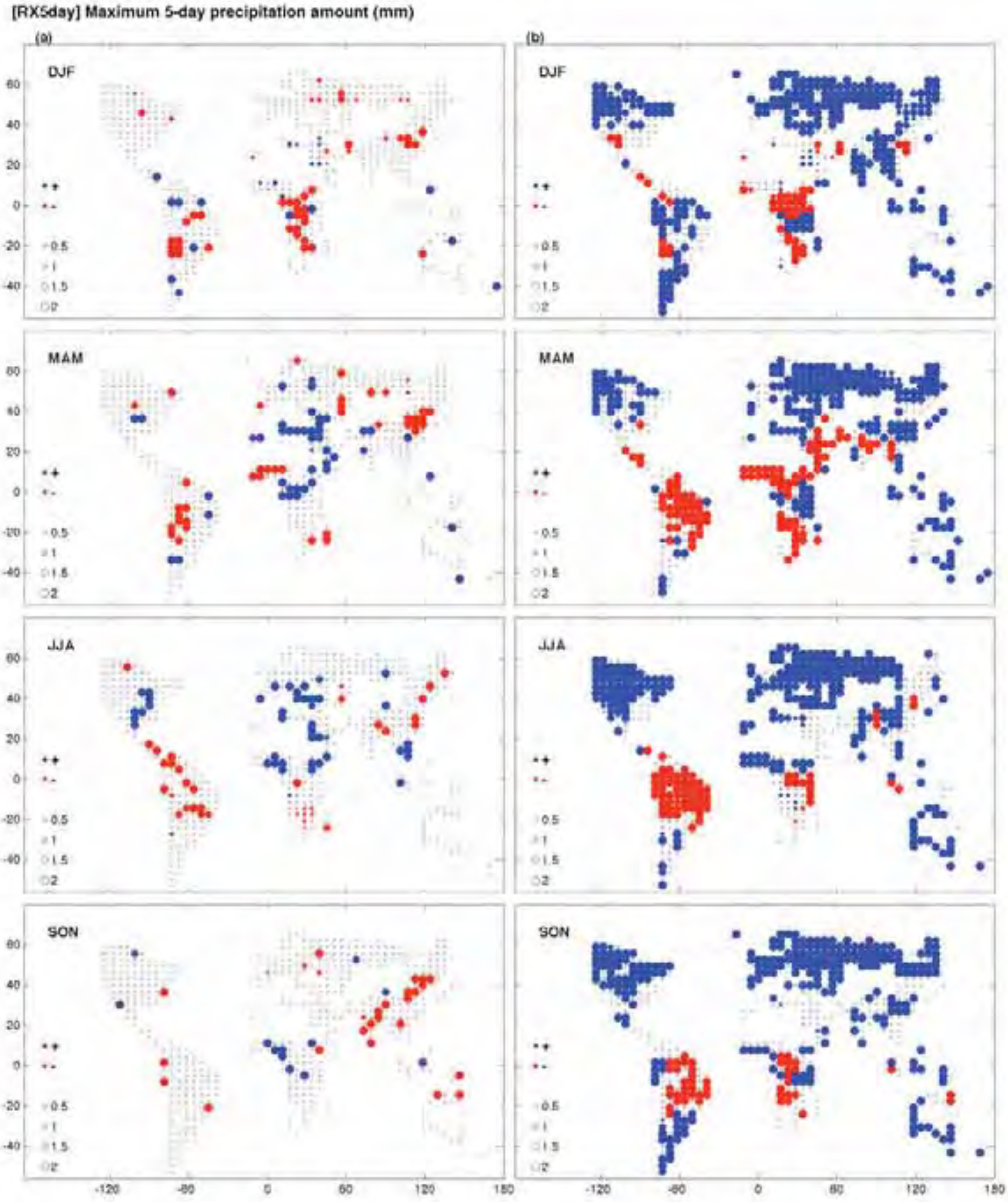

Figure 5-12: As Figure 5-1 but for the seasonal maximum 5-day precipitation, RX5day (mm). Note that blue represents an increase in rainfall.

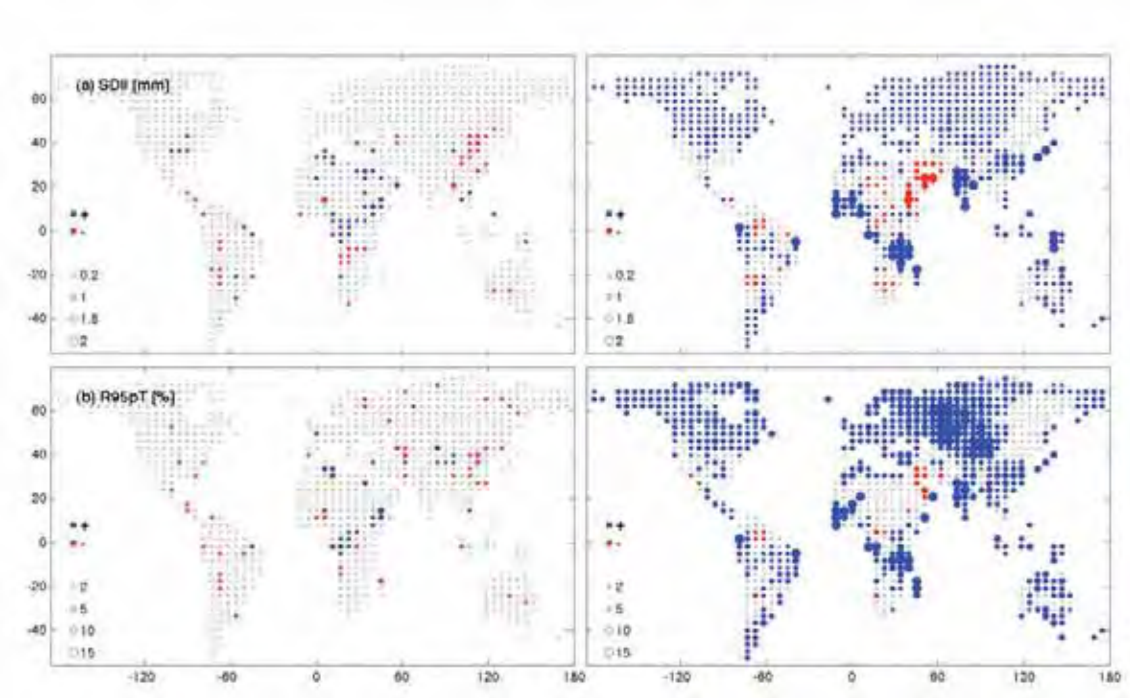

Figure 5-13: As Figure 5-1 but for (a) simple daily intensity index, SDII (mm/day) and (b) annual contribution from very wet days, R95pT (%). Note that blue represents an increase in rainfall.

The extent of the LULCC impact on the ETCCDI indices at large spatial scales, relative to the impact of 2 x CO_2, is summarized in Figures 5-15 and 5-16, for the seasonal and annual indices, respectively. The extents of the statistically significant grid points for each of the indices are assessed over several regions: global, tropics (~24°S-24°N), northern hemisphere (~0-90°N), southern hemisphere (~0-90°S), northern mid-latitudes (~27-60°N) and southern mid-latitudes (~27-60°S). Indices are considered field significant when the number of grid points which are statistically significant at the 95% level using the two-tailed Kolomogorov-Smirnov (KS) test exceeds the calculated field significance threshold (see Section 3.6). Indices that are field significant are shown in coloured cells and the percentage of significant grid points within the region are is shown; non-field significant indices are represented by a hyphen on a white background.

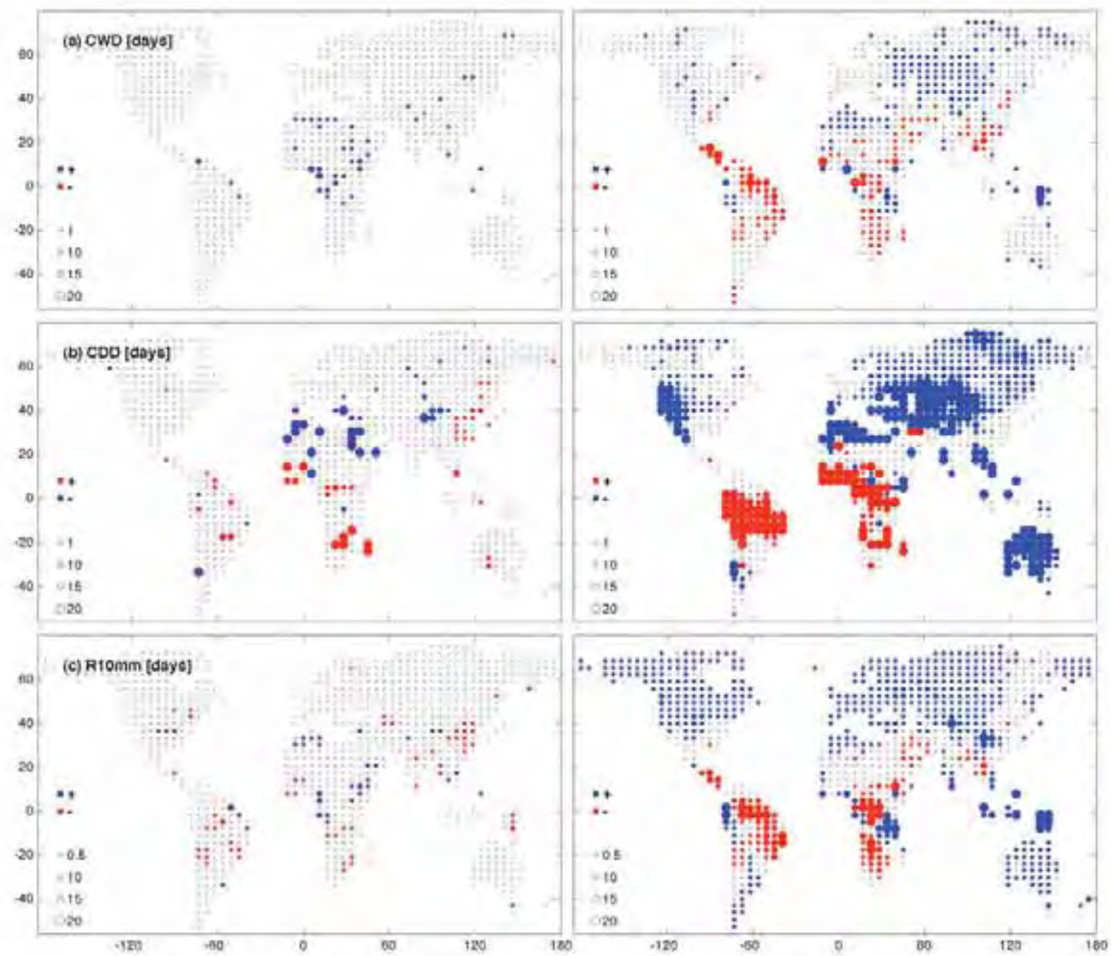

Figure 5-14: As Figure 5-1 but for (a) consecutive wet days, CWD; (b) consecutive dry days, CDD; and (c) heavy precipitation days, R10mm (all in days per year). Note that blue represents an increase in the number of wet days (a), a decrease in dry days (b) and an increase in heavy precipitation days (c).

For almost all temperature indices, 2 x CO_2 typically affects 70-100% of land grid points in all six regions in all seasons and this is consistently field significant for most regions and most indices (Figure 5-15). In contrast the LULCC impacts on the temperature indices, although they are field significant in a lot of cases, indicate much less consistency with 40-80% of land grid points in the tropics, 20-50% in the northern hemisphere, and 20-60% in the southern hemisphere indicating significant changes. Thus, while LULCC does induce field significant changes, the extent of its impact is much lower compared to that of CO_2. It is noteworthy that those indices that display the strongest field significance include TXx, WSDI and Tx90p (tropics only) where LULCC drives changes of the same sign as 2 x CO_2.

The rainfall indices are much less sensitive to both the increase in CO_2 and LULCC. However 2 x CO_2 affects around 40% of grid points for all the rainfall indices (up to 83% for during DJF) and all are field significant. The percentage of grid points experiencing significant changes in rainfall indices due to 2 x CO_2 is still generally larger compared to LULCC-induced changes for the temperature indices. The percentage of grid points displaying statistically significant changes due to LULCC is commonly close to or below 10% (Figure 5-15 and 5-16).

DJF

	dLULCC Globe	dLULCC Tropics	dLULCC Northern Hemisphere	dLULCC Southern Hemisphere	dLULCC Northern mid-latitudes	dLULCC Southern mid-latitudes	dCO2 Globe	dCO2 Tropics	dCO2 Northern Hemisphere	dCO2 Southern Hemisphere	dCO2 Northern mid-latitudes	dCO2 Southern mid-latitudes
Temperature												
TXn	25	35	28	17	18	-	89	81	92	84	97	83
TNn	42	70	34	61	24	28	96	93	99	91	100	95
TXx	39	71	30	63	18	30	86	76	90	76	93	83
TNx	20	32	20	18	13	-	97	96	96	100	98	100
DTR	60	69	60	60	58	45	83	84	85	79	81	98
TX10p	36	51	33	45	26	45	93	90	96	87	98	78
TN10p	41	52	40	43	36	30	98	96	98	99	100	100
TX90p	42	67	35	58	25	35	89	83	94	74	97	60
TN90p	33	46	29	42	22	33	99	97	98	100	100	100
Precipitation												
RX1day	12	21	12	14	8	-	70	65	71	67	70	83
RX5day	16	25	14	20	10	-	68	64	70	66	68	83

JJA

	dLULCC Globe	dLULCC Tropics	dLULCC Northern Hemisphere	dLULCC Southern Hemisphere	dLULCC Northern mid-latitudes	dLULCC Southern mid-latitudes	dCO2 Globe	dCO2 Tropics	dCO2 Northern Hemisphere	dCO2 Southern Hemisphere	dCO2 Northern mid-latitudes	dCO2 Southern mid-latitudes
Temperature												
TXn	19	25	18	21	16	-	73	82	69	82	61	95
TNn	25	33	20	38	18	43	99	99	100	98	100	100
TXx	57	74	54	66	52	20	90	94	91	90	89	80
TNx	27	41	29	23	21	-	93	100	90	99	87	100
DTR	57	71	51	72	48	58	86	77	86	85	92	88
TX10p	36	46	36	37	31	-	81	88	78	87	73	90
TN10p	35	46	31	44	28	40	98	100	98	100	97	100
TX90p	58	80	54	68	49	33	89	92	89	88	88	80
TN90p	39	50	43	28	37	-	98	100	97	100	96	100
Precipitation												
RX1day	16	23	15	18	13	-	69	60	72	62	79	50
RX5day	16	25	16	18	13	-	67	60	68	65	74	50

MAM

	dLULCC Globe	dLULCC Tropics	dLULCC Northern Hemisphere	dLULCC Southern Hemisphere	dLULCC Northern mid-latitudes	dLULCC Southern mid-latitudes	dCO2 Globe	dCO2 Tropics	dCO2 Northern Hemisphere	dCO2 Southern Hemisphere	dCO2 Northern mid-latitudes	dCO2 Southern mid-latitudes
Temperature												
TXn	18	23	18	16	16	-	91	87	91	92	95	90
TNn	34	25	38	25	39	53	96	90	94	99	99	100
TXx	54	73	54	53	43	40	78	87	75	87	71	83
TNx	29	43	31	24	22	-	99	100	99	99	99	98
DTR	52	59	52	52	52	38	86	75	89	78	94	88
TX10p	47	41	54	30	53	30	89	88	89	90	90	88
TN10p	43	37	48	30	47	35	99	97	98	100	100	100
TX90p	58	66	60	53	54	35	89	89	89	91	89	90
TN90p	37	49	41	29	31	-	100	100	100	100	100	100
Precipitation												
RX1day	15	18	17	12	14	-	68	65	70	62	72	48
RX5day	17	20	18	14	17	-	67	71	68	66	67	45

SON

	dLULCC Globe	dLULCC Tropics	dLULCC Northern Hemisphere	dLULCC Southern Hemisphere	dLULCC Northern mid-latitudes	dLULCC Southern mid-latitudes	dCO2 Globe	dCO2 Tropics	dCO2 Northern Hemisphere	dCO2 Southern Hemisphere	dCO2 Northern mid-latitudes	dCO2 Southern mid-latitudes
Temperature												
TXn	7	15	-	14	-	-	90	86	90	92	94	88
TNn	18	19	19	16	17	28	100	100	100	99	100	100
TXx	43	75	33	69	24	28	81	91	79	86	76	75
TNx	19	32	18	20	12	-	96	100	95	98	93	93
DTR	47	65	39	68	36	45	86	81	89	78	90	83
TX10p	26	44	20	39	16	-	85	86	85	84	84	75
TN10p	27	35	29	24	23	25	100	100	100	100	100	100
TX90p	48	76	38	73	33	30	92	95	91	95	90	85
TN90p	24	42	22	28	15	-	100	100	100	100	100	100
Precipitation												
RX1day	8	12	9	-	-	-	61	38	64	51	73	80
RX5day	8	11	9	-	-	-	61	49	60	62	65	78

Percentage of significant grid points

5 20 40 60 80 90 95

Figure 5-15: Seasonal field significance of the seasonal extreme indices for the Globe, Tropics, Northern Hemisphere, Southern Hemisphere, Northern mid-latitudes and Southern mid-latitudes. Indices that are field significant are coloured and shown with the percentages of statistically significant grid points in each region. Indices that are not field significant are represented by a hyphen.

	dLCC							dCO2					
	Global	Tropics	Northern Hemisphere	Southern Hemisphere	Northern mid-latitudes	Southern mid-latitudes		Global	Tropics	Northern Hemisphere	Southern Hemisphere	Northern mid-latitudes	Southern mid-latitudes
Temperature													
TXn	26	40	26	25	17	-		90	81	91	90	97	98
TNn	40	63	34	56	24	43		99	98	98	100	100	100
TXx	63	86	58	73	52	38		89	90	89	88	89	83
TNx	30	49	33	24	21	-		93	100	90	100	87	100
DTR	59	76	55	70	51	48		92	84	94	85	97	98
GSL	14	-	20	-	21	-		54	-	72	11	93	40
CSDI	37	46	40	31	33	-		82	94	84	76	83	-
WSDI	50	81	41	71	32	25		94	94	98	86	98	73
TX10p	54	57	54	53	53	45		89	89	88	93	88	93
TN10p	56	57	58	50	57	43		100	100	100	100	100	100
TX90p	63	88	59	75	49	40		96	96	98	91	98	83
TN90p	46	60	44	51	38	30		100	100	100	100	100	100
Precipitation													
RX1day	9	10	10	-	10	-		67	56	69	62	74	65
RX5day	12	16	14	9	12	-		64	54	68	55	72	55
SDII	15	22	14	16	11	-		69	61	72	63	75	65
R95pT	12	15	12	11	10	-		71	66	71	70	75	65
CWD	-	11	-	-	-	-		43	56	40	50	37	25
CDD	12	14	13	-	12	-		61	58	61	60	65	40
R10mm	14	23	12	20	10	-		74	72	71	80	74	73

Percentage of significant grid points

5 20 40 60 80 90 95

Figure 5-16: As Figure 5-15 but for annual field significance.

5.7 Summary

This chapter used the daily precipitation and temperature data resulting from 50 years of simulation using Mk3L-CABLE model to examine how LULCC affects the global pattern of extremes using the ETCCDI extreme climate indices. It has demonstrated that LULCC affects the ETCCDI temperature and rainfall indices in complex ways. In particular, this chapter has shown that:

- LULCC affects the temperature extremes more then the precipitation extremes. This may be linked to the model's coarse resolution or may indicate a low sensitivity of precipitation to LULCC.

- Among the temperature extremes, LULCC affects the daytime extremes more than the nighttime extremes, mostly because daytime temperatures are directly influenced by insolation.

- As with the mean, the impact of LULCC is regional and not as widespread as the impact of CO_2. However, in regions of LULCC the magnitude of change in the temperature indices can be as large as that due to doubling of CO_2.

- The impact of LULCC is generally towards cooling and thus opposing the general warming induced by CO_2; however, for some indices and regions, the impact of LULCC enhances the impact of CO_2 (e.g. TXx, WSDI, TX90p).

- In terms of field significance, the CO_2 impacts are overwhelmingly more field significant than the LULCC impacts, but this is to be expected given that the CO_2 is well-mixed in the atmosphere and affects the global climate while the LULCC limited by its geographical extent. Despite this, LULCC shows field significance, exceeding 50% for most temperature extremes and even reaching as high as 80% for some regions.

The results show that LULCC does significantly impact the climate extremes. However, a major problem with Mk3L-CABLE is its relatively coarse resolution. While this comes with major advantages (e.g. long and statistically significant simulations) the coarse resolution of the model means that smaller-scale processes, which remain unresolved and might affect how LULCC impacts on temperature and, in particular, rainfall extremes, are missed. To partially resolve this, further analysis was undertaken using results from the LUCID project [*Pitman et al.*, 2009; *de Noblet-Ducoudré et al.*, 2012]. These simulations were undertaken at a relatively higher resolution and over several models, helping to resolve some of the concerns around experiments conducted with a single model. Results from this work are presented in Chapter 6.

Chapter 6
Multi-model estimate of changes in extremes

This chapter extends the analysis of the impacts of LULCC on the extremes presented in the previous chapter by using results from Land-Use and Climate, Identification of robust impacts project [LUCID, *Pitman et al.*, 2009; *de Noblet-Ducoudré et al.*, 2012] project.

<u>Candidate's contributions to this work</u>

The idea to extend the analysis of the impacts of LULCC on climate extremes using the LUCID results came via discussions with my supervisor, although they were a natural extension of the results and analyses presented in Chapter 5.

The model results presented in this chapter were provided by the LUCID modelling groups: ARPEGE (Dr. Aurore Voldoire), ECHAM5 (Dr. Victor Brovkin and Dr. Veronika Gayler), ECEarth (Dr. Bart van den Hurk) and IPSL (Dr. Nathalie de Noblet-Ducoudré and Dr. Juan-Pablo Boisier). I processed the LUCID data and calculated the extremes indices using methods similar to those presented in Chapter 5. I undertook the analysis presented in this chapter.

6.1 Introduction

Climate extremes appear significantly affected by LULCC as demonstrated by the analysis of the ETCCDI indices derived from experiments using the Mk3L-CABLE model. While the impact of LULCC is geographically less extensive, and mostly smaller in magnitude compared to the impact of doubling CO_2, many of the temperature indices showed regionally strong and statistically significant responses to LULCC. In contrast, most of the rainfall indices did not show a statistically significant response to LULCC. However, these results were limited by the use of one coarse resolution model. It is important to verify these results using multiple models, with finer resolutions, running several realizations of each experiment.

This chapter therefore extends the analysis presented in Chapter 5 to examine whether the conclusions from the Mk3L-CABLE simulation are applicable across different climate models. In particular, daily maximum (Tmax) and minimum (Tmin) temperature and daily precipitation data from 4 models participating in LUCID (Table 6-1) are used to calculate the climate extreme indices defined by the ETCCDI [*Alexander et al.*, 2006].

6.2 Description of models

The LUCID project is designed to detect robust LULCC impacts. That is, it aims to identify signals due to LULCC above the noise of natural variability and consistent across models [*de Noblet-Ducoudré et al.*, 2012]. Results from the first set of LUCID experiments [*Pitman et al.*, 2009] showed that for June-July-August (JJA), five out of the 7 models simulated cooling in the near surface temperature due to LULCC while one model simulated warming. They also found few significant changes in precipitation and no common remote impacts of LULCC. This lack of consistency among the models attributed to the differences between the models, which include implementation of the land cover change, representation of the crop phenology, parameterization of albedo and the representation of the evapotranspiration for the different land cover types.

Table 6-1: List of climate models and associated land surface models from LUCID used in this chapter. The last column indicates the number of years of daily data used in the analysis of the extremes.

Climate model	**Reference**	**Grid size (lat x lon)**	**Land surface model**	**Reference**	**No. of years**
ARPEGE	Salas et al., 2005	2.8° x 2.8°	ISBA	Voldoire, 2006	29
ECHAM5	Roeckner et al., 2005	3.75° x 3.75°	JSBACH	Raddatz et al., 2007	27
ECEarth	www.ecmwf.int/research/ifsdocs/CY31r1/	1.8° x 1.8°	TESSEL	Van den Hurk et al., 2000	10
IPSL	Marti et al., 2010	2.5° x 3.75°	ORCHIDEE	Krinner et al., 2005	28

A follow-up study by de Noblet-Doucoudré et al. [2012] compared the impact of LULCC to that of increased CO_2 and changes in sea-surface temperature and sea-ice extent. They found that over North America and Eurasia, the impact of LULCC has similar magnitude but opposite sign as that due to the changes in CO_2 and sea surface temperature. While a large dispersion among the models was found, a number of robust features, concerning the surface albedo, available energy and turbulent fluxes, were identified [*de Noblet-Ducoudré et al.*, 2012]. Boisier et al. [2012] further explored these LULCC impacts on surface albedo, latent heat and total turbulent energy flux using a multivariate statistical analysis. They found that of the two major features that vary between the models, land cover distribution and simulated sensitivity to LULCC, the latter explains more than half of the inter-model spread and is dependent on the parameterization of the land-surface processes.

Since the LUCID experiments were specifically designed to explore the robust impacts of land cover change, they are well-suited for examining the robustness of the impacts of LULCC on climate extremes found using the Mk3L-CABLE model. However, while the objective of this chapter is to verify the results from Chapter 5, there are three major differences between the Mk3L-CABLE and LUCID simulations, which preclude a direct comparison of the results from these two sets of experiments. First, the Mk3L-CABLE simulations used potential vegetation and year 2000 crop and pasture fraction to define the natural and perturbed land cover maps, respectively, while the LUCID experiments used crop and pasture fraction for years 1870 (pre-industrial) and 1992 (present). Second, while the CO_2 concentrations in the Mk3L-CABLE simulations were kept constant at 280 and 560 ppmv, the LUCID experiments set the CO_2 concentrations at 280 and 375 ppmv and allowed it to vary throughout the 30-year simulation period. Third, the prescribed sea surface temperatures (SSTs) in Mk3L-CABLE were set as seasonally varying climatological values representing conditions at 1 x CO_2 and 2 x CO_2. In the LUCID experiments the SSTs were prescribed to vary seasonally and annually using Climate of the 20th Century (C20C) project specifications.

However, while the results from Chapter 5 may not be directly comparable to the results in this chapter, they can still be used to indicate the indices and regions where the impacts of LULCC might be expected; and robust results from this chapter would still be helpful in verifying previous results from Chapter 5.

For each model (Table 6-1), 4 sets of experiments were calculated (Table 6-2) and 5 independent realizations were run for each model and experiment. The simulations were run for 30 years but the actual number of daily data used in calculating the climate indices differed between the models because some years with missing data had to be discarded and some models (i.e. ECEarth) only have 10 years of daily data (Table 6-1) available.

Figure 6-1 shows the extent of land cover change imposed on the experiments (i.e. difference between the 1870 and 1992 vegetation cover). While all the modelling groups used the same land cover maps defining the crop and pasture area, the implementation onto the different land cover distributions varied. For instance, the natural land cover distribution (i.e. the base map on which the crop and pasture fraction is imposed) is usually developed with each model and any modification would require significant recalibration of land surface parameters and subsequent re-testing and re-optimization of each model. Because it is not feasible to impose common natural vegetation across all models, each model defined its own natural vegetation maps based on its own natural land cover distribution.

The models also differed in their definition of grasses and agricultural lands. For instance, ECEarth defined the grass areas to be covered by natural grass only and agricultural areas to be covered by both crop and managed grass; the other models defined grass areas to be covered by both natural and managed grass, and agriculture areas to be covered by crop only. These differences in implementation of the land cover change resulted in different areas of cover of specific land cover types (Table 6-3) and different cropland maps (Figure 6-2). Table 6-4 illustrates the difference in forest extent between the models for pre-industrial and present day land cover over North America and Eurasia, despite the use of a single crop and pasture fraction map (Figure 6-1).

Table 6-2: List of experiments performed by each climate model (table 2 of Pitman et al., 2012).

Experiment		CO_2 (ppm)	Vegetation map	Prescribed SST
Name	**Description**			
PI	re ind stria im ation with C eenho se ases aeroso s and co er ma and s ein rescri ed at their re ind stria a es	280	1870	1870-1900
PD	resent da im ation with resent da C and co er ma s and sea ice e tent ther reenho se ases ha e een added to the C concentration as C e i a ent[1] hi e aeroso s ha e een e t to their re ind stria a es.	375	1992	1972-2002
PIv	re ind stria im ation with C eenho se ases aeroso s and s ein rescri ed at their re ind stria a e t with resent da and co er ma	280	1992	1870-1900
PDv	resent da im ation with resent da C s and sea ice e tent ther reenho se ases ha e een added to the C concentration as C e i a ent whi e aeroso s ha e een e to their re ind stria a es. t and co er ma is re ind stria .	375	1870	1972-2002

[1]Except in EC-EARTH where those were changed proportionally to CO_2 changes

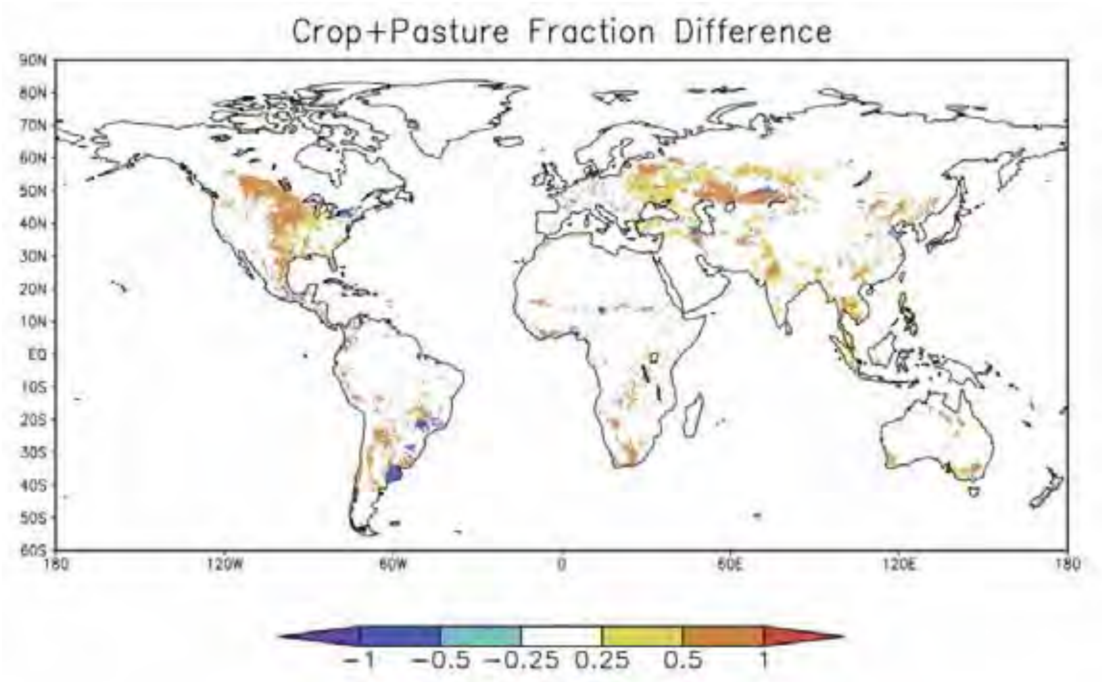

Figure 6-1: Extent of land cover change between experiments PD and PDv (PD – PDv) expressed as the difference in crop and pasture cover between the two experiments. Blue colours represent changes that decrease pasture and crop cover while yellows and browns are increases (25%-50% and 50-100%, respectively) (figure 1 of Pitman et al., 2009).

Table 6-3: Area of cover of specific land cover types (DF=Deciduous Forest; EF=Evergreen Forest; G=Grass; A=Agricultural land) implemented in each model (million km^2) (table S1 of Pitman et al., 2009).

Model	1870				1992			
	DF	EF	G	A	DF	EF	G	A
ARPEGE	7.3	33.3	46.0	8.7	6.2	28.0	45.9	16.6
ECHAM5	25.1	30.4	34.5	7.9	22.3	27.7	33.2	14.6
ECEarth*	40.0	22.0	15.0	22.0	32.0	20.0	19.0	28.0
IPSL	24.2	31.0	45.4	8.5	19.5	26.8	46.9	16.0

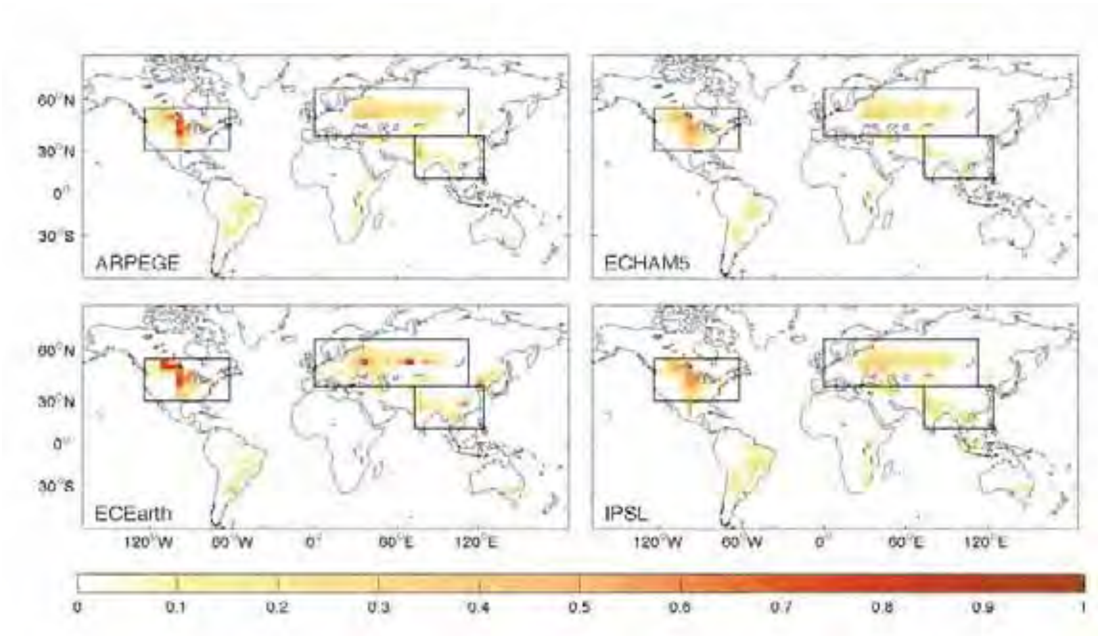

Figure 6-2: Fraction of vegetation cover converted from natural vegetation to cropland for the four models. The boxes in each panel represent the regions used for the scatter plots.

Table 6-4: Forest extent (in km²; numbers in parenthesis represent the fractional area covered by forests) at both pre-industrial and present day, together with changes in the forest areas between the two periods. Values are shown for North America and Eurasia (table 4 of de Noblet-Ducoudré et al, 2012).

Model	**Forest Area (10^6 km²) (% of covered area)**					
	North America			**Eurasia**		
	1870	**1992**	***Change***	**1870**	**1992**	***Change***
ARPEGE	2.26 (50)	1.13 (25)	*1.13 (25)*	2.05 (34)	1.1 (18)	*0.95 (16)*
ECHAM5	1.65 (36)	1.09 (24)	*0.56 (12)*	1.84 (31)	1.2 (24)	*0.64 (11)*
ECEarth	3.36 (74)	1.54 (34)	*1.82 (40)*	3.14 (31)	1.77 (30)	*1.37 (23)*
IPSL	2.53 (56)	1.26 (28)	*1.27 (28)*	2.42 (41)	1.35 (23)	*1.07 (18)*

6.3 Calculation of climate extremes indices

As with Chapter 5, 19 of the ETCCDI indices (see Table 3-8) are used to detect the changes in the extremes. Temperature indices, except for those indicating duration, are presented as seasonal extremes. All rainfall indices, except for the maximum 1-day and 5-day precipitation, are presented as annual extremes.

For each model (Table 6-1) and experiment (Table 6-2), daily maximum and minimum temperature and precipitation data from the 5 independent realizations were concatenated and interpolated into the Mk3L-CABLE grid prior to calculation of the indices. The software package FClimdex was again used to calculate the indices. For indices that require a threshold for calculation (e.g. TX10p, TN10p, TX90p, TN90p, CSDI, WSDI and R95pT), experiment PI was defined as the control simulation.

For brevity, the change in land cover using pre-industrial conditions, dLCC@280, is defined as the difference between PIv and PI (PIv - PI); the change in land cover for present day conditions, dLCC@375, is defined as the difference between PD and PDv (PD – PDv). The change due to increased CO_2 with pre-industrial vegetation cover, dCO2(1870), is defined as the difference between PDv and PI (PDv – PI).

6.4 Results

Changes in the mean temperature (Figure 6-3) and precipitation (Figure 6-4) are presented for the Northern Hemisphere with the regions of interest (Eurasia, North America and South East Asia) shown in boxes. The left column of maps shows the change due to LULCC at 280 ppmv while the middle column shows the change due to LULCC at 375 ppmv. To act as reference to the impact of LULCC, the change due to CO_2 (from 280 to 375 ppmv) at pre-industrial (1870 vegetation cover) conditions are also shown (right column).

Each row represents results from each of the LUCID models used in the analysis (from top to bottom: ARPEGE, ECHAM5, ECEarth and IPSL). Results for March-April-May (MAM) and June-July-August (JJA) are shown. These seasons were chosen because the significant changes due to LULCC are most intense and extensive during this period.

The changes in the extreme indices (Figure 6-5 to 6-8, 6-10 to 6-19, 6-21 to 6-25) are shown in the same layout as the changes in the means but are presented as bubble maps (see Chapter 5). For the indices with seasonal values, results for MAM and JJA are shown; annual values are shown for the rest of the indices.

The relationship between changes in the mean and extremes are presented as scatter plots (Figures 6-9 and 6-22). For each index, the seasonal mean and extreme values are plotted for Eurasia (left column), North America (middle column) and S.E. Asia (right column).

To summarize the results, a colour-coded table indicating the percentage of significant grid points in each region of interest for each model is shown in Figure 6-26.

6.4.1 Mean impact of LULCC at different levels of atmospheric CO_2

LULCC and changes in atmospheric CO_2 concentration affects the mean temperature and rainfall and these changes will be important in explaining the changes in the extremes.

Figure 6-3 shows that in terms of the mean response, in MAM and JJA, LULCC tends to cool but the response is varied ranging from a strong response in ARPEGE and ECEarth to a weaker response in ECHAM5 and a warming in IPSL in JJA. The different model responses to LULCC in the mean temperature is related to the intensity of land cover change (Figure 6-2 and Table 6-4 show ECHAM5 to implement change less intensely than ARPEGE or ECEarth) and how crops are parameterized in the model [*de Noblet-Ducoudré et al.*, 2012].

There are three broad conclusions from Figure 6-3. First, the impact of LULCC is generally similar at both 280 ppmv and 375 ppmv and in both cases LULCC causes mid-latitude cooling (except for the warming in IPSL during JJA), reaching 2°C in some regions. Second, the increase in CO_2 from 280 ppmv to 375 ppmv causes large-scale warming of mainly 0.4 – 1.5°C. Third, the increase in CO_2 leads to warming almost everywhere while LULCC tends to have a more regionalized impact.

An interesting result in JJA is that the model with the largest warming due to the increase in CO_2 (ECHAM5) is the model with the weakest sensitivity to LULCC suggesting that a model's sensitivity to a land cover perturbation is not simply proportional to its climate sensitivity. However, this is complicated by the intensity of LULCC, which varies between the models.

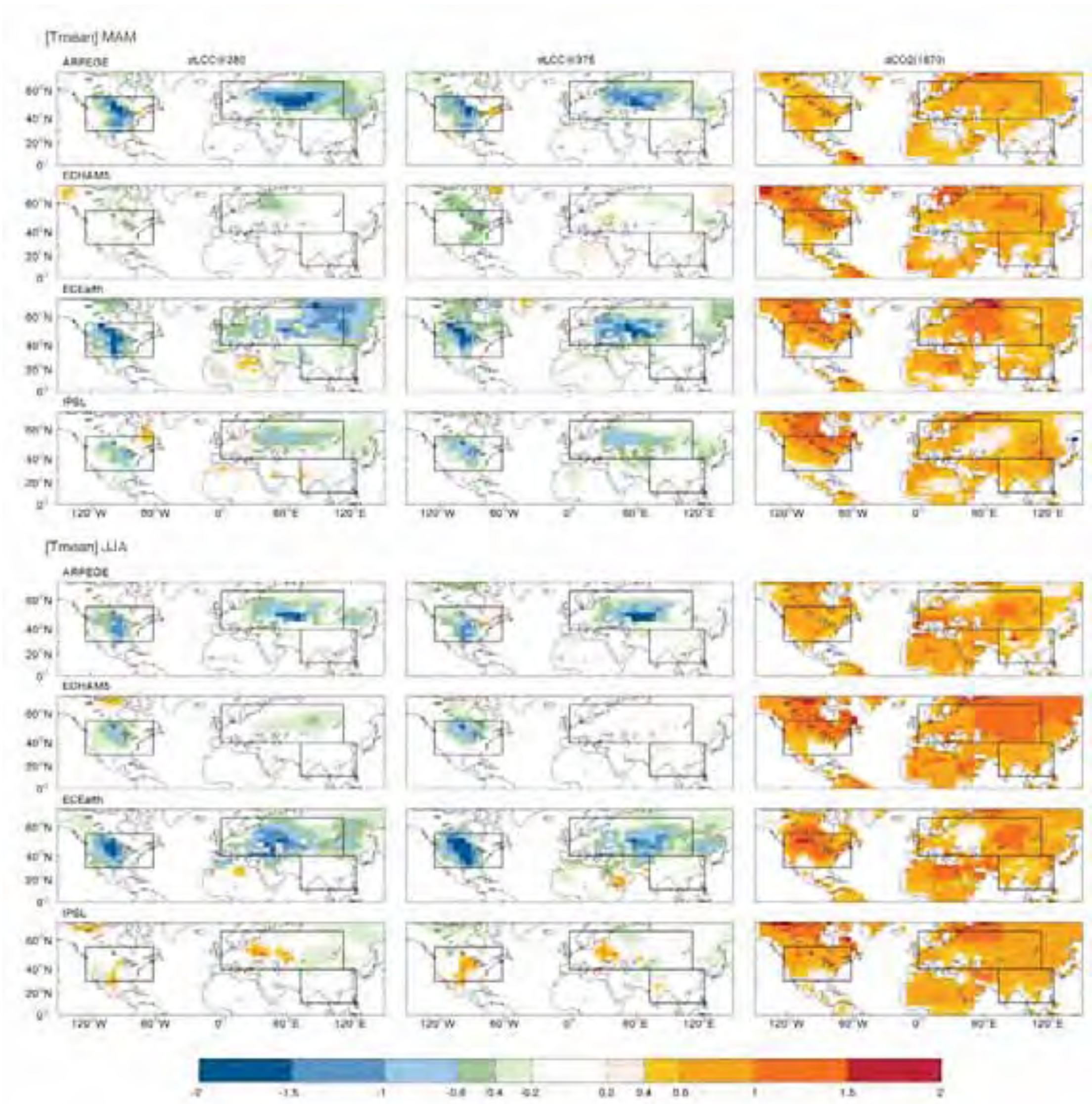

Figure 6-3: Change in the mean surface temperature (°C) in March-April-May (MAM) and June-July-August (JJA) for the four models. The left column is the impact on the mean surface air temperature of LULCC at a CO_2 concentration of 280 ppmv (PIv - PI). The middle column is the impact of LULCC at a CO_2 concentration of 375 ppmv (PD - PDv). The right column shows the impact of the increase in CO_2 alone using land cover reflecting 1870 conditions (PDv – PI).

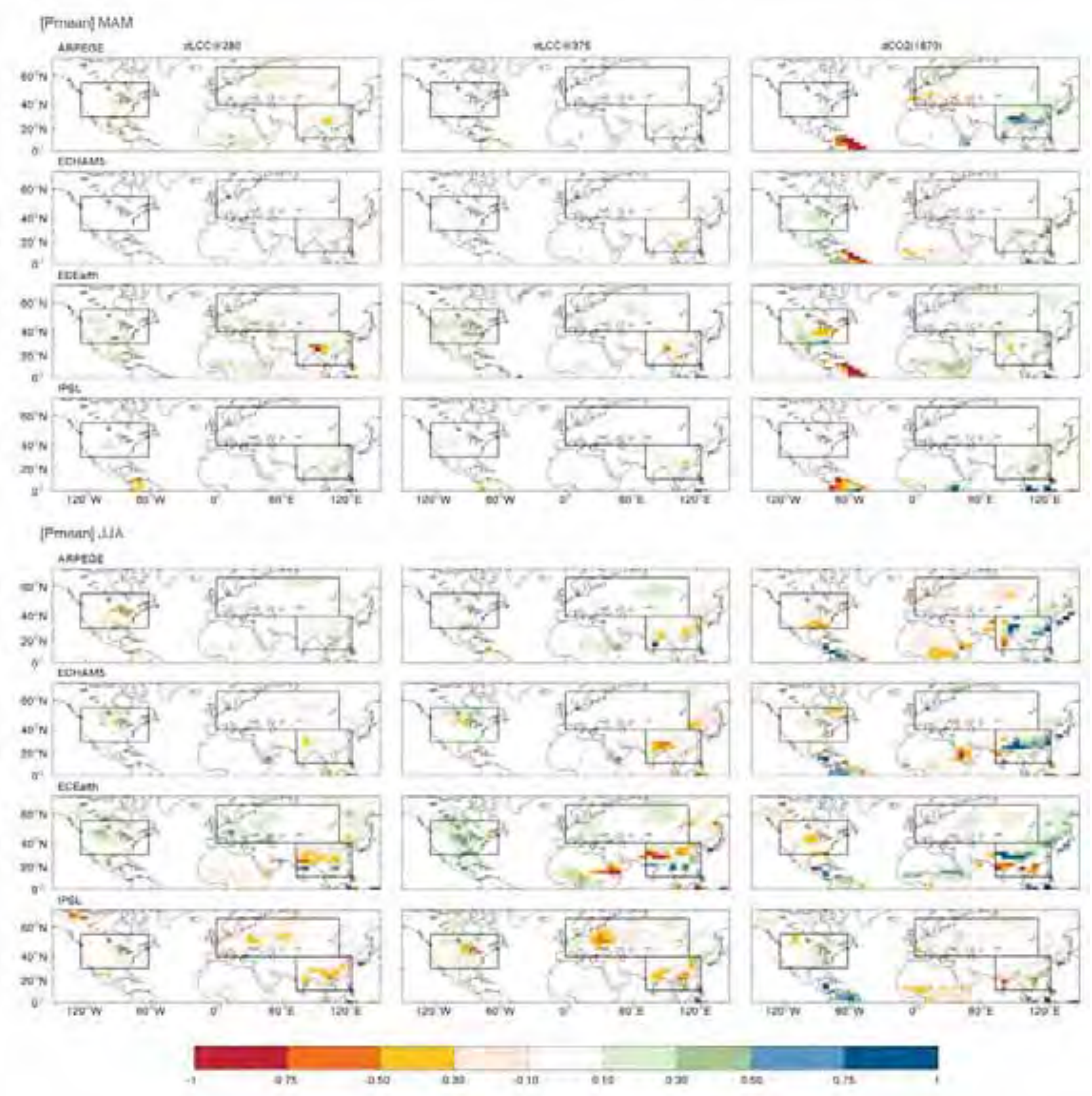

Figure 6-4: As Figure 6-3 but for mean precipitation (mm/day).

In terms of precipitation, Figure 6-4 shows that the impact of LULCC on precipitation is generally weak in all models at both 280 ppmv and 375 ppmv. However, there are similarities between the impacts of LULCC at the two CO_2 levels particularly in JJA. At both 280 ppmv and 375 ppmv, ARPEGE simulates a small increase of summer precipitation over Eurasia and a decrease over North America; ECHAM5 simulates a small increase over parts of North America;

ECEarth simulates increase over North America and Eurasia and IPSL simulates decreases over North America and Eurasia. If LULCC did not affect rainfall, then the individual regions affected by rainfall changes in Figure 6-4 would likely vary randomly between the results at 280 ppmv and 375 ppmv. Since there are similarities in the regional pattern of change in rainfall due to LULCC at both CO_2 levels it is likely that while the models disagree on the sign of the impact of LULCC on precipitation, internally each model is affected by LULCC in a consistent way.

The apparent decreases in rainfall over S.E. Asia simulated by all models in JJA due to LULCC at both 280 ppmv and 375 ppmv are intriguing (Figure 6-4). The response is weaker in ARPEGE and ECHAM5 which is expected because the models also simulate a weaker response to LULCC elsewhere (in part due to a smaller intensity of LULCC in ECHAM5, see Figure 6-2). The decline in mean rainfall covers a large region of S.E. Asia, particularly in ECEarth and IPSL, and occurs at both 280 and 375 ppmv.

Similarly, the increases in precipitation over S.E. Asia in both MAM and JJA due to the increase in CO_2 are also consistent between the models. In general, the pattern of the CO_2-induced precipitation changes seem to agree much better between the models than for LULCC-induced changes, pointing at model-dependent influences of parameterization of different processes related to precipitation. Overall, LULCC over S.E. Asia appears to decrease rainfall in all models, which is the opposite signal due to the increase in CO_2, which leads to increased precipitation in all models. Our results suggest that simulations of the impact of increasing CO_2 over S.E. Asia that omit the impacts of LULCC will lead to erroneous conclusions on the precipitation response when discussing anthropogenic induced climate change. However, because the extent of the significant the impact of LULCC on rainfall is not particularly large and the CO_2 change included here is not representative of mid- to late-21st century levels, it is possible that, despite the continuous intensive LULCC in S.E. Asia, increases in CO_2 will likely remain the dominant regional forcing on rainfall throughout the 21st century.

6.4.2 Impact of LULCC on temperature intensity extremes

The impacts of LULCC on temperature intensity extremes are shown in Figures 6-5 to 6-8. With a few exceptions (e.g., for TXx and TNx: ECHAM5 during MAM and IPSL during JJA), the general impact of LULCC is to decrease the intensity of temperature extremes. There are slight variations among the models with respect to the magnitude and extent of the change, which may be attributed to differences in the intensity of LULCC (see Figure 6-2 and Table 6-4) and the parameterization of crops between the models [*de Noblet-Ducoudré et al.*, 2012]. For example, during MAM, the reduction in TXn (Figure 6-5) varies from intense and widespread for ARPEGE, to intense but more localized for ECEarth, to less intense and more localized for IPSL, and no discernable change for ECHAM5.

There are also differences between the changes in each season and over each region. For TXn (Figure 6-5), the change over Eurasia during MAM for all models except ECHAM5 does not occur during JJA, with only ARPEGE showing a localized change that is definitely smaller both in magnitude and extent than during MAM.

There are also differences between the changes due LULCC at 280 and 375 ppmv, with some indices and models varying in intensity and extent of change at different CO_2 levels. However, the sign of the change generally do not vary between CO_2 levels. That is, if LULCC induces cooling at 280 ppmv, it would also most likely induce cooling at 375 ppmv; and if it induces warming at 280 ppmv (as in the case of TXx and TNx for IPSL during JJA) it also induces warming at 375 ppmv. Despite these differences, the patterns of the changes for the temperature intensity extremes (TXn, TNn, TXx and TNx) are similar enough (Figures 6-5 to 6-8) such that it is possible to describe them using the details of one index, for example, TXx.

Figure 6-5: As Figure 6-3 but for the coldest seasonal daily maximum temperature, TXn (°C). Only the grid points that are statistically significant at the 95% level using the two-tailed Kolmogorov-Smirnov test are shown. The red dots indicate increase in temperature; the blue dots indicate decrease in temperature. The magnitude of change is indicated by the size of the circles.

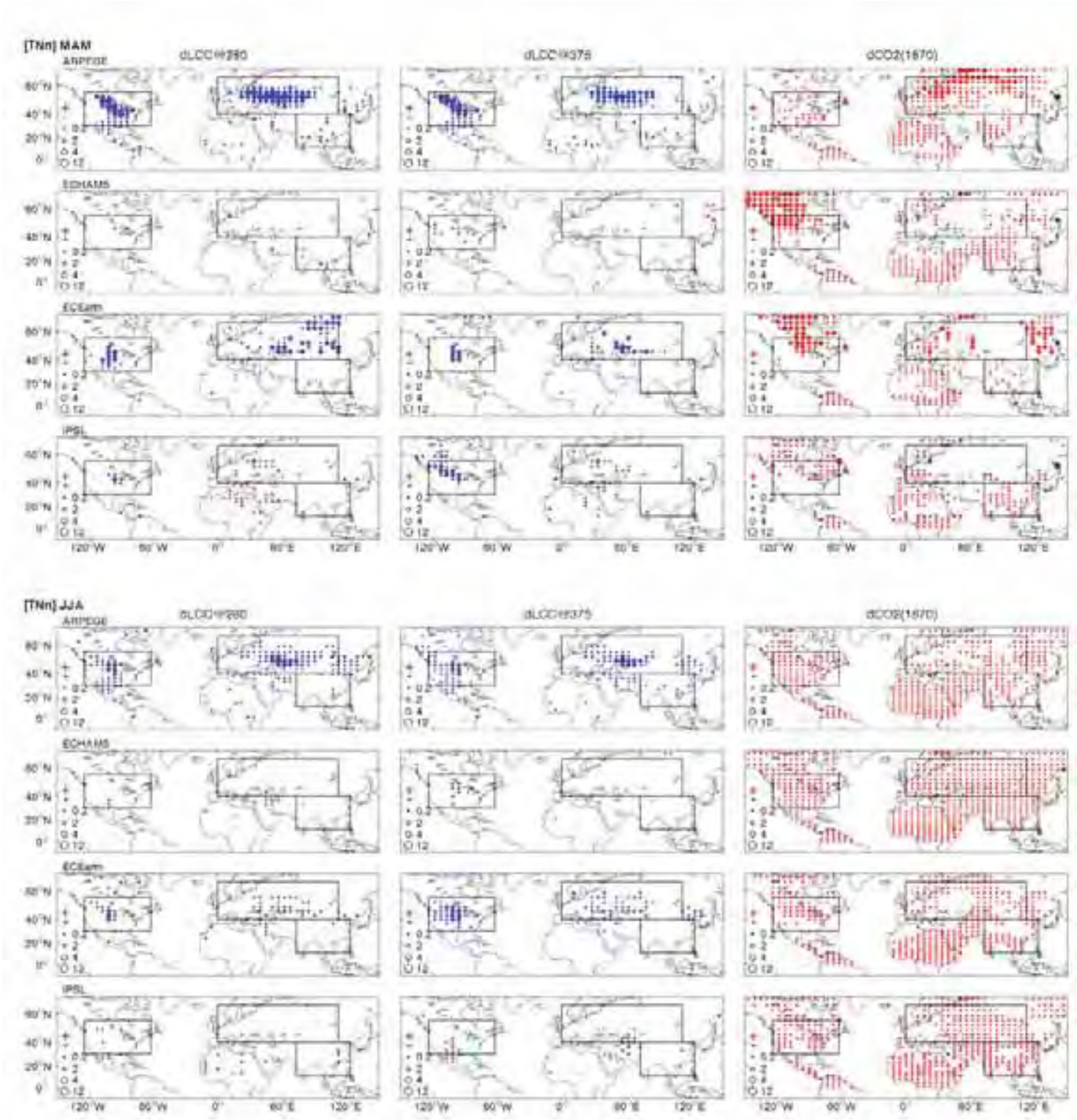

Figure 6-6: As Figure 6-5 but for the coldest seasonal daily minimum temperature, TNn (°C).

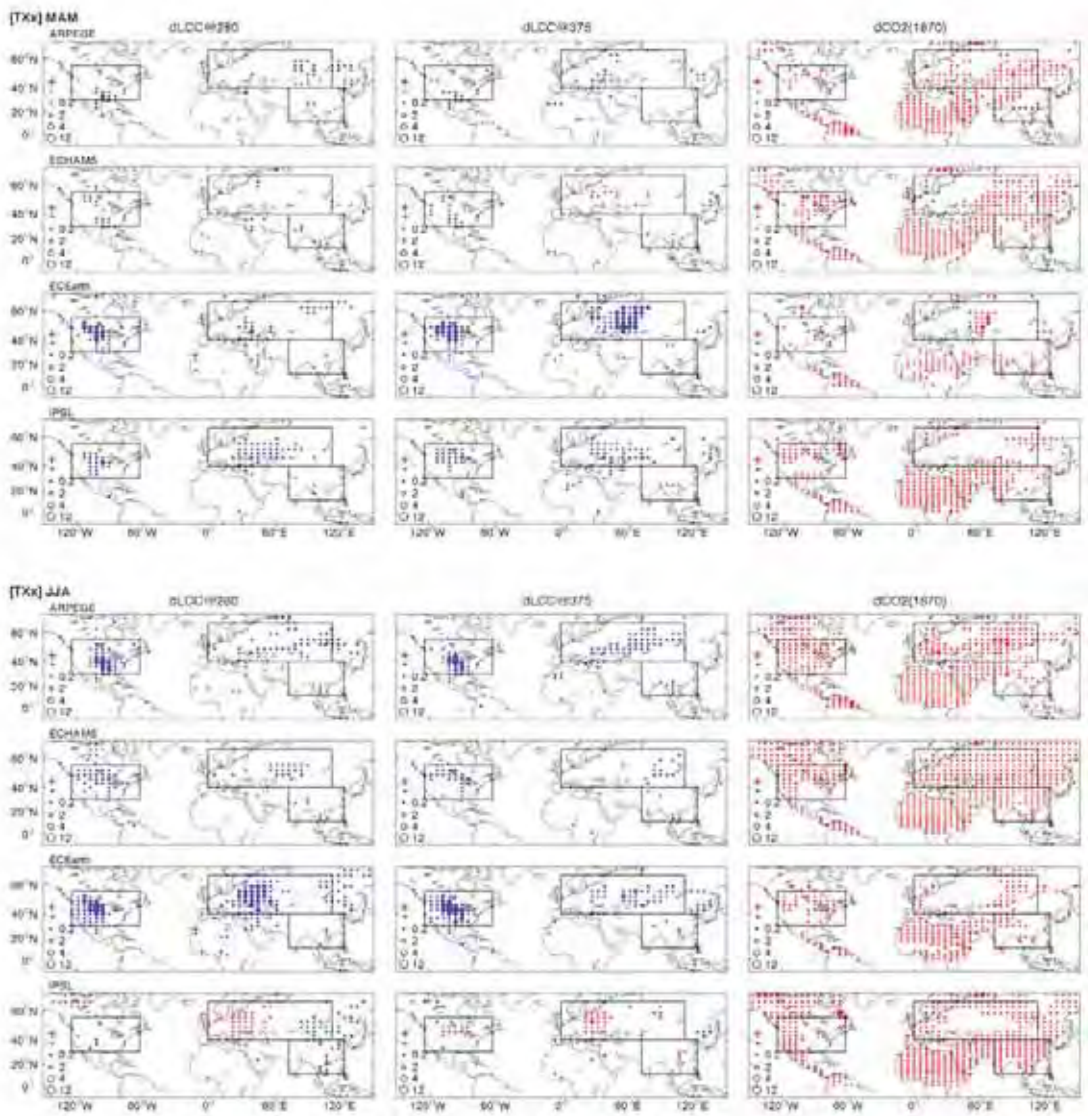

Figure 6-7: As Figure 6-5 but for the warmest seasonal daily maximum temperature, TXx (°C).

Figure 6-8: As Figure 6-5 but for warmest seasonal daily minimum temperature, TNx (°C)

The impact of LULCC on TXx is shown in Figure 6-7 for MAM and JJA. In MAM, a reduction in TXx is simulated due to LULCC by models over some parts of North America but the scale of the reduction varies in spatial scale from most of North America (ECEarth) to just a few grid points (ECHAM5). ECHAM5 simulates a region of increase in TXx coincident with the most northern region of LULCC (Figure 6-2) over North America. Results are generally consistent over North America between the models at both 280 ppmv and 375 ppmv although over Eurasia, ECEarth simulates a larger region of decreases in TXx and ECHAM5 simulates increases in TXx at 375 ppmv. The impact of the increase in CO_2 on TXx is generally more widespread and is almost always an increase. Thus, in most models the CO_2 induced increase in TXx is suppressed by LULCC. In the case of ECEarth and IPSL, the decrease in TXx due to LULCC in MAM would dominate the change due to an increase in CO_2 reversing the sign of the change over Eurasia and over large parts of North America. Results are similar for JJA with the exception of IPSL, which simulates an increase in TXx, amplifying the impact of increased CO_2 while the other models simulate a decrease in TXx locally suppressing the response to CO_2. The increase in IPSL is related to the increase in the mean temperature (Figure 6-3). In both MAM and JJA, the scale of impact of LULCC on TXx is of a similar magnitude, but much less widespread, than the impact of increasing CO_2. There are no changes in TXx remote from regions of LULCC that are consistent between the models.

Comparing Figure 6-3 with Figure 6-7 suggests some relationship between the change in the mean surface air temperature and the change in TXx for LULCC. However, while the sign of the change in TXx accurately reflects the sign of the change in the mean, and to some degree the magnitude of the change in the mean is proportional to the change in the magnitude of TXx, these are model dependent. The relationship between the change in the mean and the change in TXx is strong in ECEarth for all regions of significant LULCC (Figure 6-9). In contrast, the relationship is weaker for ARPEGE but there is still a tendency for a large increase in the mean to be reflected by a larger increase in TXx. There is no relationship between the change in the mean and the change in TXx in ECHAM5 and IPSL. The result is virtually identical for other seasons. Following how Boisier et al. [2012] explored the role of the total turbulent energy flux (the sum of the sensible and latent heat fluxes) in explaining the impact of LULCC, results show no relationship between the change in the total turbulent energy flux and the change in TXx.

Similar patterns of results are shown for TXn (Figure 6-5), TNn (Figure 6-6) and TNx (Figure 6-8). LULCC reduces temperatures in MAM and in JJA by similar amounts at 280 ppmv and 375 ppmv and in both cases this offsets increases in temperatures due to the increase in CO_2. In MAM and JJA there are quite a large temperature response to LULCC in ARPEGE and ECEarth and a weak response in ECHAM5 and IPSL. As with TXx, there are no changes in these indices remote from regions of LULCC that are consistent between the models.

The relationships between the change in the mean temperature and TXx are shown in Figure 6-9. While ECEarth shows a strong relationship, where the change in TXx increases with the increasing changes in the mean, and ARPEGE shows a slightly weak relationship, the other models do not show any relationship between the changes in the mean and TXx. The other temperature intensity extremes (TXn, TNn and TNx) show a similar lack of relationship to the changes in the mean temperature.

The changes in the diurnal temperature range (DTR), defined as the seasonal mean difference between the daily maximum and minimum temperatures, are shown in Figure 6-10. Changes over a large portion of North America are evident for all models during JJA, but the extent varies between models during MAM. The change is generally towards a cooling range except for ARPEGE during JJA and ECHAM5 during MAM. Over Eurasia, the change is not so extensive but still discernable. The DTR decreases for most models during the MAM and JJA, except for ECHAM5; and IPSL during MAM, which shows increased DTR. The changes at 375 ppmv are broadly similar to that at 280 ppmv. Compared to the change due increased CO_2, the changes in DTR due to LULCC are broadly similar (except for ECHAM5 during JJA) over North America and Eurasia. The change in DTR due to LULCC over is limited to a few grid points. The same may be said for the change due to CO_2, except for ARPEGE, which shows extensive decreases during both seasons.

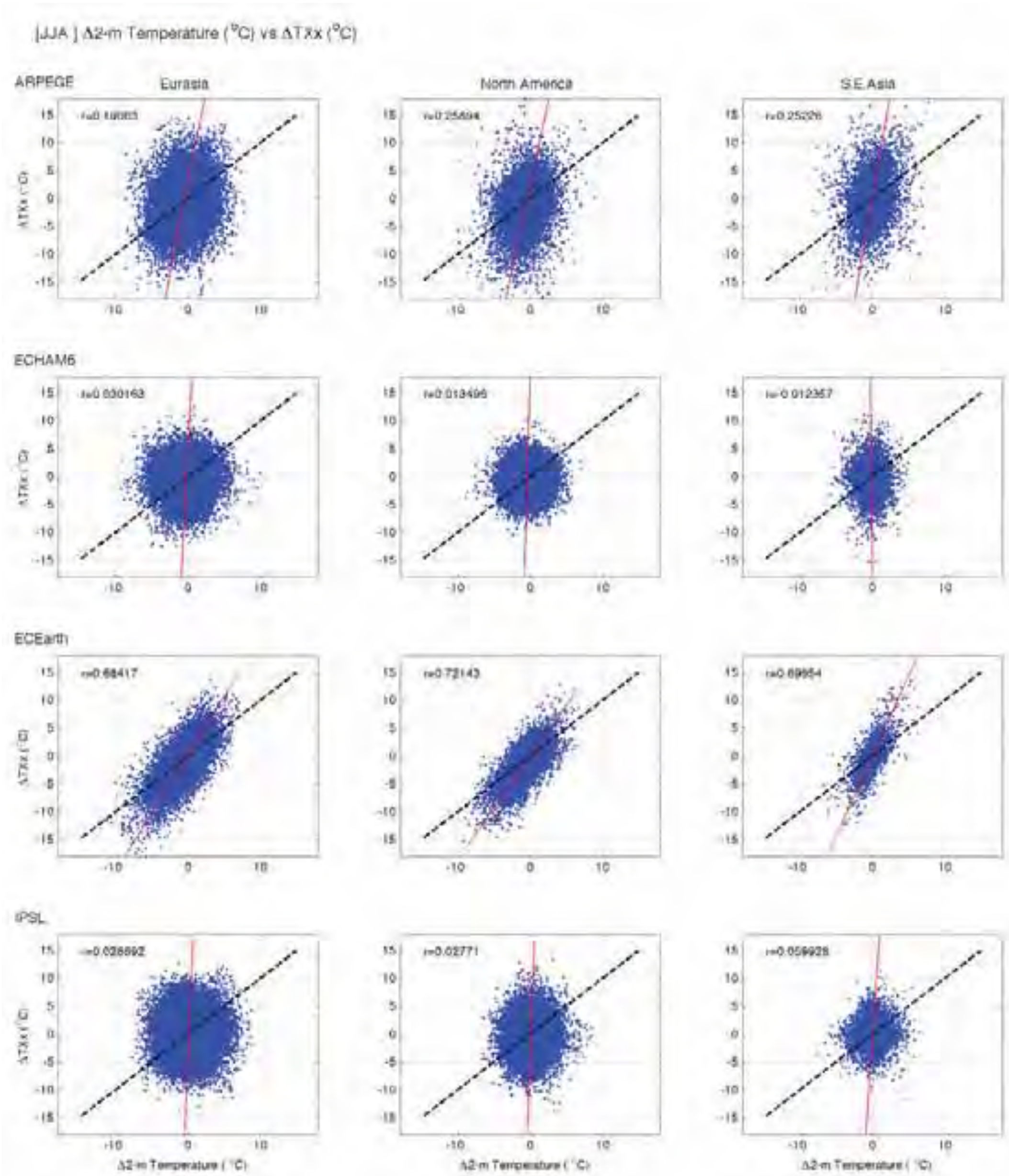

Figure 6-9: Relationship between the change in TXx (y-axis) and the change on the mean surface air temperature (x-axis) due to LULCC at 280 ppmv in JJA for each model for the LULCC grid points within the three regions shown in boxes in Figure 6-2: Eurasia (left column), North America (middle column) and S.E. Asia (right column). The dashed line is the one-to-one line and the red line is a total least-squared regression line of best fit.

Figure 6-10: As Figure 6-5 but for the diurnal temperature range, DTR (°C).

6.4.3 Impact of LULCC on temperature frequency extremes

As with the temperature intensity extremes, the patterns of change for the temperature frequency extremes (Figures 6-11 to 6-14) are similar enough that they can be described using the details of one index, for example, TX90p (Figure 6-13). To allow a comparison of the different forcing effects, all percentile exceedances relate to the $10^{th}/90^{th}$ percentile of daily maximum or minimum temperature calculated for the PI simulation.

The impact of LULCC on TX90p (warm days, defined as the number of days when Tmax > 90^{th} percentile) shows decreases in this measure over North America and Eurasia in MAM in ARPEGE, ECEarth and IPSL but little change in ECHAM5 (Figure 6-13). There are reasonable similarities between the impact at 280 ppmv and 375 ppmv. As with TXx and TNn, LULCC tends to locally offset the impact of increasing CO_2. Again, in common with TXx, IPSL simulates an increase over parts of Europe in JJA in contrast to the decrease simulated by the other models. The other models simulate decreases in TX90p to varying degrees. Thus, in JJA, LULCC locally offsets the impact of increased CO_2 on TX90p in ARPEGE, ECHAM5 and ECEarth but amplifies it in IPSL. Consistent with earlier results there are no changes in TX90p remote from regions of LULCC that are consistent between the models.

Results are very similar for TX10p (Figure 6-11), for TN10p (Figure 6-12) and for TN90p (Figure 6-14). In each case, the overall impact of LULCC is a cooling (increased TN10p and TX10p, decreased TN90p) of these measures in both North America and Eurasia offsetting the CO_2-induced warming except with IPSL in JJA where the measures suppress the CO_2-induced decreases (TN10p, TX10p) and increases (TN90p), respectively. In all cases, there are no changes in any index remote from regions of LULCC that are consistent between the models.

The relationship between the temperature frequency extremes indices with the mean temperature is similar to that of the temperature intensity extremes. ECEarth shows a strong relationship between mean temperature and the number of cool days (TX10p) and cool nights (TN10p) while ARPEGE shows a slightly weaker relationship. Both ARPEGE and ECEarth show an increase in the cold extremes consistent with the decrease in the mean temperature, at varying degrees over all three regions of LULCC. On the other hand, ECHAM5 and IPSL do not show any correlation between TX10p and TN10p with the mean temperature. For the number of warm days (TX90p) and warm nights (TN90p), ECEarth and ARPEGE show correlations with the mean temperature, again at varying degrees (stronger for ECEarth and weaker for ARPEGE) over the three LULCC regions. The number of warm days and nights increase as the mean temperature increases. As with the cold extremes, both ECHAM5 and IPSL show no correlation with the mean temperature.

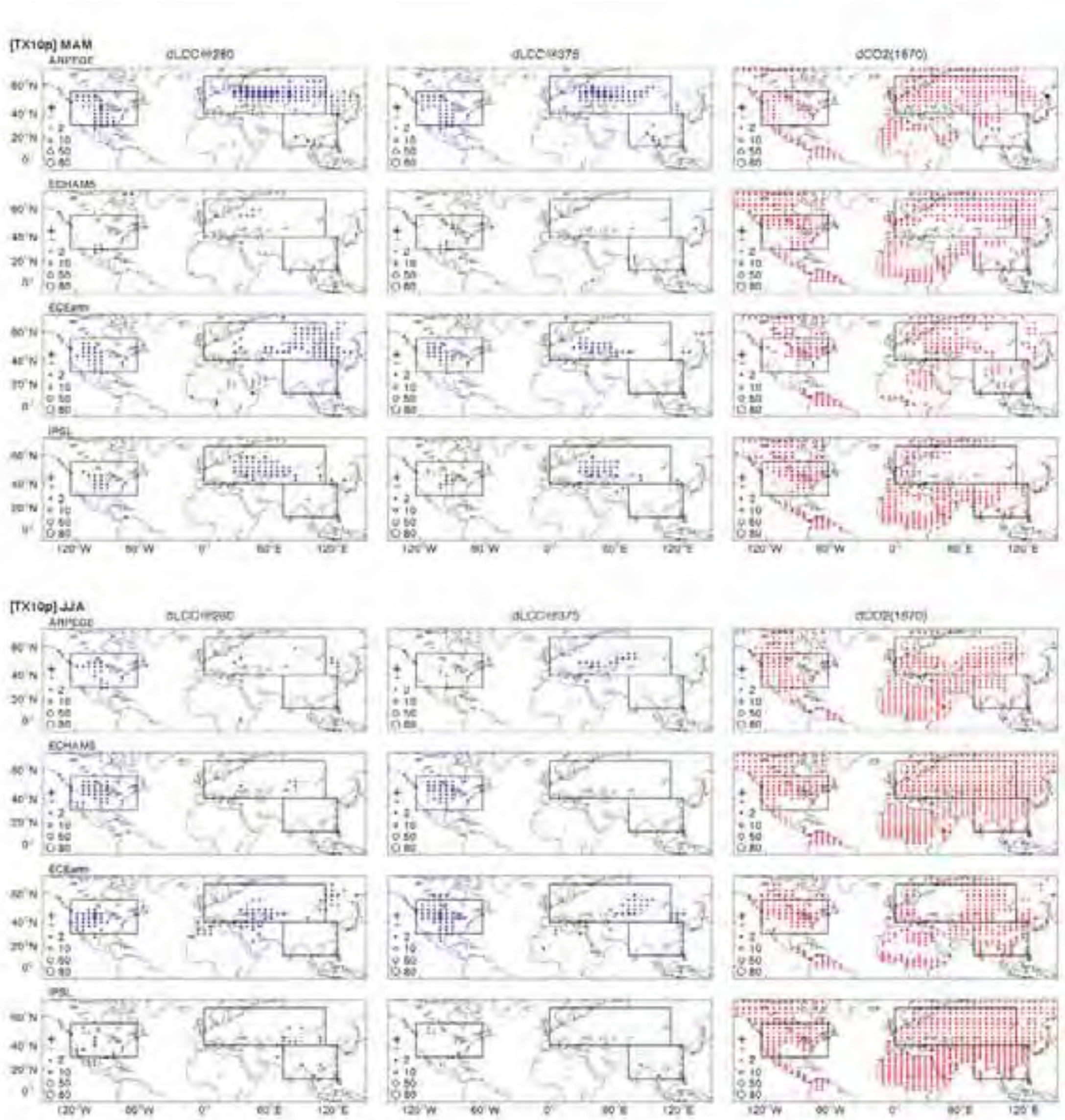

Figure 6-11: As Figure 6-5 but for the number of cool days, TX10p (days/season). The red dots indicate less frequent cool days; the blue dots indicate more frequent cool days.

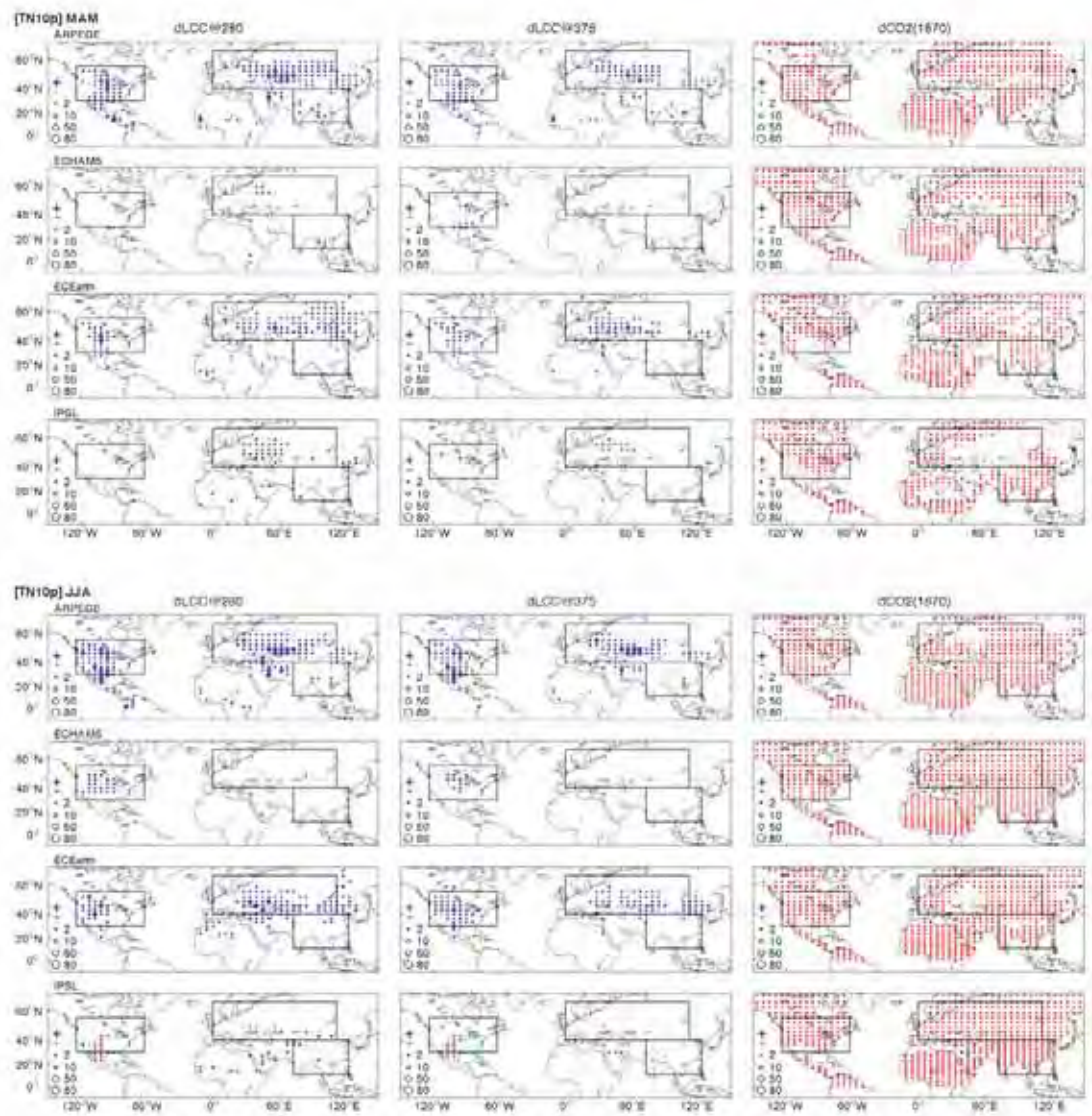

Figure 6-12: As Figure 6-5 but for the number of cool nights, TN10p (days/season). The red dots indicate less frequent cool nights; the blue dots indicate more frequent cool nights.

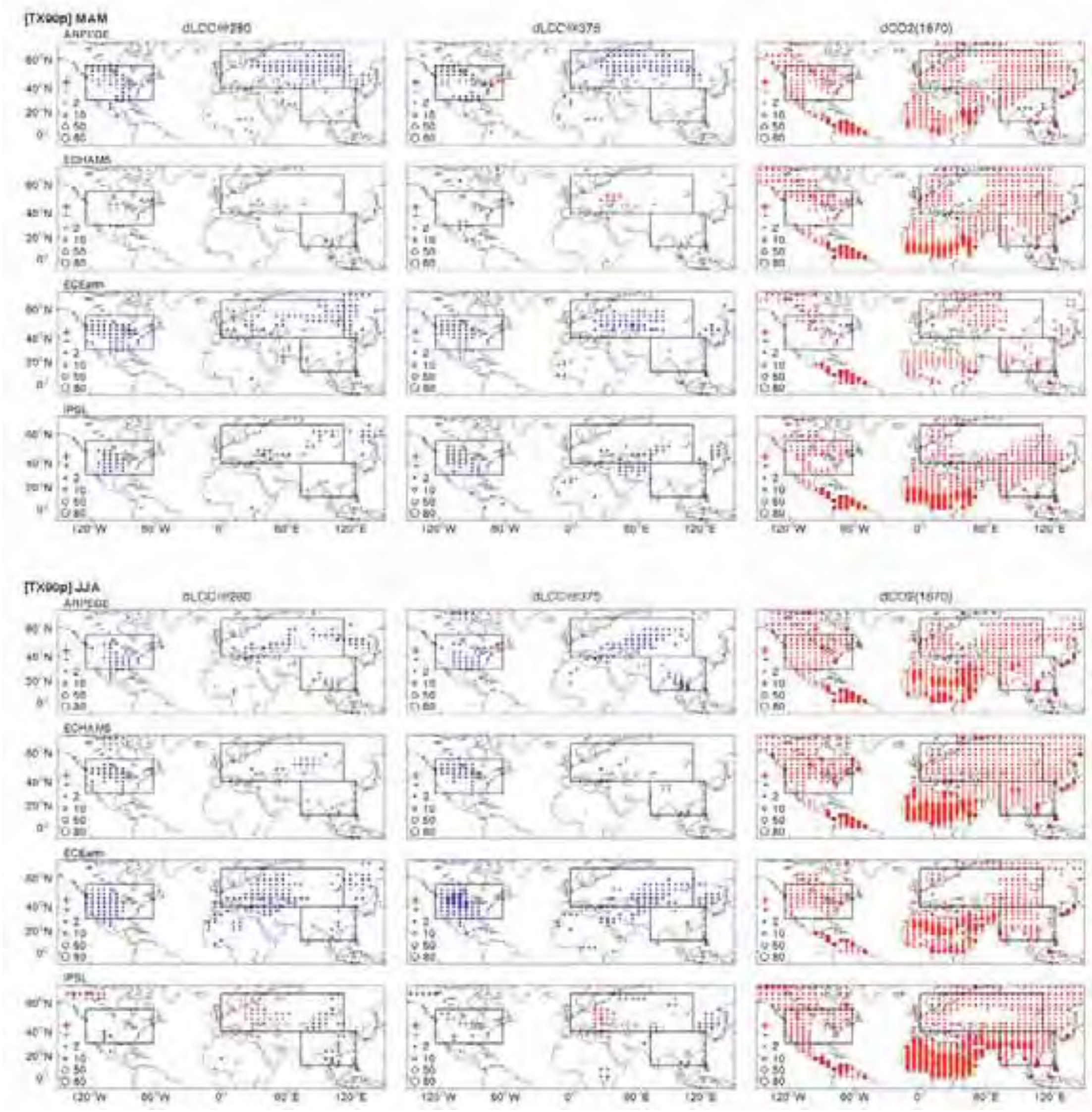

Figure 6-13: As Figure 6-5 but for number of warm days, TX90p (days/season). The red dots indicate more frequent warm days; the blue dots indicate less frequent warm days.

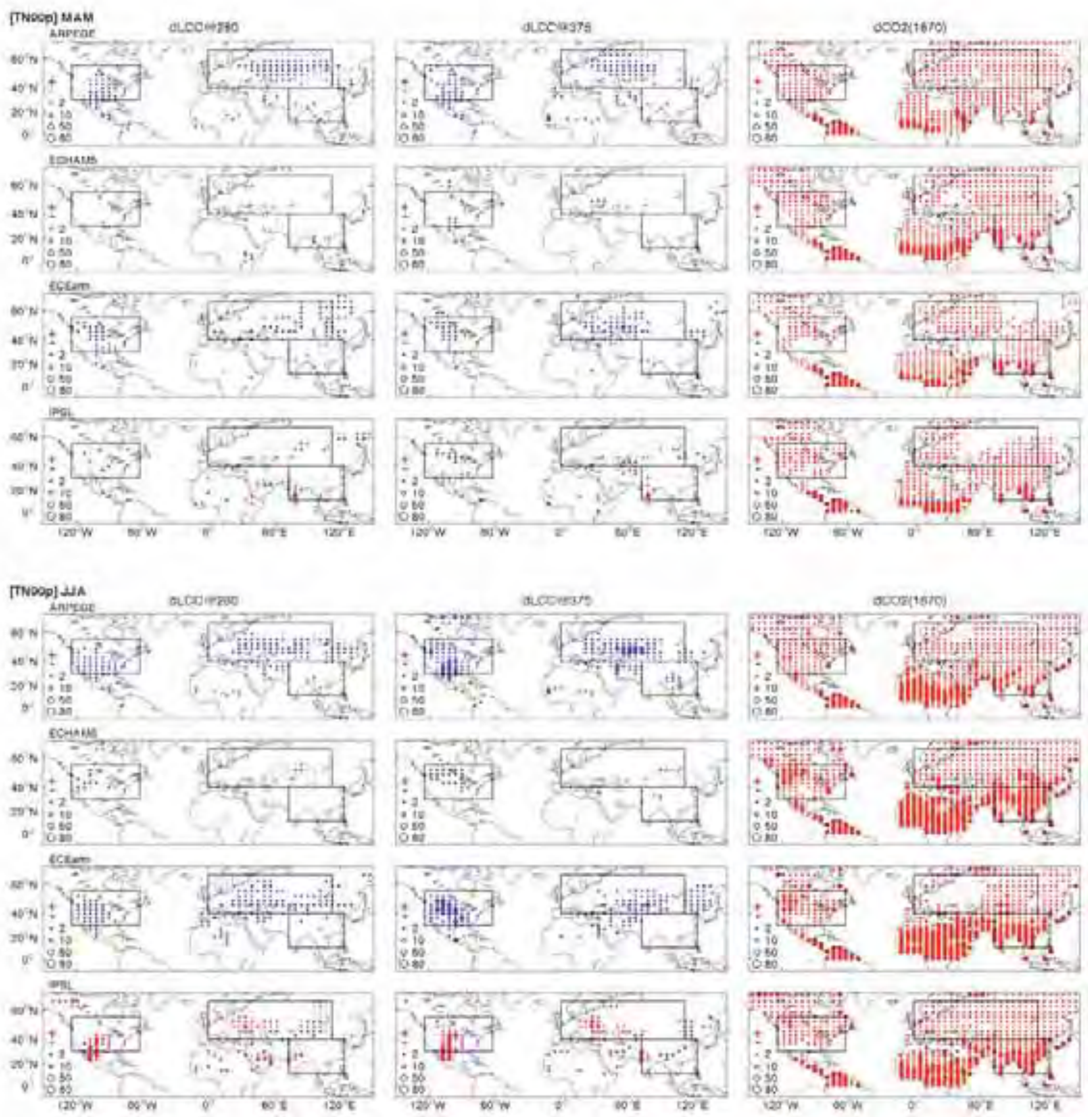

Figure 6-14: As Figure 6-5 but for the number of warm nights, TN90p (days/season). The red dots indicate more frequent warm nights; the blue dots indicate less frequent warm nights.

6.4.4 Impact of LULCC on temperature duration extremes

Consistent with the cooling impact of LULCC shown in the temperature intensity and frequency indices, Figure 6-15 shows that the impact of LULCC in the growing season length (GSL) is a shortening of the growing season over North America and Eurasia for ARPEGE and ECEarth; no change is simulated by ECHAM5 and IPSL over the same regions. GSL is defined as the count between the first span of at least 6 days with daily mean temperature > 5°C and the first span of 6 days with daily mean temperature < 5°C, where the year is defined as 1 Jan to 31 Dec for the Northern Hemisphere and 1 July to 30 June for the Southern Hemisphere. It can be interpreted as a period of mild weather and is only relevant over the mid- to high-latitudes. The LULCC-induced decrease in GSL is similar at both 280 and 375 ppmv CO_2 levels and counters the increase in GSL induced by the increase in CO_2.

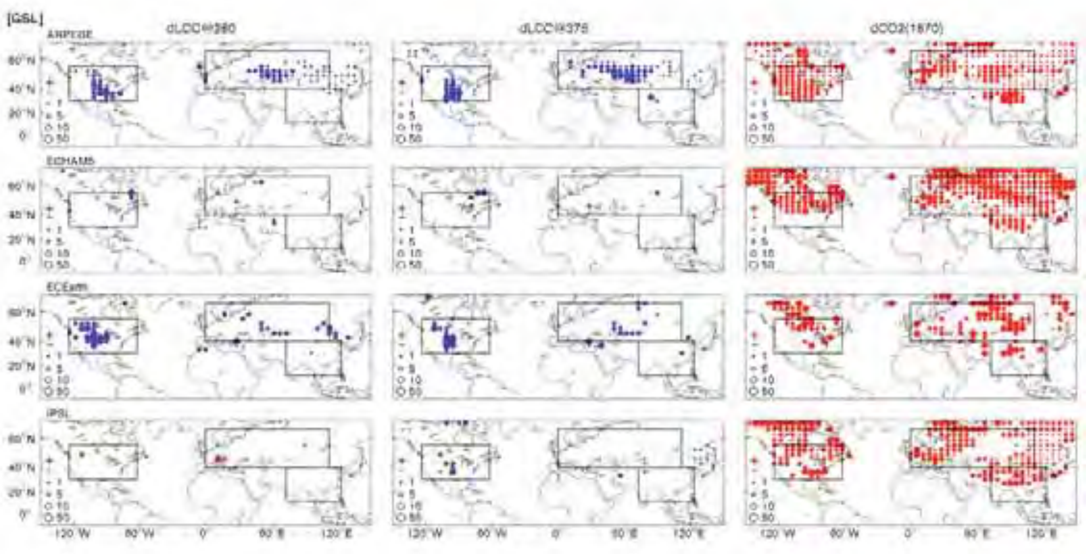

Figure 6-15: As Figure 6-5 but for growing season length, GSL (days/year). Note that red dots indicate a change towards longer growing seasons; the blue dots indicate a change towards shorter growing seasons.

There is a very strong response to LULCC in the cold spell duration (CSDI, Figure 6-16) in ARPEGE and ECEarth. Both models simulate a large increase in days with at least 6 consecutive days when Tmin < 10^{th} percentile at both 280 and 375 ppmv. These changes are large relative to the impact of the increased CO_2 and oppose the sign of the net impact from CO_2 alone. CSDI in ECHAM5 is consistently insensitive to LULCC, in part due to the lower intensity of the LULCC (Figure 6-2 and Table 6-4). Changes in CDSI are CO_2 concentration specific and the impact of LULCC declines under higher CO_2 in most models. Such a decrease is most clear in ECEarth but is also apparent in ARPEGE (North America and S.E. Asia) and IPSL (a lot of significant points disappear under higher CO_2). This is likely due to CO_2-induced warming and a loss of snow cover that reduces the sensitivity of the climate to LULCC [*Pitman et al.*, 2011].

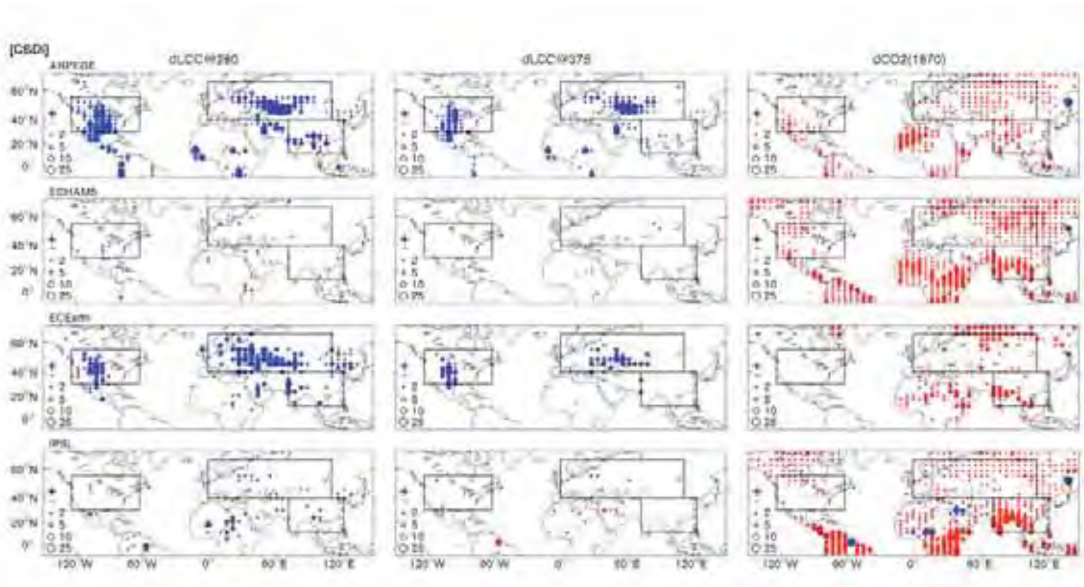

Figure 6-16: As Figure 6-5 but for the cold spell duration index (CSDI, days/year). Note that red dots indicate shorter cold spells; the blue dots indicate longer cold spells.

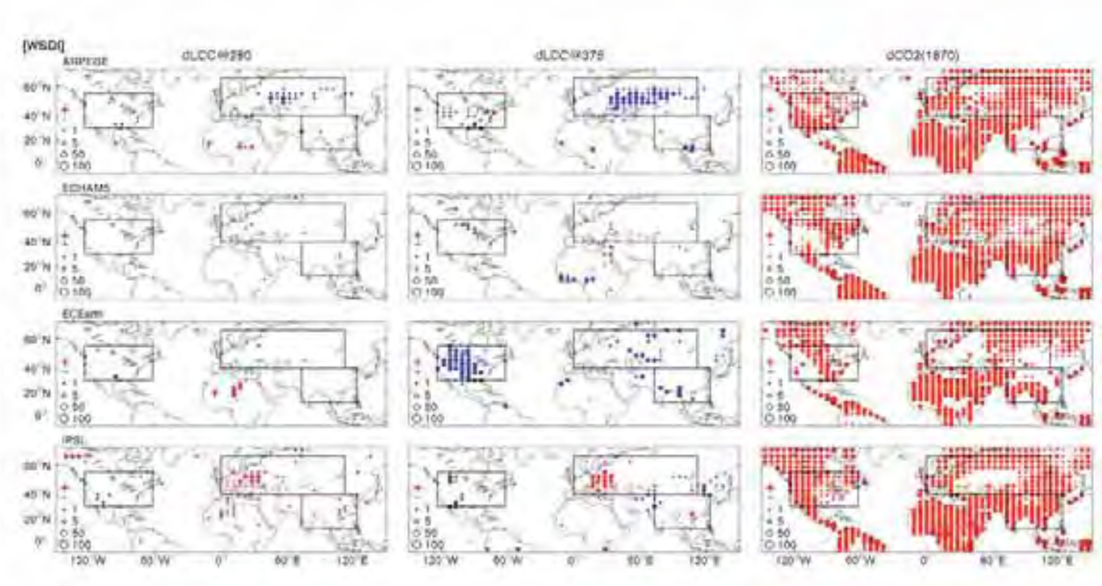

Figure 6-17: As Figure 6-5 but for the warm spell duration index (WSDI, days/year). Note that red dots indicate longer warm spells; the blue dots indicate shorter warm spells.

The impact of LULCC on WSDI (warm spell duration) is shown in Figure 6-17. ARPEGE simulates a decrease in WSDI over Eurasia, IPSL simulates an increase, ECHAM5 and ECEarth simulate negligible change at 280 ppmv. There is a strong amplification of the impact of LULCC at 375 ppmv in ARPEGE over Eurasia and in ECEarth over North America. Both of these amplifications would largely offset the CO_2-induced changes. Again, consistent with earlier results there are no changes in GSL, CSDI or WSDI remote from regions of LULCC that are consistent between the models.

6.4.5 Impact of LULCC on rainfall extremes

Figures 6-18 and 6-19 show the results for RX1day and RX5day, respectively. Results from RX1day, the maximum rainfall occurring over a 1-day period were similar in geographic extent and of order 20% of the magnitude shown for RX5day, the maximum rainfall occurring over a 5-day period.

The results for RX5day for MAM and JJA are shown in Figure 6-19. There are both increases and decreases in RX5day. There is a co-location of decreases in RX5day and LULCC over North America and Eurasia in both seasons in ARPEGE at 280 ppmv, but not at 375 ppmv. RX5day increases and decreases at different grid points over North America in JJA in ECHAM5 at both CO_2 levels. There are increases in RX5day at 375 ppmv in JJA in ECEarth, but not at 280 ppmv. Finally, RX5day is reduced in IPSL at both levels of CO, in JJA.

The JJA results from ARPEGE and IPSL suggest that rainfall extremes in these models do respond to LULCC, both models showing a decrease of extreme precipitation at many grid boxes affected by LULCC. One would expect the largest impact of LULCC on rainfall extremes to be during summer coincident with high net radiation, surface evaporation and convection. ECHAM5 and ECEarth do not hint at a large change in RX5day, particularly in Eurasia.

The results for ECEarth match the response of the mean precipitation to LULCC (Figure 6-4). Figures 6-20 shows the relationship between changes in RX5day and mean rainfall. ARPEGE, ECHAM5 and IPSL display very similar behaviours over the three regions of LULCC. There is a strong relationship between changes in mean rainfall and changes in RX5day in ECEarth in all three regions of LULCC where the small changes in the mean appear to be related to large changes in RX5day. In contrast, in ARPEGE, ECHAM5 and IPSL, changes in the mean rainfall do not appear related to changes in RX5day. The relationship between RX5day and the total turbulent energy flux was also explored. ARPEGE and ECEarth suggest a negative correlation between total turbulent fluxes and decreasing RX5day pointing towards a suppression of heavy precipitation events at larger surface heat flux values [*Schar et al.*, 1999]. However, ECHAM5 and IPSL show no correlation between changes in the total turbulent fluxes and RX5day, suggesting that LULCC is not the cause of the change in RX5day in these models.

The scale of the simulated change in RX5day is worthy of note. The largest change in RX5day is of order 2 mm day^{-1} in the 5-day rainfall total on the seasonal timescale (Figure 6-19). In the four models used here, even if LULCC does perturb rainfall extremes, the scale of the change is very small relative to the size of the event. While changes in the individual RX5day can exceed 50 mm (Figure 6-20), these cannot be attributed to LULCC because the correlations are too uncertain.

The succeeding figures show the changes in the other precipitation extremes indices: SDII (Figure 6-21), defined as the daily precipitation amount during wet days; R95pT (Figure 6-22), the annual contribution from very wet days; R10mm (Figure 6-23), the annual number of days when precipitation exceeds 10 mm; CWD (Figure 6-24), the annual number of consecutive wet days; and CDD, the annual number of consecutive dry days (Figure 6-25).

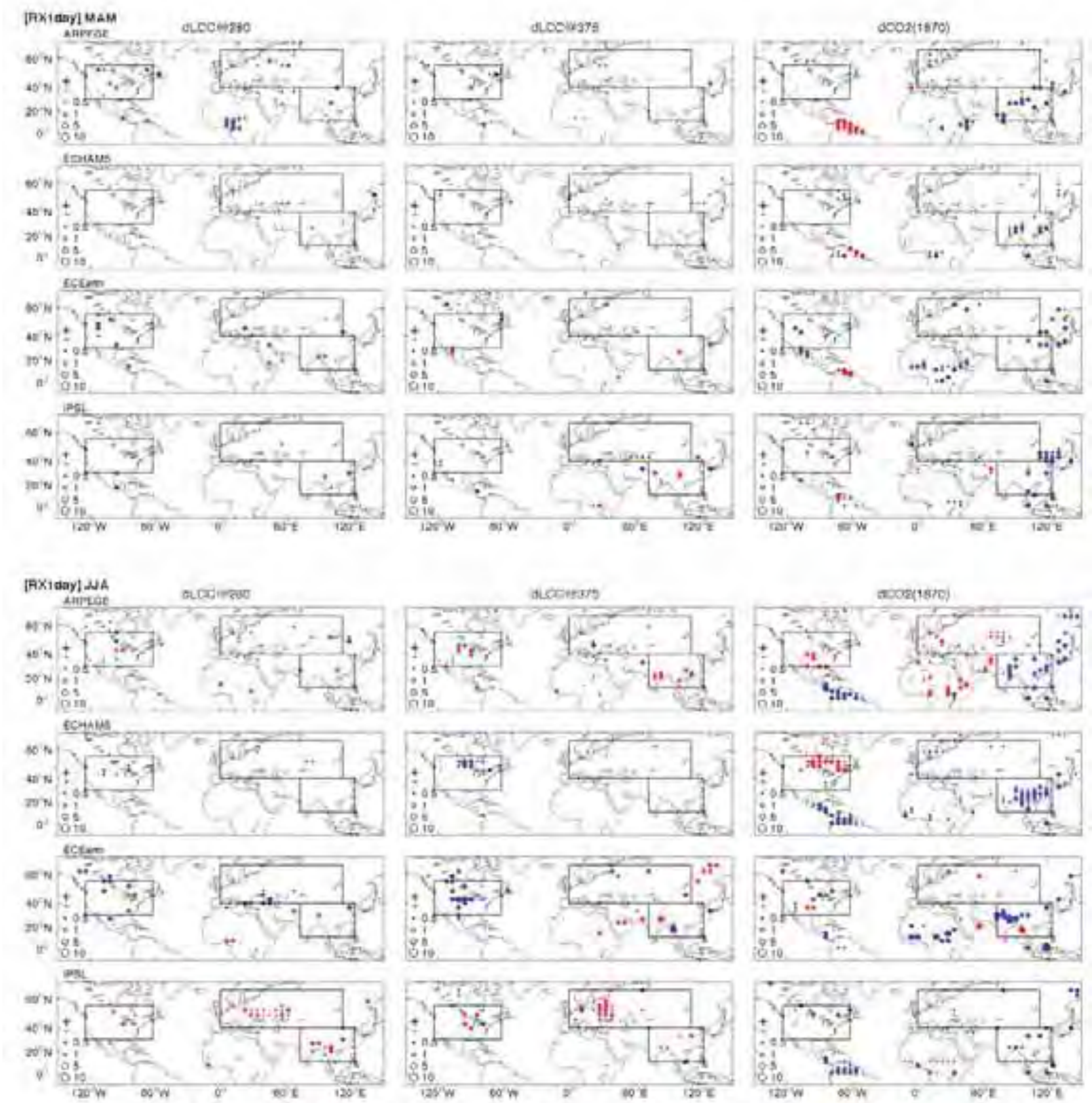

Figure 6-18: As Figure 6-5 but for the seasonal maximum 1-day precipitation, RX1day (mm). The red dots indicate decreased rainfall; the blue dots indicate increased rainfall.

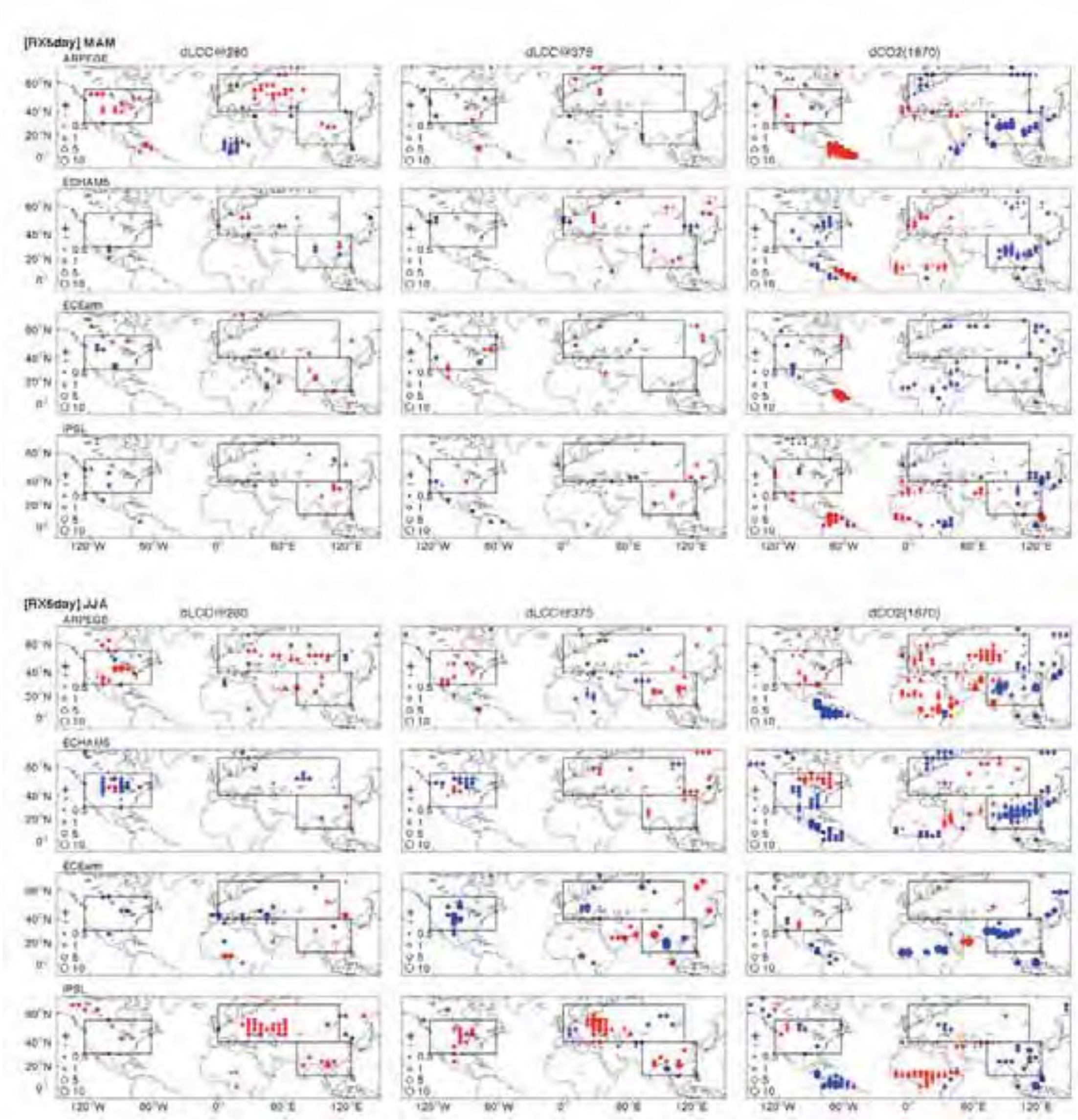

Figure 6-19: As Figure 6-5 but for the seasonal maximum rainfall occurring during a 5-day consecutive period, RX5day (mm). The red dots indicate decreased rainfall; the blue dots indicate increased rainfall.

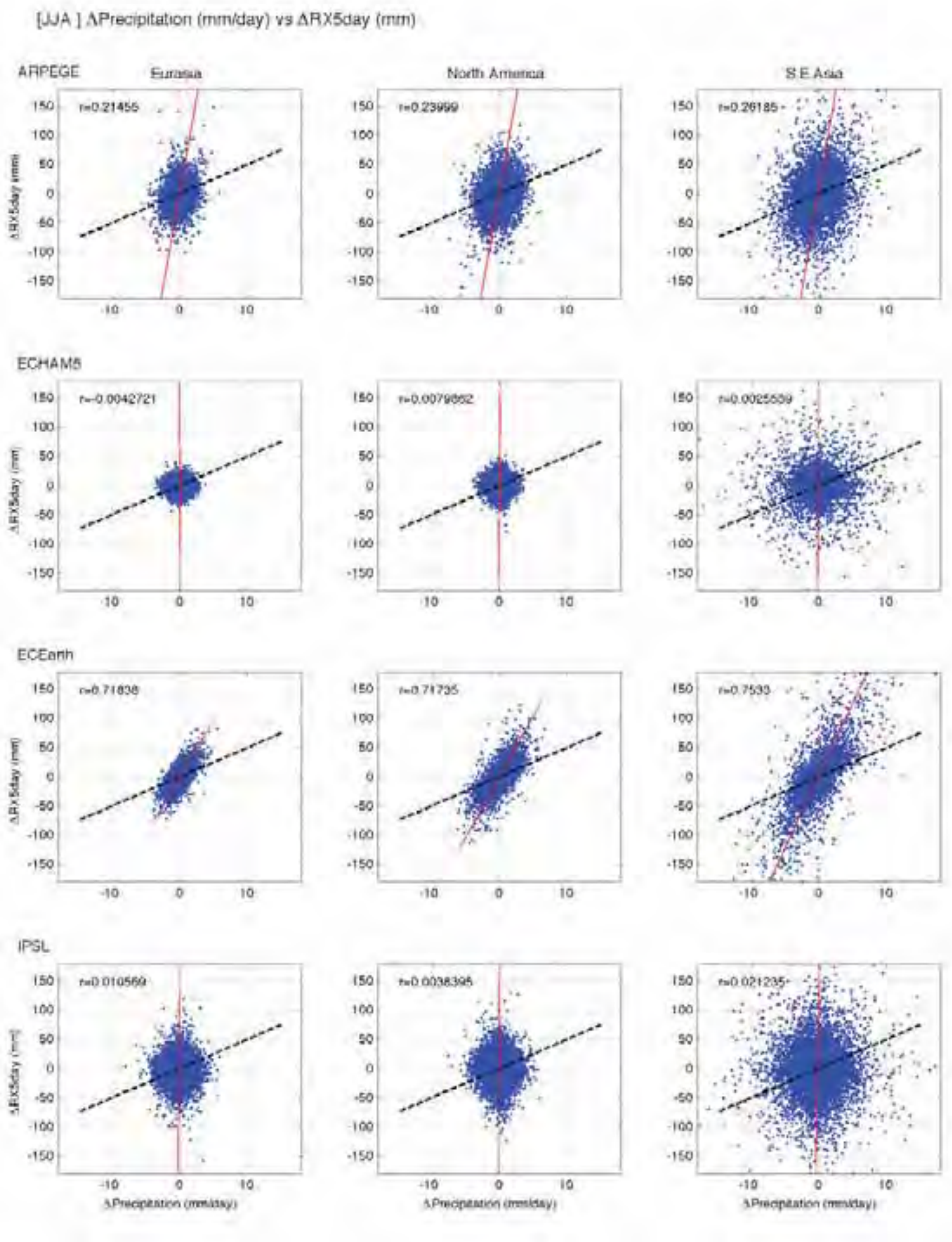

Figure 6-20: As Figure 6-10 but for the change in RX5day relative to the change in mean precipitation (mm).

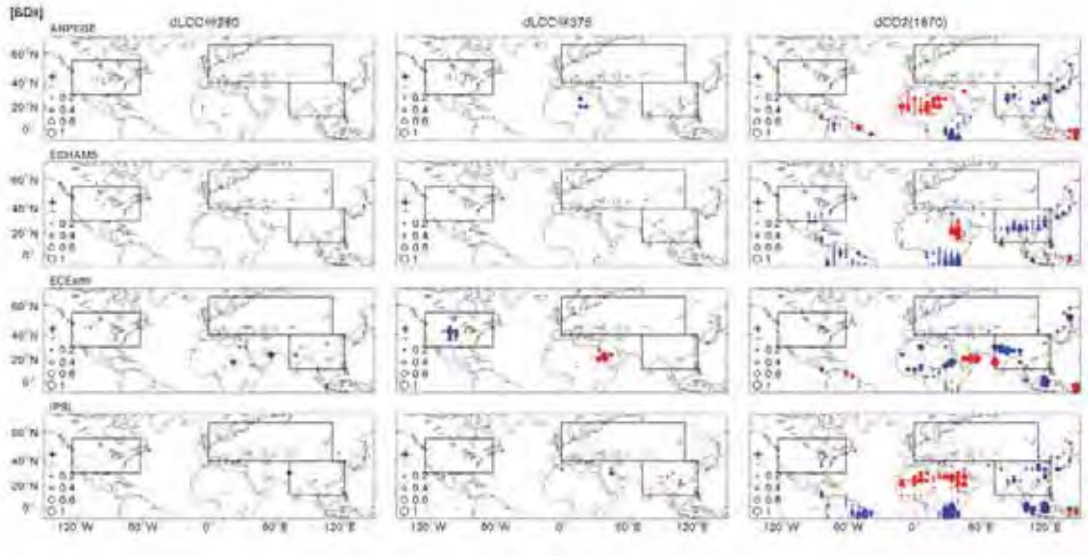

Figure 6-21 As Figure 6-5 but for the simple daily intensity index, SDII (mm/day). The red dots indicate decreased rainfall; the blue dots indicate increased rainfall.

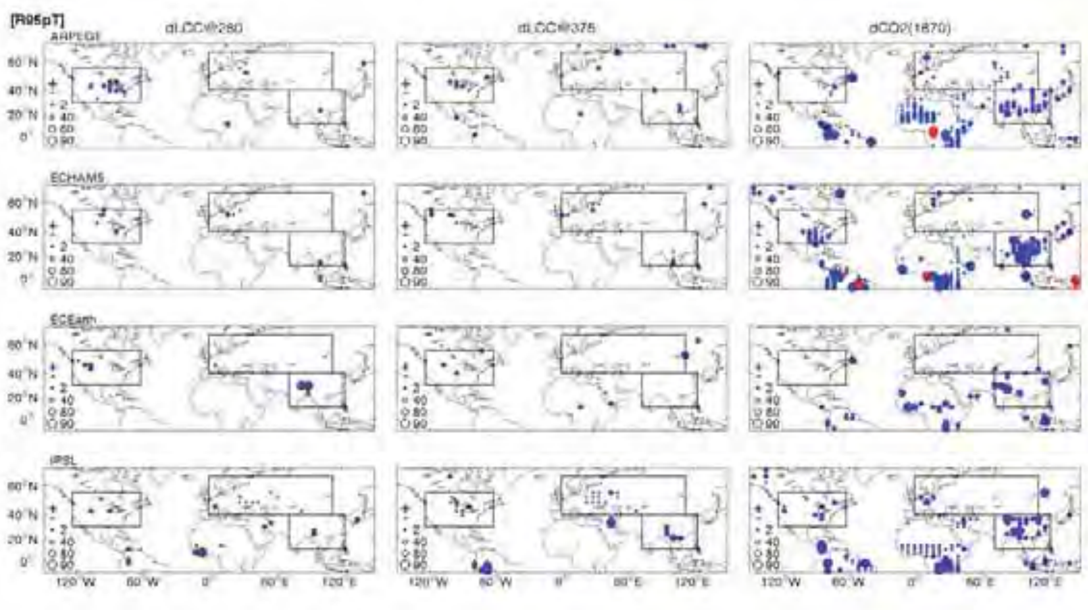

Figure 6-22: As Figure 6-5 but for the annual contribution from very wet days, R95pT (%). The red dots indicate decreased contribution of high-intensity rainfall to the annual rainfall total; the blue dots indicate increased contribution of high-intensity rainfall to the annual rainfall total.

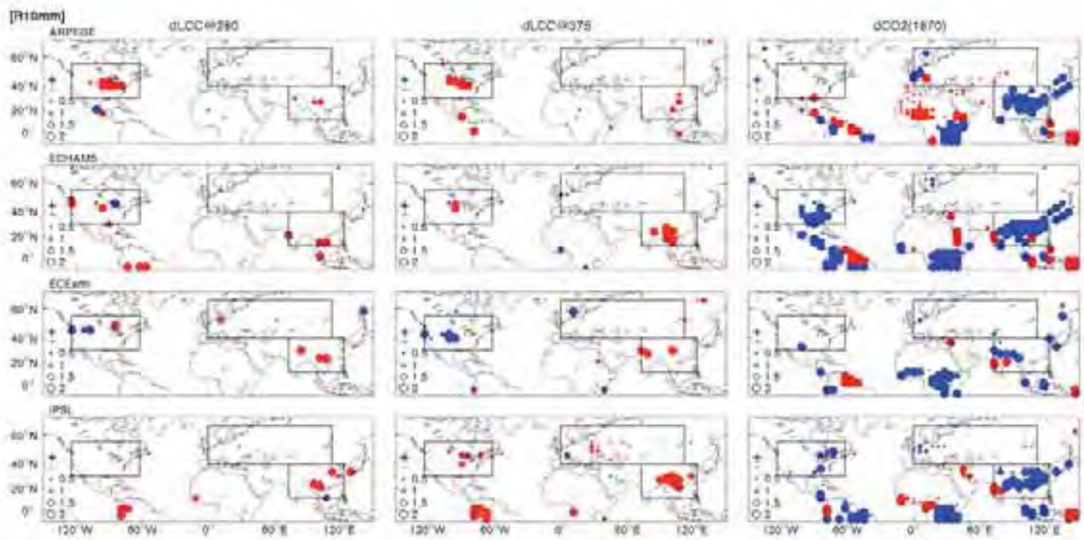

Figure 6-23: As Figure 6-5 but for heavy precipitation days, R10mm (days). The red dots indicate decreased frequency of days with rainfall >= 10mm; the blue dots indicate increased frequency of heavy rainfall days.

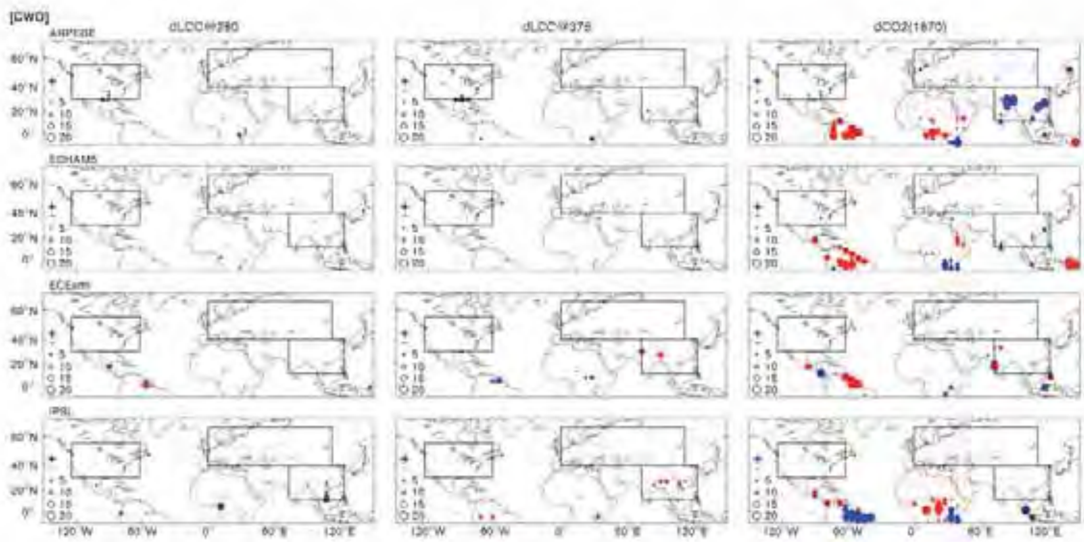

Figure 6-24: As Figure 6-5 but for consecutive wet days, CWD (days). The red dots indicate shorter wet spells; the blue dots indicate longer wet spells.

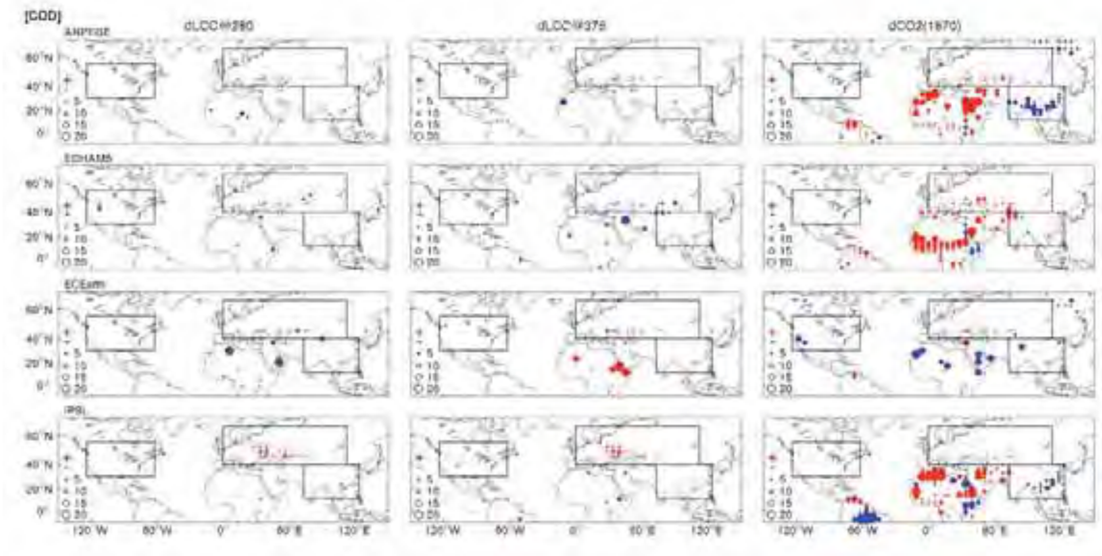

Figure 6-25: As Figure 6-5 but for consecutive dry days, CDD (days). The red dots indicate longer dry spells; the blue dots indicate shorter dry spells.

While most of the indices shown in Figures 6-21 to 6-25 do not show significant change due to LULCC, it is interesting to note that over Asia, R10mm (Figure 6-23) shows a larger region of decrease in the number of heavy precipitation days at 375 ppmv than at 280 ppmv. This change occurs on all models at varying degrees, with ECHAM5 and IPSL showing the largest extent of change. This LULCC-induced decrease counters the large and extensive increase due to CO_2. This is interesting because it suggests that while the intensity of precipitation extremes do not appear to change significantly over the region (Figures 6-18, 6-19, 6-21), there seems to be a consistent change in the frequency of the precipitation extremes (Figure 6-23).

Figure 6-26 summarizes the impact of LULCC at 280 ppmv and 375 ppmv relative to the increase in CO_2 the field significance, expressed as a percentage of grid points that underwent statistically significant changes. The increase in CO_2

from 280 ppmv to 375 ppmv led to statistically significant changes in all temperature indices in all models in both MAM and JJA. The number of statistically significant points varied by region, by model, and by season but there is clearly a strong and coherent change in the ETCCDI temperature indices due to the increase in CO_2. In contrast, the rainfall indices change in a smaller percentage of grid points. In ECEarth, no statistically significant changes in the rainfall indices occur due to the increase in CO_2 in some regions. In terms of LULCC's impact on the ETCCDI indices, the percentage of points showing a field significant change is smaller than the impact due to increased CO_2, but the impact of LULCC is not negligible. One would expect a smaller impact because while increased CO_2 affects every grid point within every region, there are grid points within each region where there is no, or only a very weak land cover perturbation. Despite this contrast between the scale of perturbation, in ARPEGE, ECEarth and to a smaller degree IPSL, 20-50% of grid points undergo statistically significant changes in the temperature indices in both MAM and JJA. ECHAM5, which demonstrated a relatively high sensitivity to the change in CO_2, is the least sensitive to LULCC with only North America experiencing more than 20% of grid points undergoing field significant change. However, this is likely related, at least in part, to the relatively low intensity of LULCC imposed in the model (Figure 6-2). While the percentage of grid points undergoing significant change in the rainfall indices due to LULCC is generally small, in JJA the scale of impact is not much smaller than the impact due to the increase in CO_2.

	MAM												JJA											
	dLULCC @ 280				dLULCC @ 375				dCO2 (1870)				dLULCC @ 280				dLULCC @ 375				dCO2 (1870)			
	N. Hemisphere	Eurasia	North America	Southeast Asia	N. Hemisphere	Eurasia	North America	Southeast Asia	N. Hemisphere	Eurasia	North America	Southeast Asia	N. Hemisphere	Eurasia	North America	Southeast Asia	N. Hemisphere	Eurasia	North America	Southeast Asia	N. Hemisphere	Eurasia	North America	Southeast Asia
ARPEGE																								
TXn	16	33	35	-	11	22	31	-	36	60	13	13	6	8	13	-	7	12	-	-	56	51	51	57
TNn	23	38	40	17	20	29	43	13	52	65	39	40	24	42	45	13	22	28	43	21	73	60	87	70
TXx	9	13	14	6	9	13	18	-	49	54	29	44	18	28	40	10	17	31	32	14	71	73	89	44
TNx	18	30	36	11	16	23	31	14	64	59	61	69	23	38	45	13	21	39	48	13	88	82	99	96
DTR	23	25	42	21	19	29	33	13	39	44	8	63	23	33	42	17	29	43	54	30	35	39	29	34
TX10p	29	52	48	19	19	35	44	13	69	92	83	33	12	14	31	-	14	27	25	6	77	73	93	63
TN10p	33	55	52	39	25	33	56	23	87	96	92	84	37	60	74	27	30	44	64	27	94	92	100	99
TX90p	30	54	57	9	23	46	51	-	71	86	74	53	21	34	38	16	20	33	43	23	82	87	99	66
TN90p	29	52	43	14	25	44	50	13	87	98	90	99	30	49	57	19	31	46	63	30	96	97	100	100
RX1day	12	13	11	-	-	-	6	-	14	10	11	26	6	9	12	-	8	6	12	11	21	19	14	24
RX5day	13	15	14	7	-	-	6	-	15	11	10	26	9	12	19	6	8	6	11	11	21	20	11	21
ECHAM5																								
TXn	-	-	-	-	-	7	8	-	41	11	40	43	5	-	21	-	7	-	24	-	86	83	73	86
TNn	-	-	6	13	-	-	10	-	58	30	57	67	-	-	6	-	-	-	12	-	96	99	90	100
TXx	8		20	13	7	7	19	9	58	52	50	60	12	13	39	11	8	9	29	14	89	93	76	83
TNx	8	10	15	10	-	-	14	-	67	56	61	84	7	7	24	-	6	7	21	9	97	100	87	96
DTR	8	9	15	21	11	10	13	11	35	22	17	23	14	19	42	9	14	14	55	19	34	25	52	9
TX10p	6	7	11	-	10	-	37	10	81	77	85	60	11	12	48	-	11	9	44	10	95	100	82	91
TN10p	-	8	-	10	6	-	30	9	93	85	95	91	9	10	38	7	8	-	30	10	99	100	95	100
TX90p	7	7	17	13	8	11	11	6	76	81	56	81	13	17	37	9	9	7	42	16	96	100	81	100
TN90p	6	6	7	11	-	6	10	-	87	93	83	100	10	18	24	-	8	7	31	10	99	100	95	100
RX1day	-	6	-	6	6	9	6	7	13	9	7	21	5	8	10	-	8	10	19	9	24	12	29	40
RX5day	6	7	-	7	5	10	-	7	12	8	11	24	6	7	25	-	8	12	19	7	24	15	32	43
ECEarth																								
TXn	10	25	15	-	-	6	7	-	21	15	12	16	6		12		10	6	46	-	39	35	48	36
TNn	12	27	18	-	7	13	11	7	38	23	27	36	12	20	19		14	24	39	-	63	60	58	61
TXx	13	15	36	-	17	30	44	9	25	17	17	31	25	40	45	6	18	24	56	7	42	29	51	34
TNx	11	17	24	-	15	29	31	6	38	39	39	44	21	42	35		16	23	42	-	58	43	70	80
DTR	10	15	24	-	11	15	29	6	30	20	13	19	16	20	38	6	18	17	58	6	24	17	18	19
TX10p	19	31	33	7	11	16	36	-	46	46	52	43	15	20	32		17	21	52	6	60	57	77	79
TN10p	23	45	32	16	16	29	30	13	75	70	77	76	24	42	37	11	21	36	54	11	90	86	94	90
TX90p	23	36	54	13	18	29	49	6	37	33	20	46	26	38	54	10	24	30	62	6	61	48	76	76
TN90p	18	30	32	16	16	28	31	9	64	65	51	86	23	43	42	6	23	31	51	7	82	67	87	99
RX1day	-	-	8	-	-	-	7	-	9	-	-	7	5	6	8	6	6	-	13	-	8	-	12	17
RX5day	-	-	7	-	-	-	10	-	8	-	6	7	6	6	6		7	6	12	7	8	-	10	13
IPSL																								
TXn	8	17	8	-	11	15	21	-	31	12	24	37	-	-	18	7	-	-	-	6	71	70	73	59
TNn	8	8	7	6	9	9	20	-	39	18	42	56	5	-	7	-	6	7	12	-	75	70	71	83
TXx	11	25	23	7	14	24	27	9	49	28	50	59	16	28		21	11	19	17	11	77	60	52	91
TNx	9	14	6	14	9	9	21	16	56	47	57	79	20	36	18	14	14	20	29	13	89	91	67	97
DTR	18	15	42	21	18	19	29	21	43	23	12	39	20	17	29	27	21	16	36	39	41	35	32	41
TX10p	13	29	21	7	12	19	26	9	73	52	89	81	11	17	18	16	8	9	11	19	96	99	89	93
TN10p	12	19	-	21	9	12	17	7	76	57	92	90	12	14	19	13	11	9	25	17	97	100	89	100
TX90p	14	17	36	7	17	19	37	13	62	53	61	86	19	38	7	29	14	23	17	13	90	80	75	97
TN90p	11	7	12	20	13	13	25	14	69	63	80	97	23	38	25	19	17	22	37	20	95	98	86	100
RX1day	-	-	-	6	6	-	6	7	16	7	7	17	8	13	-	13	7	12	12	10	14	6	8	14
RX5day	-	-	6	7	5	-	-	7	17	9	7	16	9	15	6	9	9	17	13	14	17	6	11	19

Percentage of significant grid points

5 20 40 60 80 90 95

Figure 6-26: Percentage of significant grid points in four regions (Northern Hemisphere, Eurasia, North America and S.E. Asia) for MAM and JJA for each model. The first set of columns of data is for the impact of LULCC at 280 ppmv; the second set of columns is for the impact of LULCC at 375 ppmv; and the third set of columns is for the impact of the increase in CO_2 from 280 ppmv to 375 ppmv. Dashes represent regions and indices where no grid points are significant. The colour scheme emphasizes the percentage of significant grid.

6.5 Summary

The impact of LULCC on regional-scale climate averages has been thoroughly studied and a significant impact on the mean temperature should be anticipated over regions of intense LULCC [*Pielke et al.*, 2011]. However, the impact of LULCC on climate model simulated extremes has been less well studied. In this chapter, the indices recommended by the CCl/CLIVAR/JCOMM Expert Team on Climate Change Detection and Indices (ETCCDI) based on daily maximum and minimum temperature and daily precipitation were used to analyse changes in the extremes from model simulations of the Land Use Change IDentification of robust impacts (LUCID) project [*Pitman et al.*, 2009; *de Noblet-Ducoudré et al.*, 2012]. Using four climate models, the changes in the ETCCDI indices due to the large-scale impact from LULCC were compared with changes due to an increase in atmospheric CO_2 from 280 ppmv to 375 ppmv. The LULCC perturbation focused on conversion of forests to crops and pasture and ignores other types of land use change, such as urbanization and irrigation, that could also strongly affect regional climate [e.g. *Marshall et al.*, 2004; *Degu et al.*, 2011; *Pielke et al.*, 2011].

In terms of the temperature intensity extremes (TXn, TNn, TXx TNx and DTR), LULCC generally induces regionalized cooling, in contrast to the large-scale warming induced by increased CO_2. The models vary in the degree of change and in some cases (e.g. for TXx and TNx, IPSL during JJA and ECHAM5 during MAM; for DTR, ARPEGE during JJA), the sign of the change is contrary to the rest of the models. The changes at 280 and 375 ppmv are generally similar but with slight variation in the magnitude and extent.

Similar regionalized cooling patterns are found in the temperature frequency extremes (TX10p, TN10p, TX90p, TN90p) and duration extremes (GSL, CSDI, WSDI), with models varying in the degree of change. It is interesting to note, however, that while most of the models show some degree of cooling, IPSL showed warming (i.e. during JJA: decrease in the number of cool nights, increase in the number of warm days and warm nights; and annually: increase in the length of warm spells).

In terms of precipitation extremes (RX1day, RX5day, SDII, R95pT, R10mm, CWD and CDD), it was not possible to determine any robust change from the model results, as many of the significant grid points are localized and generally not consistent across models. However, it is interesting to note that there seems to be a localized but consistent change over parts of Southeast Asia in the number of heavy precipitation days (R10mm), which suggest an LULCC impact.

Results demonstrate that the impact of the increase in CO_2 on the ETCCDI indices is much more geographically extensive but often of a similar magnitude than the impact of LULCC. However, many of the temperature indices show locally strong and statistically significant responses to LULCC, such that commonly 20-50% of the Northern Hemisphere, Eurasia and North America are affected statistically significantly by LULCC. To avoid any risk of misunderstanding, it should be noted that the increase in CO_2 imposed here is 280 ppmv to 375 ppmv and not an increase representative of future concentrations. It certainly does not imply that LULCC would likely affect the ETCCDI indices as much as a doubling or tripling of CO_2.

There is a great deal more to be done in associating LULCC with temperature and rainfall extremes. LUCID provided a starting point for this analysis but only four models were available and these four models contrasted in how they responded to LULCC in terms of simulated extremes. Results showed that LULCC does impact the climate extremes over regions of LULCC, with results for temperature extremes more robust than for precipitation extremes. However, differences in how LULCC is imposed on different models and issues with the simulation of precipitation still limits the ability to determine these changes more confidently. These and other issues will be discussed in Chapter 7.

Chapter 7
Discussion

The geophysical impacts of LULCC on surface climate have been presented in the previous chapters. LULCC, in the form of deforestation, was implemented by converting forests (i.e. natural vegetation) to cropland (i.e. perturbed vegetation) based on published estimates of crop and pasture cover. The CSIRO Mk3L general circulation model, coupled to the CABLE land surface model, was used to simulate LULCC at two different CO_2 levels. Sea surface temperatures corresponding to the two CO_2 levels were prescribed in the experiments. Changes in the mean climate were presented in Chapter 4. This provided the foundation to examine changes in the simulated climate extremes, analysed using the ETCCDI indices and presented in Chapter 5. The analysis undertaken with the climate extreme indices from the Mk3L-CABLE model in Chapter 5 was then extended in Chapter 6 using the results from the four LUCID models that were able to provide daily data. The LUCID models had higher horizontal resolution than the simulations performed with the Mk3L-CABLE model and each LUCID model also performed several realizations. In this chapter, the overall results are discussed in the context of the available literature to identify the key outcomes from this research.

7.1 Changes in the mean climate

The impact of LULCC on the mean climate was determined by calculating the difference between experiments with perturbed and natural vegetation cover. For comparison, the impact of increased CO_2 was also calculated as the difference between two experiments that had natural vegetation cover but different atmospheric CO_2 concentrations. Finally, the impacts of LULCC at both CO_2 levels were compared.

Results show that, consistent with previous studies, LULCC affects regional climate and these changes are well correlated with regions of intense LULCC [*Pielke et al.*, 2011]. The regional effect of LULCC contrasts with the global effect of increased CO_2 [e.g. *IPCC*, 2007]. This is expected because LULCC directly affects the energy and water balance only within its immediate vicinity (i.e. via changes in surface albedo, roughness length and evaporative efficiency) and mainly in seasons with significant net radiation. In addition, any changes remote from the regions of intense LULCC have to be propagated via teleconnections increasing the likelihood that any LULCC signal will be damped, at least, to some degree. In contrast, CO_2 is a well-mixed greenhouse gas and affects the radiative balance to some degree everywhere and through every season. This difference in the spatial and temporal scale of LULCC relative to CO_2 is why the impact of LULCC has little relevance when assessing the significance of human forcing in global mean estimates [*Pielke et al.*, 2011].

Results presented in this thesis also confirm earlier results that the effect of LULCC on the mid-latitude climate is different from its effect in the tropics, with cooling evident in the mid-latitudes and warming evident in the tropics [*Lawrence and Chase*, 2010]. This is because the impact of changes in surface albedo dominates over the mid-latitudes due to interactions with seasonal snow cover while the impact of the changes in roughness length and evaporative efficiency dominates over the tropics [*Davin and de Noblet-Ducoudré*, 2010; *Lawrence and Chase*, 2010]. Again, this geographically varying signal contributes little value to the globally averaged estimate of the impact of LULCC since large changes of opposite sign, which could be very important regionally, would sum to approximately zero globally.

In contrast to previous studies, which were usually limited to simulations of selected seasons (e.g. JJA and/or DJF), the multi-year simulations presented in this thesis showed that the impact of LULCC varies seasonally, as the dominant mechanisms in each region also vary seasonally. In terms of the magnitude and extent of change, LULCC is most dominant during MAM and JJA. The cooling due to albedo is most evident over the mid-latitudes during MAM when snow is still present but net radiation is larger than in DJF. This is important because MAM is not one of the common seasons analysed in most publications. This seasonality indicates that the exclusion of some seasons, MAM in particular, risks an underestimation of the impact of LULCC.

Comparison of the LULCC impacts at different CO_2 levels also showed that the impact of LULCC varies at different CO_2 levels and the overall effect of LULCC is significantly controlled by the background climate. That is, how LULCC affects climate depends on whether or not increased CO_2 changes the snow depth during MAM over the mid-latitudes; or whether increased CO_2 changes precipitation during MAM or JJA over the tropics. Results show that doubling the atmospheric CO_2 concentrations from 280 ppmv to 560 ppmv can significantly reduce the snow cover in the Mk3L-CABLE model. This removes a significant amplifier of the impact of LULCC [*Betts*, 2000], decreasing the cooling effect of LULCC over the mid-latitudes. This impact is strongly seasonal; it is most apparent in MAM in the Mk3L-CABLE simulations because this is the season where the decrease in snow is most apparent. Doubling atmospheric CO_2 also significantly affects the precipitation in many regions. In the Mk3L-CABLE model, changes in rainfall in the tropics cause the sign of the LULCC impact over the tropics to change from warming to cooling. Projections of regional changes in rainfall associated with increasing CO_2 are not likely reliable particularly in coarse resolution climate models [*Randall et al.*, 2007] so the detail of this result is not necessarily reliable and needs to be examined using other models. However, the basic result that changes in regional rainfall influence how LULCC interacts with atmosphere is likely robust.

The examination of the impact of LULCC on mean temperature and rainfall using the Mk3L-CABLE model is limited in several ways. The model used here has a coarse resolution, the CO_2 concentrations are kept at equilibrium and corresponding SSTs were prescribed. Despite these limitations, the results do imply that to detect the impact of LULCC, the analysis cannot be limited to global averages or to a single season. However, while the impact of LULCC is clearly principally regional, it does not imply that there is no global-scale impact. Rather, the largest and most significant impact is likely to be associated with the regions that have undergone intense LULCC [*Pitman et al.*, 2011]. Further, since the effect of LULCC depends on the background climate, models need to be able to properly simulate regional-scale hydrometeorology over regions of LULCC for its impact to be properly simulated. The results presented here suggest that changes in snow and in rainfall caused by natural variability or by increasing CO_2 have to be correctly co-located with regions of LULCC in order for the correct impact of LULCC to be simulated. This is a significant challenge since this implies that the wrong regional-scale change in snow cover or rainfall resulting from increased CO_2 would lead not only to the wrong magnitude of change from LULCC but also the wrong sign. It is not known what resolution a model needs to use to accurately capture regional rainfall but it is certainly higher than that used in the 4th assessment report of the IPCC [*Randall et al.*, 2007]. It remains to be seen if the finer resolution of the models used in the 5th assessment report [*Taylor et al.*, 2011b], currently in preparation, leads to significantly better regional rainfall simulations.

There are inherent uncertainties in simulations from a single climate model that limits its reliability. However, while there are limitations associated with the Mk3L-CABLE model, the results obtained and described in Chapter 4 are broadly consistent with those reviewed from the existing literature in Chapter 2. This provides confidence that the model is a reliable tool for exploring Earth-System problems. It certainly provided enough confidence to support and motivate an investigation of the impact of LULCC on climate extremes.

7.2 Changes in the climate extremes

Almost all research relating to how extremes have changed, or could change in the future, has focussed on observations, or on model simulations forced with increasing CO_2. Some recent analyses have begun to examine the impact of LULCC on extremes. These include Deo et al. [2009] who examined the impact of LUCC on extremes over south eastern Australia; Gero et al. [2006] who analysed how land cover change affects local convective storms in the Sydney Basin; and several groups [e.g. *Hossain and Pielke*, 2009; *Hossain et al.*, 2010; *Degu et al.*, 2011] focused on the impact of dams on extreme precipitation. However, this is an area of research under-represented in climate science and prior to this thesis no global analysis of the role of LULCC, using a set of globally applicable extremes indices, has been undertaken.

Extremes occur, by definition, at sub-global scales, principally at regional to local scales, and it is therefore expected that a phenomenon that only exists at regional scales would have a significant impact on the pattern, frequency and intensity of extremes [*Pitman et al.*, 2012].

Chapter 5 presents the changes in the ETCCDI extremes indices due to LULCC. The changes in the ETCCDI indices showed the impact of LULCC on the intensity, frequency and duration of temperature and precipitation extremes. For comparison, the impacts of increased CO_2 on the extremes were also presented.

Results show that consistent with the changes in the mean and in contrast to the large-scale changes due to increased CO_2, the changes in the extremes are regional and correlated with regions of intense LULCC. Results also show that while the magnitude and extent of the LULCC-induced changes vary between indices, the temperature extremes are generally more spatially coherent than the changes in the precipitation extremes. The LULCC-induced changes in the temperature extremes generally point towards surface cooling because intensive LULCC is quite constrained to the northern mid-latitudes where LULCC tends to cool on average. This cooling tends to oppose the general warming induced by CO_2 doubling. If, in the future, LULCC becomes increasingly a tropical phenomenon it seems likely that extremes linked to LULCC will tend to exacerbate warming. The general warming associated with the increase in CO_2 does not imply warming at all land grid points during all seasons for all indices. On the contrary, despite the general CO_2-induced warming, there are also regions where CO_2 induces cooling during some seasons as indicated by some indices (e.g., TXx over the mid-latitudes during MAM, JJA and SON; TX10p and TX90p over parts of the tropics during DJF and MAM, and mid-latitudes during JJA). Over regions of LULCC, this pattern of change is further complicated for some indices and seasons (e.g., TXx over the S.E. Asia during MAM, JJA and SON) when the LULCC-induced change in the extremes is similar to the change due to CO_2 which then adds to the warming; however, there are other cases (e.g., TX10p and TX90p over the mid-latitudes during MAM) where LULCC causes cooling, opposing the change due to CO_2, which results in a less discernable signal. The magnitude of change in the extremes due to LULCC is usually smaller than that of CO_2 but for some indices (e.g., CSDI, WSDI), over regions of intense LULCC, the magnitude of the changes can be as large as that of CO_2 for a particular season.

The changes in the precipitation extremes due to LULCC are not as spatially coherent as those linked to increases in CO_2 but this is potentially associated with limitations in the Mk3L-CABLE's ability to simulate the detail of regional-scale precipitation and should not be interpreted as an indication that LULCC does not affect precipitation extremes. On the contrary, for some indices (e.g., Rx1day and Rx5day over some parts S.E. Asia for most of the year) the changes in precipitation extremes are locally and field significant. As with the changes in temperature extremes, the changes in precipitation extremes could either oppose or enhance, and have a magnitude as large as the changes due to CO_2. However, because the changes in precipitation are less coherent than those of temperature, these estimates are more uncertain.

These results have interesting implications for those analysing the impact of anthropogenic climate change on these extreme indices from climate model simulations that do not include LULCC. In the case of some indices, where LULCC triggers local changes in the measure of similar scale to 2 x CO_2, interpretation of climate model results should be undertaken very cautiously. Assumptions that the changes in these indices can only be attributed to CO_2 changes are flawed, particularly for TXx, CSDI, WSDI, TX10p, and TX90p. However, for some regions, indices can likely be captured without accounting for LULCC (TN90p, TXn, TNn, TNx) since results provide no evidence that the inclusion of LULCC would have made a significant difference in terms of any conclusions reached at large spatial scales.

These results also have an interesting implication for detection and attribution studies. Where LULCC has a negligible impact, the detection of changes in these indices can be more safely attributed to other forcings such as CO_2. However, where LULCC adds to other forcings, a stronger signal might be expected, leading to a clearer detection of a trend, but this might also lead to a potential misattribution of that trend to non-LULCC forcing if LULCC is omitted. Similarly, where LULCC counters other forcings, a weaker net signal would tend to lead to a failure to recognise a signal because it has been masked by LULCC. This complicating feature of LULCC is seasonally and regionally dependent. While this might complicate detection and attribution studies, it also offers a way forward to refine existing methodologies. By including LULCC in future studies, a clearer and an even more robust attribution of the impact of increasing CO_2 at regional scales might be possible. It is welcome therefore that LULCC is one of the forcings included in the CMIP-5 experimental design [*Taylor et al.*, 2011b].

The impact of LULCC on rainfall extremes remains unreliable at the coarse model resolutions used in this thesis. However, this limitation does not constitute a proof that LULCC does not affect the rainfall extremes. In terms of using the ETCCDI indices for climate impacts studies at large spatial scales, the assessment of the impact of LULCC on the rainfall indices requires improved climate models able to simulate regional-scale rainfall reliably. An important caveat here is that the CSIRO Mk3L model used was designed to enable very long simulations and is used at a spatial resolution that is coarse relative to a state-of-the-art climate model. Finer resolution climate models have shown significant sensitivity of rainfall to LULCC [e.g. *Marshall et al.*, 2004; *Degu et al.*, 2011] but based on previous studies using coarse resolutions models [*Pitman et al.*, 2009], the lack of sensitivity of rainfall to LULCC at climatologically significant scales is to be anticipated..

These results were limited because the simulations were performed using a relatively coarse resolution model with prescribed seasonally varying SST. Undertaking long simulations to maximize the statistical rigour of the analyses offset the limitation due to the single realization performed for each experiment. However, using a single model inevitably leads to questions as to whether these results are robust. To address these issues, the analysis was extended to include several independent models integrated at higher resolution and using prescribed interannually varying SSTs. In addition, five realizations of each experiment were performed for each model.

7.3 Multi-model estimates of changes in climate extremes

Using four global climate models that submitted results as part of the LUCID intercomparison project [*Pitman et al.*, 2009; *de Noblet-Ducoudré et al.*, 2012] the impact of LULCC on daily extremes were examined. Results showed that changes in the extremes within regions of LULCC are generally consistent among models. As with the Mk3L-CABLE simulations, the LULCC-induced regional changes in the extremes were generally opposed to the large-scale changes due to CO_2. Further, as with the earlier analysis, changes in the temperature extremes were more spatially coherent than changes in the precipitation extremes.

The LUCID models generally agree that LULCC impacts the extremes but not all models agree on the degree and sign of the change. These variations are mostly due to differences in how the models impose the LULCC [*Pitman et al.*, 2009] and how they calculate the surface albedo and the changes in surface fluxes [*Boisier et al.*, 2012; *de Noblet-Ducoudré et al.*, 2012]. These differences between models result in changes where, for the some extremes indices, the LULCC-induced generally oppose the changes due to CO_2 at varying degrees for some models, but one model could show the that changes due to LULCC enhances the change due to CO_2.

Perhaps the most important implication of the results is that the sign of the change in the mean due to LULCC predicts the sign of the change in the extreme index. However, there was a negligible relationship between the *magnitude* of the change in the mean and the *magnitude* of the change in the extreme indices. Overall, this suggests that the *location* of the probability density function is moving in a common way among models (i.e. towards warmer values in the context of maximum and minimum temperatures for example). However, the *shape* of the probability density function is responding in different ways which are associated with the kinds of controls on land-surface processes highlighted by Boisier et al. [2012]. Many of these relate to the efficiency of how a land surface model can transfer water from within the soil, through the plants and out through the stomates. These same processes likely trigger changes in the tails of the probability density function, but the intensity of the changes in the tails of the distribution depends critically on the intensity of LULCC, how processes are parameterized and the overlying climate.

Comparing the LULCC-induced changes at 280 ppmv and 375 ppmv, results show that they are broadly similar but not identical, implying that, as with the changes in the mean climate using Mk3L-CABLE, CO_2 conditions do impact how LULCC changes the extremes. This is to be expected because changes in moisture availability, for example, affects which processes within a land surface model operate at any given time to link LULCC to changes in the energy fluxes. A regional increase in rainfall, reducing moisture stress, will tend to increase the significance of evaporative processes that become less moisture limited. In contrast, strong regional drying will negate changes in the land surface model linked to evaporation.

As with the earlier analysis, the changes in the precipitation extremes are less spatially coherent than the changes in temperature. There is also little correlation between the change in the mean and extreme rainfall (e.g. RX5day), apart from a weak correlation in one model (i.e., ECEarth). However, for some indices and localized regions (i.e., R10mm over South East Asia), there are significant changes, which are consistent among the models, indicating that LULCC could have a significant impact on these extremes.

The multi-model estimates show that over regions of intense LULCC, there are robust changes in the extremes due to LULCC, with changes in temperature extremes more consistent than the changes in precipitation extremes. Despite differences in the extent and sign of the change, most models agree that LULCC does impact extremes in these regions. Many of the temperature indices show locally strong and statistically significant responses to LULCC, such that during MAM and JJA, commonly 30-50% of Eurasia and North America are affected statistically significantly by LULCC. However, not all models show consistent changes in the precipitation extremes. This may indicate that the model resolutions are still too coarse to resolve small-scale precipitation phenomena required to capture the extremes, or that the models lack the correct sensitivity to LULCC or that there is no significant impact from LULCC on precipitation extremes. The persistent and consistent change in R10mm over parts of S.E. Asia is fascinating. It is not possible to determine whether these changes are robust using four models in this thesis but this change is clearly worthy of further investigation using finer resolution models.

7.4 Limitations of the study

In this thesis, the computationally efficient CSIRO Mk3L global climate model was coupled to CABLE, a sophisticated land surface model, to simulate the changes in the climate extremes brought about by the modification of the surface land cover from forest to cropland. The experiments were performed at two different CO_2 levels to determine whether the changes induced by LULCC varied at different CO_2 concentrations. Seasonally varying SSTs, corresponding to these two CO_2 concentrations, were prescribed. This set-up provided answers to the main questions of this thesis (whether LULCC in the form of deforestation can affect the climate extremes and how the impact of LULCC compares to the impact of increased CO_2) but also revealed its limitations, mainly with regards to model resolution and the use of prescribed SSTs.

The use of SSTs from a 2 x CO_2 model run raises the issue that the prescribed SSTs are higher than what would occur in the real world. This could overestimate the impact of increased CO_2 [*Sun et al.*, 2009] and therefore minimize the importance of the impact of LULCC.

The use of a single model performing a single realization, albeit one that ran for multiple-years to maximize the statistical rigour, also raised issues regarding the reliability of the simulations.

To deal with these issues, the same method for analysing the simulations from the Mk3L-CABLE model was applied to the results of LULCC experiments from four independent models from the LUCID project. These models have relatively higher resolutions than Mk3L-CABLE, used inter-annually varying SSTs, and performed 5 realizations of each experiment. Results from the LUCID model confirmed the results from the Mk3L-CABLE model but also highlighted the limitations of current models especially over regions of LULCC, which is related mainly to the proper simulation of regional-scale climate.

Global climate models, by design, have coarse resolutions to enable efficient computation of the multi-year integrations required for climate analysis. This compromise between spatial resolution and length of simulation has been suitable for experiments involving the well-mixed GHGs whose influence on the radiative budget were essentially insensitive to the model resolution. However, with the growing evidence of the major influence of the land surface on the climate system, the need to capture LULCC demands for a much higher model resolution than is possible with the current generation of climate models.

Downscaling has been successfully used in weather forecasting such that various operational centres now routinely produce forecasts with spatial resolutions of 10-30 km using mesoscale models embedded in global forecast models.

However, while the demand for higher spatial resolution regional climate information has been steadily increasing, there is still no consensus on what can be accomplished or how the goal can be achieved [*Leung et al.*, 2003]. Pielke and Wilby [2012] assert that multi-decadal dynamic downscaling for the purpose of climate prediction fails to improve accuracy beyond what can be achieved by interpolating global model predictions but maintains that the same type of regional climate downscaling does have practical value for model sensitivity experiments. It is thus worth examining the results presented here within an intercomparison framework such as COordinated Regional Downscaling Experiment [CORDEX, *Giorgi et al.*, 2009] which might provide a useful way of bridging the resolution gap. However, evidence that LULCC affects weather and climate depending on the detail of the precise land cover change [*Mei and Wang*, 2010] suggests that the resolutions being used in CORDEX (using grid sizes of around 50km) will remain worryingly coarse.

The need to correctly locate changes in rainfall, temperature and snow over regions of intense LULCC presents a significant challenge for climate models. Several studies [e.g. *Anagnostopoulos et al.*, 2010; *Stephens et al.*, 2010; *van Haren et al.*, 2012] have highlighted the lack of skill of current climate models in simulating precipitation, particularly instantaneous precipitation. This is important because even if the modelled accumulated precipitation (e.g. daily or seasonal mean accumulations) show remarkable agreement with observations, the same amount of precipitation with different frequency and intensity could lead to different amounts of runoff, evaporation and soil condition [*Sun et al.*, 2006] and therefore very different impacts. And while the capacity of climate models to capture the background regional climate depends in part on the horizontal resolution of the model, a rigorous assessment of the relationship between climate model resolution and region simulation skill is needed. While finer spatial resolutions may improve global-scale simulations [*Boville*, 1991], how fine a model needs to be to enable reliable co-location of changes in rainfall and temperature with LULCC is unknown. Most climate models also lack many processes that might affect how LULCC affects precipitation and associated processes. In this thesis, this has been addressed by coupling a more sophisticated land surface model to the host climate model, as the capability to simulate LULCC is not available in the host model. Further, there is emerging evidence that coupled ocean models are required in LULCC experiments since these amplify the perturbation and enable affects to be captured distant from the perturbation [*Davin and de Noblet-Ducoudré*, 2010]. This suggests that while the large-scale signal from LULCC on future climates is likely right [*Feddema et al.*, 2005; *Arora and Montenegro*, 2011] much higher resolution fully coupled model simulations need to be conducted to build confidence in how LULCC interacts with a changing climate at regional scales. The use of a coarse resolution model and fixed SSTs likely affects many aspects of the results and the changes due to CO_2 and LULCC may not be correctly co-located. However, the main conclusion that changes in rainfall and snow caused by increases in CO_2 dominate how LULCC affects climate, thereby necessitating climate models to correctly locate changes in rainfall and temperature relative to LULCC, is quite robust as shown by the results from the LUCID experiments.

There is a great deal more to be done in associating LULCC with temperature and rainfall extremes. LUCID provided a starting point for this analysis but only four models were available, and these four models contrasted sharply in how they responded to LULCC in terms of simulated extremes. De Noblet-Ducoudré *et al.* [2012] therefore argued that land surface modellers need to systematically evaluate models using observations where land use change has been imposed in order to better resolve how this change affects the mean climate. Analyses of these types will also help resolve the impact of LULCC on extremes. A lot of the differences noted here relate to differences in the mean responses of the models to LULCC so resolving the mean response will be very helpful. The use of well-designed environments for testing and evaluating land surface models are now being built [*Abramowitz*, 2012] which should provide a more systematic approach in the future.

While the land surface models used here (CABLE as well the other LSMs used in the LUCID project) are state-of-the-art, the variations in the results highlight the need for a closer examination of how these models simulate the changes in the surface energy and water balance. There is an urgent need to make the simulations more realistic: including the representation of surface albedo, vegetation types (e.g., to include urban or irrigated land surfaces; or include eucalypts and differentiate between different types of crops), vegetation phenology, and soil hydrology. The "anomalous" simulations in the IPSL model, which simulated summer warming from LULCC over Europe in contrast to other LUCID models, was linked by de Noblet-Ducoudré *et al.* [2012] to how crops and crop seasonality was represented in the model. Finally, while it is important to use different models to examine a range of all possible outcomes, resolving issues such as how the detail of LULCC should be implemented in models would be helpful in future multi-model comparisons.

Chapter 8
Conclusions

Changes in the global climate due to natural variability and anthropogenic forcing are affecting the environment and human society. While most previous studies have focused on the impacts of greenhouse gases (GHGs) and aerosols, these are not the only major climate forcings that affect climate [*National Research Council*, 2005]. Land use-induced land cover change (LULCC) is one major forcing that has been under-represented in the IPCC assessments, in part, because most previous studies focus on its contribution to radiative forcing which are small compared to those due to increases in atmospheric CO_2 concentrations due to the burning of fossil fuels. LULCC can affect the climate, via changes in the surface albedo, roughness length and evaporative efficiency, and there is mounting evidence that these impacts due to LULCC are more important than previously thought, particularly at regional scales.

As a result of the focus on GHGs, which are part of the well-mixed atmosphere, most previous studies have tended to focus on global-scale changes in climate. There has been an increased focus on changes in extremes in recent years but these too have focused mainly on the role of GHGs. LULCC-related studies understandably focused at regional scales and in cases where they tackled extremes, faced the challenge of regional differences in climate types and surface characteristics. In addition, different research groups inevitably focus on different extremes and use different approaches in analysing these extremes. This situation has made it particularly difficult to make sense of any association between LULCC and extremes in the global scale.

This thesis therefore focused on the following questions:

Does LULCC significantly affect simulated climate extremes?

How does the impact of LULCC compare relative to the impact of elevated CO_2?

To address these questions, the CSIRO Mk3L global model was coupled to the CABLE land surface model and a series of simulations were conducted. Results from these simulations were then analysed using the ETCCDI extremes indices. To test the robustness of the results, simulations from four other models from the LUCID project were also analysed using the ETCCDI indices.

In Chapter 1 of this thesis, five main objectives were identified. This chapter re-states these goals and presents how the results and key findings from the experiments have addressed each of these objectives.

The first aim was to configure a computationally efficient global climate model that was coupled to a sophisticated land surface model to simulate changes in the land surface and atmospheric CO_2 concentrations. As described in Chapter 3, the default configuration of the CSIRO Mk3L global model coupled to the CABLE land surface model was competitive in terms of simulating the present day climate. However, it was not configured by default to simulate LULCC. Several modifications to the land surface model were performed so that it would correctly represent the changes in surface characteristics brought about by changes in the vegetation cover. These modifications involved calibrating the soil albedo and vegetation transmittance and reflectance characteristics so that the model could simulate a more realistic surface albedo. In addition, the model was modified to enable tiling, or the representation of several vegetation types at each model grid point. Results showed that the modified model was able to successfully perform the LULCC experiments (i.e., representing the change from a natural to perturbed vegetation cover) required for the thesis. By changing the input CO_2 transmission coefficients and corresponding SST fields, the model was also able to simulate the changes due to increased atmospheric CO_2.

The second aim was to develop the input datasets required for the LULCC simulations. To represent LULCC, several datasets describing the surface were created, as described in Chapter 3. These include the natural vegetation cover (developed from the potential vegetation map of Rammankutty and Foley [1999]), the perturbed vegetation cover (developed by applying the crop and pasture data for year 2000 from the Land Use Harmonization data [*Hurtt et al.*, 2006]) and their corresponding leaf area index (LAI). Input parameters such as the soil albedo map (developed from MODIS broadband data) and the vegetation specific leaf transmittance and reflectance (adapted from Dorman and Sellers [1989]) were also created. Results showed that these datasets were effective in representing LULCC in the simulations.

The third aim was to evaluate whether this coupled model was suitable for the analysis of changes due to LULCC by analysing changes in the mean climate. This was explored in Chapter 4. The results confirmed findings from previous studies that:

- LULCC affects regional climate and that these changes are correlated with regions of intense LULCC;
- The regional effect of LULCC contrasts with the global effect of increased CO_2; and
- The effect of LULCC differs between regions. Deforestation induces cooling in the mid-latitudes due to increased surface albedo and warming in the tropics due to decreased roughness length and evapotranspiration efficiency.

Analysis of the changes in the mean climate also provided the following new results:

- The impact of LULCC varies seasonally, controlled, in part, by snow depth during MAM and by changes in the latent heat flux during JJA;
- The impact of LULCC depends on the CO_2 levels. At increased atmospheric CO_2 conditions, decreased snow depth leads to decreased cooling over the mid-latitudes, and increased latent heat flux associated with increased precipitation increases cooling of the surface, particularly in the tropics.

These results demonstrate that the Mk3L-CABLE model is suitable for use in LULCC experiments as it is sensitive enough to simulate the changes in the mean climate due to changes in the vegetation cover. These provided motivation for the examination of changes in the extremes.

The fourth aim was to investigate changes in the extremes due to LULCC relative to changes due to increases in the CO_2 concentrations using a specific set of extremes indices. To investigate changes in the extremes, the simulations performed for the analysis of the mean climate were extended to create the daily output required for the calculation of the ETCCDI extremes indices. The results of this analysis were presented in Chapter 5 and showed that:

- As with the changes in the mean, the impact of LUCC on the extremes were regional and are correlated with regions of LULCC;
- The extent of the LULCC-induced changes varied between indices, with changes in the temperature extremes more spatially coherent than changes in the precipitation extremes;
- The magnitude of the impact of LULCC was usually smaller than the impact due to increased CO_2. However, for some indices and regions, the magnitude of the change in the temperature indices could be as large as that due to a doubling of CO_2;
- The impact of LULCC is generally towards cooling and thus opposite that of the general warming induced by CO_2; however, for some indices and

regions, the impact of LULCC enhances the impacts of CO_2.

These results have implications for those analysing the impacts of anthropogenic climate change on extremes from climate simulations that do not include LULCC. Since LULCC can induce changes that may be comparable in magnitude to the changes induced by CO_2 it is important to interpret climate model results very cautiously especially over regions of intense LULCC. For indices where LULCC has been negligible, detected changes may be safely attributed to other forcings such as CO_2 or aerosols. However, for indices that indicate significant changes due to LULCC, simulations should include LULCC forcing because it could either mask or enhance the anthropogenic signal due to other forcings. Failure to include LULCC in these circumstances risks either non-detection of a real signal or a misattribution of an apparent signal to the wrong forcings.

The last aim was to verify whether these changes in the extremes are robust using results from independent model simulations. To address issues concerning the reliability of the results from simulations performed by a single coarse resolution model, the analysis was extended to examine the results from four LUCID models. The same land use perturbation (i.e., a change from 1870 to 1992 vegetation cover based on estimates of crop and pasture fraction) was imposed on the four models. Despite differences in how the four models responded to LULCC, several robust results were found:

- Over regions of LULCC, models agree that LULCC does impact some climate extremes;

- The changes in temperature extremes are relatively consistent, spatially coherent, and coincident with regions of intense LULCC;

- The changes in precipitation extremes are uncertain, captured quite differently between the four models, and no robust conclusions can be made at this time.

Results from the LUCID models generally confirmed those from the Mk3L-CABLE model. However, they also highlighted the limitations of current models in capturing the impact of LULCC at regional scales over regions of intense LULCC. To address some of these limitations, future work needs to focus on the following:

1. Capturing the detail of LULCC in models. It is not clear how best to represent LULCC over time in models, or how best to reflect the change in the character of the land resulting from LULCC. Improving LSM simulations via a more realistic representation of surface albedo, vegetation types, spatial heterogeneity, etc. is clearly a priority.

2. Resolving the nature of smaller scale weather and climate events that affect the land surface. This probably covers mostly snow cover and precipitation and will likely involve the use of finer (regional) scale models such are those used in CORDEX, but it is not just a question of spatial resolution. To accurately capture the impact of LULCC requires the correct location of changes in snow and rainfall with changes in land cover. This is a severe challenge to existing climate models.

3. Full coupling with ocean models to allow for the assessment of interannual extremes (e.g., drought) as well as remote impacts via teleconnections is a necessary next step. This is computationally expensive but the question of robust teleconnections cannot be answered reliably using fixed sea surface temperatures.

4. Systematic evaluation of land surface models against observations to resolve how well they capture the effect of LULCC on the mean and the extremes is necessary because land models are commonly evaluated in terms of how they can capture the current situation, not how well they can capture a change in the current situation.

5. LULCC must be included when conducting detection and attribution studies. The question of whether, and if so by how much, the representation of LULCC improves detection and attribution is an open one and in urgent need of resolution.

6. In addition to the ETCCDI indices, which are based on the daily minimum and maximum temperature and precipitation, it would be helpful to include other metrics such as moist enthalpy (or equivalent temperature) which takes into account both air temperature and humidity to characterize heat storage changes [*Pielke et al.*, 2004; *Fall et al.*, 2010a; *Peterson et al.*, 2011].

7. The possible impact of LULCC on global circulation [e.g. *Zhao et al.*, 2001; *Pielke et al.*, 2007; *Jonko et al.*, 2010; *Kala et al.*, 2011] should also be explored as shifts in the major circulations have significant effects on

agricultural and weather systems that could elevate local land use policies into global issues.

8. Other forms of LULCC aside from deforestation, particularly urbanization and irrigation, should also be considered in future studies as recent evidence show the ongoing rapid expansion and intensification of these regions.

9. The land surface observational data sets used within the community are careful constructed and evaluated. However, there are always areas where these data sets might be improved and there are occasionally analyses that point to possible biases [e.g. *Spencer and Braswell*, 2008; *Murphy and Forster*, 2010; *McNider et al.*, 2012; *Svoma and Cerveny*, 2012]. There is always value in future work on these data sets at both global and regional scales.

Ultimately, for the impacts of LULCC on extremes to be relevant to adaptation policies, experiments will have to be undertaken by multiple models and at high enough resolution to provide direct and relevant advice. There are considerable benefits if LULCC can be clearly shown to affect extremes as mitigation of extremes by direct human management of the land surface may be more feasible and less risky than some other proposed geoengineering techniques (for example, sulphate injection into the stratosphere or ocean fertilization). Landscape modification for managing changes in extremes also have the potential for positive benefits in terms of food security, biodiversity, biofuels and natural amenity. However, before serious proposals to examine LULCC as a means to manage extremes can be encouraged, a systematic examination of the questions posed in this thesis must be undertaken across a range of models and approaches. The study presented in this thesis is one step towards an improved understanding of how LULCC affects extremes and it led to more questions than definitive answers. However, some specific ways forward are now clearer and provide ways to develop a significantly improved understanding of how LULCC affects past, present and future extremes.

Bibliography

Abramowitz, G. (2012), Towards a public, standardized, diagnostic benchmarking system for land surface models, *Geosci. Model Dev. Discuss.*, *5*(1), 549-570.

Alexander, L. (2011), Climate science: Extreme heat rooted in dry soils, *Nature Geosci*, *4*(1), 12-13.

Alexander, L., and C. Tebaldi (2012), Climate and weather extremes: observations, modelling and projections, in *The future of the world's climate*, edited by A. Henderson-Sellers and K. McGuffie, pp. 253-288, Elsevier B.V., Amsterdam.

Alexander, L. V., and J. M. Arblaster (2009), Assessing trends in observed and modelled climate extremes over Australia in relation to future projections, *International Journal of Climatology,* (3), 417-435, doi: 10.1002/joc.1730.

Alexander, L. V., X. Zhang, T. C. Peterson, J. Caesar, B. Gleason, A. M. G. Klein Tank, M. Haylock, D. Collins, B. Trewin, F. Rahimzadeh, A. Tagipour, K. Rupa Kumar, J. Revadekar, G. Griffiths, L. Vincent, D. B. Stephenson, J. Burn, E. Aguilar, M. Brunet, M. Taylor, M. New, P. Zhai, M. Rusticucci, and J. L. Vazquez-Aguirre (2006), Global observed changes in daily climate extremes of temperature and precipitation, *J. Geophys. Res.*, *111*(D5), D05109.

Allen, M. R., and P. A. Stott (2003), Estimating signal amplitudes in optimal fingerprinting, part I: theory, *Climate Dynamics*, *21*(5), 477-491.

Anagnostopoulos, G. G., D. Koutsoyiannis, A. Christofides, A. Efstratiadis, and N. Mamassis (2010), A comparison of local and aggregated climate model outputs with observed data, *Hydrological Sciences Journal*, *55*(7), 1094-1110.

Aoyagi, T., N. Kayaba, and N. Seino (2012), Numerical Simulation of the Surface Air Temperature Change Caused by Increases of Urban Area, Anthropogenic Heat, and Building Aspect Ratio in the Kanto-Koshin Area, *Journal of the Meteorological Society of Japan. Ser. II*, *90B*, 11-31.

Arora, V. K., and A. Montenegro (2011), Small temperature benefits provided by realistic afforestation efforts, *Nature Geosci*, *4*(8), 514-518.

Avila, F. B., A. J. Pitman, M. G. Donat, L. V. Alexander, and G. Abramowitz (2012), Climate model simulated changes in temperature extremes due to land cover change, *J. Geophys. Res.*, *117*(D4), D04108.

Avissar, R. (1992), Conceptual Aspects of a Statistical-Dynamical Approach to Represent Landscape Subgrid-Scale Heterogeneities in Atmospheric Models, *J. Geophys. Res.*, *97*(D3), 2729-2742.

Avissar, R., and R. A. Pielke (1989), A Parameterization of Heterogeneous Land Surfaces for Atmospheric Numerical Models and Its Impact on Regional Meteorology, *Monthly Weather Review*, *117*(10), 2113-2136.

Baidya Roy, S., C. P. Weaver, D. S. Nolan, and R. Avissar (2003), A preferred scale for landscape forced mesoscale circulations?, *J. Geophys. Res.*, *108*(D22), 8854.

Baldi, M., G. Dalu, R. Pielke, and F. Meneguzzo (2005), Analytical evaluation of mesoscale fluxes and pressure field, *Environmental Fluid Mechanics*, *5*(1), 3-33.

Betts, A. K. (2009), Land-Surface-Atmosphere Coupling in Observations and Models, *Journal of Advances in Modeling Earth Systems*, *1*(4), 18 pp.

Betts, R. A. (2000), Offset of the potential carbon sink from boreal forestation by decreases in surface albedo, *Nature*, *408*(6809), 187-190.

Bi, D. (2002), Transient and Long-Term Behaviour of the World Ocean Under Global Warming, 566 pp, University of Tasmania.

Boisier, J.-P., N. de Noblet-Ducoudré, A. J. Pitman, F. T. Cruz, C. Delire, B. J. J. M. van den Hurk, M. K. van der Molen, C. Müller, and A. Voldoire (2012), Attributing the impacts of Land-Cover Changes in temperate regions on surface temperature and heat fluxes to specific causes. Results from the first LUCID set of simulations, *J. Geophys. Res. (submitted)*.

Bonan, G. B. (1996), A land surface model (LSM version 1.0) for ecological, hydrological, and atmospheric studies: Technical Description and User's Guide, *Technical Note NCAR/TN-417+STR*, National Center for Atmospheric Research, Boulder, Colorado.

Bonan, G. B. (1997), Effects of Land Use on the Climate of the United States, *Climatic Change*, *37*(3), 449-486.

Bonan, G. B. (2008a), *Ecological Climatology: Concepts and Applications*, 2nd ed., Cambridge University Press.

Bonan, G. B. (2008b), Forests and Climate Change: Forcings, Feedbacks, and the Climate Benefits of Forests, *Science*, *320*(5882), 1444-1449.

Boville, B. A. (1991), Sensitivity of Simulated Climate to Model Resolution, *Journal of Climate*, *4*(5), 469-485.

Bryan, K. (1969), A numerical method for the study of the circulation of the world ocean, *Journal of Computational Physics*, *4*(3), 347-376.

Butt, N., P. A. de Oliveira, and M. H. Costa (2011), Evidence that deforestation affects the onset of the rainy season in Rondonia, Brazil, *J. Geophys. Res.*, *116*(D11), D11120.

Cai, W., and T. Cowan (2006), SAM and regional rainfall in IPCC AR4 models: Can anthropogenic forcing account for southwest Western Australian winter rainfall reduction?, *Geophys. Res. Lett.*, *33*(24), L24708.

Cai, W., G. Shi, T. Cowan, D. Bi, and J. Ribbe (2005), The response of the Southern Annular Mode, the East Australian Current, and the southern mid-latitude ocean circulation to global warming, *Geophys. Res. Lett.*, *32*(23), L23706.

Chang, H.-I., D. Niyogi, A. Kumar, C. M. Kishtawal, J. Dudhia, F. Chen, U. C. Mohanty, and M. Shepherd (2009), Possible relation between land surface feedback and the post-landfall structure of monsoon depressions, *Geophys. Res. Lett.*, *36*(15), L15826.

Christidis, N., P. A. Stott, and S. J. Brown (2011), The Role of Human Activity in the Recent Warming of Extremely Warm Daytime Temperatures, *Journal of Climate*, *24*(7), 1922-1930.

Coles, S. (2001), *An Introduction to Statistical Modeling of Extreme Values*, 1st ed., 228 pp., Springer-Verlag.

Collatz, G. J., J. T. Ball, C. Grivet, and J. A. Berry (1991), Physiological and environmental regulation of stomatal conductance, photosynthesis and transpiration: a model that includes a laminar boundary layer, *Agricultural and Forest Meteorology*, *54*, 107-136.

Cox, M. D. (1984), A primitive equation 3-dimensional model of the ocean, *Technical Report No. 1*, 141 pp, Geophysical Fluid Dynamics Laboratory Ocean Group, Princeton University.

Dai, Y., X. Zeng, R. E. Dickinson, I. Baker, G. B. Bonan, M. G. Bosilovich, A. S. Denning, P. A. Dirmeyer, P. R. Houser, G. Niu, K. W. Oleson, C. A. Schlosser, and Z.-L. Yang (2003), The Common Land Model, *Bulletin of the American Meteorological Society*, *84*(8), 1013-1023.

Davin, E. L., and N. de Noblet-Ducoudré (2010), Climatic Impact of Global-Scale Deforestation: Radiative versus Nonradiative Processes, *Journal of Climate*, *23*(1), 97-112.

de Noblet-Ducoudré, N., J.-P. Boisier, A. Pitman, G. B. Bonan, V. Brovkin, F. Cruz, C. Delire, V. Gayler, B. J. J. M. van den Hurk, P. J. Lawrence, M. K. van der Molen, C. Müller, C. H. Reick, B. J. Strengers, and A. Voldoire (2012), Determining Robust Impacts of Land-Use-Induced Land Cover Changes on Surface Climate over North America and Eurasia: Results from the First Set of LUCID Experiments, *Journal of Climate*, *25*(9), 3261-3281.

DeAngelis, A., F. Dominguez, Y. Fan, A. Robock, M. D. Kustu, and D. Robinson (2010), Evidence of enhanced precipitation due to irrigation over the Great Plains of the United States, *J. Geophys. Res.*, *115*(D15), D15115.

Degu, A. M., F. Hossain, D. Niyogi, R. Pielke, Sr., J. M. Shepherd, N. Voisin, and T. Chronis (2011), The influence of large dams on surrounding climate and precipitation patterns, *Geophys. Res. Lett.*, *38*(4), L04405.

Deo, R. C., J. I. Syktus, C. A. McAlpine, P. J. Lawrence, H. A. McGowan, and S. R. Phinn (2009), Impact of historical land cover change on daily indices of climate extremes including droughts in eastern Australia, *Geophys. Res. Lett.*, *36*.

Dickinson, R. E., M. Shaikh, R. Bryant, and L. Graumlich (1998), Interactive Canopies for a Climate Model, *Journal of Climate*, *11*(11), 2823-2836.

Didham, R. K., J. M. Tylianakis, N. J. Gemmell, T. A. Rand, and R. M. Ewers (2007), Interactive effects of habitat modification and species invasion on native species decline, *Trends in Ecology & Evolution*, *22*(9), 489-496.

Diffenbaugh, N. S., J. S. Pal, F. Giorgi, and X. Gao (2007), Heat stress intensification in the Mediterranean climate change hotspot, *Geophys. Res. Lett.*, *34*(11), L11706.

Dorman, J. L., and P. J. Sellers (1989), A Global Climatology of Albedo, Roughness Length and Stomatal Resistance for Atmospheric General Circulation Models as Represented by the Simple Biosphere Model (SiB), *Journal of Applied Meteorology*, *28*(9), 833-855.

Durre, I., J. M. Wallace, and D. P. Lettenmaier (2000), Dependence of Extreme Daily Maximum Temperatures on Antecedent Soil Moisture in the Contiguous United States during Summer, *Journal of Climate*, *13*(14), 2641-2651.

Easterling, D. R., G. A. Meehl, C. Parmesan, S. A. Changnon, T. R. Karl, and L. O. Mearns (2000a), Climate Extremes: Observations, Modeling, and Impacts, *Science*, *289*(5487), 2068-2074.

Easterling, D. R., J. L. Evans, P. Y. Groisman, T. R. Karl, K. E. Kunkel, and P. Ambenje (2000b), Observed Variability and Trends in Extreme Climate Events: A Brief Review*, *Bulletin of the American Meteorological Society*, *81*(3), 417-425.

Fall, S., N. S. Diffenbaugh, D. Niyogi, R. A. Pielke, and G. Rochon (2010a), Temperature and equivalent temperature over the United States (1979–2005), *International Journal of Climatology*, *30*(13), 2045-2054.

Fall, S., D. Niyogi, A. Gluhovsky, R. A. Pielke, E. Kalnay, and G. Rochon (2010b), Impacts of land use land cover on temperature trends over the continental United States: assessment using the North American Regional Reanalysis, *International Journal of Climatology*, *30*(13), 1980-1993.

Feddema, J. J., K. W. Oleson, G. B. Bonan, L. O. Mearns, L. E. Buja, G. A. Meehl, and W. M. Washington (2005), The Importance of Land-Cover Change in Simulating Future Climates, *Science*, *310*(5754), 1674-1678.

Fels, S. B., and M. D. Schwarzkopf (1975), The Simplified Exchange Approximation: A New Method for Radiative Transfer Calculations, *Journal of the Atmospheric Sciences*, *32*(7), 1475-

1488.

Fels, S. B., and M. D. Schwarzkopf (1981), An Efficient, Accurate Algorithm for Calculating CO_2 15 μm Band Cooling Rates, *J. Geophys. Res.*, *86*(C2), 1205-1232.

Field, C. B., R. B. Jackson, and H. A. Mooney (1995), Stomatal responses to increased CO_2: implications from the plant to the global scale, *Plant, Cell & Environment*, *18*(10), 1214-1225.

Findell, K. L., T. R. Knutson, and P. C. D. Milly (2006), Weak Simulated Extratropical Responses to Complete Tropical Deforestation, *Journal of Climate*, *19*(12), 2835-2850.

Findell, K. L., E. Shevliakova, P. C. D. Milly, and R. J. Stouffer (2007), Modeled Impact of Anthropogenic Land Cover Change on Climate, *Journal of Climate*, *20*(14), 3621-3634.

Findell, K. L., A. J. Pitman, M. H. England, and P. J. Pegion (2009), Regional and Global Impacts of Land Cover Change and Sea Surface Temperature Anomalies, *Journal of Climate*, *22*(12), 3248-3269.

Finkele, K., J. J. Katzfey, E. A. Kowalczyk, J. L. McGregor, L. Zhang, and M. R. Raupach (2003), Modelling of the OASIS Energy Flux Measurements Using Two Canopy Concepts, *Boundary-Layer Meteorology*, *107*(1), 49-79.

Fischer, E. M., and C. Schar (2010), Consistent geographical patterns of changes in high-impact European heatwaves, *Nature Geosci*, *3*(6), 398-403.

Fischer, E. M., S. I. Seneviratne, D. Lüthi, and C. Schär (2007), Contribution of land-atmosphere coupling to recent European summer heat waves, *Geophys. Res. Lett.*, *34*(6), L06707.

Fischer, J., and D. B. Lindenmayer (2007), Landscape modification and habitat fragmentation: a synthesis, *Global Ecology and Biogeography*, *16*(3), 265-280.

Flato, G. M., and W. D. Hibler III (1990), On a simple sea-ice dynamics model for climate studies, *Annals of Glaciology*, *14*, 72-77.

Flato, G. M., and W. D. Hibler III (1992), Modeling Pack Ice as a Cavitating Fluid, *Journal of Physical Oceanography*, *22*(6), 626-651.

Foley, J. A., I. C. Prentice, N. Ramankutty, S. Levis, D. Pollard, S. Sitch, and A. Haxeltine (1996), An integrated biosphere model of land surface processes, terrestrial carbon balance, and vegetation dynamics, *Global Biogeochem. Cycles*, *10*(4), 603-628.

Folland, C. K., T. R. Karl, and K. Y. A. Vinnikov (1990), Observed Climate Variations and Change, in *Climate Change: The IPCC Scientific Assessment*, edited by J. T. Houghton, G. J. Jenkins and J. J. Ephraums.

Folland, C. K., T. R. Karl, N. Nicholls, B. S. Nyenzi, D. E. Parker, and K. Y. A. Vinnikov (1992), Observed Climate Variability and Change, in *Climate Change 1992: The Supplementary Report to the IPCC Scientific Assessment*, edited by J. T. Houghton, B. A. Callander and S. K. Varney, Cambridge University Press, Cambridge, UK.

Forster, P., V. Ramaswamy, P. Artaxo, B. T., R. Betts, D. W. H. Fahey, J., J. L. Lean, D.C., G. Myhre, J. Nganga, R. Prinn, G. Raga, S. M., and R. Van Dorland (2007), Changes in Atmospheric Constituents and in Radiative Forcing, in *Climate Change 2007: The Physical Science Basis. Contribution of Working Group I to the Fourth Assessment Report of the Intergovernmental Panel on Climate Change*, edited by S. Solomon, D. Qin, M. Manning, Z. Chen, M. Marquis, K. B. Averyt, T. M. and H. L. Miller, Cambridge University Press, Cambridge, United Kingdom and New York, NY, USA.

Fragkais, M., and K. C. Seto (2012), The rise and rise of urban expansion, *Global Change*(78), 16-19.

Frich, P., L. V. Alexander, P. Della-Marta, B. Gleason, M. Haylock, A. M. G. K. Tank, and T. Peterson (2002), Observed coherent changes in climatic extremes during the second half of the twentieth century, *Climate Research*, *19*(3), 193-212.

Gale, M. R., and D. F. Grigal (1987), Vertical root distributions of northern tree species in relation to successional status, *Canadian Journal of Forest Research*, *17*(8), 829-834.

Gallo, K. P., T. W. Owen, D. R. Easterling, and P. F. Jamason (1999), Temperature Trends of the U.S. Historical Climatology Network Based on Satellite-Designated Land Use/Land Cover, *Journal of Climate*, *12*(5), 1344-1348.

Georgescu, M., M. Moustaoui, A. Mahalov, and J. Dudhia (2012), Summer-time climate impacts of projected megapolitan expansion in Arizona, *Nature Clim. Change*, *advance online publication*.

Gero, A. F., A. J. Pitman, G. T. Narisma, C. Jacobson, and R. A. Pielke (2006), The impact of land cover change on storms in the Sydney Basin, Australia, *Global and Planetary Change*, *54*(1-2), 57-78.

Giorgi, F., C. Jones, and G. R. Asrar (2009), Addressing climate information needs at the regional level: the CORDEX framework, *WMO Bulletin*, *58*(3), 175-183.

Goldewijk, K. K. (2001), Estimating global land use change over the past 300 years: The HYDE Database, *Global Biogeochem. Cycles*, *15*(2), 417-433.

Goldewijk, K. K., A. Beusen, and P. Janssen (2010), Long-term dynamic modeling of global population and built-up area in a spatially explicit way: HYDE 3.1, *Holocene*, *20*(4), 565-573.

Gordon, H. B., and S. P. O'Farrell (1997), Transient Climate Change in the CSIRO Coupled Model with Dynamic Sea Ice, *Monthly Weather Review*, *125*(5), 875-908.

Gordon, H. B., L. D. Rotstayn, J. L. McGregor, M. R. Dix, E. A. Kowalczyk, S. P. O'Farrell, L. J. Waterman, A. C. Hirst, S. G. Wilson, M. A. Collier, I. G. Watterson, and T. I. Elliot (2002), The CSIRO Mk3 Climate System Model, *Technical Report No. 60*, CSIRO Atmospheric Research.

Gregory, D., and P. R. Rowntree (1990), A mass flux convection scheme with representation of cloud ensemble characteristics and stability-dependent closure, *Monthly Weather Review*, *118*(7), 1483-1506.

Hegerl, G. C., F. W. Zwiers, P. A. Stott, and V. V. Kharin (2004), Detectability of Anthropogenic Changes in Annual Temperature and Precipitation Extremes, *Journal of Climate*, *17*(19), 3683-3700.

Hillel, D. (1982), *Introduction to Soil Physics*, Academic Press, New York.

Hirst, A. C., S. P. O'Farrell, and H. B. Gordon (2000), Comparison of a Coupled Ocean-Atmosphere Model with and without Oceanic Eddy-Induced Advection. Part I: Ocean Spinup and Control Integrations, *Journal of Climate*, *13*(1), 139-163.

Hope, P. (2006), Projected future changes in synoptic systems influencing southwest Western Australia, *Climate Dynamics*, *26*(7), 765-780.

Hossain, F., and R. A. Pielke, Sr (2009), Have large dams altered extreme precipitation patterns?, *Eos Trans. AGU*, *90*(48), 453-454.

Hossain, F., I. Jeyachandran, and R. Pielke, Sr. (2010), Dam safety effects due to human alteration of extreme precipitation, *Water Resour. Res.*, *46*(3), W03301.

Huffman, G. J., R. F. Adler, P. Arkin, A. Chang, R. Ferraro, A. Gruber, J. Janowiak, A. McNab, B. Rudolf, and U. Schneider (1997), The Global Precipitation Climatology Project (GPCP) Combined Precipitation Dataset, *Bulletin of the American Meteorological Society*, *78*(1), 5-20.

Hurtt, G. C., S. Frolking, M. G. Fearon, B. Moore, E. Shevliakova, S. Malyshev, S. W. Pacala, and R. A. Houghton (2006), The underpinnings of land-use history: three centuries of global gridded land-use transitions, wood-harvest activity, and resulting secondary lands, *Global Change Biology*, *12*(7), 1208-1229.

IPCC (2007), *Climate Change 2007: The Physical Science Basis. Contribution of Working Group I to the Fourth Assessment Report of the Intergovernmental Panel on Climate Change*, 996 pp., Cambridge University Press, Cambridge, United Kingdom and New York, USA.

IPCC (2012), Summary for Policymakers, in *Managing the Risks of Extreme Events and Disasters to Advance Climate Change Adaptation. A Special Report of Working Groups I and II of the Intergovernmental Panel on Climate Change.*, edited by C. B. Field, et al., pp. 3-21, Cambridge University Press, New York, NY, USA.

Jackson, R. B., J. Canadell, J. R. Ehleringer, H. A. Mooney, O. E. Sala, and E. D. Schulze (1996), A Global Analysis of Root Distributions for Terrestrial Biomes, *Oecologia*, *108*(3), 389-411.

Jonko, A. K., A. Hense, and J. J. Feddema (2010), Effects of land cover change on the tropical circulation in a GCM, *Climate Dynamics*, *35*(4), 635-649.

Kala, J., T. J. Lyons, and U. S. Nair (2011), Numerical Simulations of the Impacts of Land-Cover Change on Cold Fronts in South-West Western Australia, *Boundary-Layer Meteorology*, *138*(1), 121-138.

Kalnay, E., M. Kanamitsu, R. Kistler, W. Collins, D. Deaven, L. Gandin, M. Iredell, S. Saha, G. White, J. Woollen, Y. Zhu, A. Leetmaa, R. Reynolds, M. Chelliah, W. Ebisuzaki, W. Higgins, J. Janowiak, K. C. Mo, C. Ropelewski, J. Wang, R. Jenne, and D. Joseph (1996), The NCEP/NCAR 40-Year Reanalysis Project, *Bulletin of the American Meteorological Society*, *77*(3), 437-471.

Katz, R. W., and B. G. Brown (1992), Extreme events in a changing climate: Variability is more important than averages, *Climatic Change*, *21*(3), 289-302.

Kharin, V. V., and F. W. Zwiers (2000), Changes in the Extremes in an Ensemble of Transient Climate Simulations with a Coupled Atmosphere-Ocean GCM, *Journal of Climate*, *13*(21), 3760-3788.

Kharin, V. V., F. W. Zwiers, X. Zhang, and G. C. Hegerl (2007), Changes in Temperature and Precipitation Extremes in the IPCC Ensemble of Global Coupled Model Simulations, *Journal of Climate*, *20*(8), 1419-1444.

Kiktev, D., D. M. H. Sexton, L. Alexander, and C. K. Folland (2003), Comparison of Modeled and Observed Trends in Indices of Daily Climate Extremes, *Journal of Climate*, *16*(22), 3560-3571.

Kiktev, D., J. Caesar, L. V. Alexander, H. Shiogama, and M. Collier (2007), Comparison of observed and multimodeled trends in annual extremes of temperature and precipitation, *Geophys. Res. Lett.*, *34*(10), L10702.

Kishtawal, C. M., D. Niyogi, M. Tewari, R. A. Pielke, and J. M. Shepherd (2010), Urbanization signature in the observed heavy rainfall climatology over India, *International Journal of Climatology*, *30*(13), 1908-1916.

Koster, R. D., and M. J. Suarez (1992), Modeling the Land Surface Boundary in Climate Models as a Composite of Independent Vegetation Stands, *J. Geophys. Res.*, *97*(D3), 2697-2715.

Kowalczyk, E. A., J. R. Garratt, and P. B. Krummel (1991), A soil-canopy scheme for use in a numerical model of the atmosphere – 1-D stand-alone model, *Technical Paper No. 23*, CSIRO Division of Atmospheric Research, Mordialloc, Victoria, Australia.

Kowalczyk, E. A., J. R. Garratt, and P. B. Krummel (1994), Implementation of a soil-canopy scheme into the CSIRO GCM – regional aspects of the model response, *Technical Paper No. 32*, CSIRO

Division of Atmospheric Research, Mordialloc, Victoria, Australia.

Kowalczyk, E. A., Y. P. Wang, R. M. Law, H. L. Davies, J. L. McGregor, and G. Abramowitz (2006), The CSIRO Atmosphere Biosphere Land Exchange (CABLE) model for use in climate models and as an offline model, *Research Paper 013*, CSIRO Marine and Atmospheric Research, Aspendale, Victoria, Australia.

Lacis, A. A., and J. Hansen (1974), A Parameterization for the Absorption of Solar Radiation in the Earth's Atmosphere, *Journal of the Atmospheric Sciences*, *31*(1), 118-133.

Lawrence, P. J., and T. N. Chase (2010), Investigating the climate impacts of global land cover change in the community climate system model, *International Journal of Climatology*, *30*(13), 2066-2087.

Legates, D. R., and C. J. Willmott (1990), Mean seasonal and spatial variability in gauge-corrected, global precipitation, *International Journal of Climatology*, *10*(2), 111-127.

Leung, L. R., L. O. Mearns, F. Giorgi, and R. L. Wilby (2003), Regional Climate Research, *Bulletin of the American Meteorological Society*, *84*(1), 89-95.

Leuning, R., F. M. Kelliher, D. G. G. De Pury, and E. D. Schulze (1995), Leaf nitrogen, photosynthesis, conductance and transpiration: scaling from leaves to canopies, *Plant, Cell & Environment*, *18*(10), 1183-1200.

Levis, S. (2010), Modeling vegetation and land use in models of the Earth System, *Wiley Interdisciplinary Reviews: Climate Change*, *1*(6), 840-856.

Lim, Y.-K., M. Cai, E. Kalnay, and L. Zhou (2005), Observational evidence of sensitivity of surface climate changes to land types and urbanization, *Geophys. Res. Lett.*, *32*(22), L22712.

Liu, Y., and R. Liu (2011), A long-term global Leaf area index dataset (1981-2009) from AVHRR and MODIS data, paper presented at Geoscience and Remote Sensing Symposium (IGARSS), 2011 IEEE International, 24-29 July 2011.

Livezey, R. E., and W. Y. Chen (1983), Statistical Field Significance and its Determination by Monte Carlo Techniques, *Monthly Weather Review*, *111*(1), 46-59.

Loarie, S. R., D. B. Lobell, G. P. Asner, Q. Mu, and C. B. Field (2011), Direct impacts on local climate of sugar-cane expansion in Brazil, *Nature Clim. Change*, *1*(2), 105-109.

Lybanon, M. (1984), A better least-squares method when both variables have uncertainties, *American Journal of Physics*, *52*(1), 22.

Lyons, T. J., U. S. Nair, and I. J. Foster (2008), Clearing enhances dust devil formation, *Journal of Arid Environments*, *72*(10), 1918-1928.

Lyons, T. J., H. Xinmei, P. Schwerdtfeger, J. M. Hacker, I. J. Foster, and R. C. G. Smith (1993), Land-Atmosphere Interaction in a Semiarid Region: The Bunny Fence Experiment, *Bulletin of the American Meteorological Society*, *74*(7), 1327-1334.

Mahmood, R., A. I. Quintanar, G. Conner, R. Leeper, S. Dobler, R. A. Pielke, A. Beltran-Przekurat, K. G. Hubbard, D. Niyogi, G. Bonan, P. Lawrence, T. Chase, R. McNider, Y. Wu, C. McAlpine, R. Deo, A. Etter, S. Gameda, B. Qian, A. Carleton, J. O. Adegoke, S. Vezhapparambu, S. Asefi, U. S. Nair, E. Sertel, D. R. Legates, R. Hale, O. W. Frauenfeld, A. Watts, M. Shepherd, C. Mitra, V. G. Anantharaj, S. Fall, H.-I. Chang, R. Lund, A. Treviño, P. Blanken, J. Du, and J. Syktus (2010), Impacts of Land Use/Land Cover Change on Climate and Future Research Priorities, *Bulletin of the American Meteorological Society*, *91*(1), 37-46.

Mao, J., S. J. Phipps, A. J. Pitman, Y. P. Wang, G. Abramowitz, and B. Pak (2011), The CSIRO Mk3L climate system model v1.0 coupled to the CABLE land surface scheme v1.4b: evaluation of the control climatology, *Geosci. Model Dev. Discuss.*, *4*(3), 1611-1642.

Marshall, C. H., R. A. Pielke, L. T. Steyaert, and D. A. Willard (2004), The Impact of Anthropogenic Land-Cover Change on the Florida Peninsula Sea Breezes and Warm Season Sensible Weather, *Monthly Weather Review*, *132*(1), 28-52.

McAlpine, C. A., J. Syktus, R. C. Deo, P. J. Lawrence, H. A. McGowan, I. G. Watterson, and S. R. Phinn (2007), Modeling the impact of historical land cover change on Australia's regional climate, *Geophys. Res. Lett.*, *34*.

McAvaney, B. J., C. Covey, S. Joussaume, V. Kattsov, A. Kitoh, W. Ogana, A. J. Pitman, A. J. Weaver, R. A. Wood, and Z.-C. Zhao (2001), Model Evaluation, in *Climate Change 2001: The Scientific Basis. Contribution of Working Group I to the Third Assessment Report of the Intergovernmental Panel on Climate Change*, edited by J. T. Houghton, Y. Ding, D. J. Griggs, M. Noguer, P. J. van der Linden, X. Dai, K. Maskell and C. A. Johnson, p. 881, Cambridge University Press, United Kingdom and New York, NY, USA.

McCarthy, M. P., M. J. Best, and R. A. Betts (2010), Climate change in cities due to global warming and urban effects, *Geophys. Res. Lett.*, *37*(9), L09705.

McGregor, J. L. (1993), Economical Determination of Departure Points for Semi-Lagrangian Models, *Monthly Weather Review*, *121*(1), 221-230.

McGregor, J. L., and M. R. Dix (2001), The CSIRO Conformal-Cubic Atmospheric GCM, in *IUTAM Symposium on Advances in Mathematical Modelling of Atmosphere and Ocean Dynamics*, edited by P. F. Hodnett, pp. 197-202, Kluwer Academic Publishers, Dordrecht, The Netherlands.

McNider, R. T., G. J. Steeneveld, A. A. M. Holtslag, R. A. Pielke, Sr., S. Mackaro, A. Pour-Biazar, J. Walters, U. Nair, and J. Christy (2012), Response and sensitivity of the nocturnal boundary layer over land to added longwave radiative forcing, *J. Geophys. Res.*, *117*(D14), D14106.

McPherson, R. A., D. J. Stensrud, and K. C. Crawford (2004), The Impact of Oklahoma's Winter Wheat Belt on the Mesoscale Environment, *Monthly Weather Review*, *132*(2), 405-421.

Mearns, L. O., R. W. Katz, and S. H. Schneider (1984), Extreme High-Temperature Events: Changes in their probabilities with Changes in Mean Temperature, *Journal of Climate and Applied Meteorology*, *23*(12), 1601-1613.

Meehl, G. A., T. F. Stocker, W. D. Collins, P. Friedlingstein, A. T. Gaye, J. M. Gregory, A. Kitoh, R. Knutti, J. M. Murphy, A. Noda, S. C. B. Raper, I. G. Watterson, A. J. Weaver, and Z.-C. Zhao (2007), Global Climate Projections, in *Climate Change 2007: The Physical Science Basis. Contribution of Working Group I to the Fourth Assessment Report of the Intergovernmental Panel on Climate Change*, edited by S. Solomon, D. Qin, M. Manning, Z. Chen, M. Marquis, K. B. Averyt, M. Tignor and H. L. Miller, Cambridge University Press, Cambridge, UK and New York, USA.

Mei, R., and G. Wang (2010), Rain follows logging in the Amazon? Results from CAM3–CLM3, *Climate Dynamics*, *34*(7-8), 983-996.

Min, S.-K., X. Zhang, F. W. Zwiers, and G. C. Hegerl (2011), Human contribution to more-intense precipitation extremes, *Nature*, *470*(7334), 378-381.

Murphy, D. M., and P. M. Forster (2010), On the Accuracy of Deriving Climate Feedback Parameters from Correlations between Surface Temperature and Outgoing Radiation, *Journal of Climate*, *23*(18), 4983-4988.

Nair, U. S., Y. Wu, J. Kala, T. J. Lyons, R. A. Pielke, Sr., and J. M. Hacker (2011), The role of land use change on the development and evolution of the west coast trough, convective clouds, and precipitation in southwest Australia, *J. Geophys. Res.*, *116*(D7), D07103.

Nakićenović, N., J. Alcamo, G. Davis, B. de Vries, J. Fenhann, S. Gaffin, K. Gregory, A. Griibler, T. Y. Jung, T. Kram, E. L. La Rovere, L. Michaelis, S. Mori, T. Morita, W. Pepper, H. Pitcher, L. Price, K. Riahi, A. Roehrl, H.-H. Rogner, A. Sankovski, M. Schlesinger, P. Shukla, S. Smith, R. Swart, S. van Rooijen, N. Victor, and D. Zhou (2000), *Special Report on Emissions Scenarios*, Cambridge University Press, Cambridge and New York.

Narisma, G. T., and A. J. Pitman (2003), The Impact of 200 Years of Land Cover Change on the Australian Near-Surface Climate, *Journal of Hydrometeorology*, *10*(7), 424-436.

National Research Council (2005), *Radiative Forcing of Climate Change: Expanding the Concept and Addressing Uncertainties*, The National Academies Press, Washington, D.C.

New, M., M. Hulme, and P. Jones (2000), Representing Twentieth-Century Space-Time Climate Variability. Part II: Development of 1901-96 Monthly Grids of Terrestrial Surface Climate, *Journal of Climate*, *13*(13), 2217-2238.

Nicholls, N., and L. Alexander (2007), Has the climate become more variable or extreme? Progress 1992-2006, *Progress in Physical Geography*, *31*(1), 77-87.

Nicholls, N., G. V. Gruza, J. Jouzel, T. R. Karl, L. A. Ogallo, and D. E. Parker (1996), Observed Climate Variability and Change, in *Climate Change 1995: The Science of Climate Change. Contribution of WGI to the Second Assessment Report of the Intergovernmental Panel on Climate Change*, edited by J. T. Houghton, L. G. Meira Filho, B. A. Callander, N. Harris, A. Kattenberg and K. Maskell, Cambridge University Press, Cambridge, United Kingdom.

O'Farrell, S. P. (1998), Investigation of the dynamic sea ice component of a coupled atmosphere-sea ice general circulation model, *J. Geophys. Res.*, *103*(C8), 15751-15782.

Perkins, S. E. (2011), Biases and Model Agreement in Projections of Climate Extremes over the Tropical Pacific, *Earth Interactions*, *15*(24), 1-36.

Peterson, T. C., and M. J. Manton (2008), Monitoring Changes in Climate Extremes: A Tale of International Collaboration, *Bulletin of the American Meteorological Society*, *89*(9), 1266-1271.

Peterson, T. C., K. M. Willett, and P. W. Thorne (2011), Observed changes in surface atmospheric energy over land, *Geophys. Res. Lett.*, *38*(16), L16707.

Phipps, S. J., L. D. Rotstayn, H. B. Gordon, J. L. Roberts, A. C. Hirst, and W. F. Budd (2011), The CSIRO Mk3L climate system model version 1.0 - Part 1: Description and evaluation, *Geosci. Model Dev. Discuss.*, *4*(1), 219-287.

Pielke, R. A. (2005), Land Use and Climate Change, *Science*, *310*(5754), 1625-1626.

Pielke, R. A., and M. Uliasz (1993), Influence of landscape variability on atmospheric dispersion, *J. Air Waste Manage. Assoc.*, *43*, 989-994.

Pielke, R. A., and L. Bravo de Guenni (2004), Conclusions, in *Vegetation, Water, Humans and the Climate: A New Perspective on an Interactive System*, edited by P. Kabat, M. Claussen, P. A. Dirmeyer, J. H. C. Gash, L. Bravo de Guenni, M. Meybeck, R. Pielke, C. J. Vörösmarty, R. W. A. Hutjes and S. Lütkemeier, pp. 537-538.

Pielke, R. A., A. Pitman, D. Niyogi, R. Mahmood, C. McAlpine, F. Hossain, K. K. Goldewijk, U. Nair, R. Betts, S. Fall, M. Reichstein, P. Kabat, and N. de Noblet (2011), Land use/land cover changes and climate: modeling analysis and observational evidence, *Wiley Interdisciplinary Reviews: Climate Change*, *2*(6), 828-850.

Pielke, R. A., Sr, and R. L. Wilby (2012), Regional climate downscaling: What's the point?, *Eos Trans. AGU*, *93*(5), 52-53.

Pielke, R. A. S., C. Davey, and J. Morgan (2004), Assesing "global warming" with surface heat content, *Eos Trans. AGU*, *85*(21), 210-211.

Pielke, S. R. A., J. O. Adegoke, T. N. Chase, C. H. Marshall, T. Matsui, and D. Niyogi (2007), A new paradigm for assessing the role of agriculture in the climate system and in climate change, *Agricultural and Forest Meteorology*, *142*(2-4), 234-254.

Pitman, A., and N. de Noblet-Ducoudré (2012), Human effects on climate through land-use-induced land-cover change, in *The future of the world's climate*, edited by A. Henderson-Sellers and K. McGuffie, pp. 253-288, Elsevier B.V., Amsterdam.

Pitman, A. J. (2003), The evolution of, and revolution in, land surface schemes designed for climate models, *International Journal of Climatology*, *23*(5), 479-510.

Pitman, A. J., and G. T. Narisma (2005), The role of land surface processes in regional climate change: a case study of future land cover change over south western Australia, *Meteorology and Atmospheric Physics*, *89*(1), 235-249.

Pitman, A. J., A. Arneth, and L. Ganzeveld (2012), Regionalizing global climate models, *International Journal of Climatology*, *32*(3), 321-337.

Pitman, A. J., G. T. Narisma, R. A. Pielke, Sr., and N. J. Holbrook (2004), Impact of land cover change on the climate of southwest Western Australia, *J. Geophys. Res.*, *109*(D18), D18109.

Pitman, A. J., F. B. Avila, G. Abramowitz, Y. P. Wang, S. J. Phipps, and N. de Noblet-Ducoudré (2011), Importance of background climate in determining impact of land-cover change on regional climate, *Nature Clim. Change*, *1*(9), 472-475.

Pitman, A. J., N. de Noblet-Ducoudré, F. T. Cruz, E. L. Davin, G. B. Bonan, V. Brovkin, M. Claussen, C. Delire, L. Ganzeveld, V. Gayler, B. J. J. M. van den Hurk, P. J. Lawrence, M. K. van der Molen, C. Müller, C. H. Reick, S. I. Seneviratne, B. J. Strengers, and A. Voldoire (2009), Uncertainties in climate responses to past land cover change: First results from the LUCID intercomparison study, *Geophys. Res. Lett.*, *36*(14), L14814.

Puma, M. J., and B. I. Cook (2010), Effects of irrigation on global climate during the 20th century, *J. Geophys. Res.*, *115*(D16), D16120.

Raddatz, R. L. (1998), Anthropogenic vegetation transformation and the potential for deep convection on the Canadian prairies, *Canadian journal of soil science*, *78*(4), 657-666.

Ramankutty, N., and J. A. Foley (1999), Estimating historical changes in global land cover: Croplands from 1700 to 1992, *Global Biogeochem. Cycles*, *13*(4), 997-1027.

Randall, D. A., R. A. Wood, S. Bony, R. Colman, T. Fichefet, J. Fyfe, V. Kattsov, A. Pitman, J. Shukla, J. Srinivasan, R. J. Stouffer, A. Sumi, and K. E. Taylor (2007), Climate Models and Their Evaluation, in *Climate Change 2007: The Physical Science Basis. Contribution of Working Group I to the Fourth Assessment Report of the Intergovernmental Panel on Climate Change*, edited by S. Solomon, D. Qin, M. Manning, Z. Chen, M. Marquis, K. B. Averyt, M. Tignor and H. L. Miller, pp. 589-662, Cambridge University Press, Cambridge, United Kingdom and New York, NY, USA.

Raupach, M. R., K. Finkele, and L. Zhang (1997), SCAM (Soil-Canopy-Atmosphere Model): Description and comparison with field data, *Technical Report No.132*, CSIRO Center for Environmental Mechanics.

Ray, D. K., U. S. Nair, R. M. Welch, Q. Han, J. Zeng, W. Su, T. Kikuchi, and T. J. Lyons (2003), Effects of land use in Southwest Australia: 1. Observations of cumulus cloudiness and energy fluxes, *J. Geophys. Res.*, *108*(D14), 4414.

Reynolds, R. W., N. A. Rayner, T. M. Smith, D. C. Stokes, and W. Wang (2002), An Improved In Situ and Satellite SST Analysis for Climate, *Journal of Climate*, *15*(13), 1609-1625.

Rotstayn, L. D. (1997), A physically based scheme for the treatment of stratiform clouds and precipitation in large-scale models. I: Description and evaluation of the microphysical processes, *Quarterly Journal of the Royal Meteorological Society*, *123*(541), 1227-1282.

Rotstayn, L. D. (1998), A physically based scheme for the treatment of stratiform clouds and precipitation in large-scale models. II: Comparison of modelled and observed climatological fields, *Quarterly Journal of the Royal Meteorological Society*, *124*(546), 389-415.

Rotstayn, L. D. (2000), On the "tuning" of autoconversion parameterizations in climate models, *J. Geophys. Res.*, *105*(D12), 15495-15507.

Rotstayn, L. D., W. Cai, M. R. Dix, G. D. Farquhar, Y. Feng, P. Ginoux, M. Herzog, A. Ito, J. E. Penner, M. L. Roderick, and M. Wang (2007), Have Australian rainfall and cloudiness increased due to the remote effects of Asian anthropogenic aerosols?, *J. Geophys. Res.*, *112*(10.1029/2006JD007712).

Roy, S. S., R. Mahmood, D. Niyogi, M. Lei, S. A. Foster, K. G. Hubbard, E. Douglas, and R. Pielke, Sr. (2007), Impacts of the agricultural Green Revolution-induced land use changes on air temperatures in India, *J. Geophys. Res.*, *112*(D21), D21108.

Russo, S., and A. Sterl (2011), Global changes in indices describing moderate temperature extremes from the daily output of a climate model, *J. Geophys. Res.*, *116*(D3), D03104.

Rusticucci, M., and B. Tencer (2008), Observed Changes in Return Values of Annual Temperature Extremes over Argentina, *Journal of Climate*, *21*(21), 5455-5467.

Schar, C., D. Luthi, U. Beyerle, and E. Heise (1999), The Soil-Precipitation Feedback: A Process Study with a Regional Climate Model, *Journal of Climate*, *12*(3), 722-741.

Schwarzkopf, M. D., and S. B. Fels (1985), Improvements to the Algorithm for Computing CO_2 Transmissivities and Cooling Rates, *J. Geophys. Res.*, *90*(D6), 10541-10550.

Schwarzkopf, M. D., and S. B. Fels (1991), The Simplified Exchange Method Revisited: An Accurate, Rapid Method for Computation of Infrared Cooling Rates and Fluxes, *J. Geophys. Res.*, *96*(D5), 9075-9096.

Scurlock, J. M. O., G. P. Asner, and S. T. Gower (2001), Global Leaf Area Index Data from Field Measurements, 1932-2000, edited by O. R. N. L. D. A. A. Center, Oak Ridge, Tennessee, U.S.A.

Sellers, P. (1992), Biophysical models of land surface processes, in *Climate System Modelling*, edited by K. E. Trenberth, Cambridge University Press.

Sellers, P. J., L. Bounoua, G. J. Collatz, D. A. Randall, D. A. Dazlich, S. O. Los, J. A. Berry, I. Fung, C. J. Tucker, C. B. Field, and T. G. Jensen (1996), Comparison of Radiative and Physiological Effects of Doubled Atmospheric CO_2 on Climate, *Science*, *271*(5254), 1402-1406.

Sellers, P. J., R. E. Dickinson, D. A. Randall, A. K. Betts, F. G. Hall, J. A. Berry, G. J. Collatz, A. S. Denning, H. A. Mooney, C. A. Nobre, N. Sato, C. B. Field, and A. Henderson-Sellers (1997), Modeling the Exchanges of Energy, Water, and Carbon Between Continents and the Atmosphere, *Science*, *275*(5299), 502-509.

Semtner, A. J. (1976), A Model for the Thermodynamic Growth of Sea Ice in Numerical Investigations of Climate, *Journal of Physical Oceanography*, *6*(3), 379-389.

Seneviratne, S. I., D. Luthi, M. Litschi, and C. Schär (2006a), Land-atmosphere coupling and climate change in Europe, *Nature*, *443*(7108), 205-209.

Seneviratne, S. I., T. Corti, E. L. Davin, M. Hirschi, E. B. Jaeger, I. Lehner, B. Orlowsky, and A. J.

Teuling (2010), Investigating soil moisture-climate interactions in a changing climate: A review, *Earth-Science Reviews*, *99*(3-4), 125-161.

Seneviratne, S. I., R. D. Koster, Z. Guo, P. A. Dirmeyer, E. Kowalczyk, D. Lawrence, P. Liu, D. Mocko, C.-H. Lu, K. W. Oleson, and D. Verseghy (2006b), Soil Moisture Memory in AGCM Simulations: Analysis of Global Land-Atmosphere Coupling Experiment (GLACE) Data, *Journal of Hydrometeorology*, *7*(5), 1090-1112.

Sillmann, J., and E. Roeckner (2008), Indices for extreme events in projections of anthropogenic climate change, *Climatic Change*, *86*(1), 83-104.

Silva Dias, M. A. F., S. Rutledge, P. Kabat, P. L. Silva Dias, C. Nobre, G. Fisch, A. J. Dolman, E. Zipser, M. Garstang, A. O. Manzi, J. D. Fuentes, H. R. Rocha, J. Marengo, A. Plana-Fattori, L. D. A. S·, R. C. S. Alval·, M. O. Andreae, P. Artaxo, R. Gielow, and L. Gatti (2002), Cloud and rain processes in a biosphere-atmosphere interaction context in the Amazon Region, *J. Geophys. Res.*, *107*(D20), 8072.

Souza, E. P., N. O. Rennó, and M. A. F. Silva Dias (2000), Convective Circulations Induced by Surface Heterogeneities, *Journal of the Atmospheric Sciences*, *57*(17), 2915-2922.

Spencer, R. W., and W. D. Braswell (2008), Potential Biases in Feedback Diagnosis from Observational Data: A Simple Model Demonstration, *Journal of Climate*, *21*(21), 5624-5628.

Stephens, G. L., T. L'Ecuyer, R. Forbes, A. Gettlemen, J.-C. Golaz, A. Bodas-Salcedo, K. Suzuki, P. Gabriel, and J. Haynes (2010), Dreary state of precipitation in global models, *J. Geophys. Res.*, *115*(D24), D24211.

Stephenson, D. (2008), Definition, diagnosis, and origin of extreme weather and climate events, in *Climate Extremes and Society*, edited by H. F. Diaz and R. J. Murnane, Cambridge University Press, Cambridge University Press, New York.

Stott, P. A., M. R. Allen, and G. S. Jones (2003), Estimating signal amplitudes in optimal fingerprinting. Part II: application to general circulation models, *Climate Dynamics*, *21*(5), 493-500.

Strack, J. E., R. A. Pielke, Sr., L. T. Steyaert, and R. G. Knox (2008), Sensitivity of June near-surface temperatures and precipitation in the eastern United States to historical land cover changes since European settlement, *Water Resour. Res.*, *44*(11), W11401.

Sun, D.-Z., Y. Yu, and T. Zhang (2009), Tropical Water Vapor and Cloud Feedbacks in Climate Models: A Further Assessment Using Coupled Simulations, *Journal of Climate*, *22*(5), 1287-1304.

Sun, J., S. P. Burns, A. C. Delany, S. P. Oncley, T. W. Horst, and D. H. Lenschow (2003), Heat Balance in the Nocturnal Boundary Layer during CASES-99, *Journal of Applied Meteorology*, *42*(11), 1649-1666.

Sun, Y., S. Solomon, A. Dai, and R. W. Portmann (2006), How Often Does It Rain?, *Journal of Climate*, *19*(6), 916-934.

Svoma, B. M., and R. Cerveny (2012), Analyzing bias in prominent climatic data sets, *Progress in Physical Geography*, *36*(3), 333-347.

Takata, K., K. Saito, and T. Yasunari (2009), Changes in the Asian monsoon climate during 1700–1850 induced by preindustrial cultivation, *Proceedings of the National Academy of Sciences*, *106*(24), 9586-9589.

Taylor, C. M., A. Gounou, F. Guichard, P. P. Harris, R. J. Ellis, F. Couvreux, and M. De Kauwe (2011a), Frequency of Sahelian storm initiation enhanced over mesoscale soil-moisture patterns, *Nature Geosci*, *4*(7), 430-433.

Taylor, K. E., R. J. Stouffer, and G. A. Meehl (2011b), An Overview of CMIP5 and the Experiment Design, *Bulletin of the American Meteorological Society*, *93*(4), 485-498.

Tebaldi, C., K. Hayhoe, J. Arblaster, and G. Meehl (2006), Going to the Extremes: An intercomparison of model-simulated historical and future changes in extreme events, *Climatic Change*, *79*(3), 185-211.

Teuling, A. J., S. I. Seneviratne, R. Stockli, M. Reichstein, E. Moors, P. Ciais, S. Luyssaert, B. van den Hurk, C. Ammann, C. Bernhofer, E. Dellwik, D. Gianelle, B. Gielen, T. Grunwald, K. Klumpp, L. Montagnani, C. Moureaux, M. Sottocornola, and G. Wohlfahrt (2010), Contrasting response of European forest and grassland energy exchange to heatwaves, *Nature Geosci*, *3*(10), 722-727.

Timbal, B., and J. M. Arblaster (2006), Land cover change as an additional forcing to explain the rainfall decline in the south west of Australia, *Geophys. Res. Lett.*, *33*(7), L07717.

Timbal, B., J. M. Arblaster, and S. Power (2006), Attribution of the Late-Twentieth-Century Rainfall Decline in Southwest Australia, *Journal of Climate*, *19*(10), 2046-2062.

Townshend, J. R. G. (1992), *Improved global data for land applications: a proposal for a new high resolution data set: report of the Land Cover Working Group of IGBP-DIS*, 87 pp., IGBP Secretariat, the Royal Swedish Academy of Science, Stockholm.

Trenberth, K. E., P. D. Jones, P. Ambenje, R. Bojariu, D. Easterling, A. Klein Tank, D. Parker, F. Rahimzadeh, J. A. Renwick, M. Rusticucci, B. Soden, and P. Zhai (2007), Observations: Surface and Atmospheric Climate Change, in *Climate Change 2007: The Physical Science Basis. Contribution of Working Group I to the Fourth Assessment Report of the Intergovernmental Panel on Climate Change*, edited by S. Solomon, D. Qin, M. Manning, Z. Chen, M. Marquis, K. B. Averyt, M. Tignor and H. L. Miller, pp. 235-336, Cambridge University Press, Cambridge, United Kingdom and New York, NY, USA.

UN (2012), World Urbanization Prospects: The 2011 Revision.

van Haren, R., G. J. van Oldenborgh, G. Lenderink, M. Collins, and W. Hazeleger (2012), SST and circulation trend biases cause an underestimation of European precipitation trends, *Climate Dynamics*, 1-20.

von Storch, H., and F. W. Zwiers (1999), *Statistical Analysis in Climate Research*, Cambrige University Press.

Vose, R. S., D. R. Easterling, and B. Gleason (2005), Maximum and minimum temperature trends for the globe: An update through 2004, *Geophys. Res. Lett.*, *32*(23), L23822.

Wang, J., F. d. r. J. F. Chagnon, E. R. Williams, A. K. Betts, N. O. Renno, L. A. T. Machado, G. Bisht, R. Knox, and R. L. Bras (2009), Impact of deforestation in the Amazon basin on cloud climatology, *Proceedings of the National Academy of Sciences*, *106*(10), 3670-3674.

Wang, W. C., X. Z. Liang, M. P. Dudek, D. Pollard, and S. L. Thompson (1995), Atmospheric ozone as a climate gas, *Atmospheric Research*, *37*(1-3), 247-256.

Wang, Y. P., and R. Leuning (1998), A two-leaf model for canopy conductance, photosynthesis and partitioning of available energy I: Model description and comparison with a multi-layered model, *Agricultural and Forest Meteorology*, *91*(1-2), 89-111.

Wang, Y. P., E. Kowalczyk, R. Leuning, G. Abramowitz, M. R. Raupach, B. Pak, E. van Gorsel, and A. Luhar (2011), Diagnosing errors in a land surface model (CABLE) in the time and frequency domains, *J. Geophys. Res.*, *116*(G1), G01034.

Wardle, R., and I. Smith (2004), Modeled response of the Australian monsoon to changes in land surface temperatures, *Geophys. Res. Lett.*, *31*(16), L16205.

Wichansky, P. S., L. T. Steyaert, R. L. Walko, and C. P. Weaver (2008), Evaluating the effects of historical land cover change on summertime weather and climate in New Jersey: Land cover and surface energy budget changes, *J. Geophys. Res.*, *113*(D10), D10107.

Wilks, D. S. (1997), Resampling Hypothesis Tests for Autocorrelated Fields, *Journal of Climate*, *10*(1), 65-82.

Williams, M. (2002), *Deforesting the earth: From prehistory to global crisis*, 715 pp., The University of Chicago Press, Chicago.

Willmott, C. J., and K. Matsuura (2001), Terrestrial Air Temperature and Precipitation: Monthly and Annual Time Series (1950 - 1999) Version 1.02 (Archive), edited, Center for Climatic Research, Department of Geography, University of Delaware, Newark, DE 19716.

Xie, P., and P. A. Arkin (1997), Global Precipitation: A 17-Year Monthly Analysis Based on Gauge Observations, Satellite Estimates, and Numerical Model Outputs, *Bulletin of the American Meteorological Society*, *78*(11), 2539-2558.

Yuan, H., Y. Dai, Z. Xiao, D. Ji, and W. Shangguan (2011), Reprocessing the MODIS Leaf Area Index products for land surface and climate modelling, *Remote Sensing of Environment*, *115*(5), 1171-1187.

Zhang, X., L. Alexander, G. C. Hegerl, P. Jones, A. K. Tank, T. C. Peterson, B. Trewin, and F. W. Zwiers (2011), Indices for monitoring changes in extremes based on daily temperature and precipitation data, *Wiley Interdisciplinary Reviews: Climate Change*, *2*(6), 851-870.

Zhang, Y., W. B. Rossow, A. A. Lacis, V. Oinas, and M. I. Mishchenko (2004), Calculation of radiative fluxes from the surface to top of atmosphere based on ISCCP and other global data sets: Refinements of the radiative transfer model and the input data, *J. Geophys. Res.*, *109*(D19), D19105.

Zhao, M., A. J. Pitman, and T. Chase (2001), The impact of land cover change on the atmospheric circulation, *Climate Dynamics*, *17*(5), 467-477.

Zobler, L. (1986), A world soil file for global climate modeling, *NASA Technical Memorandum 87802*, 32 pp, National Aeronautic and Space Administration, Goddard Space Flight Center, Institute for Space Studies.

Zwiers, F. W., and H. von Storch (1995), Taking Serial Correlation into Account in Tests of the Mean, *Journal of Climate*, *8*(2), 336-351.

Zwiers, F. W., and V. V. Kharin (1998), Changes in the Extremes of the Climate Simulated by CCC GCM2 under CO_2 Doubling, *Journal of Climate*, *11*(9), 2200-2222.

APPENDIX 1
ETCCDI Climate Change Indices

This appendix contains a copy of the ETCCDI Climate Change Indices available at *http://cccma.seos.uvic.ca/ETCCDI/list_27_indices.shtml* which was last accessed on 4 June 2012.

ETCCDI/CRD Climate Change Indices

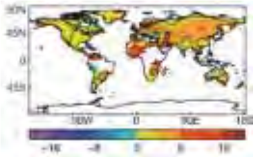

Climate Change Indices

Definitions of the 27 core indices

1. FD, *Number of frost days*: Annual count of days when TN (daily minimum temperature) < 0^{o}C.

Let TN_{ij} be daily minimum temperature on day *i* in year *j*. Count the number of days where:

TN_{ij} < 0^{o}C.

2. SU, *Number of summer days*: Annual count of days when TX (daily maximum temperature) > 25^{o}C.

Let TX_{ij} be daily maximum temperature on day *i* in year *j*. Count the number of days where:

TX_{ij} > 25^{o}C.

3. ID, *Number of icing days*: Annual count of days when TX (daily maximum temperature) < 0^{o}C.

Let TX_{ij} be daily maximum temperature on day *i* in year *j*. Count the number of days where:

TX_{ij} < 0^{o}C.

4. TR, *Number of tropical nights*: Annual count of days when TN (daily minimum temperature) > 20^{o}C.

Let TN_{ij} be daily minimum temperature on day *i* in year *j*. Count the number of days where:

TN_{ij} > 20^{o}C.

5. GSL, *Growing season length*: Annual (1st Jan to 31st Dec in Northern Hemisphere (NH), 1st July to 30th June in Southern Hemisphere (SH)) count between first span of at least 6 days with daily mean temperature TG>5^{o}C and first span after July 1st (Jan 1st in SH) of 6 days with TG<5^{o}C.

Let TG_{ij} be daily mean temperature on day *i* in year *j*. Count the number of days between the first occurrence of at least 6 consecutive days with:

TG_{ij} > 5^{o}C.

and the first occurrence after 1st July (1st Jan. in SH) of at least 6 consecutive days with:

TG_{ij} < 5^{o}C.

6. TX_x, *Monthly maximum value of daily maximum temperature*:

Let TX_x be the daily maximum temperatures in month *k*, period *j*. The maximum daily maximum temperature each month is then:

$TX_{x_{kj}}=\max(TX_{x_{kj}})$

7. TN_x, *Monthly maximum value of daily minimum temperature*:

Let TN_x be the daily minimum temperatures in month *k*, period *j*. The maximum daily minimum temperature each month is then:

$TN_{x_{kj}}=\max(TN_{x_{kj}})$

8. TX_n, *Monthly minimum value of daily maximum temperature*:

Let TX_n be the daily maximum temperatures in month *k*, period *j*. The minimum daily maximum temperature each month is then:

$TX_{n_{kj}}=\min(TX_{n_{kj}})$

9. TN_n, *Monthly minimum value of daily minimum temperature*:

Let TN_n be the daily minimum temperatures in month *k*, period *j*. The minimum daily minimum temperature each month is then:

$TN_{n_{kj}}=\min(TN_{n_{kj}})$

10. TN10p, *Percentage of days when TN < 10^{th} percentile*:

Let TN_{ij} be the daily minimum temperature on day *i* in period *j* and let $TN_{in}10$ be the calendar day 10^{th} percentile centred on a 5-day window for the base period 1961-1990. The percentage of time for the base period is determined where:

$TN_{ij} < TN_{in}10$

To avoid possible inhomogeneity across the in-base and out-base periods, the calculation for the base period (1961-1990) requires the use of a bootstrap processure. Details are described in Zhang et al. (2004) .

11. TX10p, *Percentage of days when TX < 10^{th} percentile*:

Let TX_{ij} be the daily maximum temperature on day *i* in period *j* and let $TX_{in}10$ be the calendar day 10^{th} percentile centred on a 5-day window for the base period 1961-1990. The percentage of time for the base period is determined where:

$TX_{ij} < TX_{in}10$

To avoid possible inhomogeneity across the in-base and out-base periods, the calculation for the base period (1961-1990) requires the use of a bootstrap processure. Details are described in Zhang et al. (2004) .

12. TN90p, *Percentage of days when TN > 90^{th} percentile*:

Let TN_{ij} be the daily minimum temperature on day *i* in period *j* and let $TN_{in}90$ be the calendar day 90^{th} percentile centred on a 5-day window for the base period 1961-1990. The percentage of time for the base period is determined where:

$TN_{ij} > TN_{in}90$

To avoid possible inhomogeneity across the in-base and out-base periods, the calculation for the base period (1961-1990) requires the use of a bootstrap processure. Details are described in Zhang et al. (2004) .

13. TX90p, *Percentage of days when TX > 90th percentile*:

Let TX_{ij} be the daily maximum temperature on day *i* in period *j* and let $TX_{in}90$ be the calendar day 90^{th} percentile centred on a 5-day window for the base period 1961-1990. The percentage of time for the base period is determined where:

$TX_{ij} > TX_{in}90$

To avoid possible inhomogeneity across the in-base and out-base periods, the calculation for the base period (1961-1990) requires the use of a bootstrap processure. Details are described in Zhang et al. (2004) .

14. WSDI, *Warm speel duration index*: Annual count of days with at least 6 consecutive days when TX > 90^{th} percentile

Let TX_{ij} be the daily maximum temperature on day *i* in period *j* and let $TX_{in}90$ be the calendar day 90^{th} percentile centred on a 5-day window for the base period 1961-1990. Then the number of days per period is summed where, in intervals of at least 6 consecutive days:

$TX_{ij} > TX_{in}90$

15. CSDI, *Cold speel duration index*: Annual count of days with at least 6 consecutive days when TN < 10^{th} percentile

Let TN_{ij} be the daily maximum temperature on day *i* in period *j* and let $TN_{in}10$ be the calendar day 10^{th} percentile centred on a 5-day window for the base period 1961-1990. Then the number of days per period is summed where, in intervals of at least 6 consecutive days:

$TN_{ij} < TN_{in}10$

16. DTR, *Daily temperature range*: Monthly mean difference between TX and TN

Let TX_{ij} and TN_{ij} be the daily maximum and minimum temperature respectively on day *i* in period *j*. If *I* represents the number of days in *j*, then:

$$DTR_j = \frac{\sum_{i=1}^{I} (Tx_{ij} - Tn_{ij})}{I}$$

17. Rx1day, *Monthly maximum 1-day precipitation*:

Let RR_{ij} be the daily precipitation amount on day *i* in period *j*. The maximum 1-day value for period *j* are:

$Rx1day_j = \max(RR_{ij})$

18. Rx5day, *Monthly maximum consecutive 5-day precipitation*:

Let RR_{kj} be the precipitation amount for the 5-day interval ending $_k$, period *j*. Then maximum 5-day values for period *j* are:

$Rx5day_j = \max(RR_{kj})$

19. SDII *Simple pricipitation intensity index*: Let RR_{wj} be the daily precipitation amount on wet days, *w (RR ≥ 1mm)* in period *j*. If *W* represents number of wet days in *j*, then:

$$SDII_j = \frac{\sum_{w=1}^{W} RR_{wj}}{W}$$

20. R10mm *Annual count of days when PRCP≥ 10mm*: Let RR_{ij} be the daily precipitation amount on day *i* in period *j*. Count the number of days where:

$RR_{ij} \geq 10mm$

21. R20mm *Annual count of days when PRCP≥ 20mm*: Let RR_{ij} be the daily precipitation amount on day *i* in period *j*. Count the number of days where:

$RR_{ij} \geq 20mm$

22. Rnnmm *Annual count of days when PRCP≥ nnmm, nn is a user defined threshold*: Let RR_{ij} be the daily precipitation amount on day *i* in period *j*. Count the number of days where:

$RR_{ij} \geq nnmm$

23 CDD. *Maximum length of dry spell, maximum number of consecutive days with RR < 1mm*: Let RR_{ij} be the daily precipitation amount on day *i* in period *j*. Count the largest number of consecutive days where:

$RR_{ij} < 1mm$

24 CWD. *Maximum length of wet spell, maximum number of consecutive days with RR ≥ 1mm*: Let RR_{ij} be the daily precipitation amount on day *i* in period *j*. Count the largest number of consecutive days where:

$RR_{ij} \geq 1mm$

25. R95pTOT. *Annual total PRCP when RR > 95p*. Let RR_{wj} be the daily precipitation amount on a wet day *w (RR ≥ 1.0mm)* in period *i* and let $RR_{wn}95$ be the 95th percentile of precipitation on wet days in the 1961-1990 period. If *W* represents the number of wet days in the period, then:

$$R95p_j = \sum_{w=1}^{W} RR_{wj} \text{ where } RR_{wj} > RR_{wn}95$$

26. R99pTOT. *Annual total PRCP when RR > 99p*: Let RR_{wj} be the daily precipitation amount on a wet day *w* ($RR \geq 1.0mm$) in period *i* and let $RR_{wn}99$ be the 99th percentile of precipitation on wet days in the 1961-1990 period. If *W* represents the number of wet days in the period, then:

$$R99p_j = \sum_{w=1}^{W} RR_{wj} \text{ where } RR_{wj} > RR_{wn}99$$

27. PRCPTOT. *Annual total precipitation in wet days*: Let RR_{ij} be the daily precipitation amount on day *i* in period *j*. If *I* represents the number of days in *j*, then

$$PRCPTOT_j = \sum_{i=1}^{I} RR_{ij}$$

References

- Karl, T.R., N. Nicholls, and A. Ghazi, 1999: CLIVAR/GCOS/WMO workshop on indices and indicators for climate extremes: Workshop summary. *Climatic Change*, **42**, 3-7.
- Peterson, T.C., and Coauthors: Report on the Activities of the Working Group on Climate Change Detection and Related Rapporteurs 1998-2001. WMO, Rep. WCDMP-47, WMO-TD 1071, Geneve, Switzerland, 143pp.

Last updated 2009-09-15